The Effect of Humpback Whale-Like Leading Edge Protuberances on Hydrofoil Performance

By

Derrick Custodio

A Dissertation

Submitted to the Faculty

of the

WORCESTER POLYTECHNIC INSTITUTE

in partial fulfillment of the requirements for the

Degree of Doctor of Philosophy

In

Mechanical Engineering

By

_____

May 2012

APPROVED:

_____

Dr. Hamid Johari, Advisor

_____

Dr. John J. Blandino, Graduate Committee Representative

_____

Dr. David J. Olinger, Committee Member

_____

Dr. Charles W. Henoch, Committee Member

_____

Dr. Mark W. Richman, Committee Member

Abstract

The humpback whale is very maneuverable despite its enormous size and rigid body. This agility has been attributed to the use of its pectoral flippers, along the leading edge of which protuberances are present. The leading edge protuberances are considered by some biologists to be a form of passive flow control and/or drag reduction. Force and moment measurements along with qualitative and quantitative flow visualizations were carried out in water tunnel experiments on full-span and finite-span hydrofoil models with several different planforms and protuberance geometries. A NACA 63_4-021 cross-sectional airfoil profile was used for the baseline foil in all tests. Four planform geometries chosen included: a full-span set of foils which spanned the breadth of the water tunnel, a finite-span rectangular planform, a finite-span swept hydrofoil, and a scale flipper model that resembled the morphology of the humpback whale flipper. A variety of sinusoidal protuberance geometries which included three amplitudes equal to 2.5%, 5%, and 12% and wavelengths of 25% and 50% of the local chord were examined in combination with the different planform geometries. Testing included force and moment measurements and Particle Image Velocimetry (PIV) to examine the load characteristics and flow field surrounding the modified foils. Load measurements show that modified foils are capable of generating higher lift than the baseline at high angles of attack while at low angle of attack the baseline generally produces a lift coefficient equal to or greater than the modified cases. With the exception of the modified flipper model, the drag coefficients of the modified hydrofoils are either equal to or greater than their baseline counterparts. The increased drag reduces the lift-to-drag ratio. Flow visualizations show that vortical structures emanating from the shoulders of the protuberances are responsible for increased lift and drag at high angles. Cavitation tests show that modified foils cavitate in pockets behind the troughs of protuberances whereas the baseline foils produce cavitation along the entire foil span. Also, the cavitation numbers on modified hydrofoils were consistently higher than their baseline counterparts. This work shows the effect of leading edge protuberances on the aforementioned performance characteristics.

Contents

Nomenclature

A	=	protuberance amplitude
AR	=	semi-span aspect ratio
b	=	length of span
c	=	mean length of chord
C_L	=	lift coefficient
C_D	=	drag coefficient
$C_{M1/4}$	=	quarter chord pitching moment coefficient
D	=	drag force
h	=	vortex height above foil surface
k	=	cavitation number
L	=	lift force
M	=	pitching moment
p	=	local static pressure
p_v	=	vapor pressure of water
Re_c	=	Reynolds number with respect to chord length
U_∞	=	freestream velocity
x	=	chordwise coordinate
α	=	angle of attack
λ	=	protuberance wavelength
Γ	=	vortex circulation
ρ	=	freestream density of water
4S	=	hydrofoil with wavelength of 0.050 c, and amplitude of 0.025 c
4M	=	hydrofoil with wavelength of 0.050 c, and amplitude of 0.050 c
4L	=	hydrofoil with wavelength of 0.050 c, and amplitude of 0.120 c
8S	=	hydrofoil with wavelength of 0.250 c, and amplitude of 0.025 c
8M	=	hydrofoil with wavelength of 0.250 c, and amplitude of 0.050 c
8L	=	hydrofoil with wavelength of 0.250 c, and amplitude of 0.120 c

I. Introduction

The humpback whale (*Megaptera novaeangliae*) is unique in that despite its large size and rigid body, it is quite maneuverable. Biologists speculate that the maneuverability can be attributed to the use of the pectoral flippers. The flipper has several distinguishable characteristics; it has a very unique planform shape which is quite flexible, a long aspect ratio with the span being as much as 1/3 the body length of the whale, and large distinct protuberances along the leading edge. The theory of natural selection provides an indication that the protuberances perform a function that aids in the whale's ability to survive. In fact, scientists have hypothesized that the protuberances act as a form of flow control, which leads to the ability of the whale to capture prey.

The focus of this dissertation will be on these leading edge protuberances and their potential role in enhancing existing airfoil and hydrofoil technology. If it is true that the whale does take advantage of the protuberances, it is very likely that the protuberances have evolved over time and are specialized to perform a very specific role in the whale's ability to survive. However, due to the large variety of parameters that lead to the modification of the flow field surrounding the natural flipper, the following work has been simplified so that only the effect of the protuberances on the flow field is inspected. Also, due to the wide range of potential applications of the technology presented here, the parameters have been chosen in such a way that practical engineering applications are kept in mind.

Background

Recently, there has been considerable interest in biomimetic flow control systems. This has brought about a number of investigations into the study of bio-inspired passive and active flow control mechanisms similar to the morphology of swimming animals. The review article by

Fish and Lauder[2] mentions the humpback whales' exceptional mobility, examines the unsteady motions of aquatic animals, and discusses their use of flow control mechanisms to maneuver though water. Despite their large size (ranging from 12 – 16 m), the humpback whale is quite maneuverable compared to other species and is capable of extreme turning maneuvers and tight turning radii for its body size especially during the pursuit of prey. This agility has been attributed to the humpback whales' use of its unique pectoral flipper shown in Figure 1[1]. Biologists have determined that the tight turning radii of extreme maneuvers such as bubble netting are unique to the humpback whale and speculate that the protuberances located along the leading edge of the pectoral flipper are used as a mechanism of passive flow control and/or drag reduction[1,3].

Figure 1: Pectoral flipper of the humpback whale[30,31].

The humpback whale flipper has a relatively large aspect ratio ($b/c \approx 6$) and large scale protuberances along the leading edge[1]. For the most part, the cross-section of the humpback whale flipper, shown in Figure 2, has a symmetric profile with a round leading edge and a sharp trailing edge. The protuberances found along the leading edge of the humpback flipper vary in amplitude and wavelength with span. The amplitude of the protuberances range from 2.5% to 12% of the chord length and the wavelength varies from 10% to 50% of the chord. The thickness

ratio varies over the span and has a maximum thickness that ranges from 0.20*c* to 0.28*c*, with an average of 0.23*c,* decreasing from mid-span to tip. The point of maximum thickness ratio varies from 0.20*c* to 0.40*c*. The cross-section of the flipper has a profile similar to a NACA 63_4-021 airfoil profile, as determined by Fish and Battle[1]. This profile was used for all of the baseline foils throughout this work.

The baseline airfoil generates lift by accelerating flow over the suction surface of the hydrofoil, thereby creating a pressure differential on opposing sides. This pressure differential is also responsible for the formation of wingtip vortices on finite-span hydrofoils[29]. The high thickness ratio, large leading edge radius, and symmetry of the baseline airfoil profile used in this work result in a flow separation bubble that begins at the trailing edge of the hydrofoil and move toward the leading edge with increasing angle of attack. When flow separation reaches the leading edge, a dramatic loss in lift, along with an increase in drag typically occur. The angle at which flow attachment is lost on the leading edge is considered the stall angle. This is contrary to a profile with a lower thickness ratio, which has a tendency to initially separate dramatically at the leading edge. A comparison between the humpback whale flipper cross-sections and the NACA 63_4-021 airfoil profile is shown in Figure 2**.**

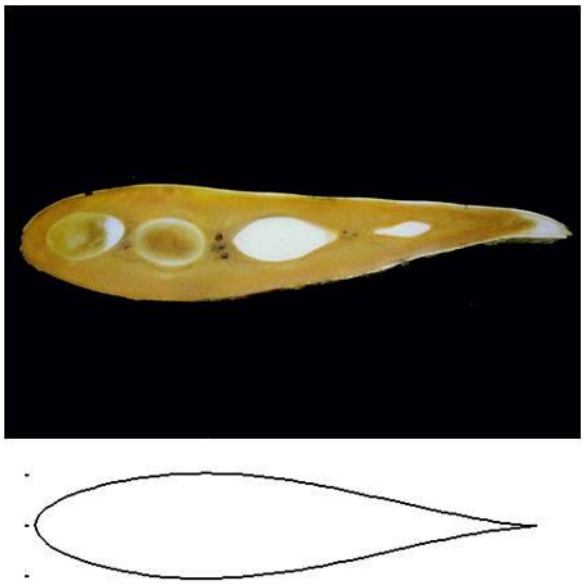

Figure 2: Top) Cross-section of the humpback whale pectoral flipper. Bottom) NACA 63_4-021 airfoil profile.

Several experimental and numerical studies have been carried out on airfoil and hydrofoil models with leading edge protuberances. Using panel methods, Watts and Fish computed the flow on a low aspect ratio wing with leading edge protuberances at an angle of attack $\alpha = 10°$ and showed a lift increase of 4.8% over the baseline wing[18]. Miklosovic et al. measured the lift and drag of humpback whale flipper models in a wind tunnel at a chordwise Reynolds number of $Re_c = 5.0 \times 10^5$. A 6% increase in the maximum lift and a 4° higher stall angle of attack for the flipper model with the protuberances was reported[18], see Figure 3. The models examined by Miklosovic et al. had planforms that resembled the morphology of the humpback whale flipper. The study compared a baseline flipper model to a protuberance modified model with much more uniform leading edge geometry than of the humpback whale. Unique to Miklosovic's study, the results show that over a limited range of angles of attack, $10° \leq \alpha \leq 18°$, drag coefficient was reduced by as much as 5% compared to the baseline case. Due to the increase in lift coefficient

and reduced drag at high angle, an increased lift-to-drag ratio was found. Also, increased lift generation was observed on the modified model in the post-stall regime of the baseline.

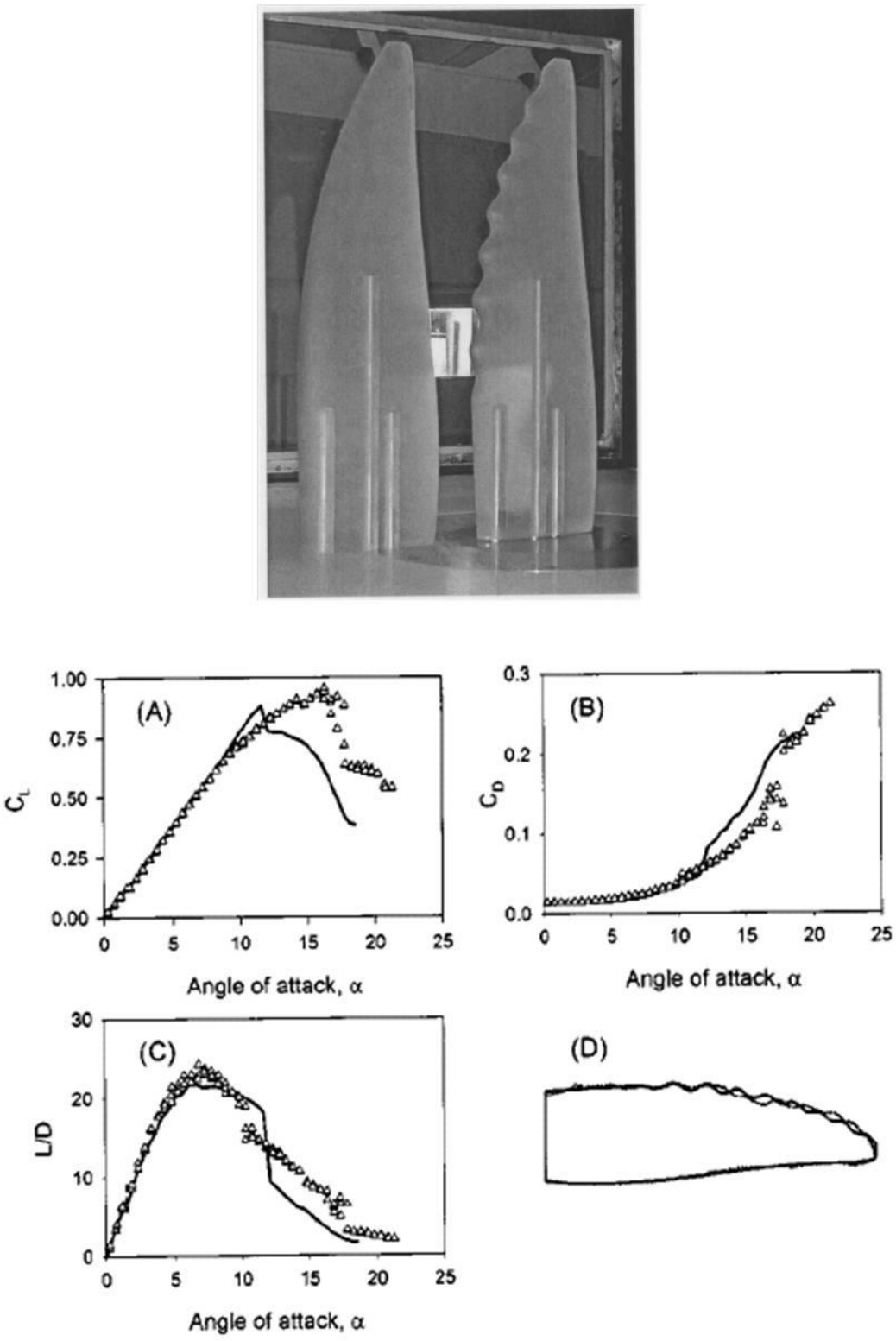

Figure 3: Top: Flipper models tested by Miklosovic5. Bottom: a) Lift coefficient b) Drag coefficient c) Lift-to-drag ratio d) flipper model design.

Experimental work by the present author examined the effect of spanwise uniform sinusoidal leading edge protuberances on a set of full-span hydrofoils with variable protuberance wavelength and amplitude at a Reynolds number of $Re_c = 1.8 \times 10^5$. No drag reduction was observed on any of the hydrofoils tested, but the lift coefficient of modified hydrofoils could be increased by as much as 50% over the baseline in the post-stall regime, see Figure 4. The variance of leading edge geometry played a large role in establishing the lift and drag characteristics of modified hydrofoils as well. In the pre-stall regime, lift was typically observed to be significantly lower while drag was increased and in the post-stall regime lift was generally much higher on modified foils with little to no drag penalty. At angles of attack greater than 10°, the foils with the largest amplitude protuberances showed little variation in lift coefficient when compared to the baseline foil over the entire range of angles tested. Johari et al.[7] shows that while amplitude plays a large role in establishing the lift and drag characteristics of modified hydrofoils, wavelength plays a very minor role, at least for the range examined. Also, through flow visualizations using surface tufts, patterns of vorticity stemming from the shoulders of protuberances are responsible for establishing flow field patterns.

Coinciding with Miklosovic[5] and Johari et al.[7], Stein and Murray[19] show that a loss of lift and increased drag is seen in a full-span study at pre-stall angles of attack. Similar to Johari et al.[7], Stein and Murray[19] examined full-span hydrofoils, whereas others typically looked at finite-span models.

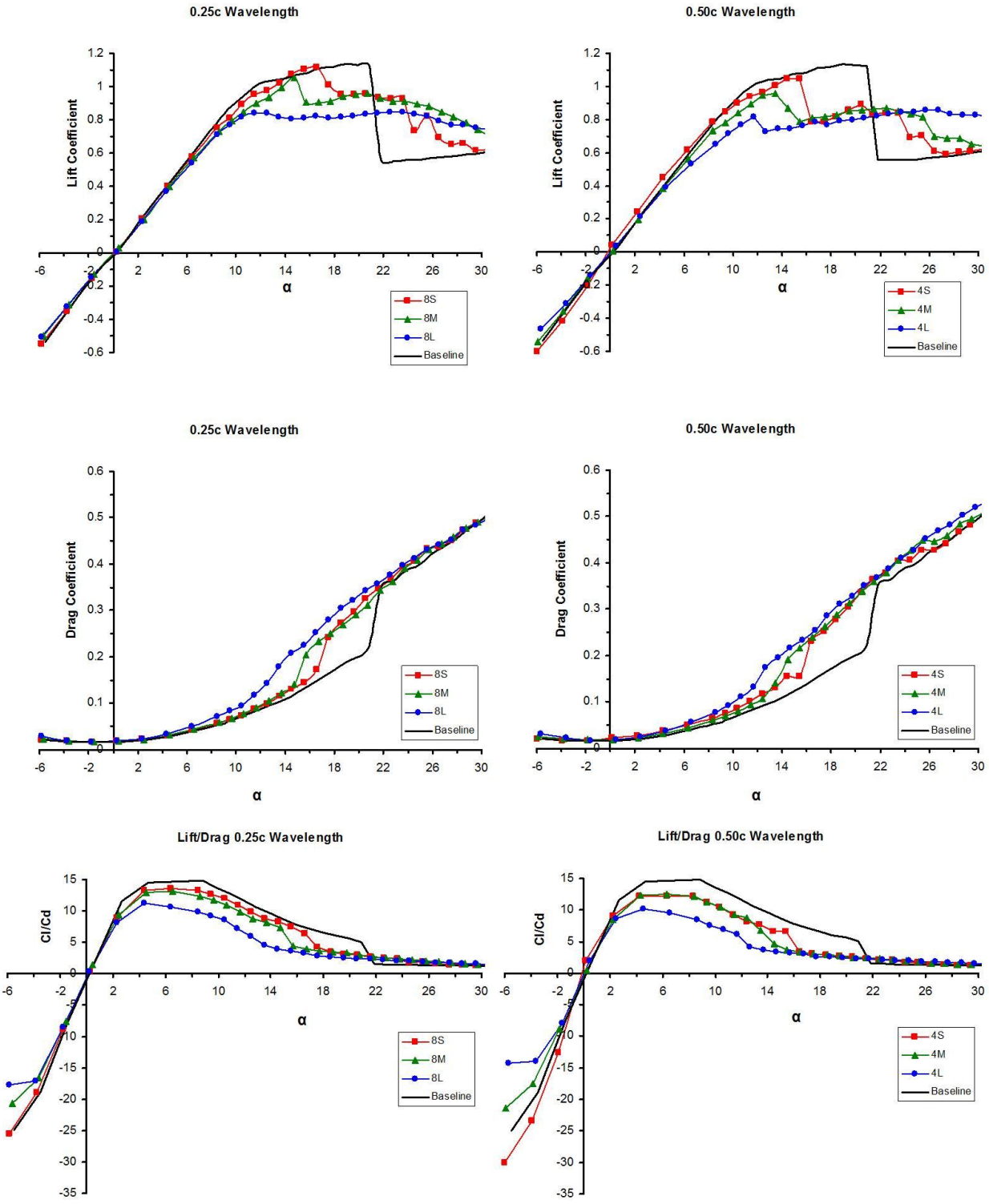

Figure 4: Lift and drag performance of hydrofoils tested by Johari et al.[7].

With the exception of Miklosovic et. al[5], previous work by other authors showing load measurements at Reynolds numbers greater than 2.7×10^5 is not available. Several experimental studies have examined the force and moment characteristics of hydrofoils resembling the humpback whale flipper, however, with the exception of the work of Johari et al.[7], to date there has been no systematic study the effect of protuberance geometry on the performance of hydrofoils with leading edge protuberances.

Several recent works have also compared the lift and drag of rudders and finite-span foils with and without leading edge protuberances [21,22,8]. The flow field over a model flipper was examined at an angle of attack of $\alpha = 15°$ using the Detached Eddy Simulation technique at Reynolds number of 5.0×10^5. The lift and drag of a series of finite-span foils were investigated in the wind tunnel experiments of Hansen et al.[22] at Reynolds numbers of 1.2×10^5. Rudders with and without leading edge protuberances were tested in a water tunnel at Reynolds numbers up to 8.8×10^5. The latter two studies indicate that Reynolds number plays a nontrivial role, especially at low Reynolds numbers.

Applications

Nearly all systems which take advantage of lifting surfaces such as hydrofoils or airfoils could potentially benefit from leading edge protuberances. Some applications for this technology might include passive or active flow control mechanisms, propulsion systems, and control surfaces. Specifically, the focus of this work is on investigating the fundamental nature of flow modifications resulting from leading edge protuberances. The humpback whale has evolved to use its tail as a method of propulsion while the pectoral flippers are reserved for maneuvering. With this in mind, the scope of this report has been confined to maneuvering purposes. For example, the placement of protuberances on the rudders or tail fins of underwater vessels are

possible implementations of this technology. It will be shown later that leading edge protuberances tend to increase performance only over limited ranges of angle. Consequently, it is likely that protuberances are most useful as an active flow control mechanism that is activated at only certain angles of attack or as a passive flow control mechanism that only operates at specific angles of attack. As an active mechanism, protuberances could be activated in the same manner as wing flaps. Potentially, they could be retracted into a wing or control surface and, when necessary, be activated so that they protrude from the leading edge. Ref. 24 shows that there is little detrimental effect when protuberances are added to the leading edge of a straight leading edge geometry.

Propulsion systems could also be enhanced with leading edge protuberances. Propellers, impellers, and turbomachinery all take advantage of hydrofoil/airfoil technology. There has also been recent interest in biomimetic propulsion devices that propel vessels through water in a manner that resembles fish and other underwater animals. Leading edge protuberances could potentially be used as a supplement to propulsions systems which take advantage of flapping/dynamic propulsion systems. The scope of this report stays within the realm of rigid, dynamic hydrofoils; however, an examination of the effect of leading edge protuberances on mobile or flexible hydrofoil structures would be a very useful extension of this work.

Objectives

The work presented here examines the effect of leading edge protuberances on a specific hydrofoil profile geometry as well as several different planform geometries. Past work by the present author[24] focused only on the effect of leading edge protuberances on full-span geometries at a chordwise Reynolds number of 1.8×10^5. The current work is an extension of past research in that protuberance geometries similar to those examined in Johari et. al and Custodio[7,24] are

being studied, but with a range of implementation that has been extended to both higher Reynolds number and finite-span planform geometries. This research is focused on both more practical hydrofoil geometries and Reynolds numbers. The objectives of this report can be summarized in the following way:

- To examine the effect of Reynolds number on the load characteristics and flow field of infinite and finite-span hydrofoil geometries.
- To examine the effect of protuberance amplitude and wavelength on the load characteristics and flow field of finite-span rectangular planform geometries.
- To examine the lift and drag response of hydrofoils with different planform geometries to leading edge protuberances. These geometries include swept leading edge as well as a flipper model.
- To understand the mechanisms responsible for performance modifications and the flow fields causing such changes.
- To examine the cavitation characteristics of hydrofoils with leading edge protuberances.

II. Experimental Setup

NUWC High-speed Water Tunnel Facility

All experiments presented here, with the exception of low-speed Particle Image Velocimetry (PIV) flow visualization tests, were carried out at the Naval Undersea Warfare Center (NUWC) high-speed closed loop water tunnel facility in Newport, RI. A schematic of this facility is shown in Figure 5. The water tunnel test section is 0.30 m square, and capable of reaching freetstream velocities of $U_\infty = 10.0$ m/s.

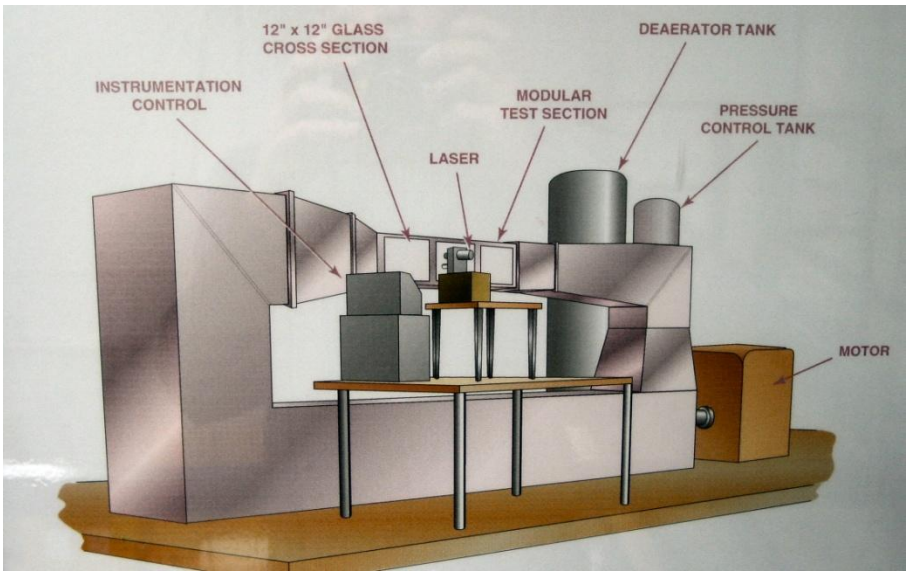

Figure 5: Schematic of the NUWC water Tunnel

The freestream velocity for all tests was recorded and held constant at a point located in the center of the water tunnel test section at a point 6.5*c* upstream of the model. The velocity was monitored so that it was always held constant using the Laser Doppler Velocimetry (LDV) technique, a non-invasive method of evaluating instantaneous flow velocities. Due to the confined nature of a model in a closed water tunnel, the cross-sectional area of the tunnel test section is partially occupied, or blocked, by the model being examined. As a result of blockage effects, the velocity in the vicinity of the model is increased; therefore the model experiences

increased local freestream velocities. To account for this effect, it was necessary to monitor the upstream freestream velocity at a point at which it could be considered unaffected by the model. To account for tunnel blockage effects beyond freestream variations, all recorded forces and moments were corrected for blockages using the traditional methods outlined by Pope and Ray[25].

The freestream velocities used in testing varied widely, ranging from $0.15 \leq U_\infty \leq 9.00$ m/s, which corresponds to chordwise Reynolds numbers ranging from $1.50 \times 10^4 \leq Re_c \leq 9.00 \times 10^5$, depending on the objective of the experiment.

WPI Low-speed Water Tunnel Facility

The low-speed full-span Particle Image Velocimetry (PIV) tests presented here were carried out in the Worcester Polytechnic Institute (WPI) Hydrodynamics Lab, in Worcester, MA, which housed a free surface low-speed water tunnel, with a 0.61 m square test section capable of sustaining freestream velocities of up to 0.4 m/s.

Hydrofoil Sections

A variety of hydrofoil models, described in detail below, with modified sinusoidal leading edge geometries similar to the wavelength and amplitude range of the protuberances found on the humpback whale flipper, were designed using Pro-Engineer and SolidWorks computer-aided design (CAD) software suites. All hydrofoils tested maintained an underlying NACA 63_4-021 airfoil profile, a symmetric profile with a maximum thickness to chord ratio of 21%. This profile was chosen for its cross-sectional similarity to the humpback whale flipper. Four different sets of hydrofoils distinguished by planform shape were examined: (a) infinite-span rectangular which was bounded at the ends by the tunnel walls, (b) finite-span rectangular planforms with rounded tips, (c) a swept leading edge planform hydrofoil model, and (d) a flipper model whose planform shape closely resembled the morphology of the humpback whale

flipper. With the exception of the flipper models, the leading edge protuberance amplitude and wavelength was spanwise uniform as a constant fraction of the local chordlength. The leading edge geometries were defined by sinusoidal protuberances which were defined by amplitude and wavelength. The local chord as a function of span of the modified hydrofoils can be described by the following equation:

$$c(z) = c + Asin(2\pi\frac{z}{\lambda} - \frac{\pi}{2}).$$

Three amplitudes were examined, $A = 0.025c$, $A = 0.050c$, and $A = 0.120c$, along with two wavelengths $\lambda = 0.25c$, and $\lambda = 0.50c$. For ease of understanding, the nomenclature used throughout describes the leading edge geometries as follows; 8 and 4 represent wavelengths of $\lambda = 0.25c$, and $\lambda = 0.50c$, respectively, and S (small), M (medium), and L (large) represent amplitudes of $A = 0.025c$, $A = 0.050c$, and $A = 0.120c$, respectively. These values were chosen as they are representative of those found on the humpback whale in nature. Table 1shows the nomenclature that will be used to differentiate the hydrofoils throughout this report:

Table 1: Nomenclature used to describe modified hydrofoils.

	$\boldsymbol{A = 0.025c}$	$\boldsymbol{A = 0.050c}$	$\boldsymbol{A = 0.120c}$
$\boldsymbol{\lambda = 0.25c}$	**8S**	**8M**	**8L**
$\boldsymbol{\lambda = 0.50c}$	**4S**	**4M**	**4L**

For the given set of hydrofoils, the mean chord length was kept the same. This was done to ensure that the planform area of all hydrofoils of a set remained equal. All modified hydrofoils were compared to a protuberance-free baseline hydrofoil of equivalent planform shape.

Infinite-span Hydrofoils

Two hydrofoils of mean chord length $c = 102$ mm, and span $b = 305$ mm, shown in Figure 6, which spanned the entirety of the NUWC water tunnel test section, were used in the

examination of the load and moment characteristics of full-span modified hydrofoils. The hydrofoils were machined out of aluminum stock on a 3-axis computer numerical code (CNC) machine and anodized matte black to generate contrast for flow visualization experiments. One protuberance geometry was studied, the 4L, which is shown in Figure 6. This specific geometry was chosen because it was representative of significant performance variations from the baseline in the past experiments[7].

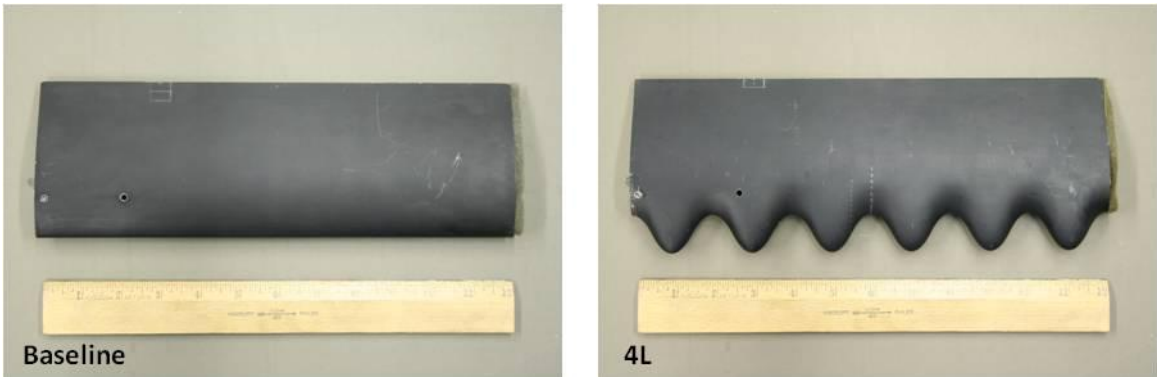

Figure 6: Hydrofoils of 305 mm span.

A second 4L hydrofoil of mean chord length $c = 102$ mm, and span $b = 305$ mm was also designed and fabricated using a rapid prototyping stereolithography apparatus (SLA), shown in Figure 7, for use in low-speed PIV experiments in the WPI water tunnel. The sinusoidal leading edge geometry of this hydrofoil was identical to the leading edge of the aluminum 4L hydrofoil previously discussed. However, to rule out possible boundary effects the spanwise distribution of protuberances was shifted by one half wavelength.

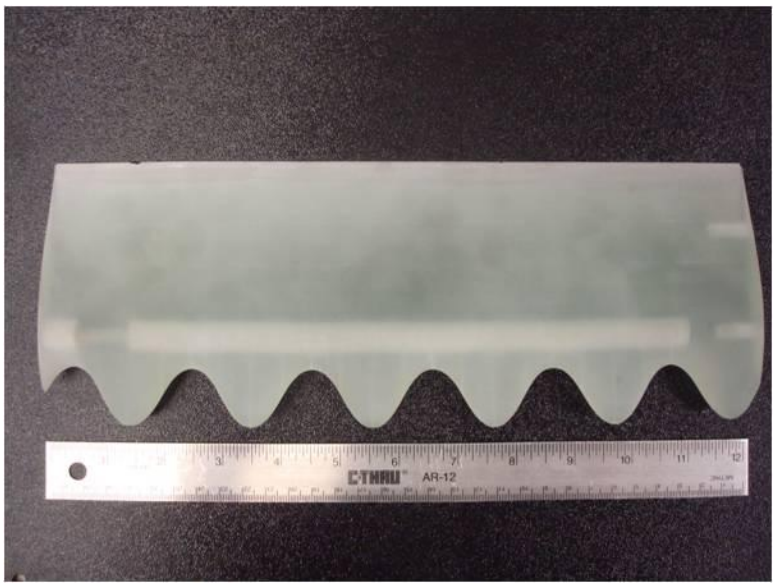

Figure 7: 4L SLA hydrofoil used in low-speed PIV water tunnel experiments.

Finite-span Hydrofoils

Seven hydrofoils of mean chord length, $c = 102$ mm, span $b = 219$ mm, and aspect ratio $AR = 2.15$ (including the wingtip endcap) were designed and fabricated in the same manner as the full-span aluminum hydrofoils. However, this set of hydrofoils was used to determine the effect of leading edge protuberances on finite-span hydrofoils and therefore, had by definition, a free tip. To eliminate the effect of a sharp, flat edge on the observed flow characteristics of the wing, rounded attachments were secured to one end of the hydrofoils so that they resembled more practical tip geometries. The finite-span rectangular hydrofoils with wingtips are shown in Figure 8.

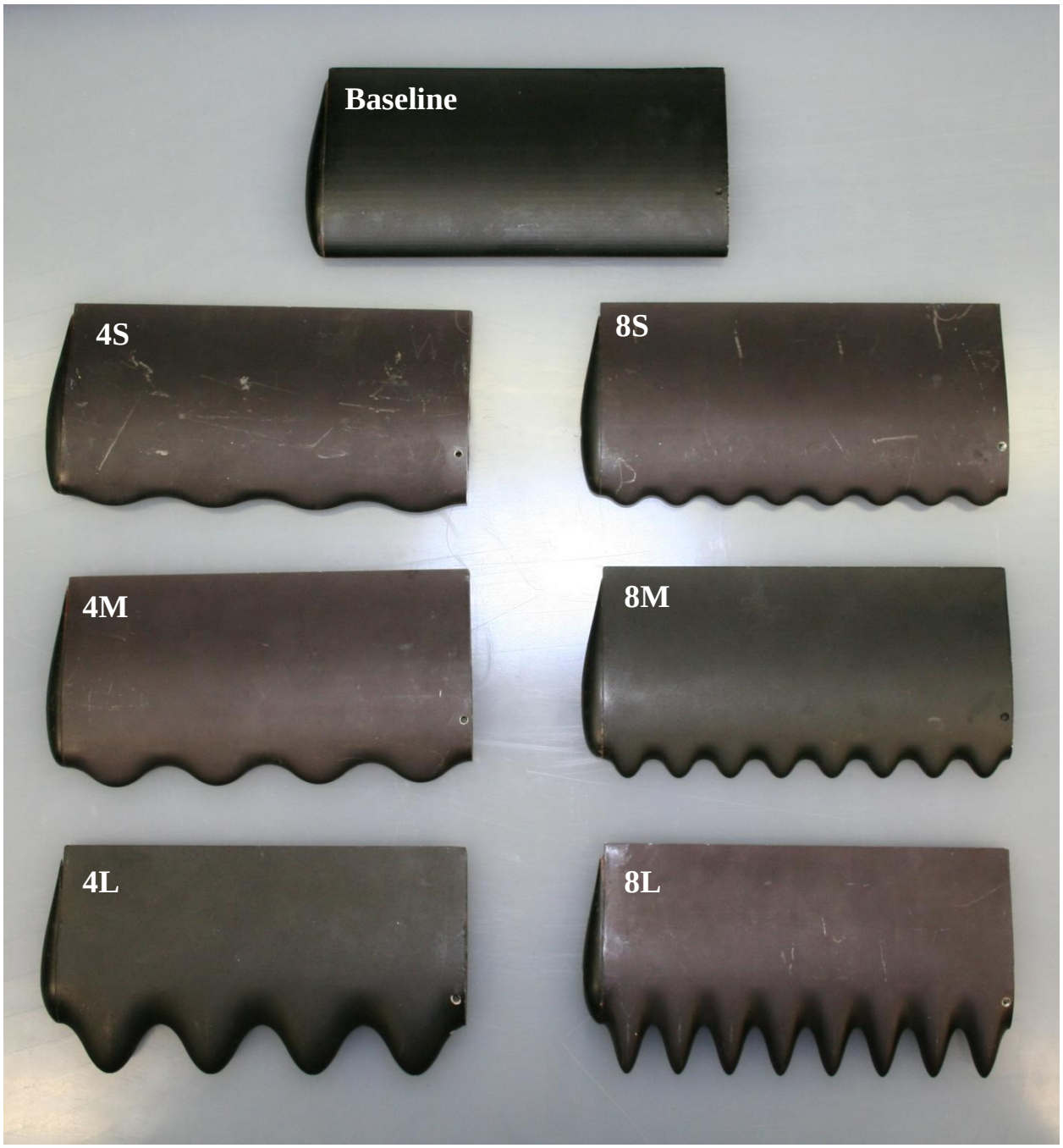

Figure 8: Hydrofoils of 219 mm span with endcaps attached.

Swept Leading Edge Hydrofoils

Two swept finite-span hydrofoils of mean root chord length $c_r = 149$ mm, span $b = 200$ mm, and a leading edge sweep angle of 26.1˚, which corresponded to a semi-span aspect ratio of $AR = 4.01$, were designed and fabricated out of aluminum stock in the same manner as the rectangular planform hydrofoils. A baseline and 4L equivalent hydrofoil (i.e. A = 12% and λ = 50% of the local chord), were designed and fabricated and are shown in Figure 9. Rounded wingtips analogous to those used on the finite-span rectangular planform hydrofoils were implemented on the swept hydrofoils as well to avoid the effects of a sharp wingtip.

Figure 9: Swept hydrofoil models.

Flipper Models

Two finite-span hydrofoils of mean root chord length $c_r = 62$ mm, span $b = 229$ mm, a semi-span aspect ratio of $AR = 4.43$, which closely resembled the humpback whale flipper morphology, shown in Figure 10, were designed and fabricated from SLA to examine the effect of protuberances on a planform shape resembling that found in nature. The planform geometry was designed using the method outlined in Murray et. al[20].

Figure 10: Flipper hydrofoil models.

Force and Moment Measurements

Load measurements were examined on all hydrofoil models at freestream velocities ranging from $0.9 \leq U_\infty \leq 4.5$ m/s and angles of attack ranging from $-12° \leq \alpha \leq 30°$. A calibrated six-axis strain gage waterproof load cell (model: AMTI MK-4741) was used to measure the forces and moments on the aforementioned hydrofoil models. The load cell that was used is capable of measuring a range of forces up to ± 2224 N along the *x*- and *y*-axis and ± 4448 N in the *z*-direction, moments of ± 113 Nm along the *x*- and *y*-axis and ± 56.5 Nm in the z-direction. All hydrofoils were mounted to the load cell by means of an adapter plate, which retained an axis of rotation centered about the quarter chord location ($0.25c$) of the hydrofoils, and transferred the forces and moments on the hydrofoils directly to the load cell. The load cell was housed inside of a yaw mechanism used to measure forces and moments at various angles of attack. The load measurement apparatus can be seen in Figure 11. The measured forces were converted to lift, drag, and pitching moment coefficients using the measured freestream dynamic pressure, the planform area of the hydrofoils, and the mean chordlength.

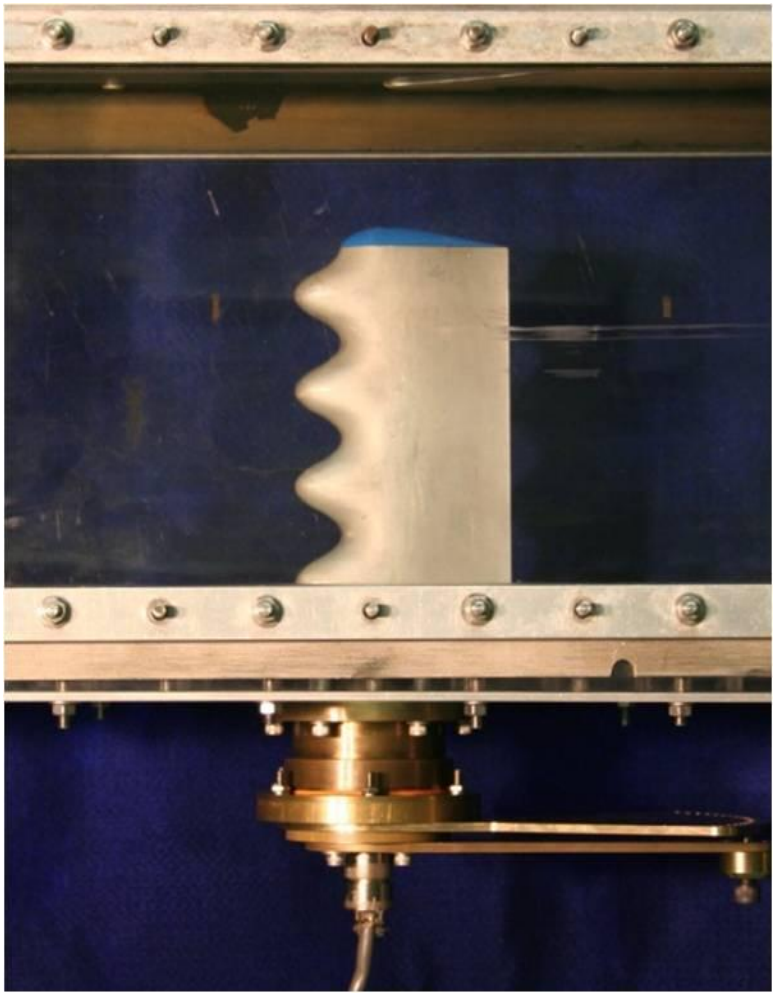

Figure 11: 4L finite-span rectangular hydrofoil in water tunnel test section with yaw mechanism attached.

NUWC Yaw Mechanism

A primary objective of the experiments presented here was to determine the effect of Reynolds number on modified hydrofoils. In doing so, it was possible to expand upon past load test results on hydrofoils with leading edge protuberances, which due to load cell limitations, were completed at a maximum freestream velocity of $U_\infty = 1.80\,\mathrm{m/s}$, corresponding to a Reynolds number $Re_c = 1.80 \times 10^5$. To record load data at higher Reynolds numbers, the load cell discussed earlier was integrated into a customized yaw mechanism capable of withstanding high forces and moments and attached to the NUWC water tunnel test section. The yaw

mechanism can be seen in the lower portions of Figure 11. The yaw mechanism was capable of precise angle of attack adjustments ranging from $-30.0° \leq \alpha \leq 30.0°$ in increments of 1.50° to an accuracy of $\alpha = \pm 0.30°$.

Flow Visualization

A low-speed flow visualization experiment using dye injection was carried out on the 219 mm span baseline and 4L hydrofoils. The purpose of this experiment was to gain a qualitative understanding of the near surface flow field on hydrofoils with leading edge protuberances. The experiment was conducted by injecting pressurized dye into an internal reservoir of 9.25 mm diameter which spanned the hydrofoil length and was located inside of the hydrofoils at the quarter chord location. A series of 1.6 mm dye ports were drilled along the leading edge of both hydrofoils that branched off from the internal dye reservoir. The ports were located at every protuberance peak, trough, and inflection point of the 4L hydrofoil, with the exception of the hydrofoil ends, while the baseline hydrofoil had ports with an equivalent spacing of 12.5 mm. A freestream velocity of $U_{\infty} = 0.15$ m/s was used when conducting dye experiments. Very low speed freestream velocities were necessary for a detailed examination of the flow field, particularly at high angles of attack, due to the breakup and diffusion of dye patterns under turbulent conditions. As the size of the NUWC water tunnel was significantly larger than the hydrofoil span, fences were located on the ends of the hydrofoil to create a nominally 2D environment for the hydrofoils, the purpose of which was to eliminate spanwise flow and prevent the formation of tip vortices.

A hand pressurized tank located outside of the water tunnel test section was used to raise the pressure of a container filled with liquid red dye of neutral buoyancy, which would in turn force the dye through towards a needle valve. The valve was capable of minute adjustments of

dye flow. After the dye left the valve, it would pass through the hydrofoil and be released into the water through the leading edge of the hydrofoil. This configuration is shown in Figure 12.

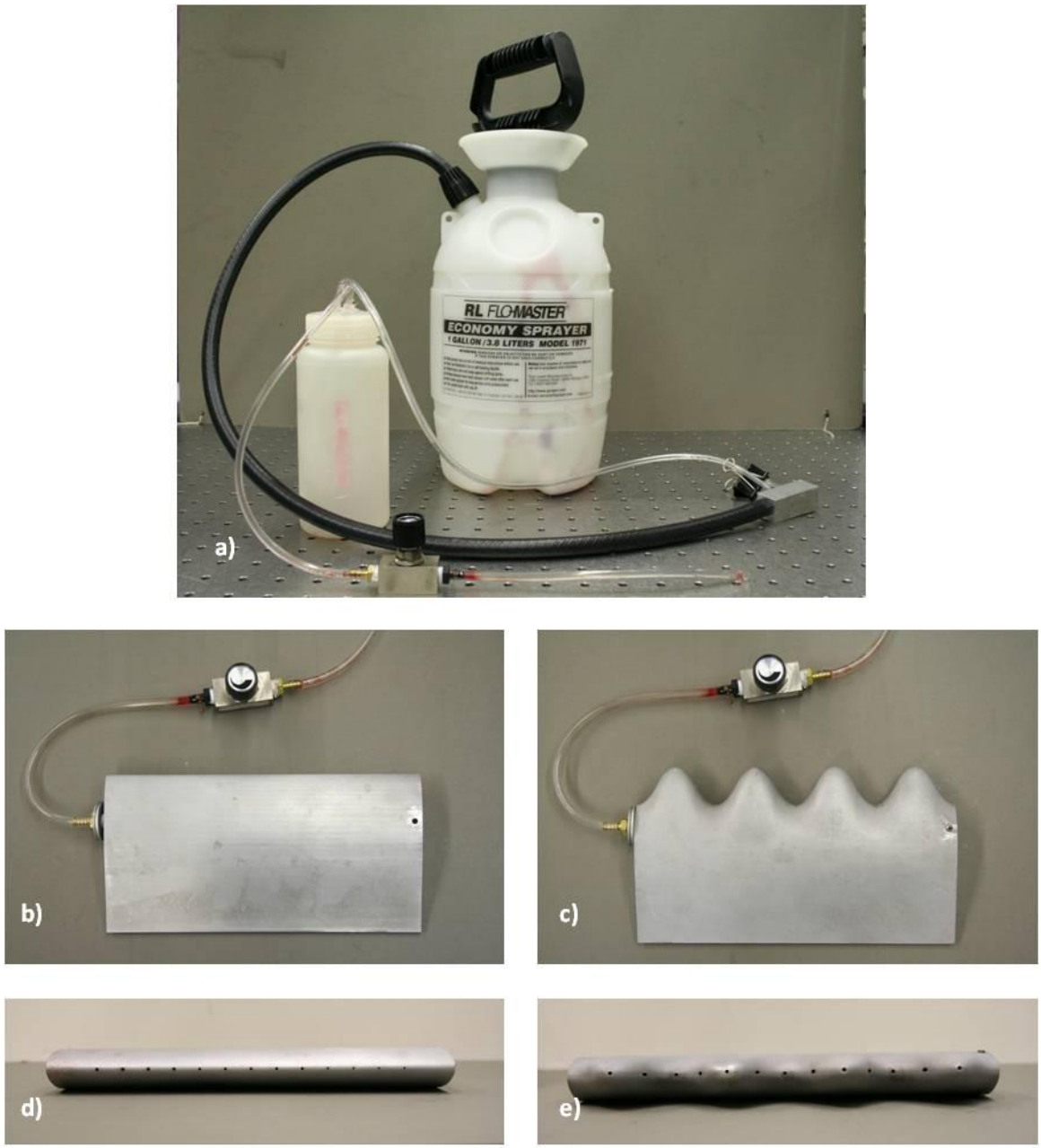

Figure 12: a) Dye injection system; b) dye valve connected to baseline foil; c) dye valve connected to 4L foil; d) leading edge of baseline foil with dye ports; e) leading edge of 4L foil with dye ports.

The dye streakline patterns were captured using still image photography using a Canon DS 126071 Digital Rebel XT. The lighting consisted of a front lit gray background lit by a

halogen floodlight. The reflected light created a clear contrast between the background and the hydrofoil. The digital camera used was capable of automatic shutter speed and aperture settings. It was necessary to use automatic settings for shutter speed and aperture because, depending on the angle of attack of the hydrofoil, different amounts of light were reflected back to the camera lens. The focus, however, was manually set at the beginning of each experiment.

Low-Speed PIV

A low-speed planar PIV experiment was carried out in the WPI Hydrodynamics Lab water tunnel facility to examine both spanwise flow and streamwise vorticity on an infinite-span hydrofoil with protuberances (4L). A freestream velocity of $U_\infty = 0.15\,\mathrm{m/s}$ was used, corresponding to the low-speed dye visualization experiments, and angles of attack of $3° \leq \alpha \leq 24°$ in 3° increments were examined to perform a direct comparison to dye visualization tests. Seven chordwise planar spatial locations were examined at each angle of attack, $\frac{x}{c} = -0.12, -0.06, 0, 0.06, 0.12, 0.25, 0.37$. For each case, 1000 image pairs were taken so that an accurate time averaged flow field could be acquired. The time delay over which each image pair was taken, Δt, ranged from $9\mathrm{ms} \leq \Delta t \leq 15\mathrm{ms}$ depending on the angle of attack being examined. A Δt that varied with angle of attack was used as local flow velocities increased with angle.

The SLA 4L equivalent hydrofoil was used for low-speed PIV testing. An experimental apparatus, seen in Figure 13, was designed, which essentially hung the hydrofoil, by means of an aluminum bar spanning the test section, from the top of the water tunnel to insert the hydrofoil into the tunnel. A simple yaw mechanism consisting of a clamped round pipe centered and attached to the hydrofoil at the quarter chord location was used to change the angle of attack. As a result, the quarter chord location was used as the axis of rotation. The hydrofoil ends were

fenced to eliminate any spanwise flow caused by the free tip and to prevent the formation of wingtip vortices.

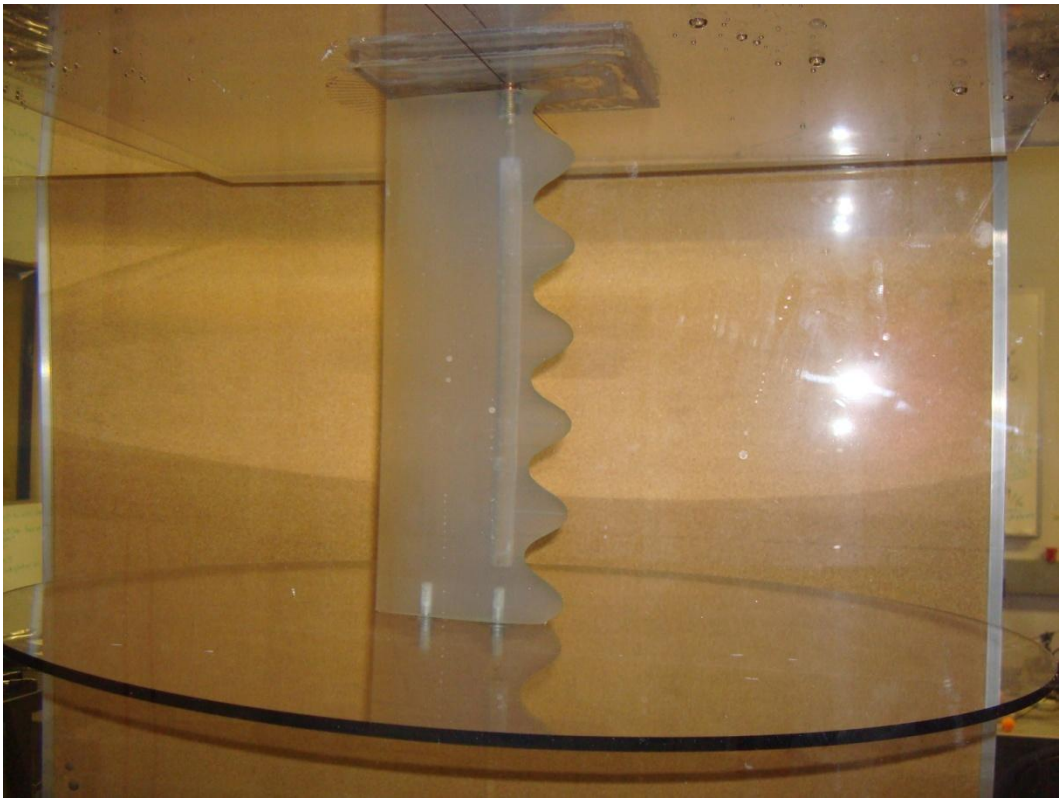

Figure 13: Low-speed PIV experimental setup.

The experiments were conducted using a LaVision PIV imaging system, which consisted of a 135 mJ/pulse double pulsed Nd: YAG laser, the corresponding sheet optics, and one ImagerPro2M 2-megapixel CCD camera. The orientation of the laser sheet was perpendicular to the freestream flow to acquire cross-stream flow field velocities needed for the calculation of streamwise vorticity. The camera used to acquire images was oriented at the rear of the water tunnel looking directly upstream. A schematic of the 2D low-speed PIV setup can be seen in Figure 14.

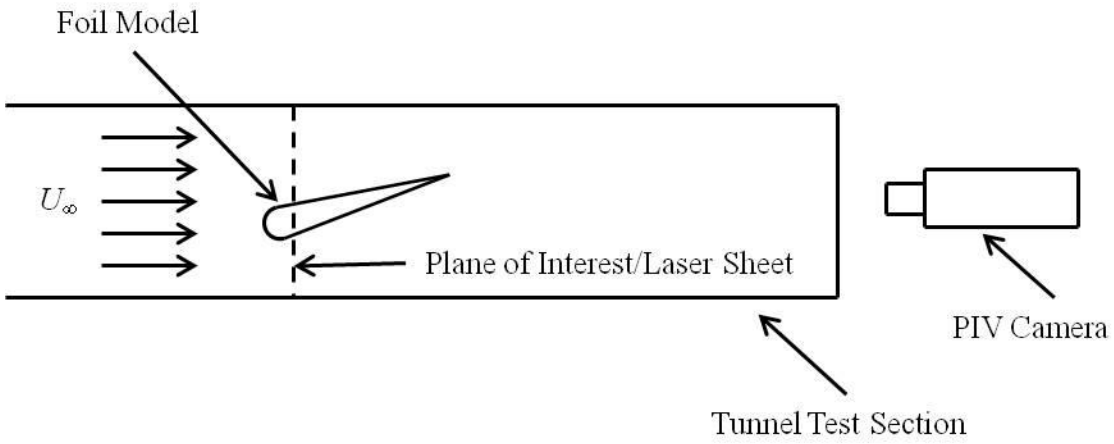

Figure 14: Schematic of full-span low-speed PIV system and water tunnel.

High-Speed Stereo-PIV

Two sets of high-speed Stereo Particle Image Velocimetry (SPIV) experiments were conducted at the NUWC water tunnel facility. An examination of the effect of Reynolds number on the flow field of infinite-span hydrofoils with leading edge protuberances was conducted along with a study of the effect of leading edge protuberances on the spanwise flow, streamwise vorticity, and tip vortex on finite-span hydrofoils at Reynolds numbers of $Re_c = 1.8 \times 10^5$ and 4.5×10^5. Due to physical limitations of the water tunnel test section, SPIV was necessary to determine the cross-stream velocities necessary for the calculation of the derived quantities such as vorticity.

The experiments were performed using a LaVision PIV imaging system, which consisted of a 135 mJ/pulse double pulse Nd: YAG laser, the associated sheet optics, and two ImagerPro4M 4-megapixel CCD cameras. For all tests, the orientation of the laser sheet was perpendicular to the freestream flow (to acquire cross-stream flow field velocities). A set of 400 image pairs were taken so that a reliable time averaged dataset could be computed. Two time delay values of Δt = 100μs and 250μs and were used at $U_\infty = 1.80$ and 4.50 m/s, respectively.

Infinite-span Flow Field Measurements

A high-speed Stereo Particle Image Velocimetry (SPIV) experiment was conducted at the NUWC water tunnel facility to examine the effect of Reynolds number on the flow characteristics of infinite-span hydrofoils. Two freestream velocities were examined $U_\infty = 1.80$ and 4.50 m/s along with a range of angles of attack of $6° \leq \alpha \leq 24°$ in increments of 6°. Two hydrofoils were examined; the baseline and 4L model, both having a mean chord length $c = 102$ mm and span $b = 305$ mm spanned the entirety of the water tunnel test section. One chordwise spatial location was examined, $\frac{x}{c} = 0.36$, for direct comparison to low-speed tests conducted at WPI.

The NUWC yaw mechanism was used. The cameras used to acquire image pairs were oriented on the same side of the water tunnel test section at 45° angles both upstream and downstream of the laser sheet. Two triangular, acrylic, water-filled prism windows were attached the water tunnel test section perpendicular to their respective camera. Prisms were necessary to eliminate refraction generated at the air/acrylic interface of the tunnel test section. A schematic of the high-speed full-span SPIV setup can be seen in Figure 15.

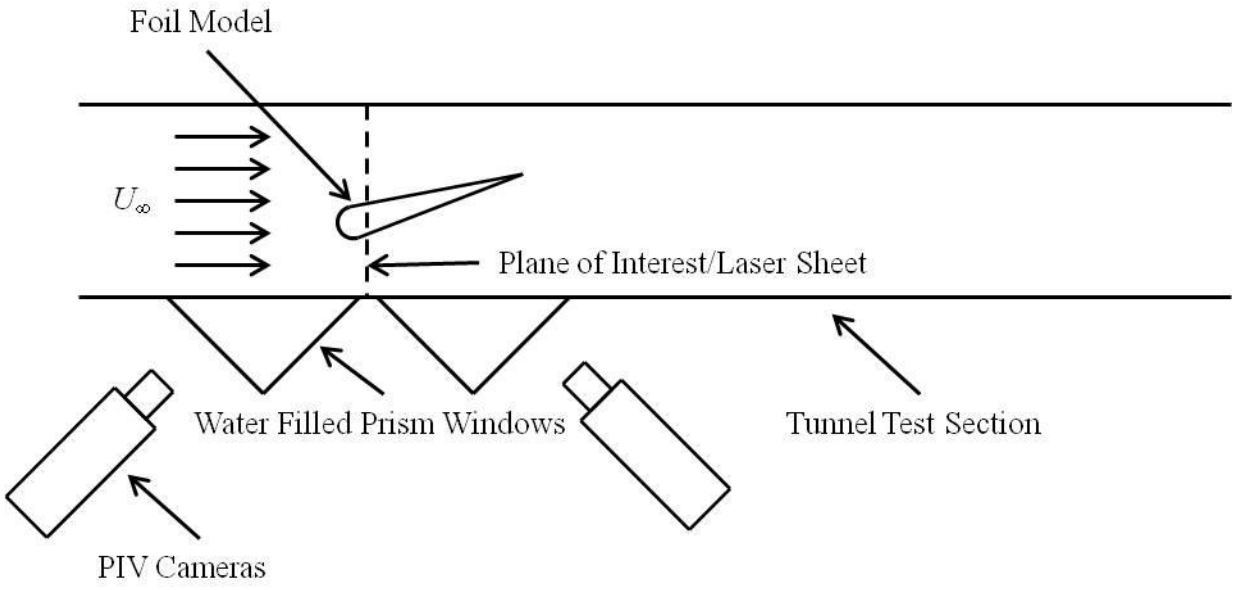

Figure 15: Schematic of full-span high-speed SPIV system and water tunnel.

Finite-span Flow Field Measurements

The previously described high-speed Stereo Particle Image Velocimetry (SPIV) setup was also used to examine the effect of leading edge protuberances on the flow field of finite-span hydrofoils with leading edge protuberances. Two freestream velocities were examined $U_\infty =$ 1.80 and 4.50 m/s along with a range of angles of attack of $6° \leq \alpha \leq 24°$ in increments of 6°. Three hydrofoil models were studied; the baseline, 8M, and 4L models all had mean chord length $c = 102$ mm and span $b = 219$ mm. To observe the development of the tip vortex, two spatial locations downstream of the trailing edge were examined, $\frac{x}{c} =$ 1.50 and 3.00.

The NUWC yaw mechanism was used for hydrofoil placement and to adjust the angle of attack. The camera orientation used for examination of the tip vortex consisted of two cameras downstream of the area of interest on opposite sides of the water tunnel test section placed at 45˚ angles to the freestream flow. Once again, the two triangular acrylic water-filled prism windows were used to eliminate the effects of refraction. A schematic of the high-speed finite-span SPIV setup used for the examination of the tip vortex is shown in Figure 16.

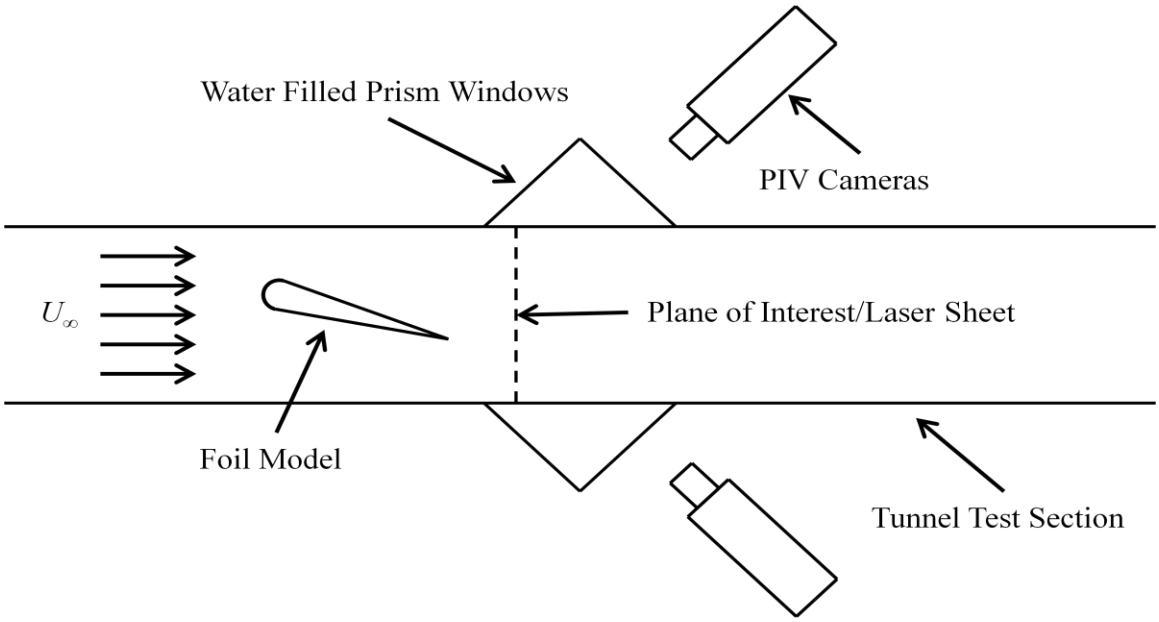

Figure 16: Schematic of finite-span high-speed SPIV system and water tunnel used for tip vortex analysis.

Cavitation

High-Speed Photographs

A high-speed qualitative flow visualization study was carried out at the NUWC research water tunnel facility to examine the cavitation characteristics of hydrofoils with leading edge protuberances. The freestream velocity of the tests was U_∞ = 7.2 m/s for correspondence with load measurements. The angles of attack examined ranged from $12° \leq \alpha \leq 24°$ in increments of 3°. Cavitation was nonexistent at angles of attack below 12° at a freestream velocity of 7.2 m/s. Images were taken with a Nikon D200 Digital SLR camera and strobe lighting to illuminate areas of cavitation. Synchronized strobe lighting with an illumination time of 200μs was used as a single flash to illuminate both the front surface of the hydrofoils as well as the background for contrast. The photographs were taken in a darkened room, with a camera shutter speed of 1s. The strobes were flashed once during the shutter open time effectively creating a shutter speed of

0.2ms, which was necessary to capture the detail of high speed cavitating flow. Images were taken on all finite-span rectangular planform hydrofoils as well as swept planform hydrofoils.

Load Measurements

Load measurements were taken on hydrofoils with and without protuberances. The procedure used was identical to the procedure described for lower Reynolds number tests. The freestream velocity used for the cavitation was U_∞ = 7.2 m/s which corresponded to a chordwise Reynolds number of $Re_c = 7.2 \times 10^5$.

Cavitation Number

An examination of the effect of leading edge protuberances on the cavitation number was carried out to determine if the presence of protuberances was capable of mitigating or delaying the freestream velocity at which a typical straight leading edge hydrofoil would cavitate. To determine the cavitation number of the hydrofoils it was necessary to monitor the freestream velocity of the water tunnel as well as the freestream static pressure. The criteria for determining the pressure and velocity at which hydrofoils would cavitate was the incipient condition. The criteria used to judge when incipient cavitation had occurred was the first visual cues of vaporous leading edge cavitation. When the incipient cavitation condition had been reached on a foil at a set angle of attack, the freestream velocity and static pressure were recorded. Subsequently it was possible to determine the cavitation number for all foils at the incipient condition within ± 5% error.

Uncertainty

There are sources of uncertainty unavoidably associated with the measurement techniques presented in this report. The force, moment, and PIV measurement uncertainties are discussed below.

Load Measurement Instrument Bias Error

Several sources of uncertainty are associated with the measurements presented here. The forces and moments measured have an uncertainty associated with them due to the intrinsic error that corresponds to the output of the load cell. The accuracy of the measured forces and moments were determined through an examination of the measured loads. The values for load cell accuracy were extracted from unprocessed data by comparing the maximum and minimum measurements of a 100 sample dataset of steady load to the mean. The resulting accuracy of the load cell force and moment components which correspond to the performance coefficients of interest are shown in Table 2.

Table 2: Low-speed and high-speed accuracy values associated with the load cell measurements.

Load Cell Accuracy	F_x (N)	F_y (N)	M_z (Nm)
U_∞ = 1.8 m/s	± 0.3	± 0.3	± 0.08
U_∞ = 4.5 m/s	± 1.78	± 1.78	± 0.05

The freestream velocity has a maximum uncertainty of ± 0.5%. The uncertainty in the angle of attack is estimated to be ± 0.3° as a result of the yaw mechanism apparatus. Due to machining error, the dimensions airfoils used in the experiments are also a source of uncertainty. To determine the error in the foil chordlength and span, measurements were taken on the foils at several spanwise locations. The total error resulted in no more than a ± 0.8% and ± 0.5% difference from the expected chordlength and span values of the models, respectively.

For a sense of the error associated with the measurements presented here, the bias errors of several important performance characteristics were calculated and are shown in Table 3 for the full-span baseline hydrofoil at an angle of attack in the linear regime and pre-stall regime of the lift coefficient for freestream velocities of U_∞ = 1.8 and 4.5 m/s. The methods for

determining bias uncertainties are outlined in Ref. 13. Several of the quantities shown in Table 3 are very low. Because of this error bars will not be plotted as they are typically quite small and are not useful when plotted alongside the measured loads.

Table 3: Uncertainty values associated with force and moment measurements.

Bias Error	C_L	C_D	$C_{M1/4}$	α	Re_c
U_∞ = 1.8 m/s; α = 6° (linear lift regime)	± 1.8%	± 16.5%	± 0.6%	± 5.5%	± 2.2%
U_∞ = 1.8 m/s; α = 19.5° (post-stall regime)	± 1.6%	± 2.1%	± 0.2%	± 1.7%	± 2.2%
U_∞ = 4.5 m/s; α = 6° (linear lift regime)	± 1.74%	± 17.0%	± 0.5%	± 5.5%	± 2.2%
U_∞ = 4.5 m/s; α = 19.5° (pre-stall regime)	± 1.42%	± 4.3%	± 0.2%	± 1.7%	± 2.2%

Standard Deviation of Measurements

The load measurements presented here are mean values of 10 second samples taken at a rate of 10 samples/sec. The standard deviation of the mean was calculated on the full-span baseline hydrofoil at comparable angles and freestream velocities to the bias error analysis and is presented in Table 4 as a percentage of the corresponding mean value. The following formula was used to calculate the standard deviation of the mean:

$$\sigma_{mean} = \frac{2}{\sqrt{N}} \sqrt{\frac{1}{N} \sum_{j=1}^{N} \left(x_j - \bar{x}\right)}$$

where N is the sample size and x is the variable of interest.

Table 4: Standard deviation of the mean on the baseline full-span hydrofoil at several important angles and freestream velocities.

Standard Deviation of the Mean	C_L	C_D	$C_{M1/4}$
U_∞ = 1.8 m/s; α = 6° (linear lift regime)	± 1.3%	± 11.3%	± 10.1%
U_∞ = 1.8 m/s; α = 19.5° (post-stall regime)	± 1.3%	± 0.26%	± 1.4%
U_∞ = 4.5 m/s; α = 6° (linear lift regime)	± 2.2%	± 0.26%	± 0.90%
U_∞ = 4.5 m/s; α = 19.5° (pre-stall regime)	± 0.14%	± 0.20%	± 0.38%

Table 4 shows that, with the exception of low-speed and low angle datasets, the standard deviation of the measurements remains very low indicating that there is little fluctuation in the load measurements.

Aerodynamic Characteristic Uncertainty

Several important aerodynamic characteristics are presented throughout this report for all planform cases examined. The overall maximum and minimum values for the uncertainty associated with the measurements were calculated and are shown in Table 5. Although the measured forces and moments have uncertainties that vary on a case to case basis, the ranges shown represent the absolute maximum and minimum uncertainties that can be expected in any of the load measurement data presented throughout this work. They are calculated using the methods outlined in Ref. 13.

Table 5: Maximum and minimum uncertainties associated with the aerodynamic characteristics.

	Minimum Uncertainty	Maximum Uncertainty
$\frac{dC_L}{d\alpha}$ [1/deg]	7.0%	10.6%
C_{Lmax}	1.4%	2.0%
α @ C_{Lmax} [deg]	1.2%	2.4%
C_{Dmin}	21%	25%
L/D_{max}	3.5%	5.5%
α @ L/D_{max} [deg]	2.3%	9.8%
α_{stall} [deg]	1.3%	2.4%

PIV Uncertainty

The uncertainty associated with the PIV results was also calculated based on the error associated with the resolution of pixel displacement. The pixel displacement error associated with the systems used was ± 0.1 pixels. In the areas of interest, the pixel displacement of a given seed particle, was measured to have a mean value of between 2 and 7 pixels. The resulting uncertainty of velocity, vorticity, and circulation are calculated and are shown in Table 6.

Table 6: Uncertainty values associated with PIV measurements.

	u	v	w	ω	Γ
$PIV_{2\ pixels}$	5%	5%	5%	15%	5%
$PIV_{7\ pixels}$	1.43%	1.43%	1.43%	4.3%	1.43%

III. Results

Force Measurements

The load characteristics of modified hydrofoils were measured as a function of angle of attack, and compared to the baseline hydrofoil. The measured loads were time averaged and converted into dimensionless coefficients in the form of lift coefficient, C_L, drag coefficient, C_D, and quarter chord moment coefficient, $C_{M_{\frac{1}{4}}}$. These values describe the hydrodynamic performance of the hydrofoils. The dimensionless coefficients were calculated in the following way:

$$C_L = \frac{L}{\frac{1}{2}\rho_\infty U_\infty^2 cb} \tag{1}$$

$$C_D = \frac{D}{\frac{1}{2}\rho_\infty U_\infty^2 cb} \tag{2}$$

$$C_{M_{\frac{1}{4}}} = \frac{M_{\frac{1}{4}}}{\frac{1}{2}\rho_\infty U_\infty^2 c^2 b} \tag{3}$$

The effect of protuberance amplitude, wavelength, and Reynolds number were examined for each of the hydrofoils. These load characteristics will be examined separately for each planform shape tested in the following sections of this report.

Infinite-span Hydrofoils

An examination of the effects of protuberances on full-span hydrofoils was used to both confirm past experiments as well as to further examine the effects of Reynolds number on

modified full-span hydrofoils. Two hydrofoils were examined; a 4L model along with its baseline equivalent.

Baseline Hydrofoil

The baseline lift coefficient, C_L, is presented in Figure 17 as a function of angle of attack, α, for Reynolds number ranging from $0.9 – 4.5 \times 10^5$. The behavior of the baseline lift coefficient is typical for the thick airfoil profile being examined. There is a linear increase in C_L with a lift curve slope of $\frac{dC_L}{d\alpha} \approx 0.09$ for all Reynolds numbers tested until $\alpha \approx 11°$. Past $\alpha = 11°$ the lift coefficient becomes nearly constant, which is an indication of flow separation. Flow separation can be distinguished in the drag characteristics as well, as drag increases rather quickly at higher angles of attack. This effect can be seen in Figure 17b as the effects of separation cause C_D to increase as a polynomial with α. As the angle of attack is increased, the lift curve remains level until there is a dramatic loss of lift and increase in drag at the stall angle. The maximum C_L is found typically just prior to the stall angle. The minimum C_D occurs at $\alpha \approx 0°$ with a value of C_{Dmin} = 0.0158 at a freestream velocity of U_∞ = 4.5 m/s, while the maximum occurs at the maximum angle of attack. This is the true for all Reynolds numbers examined. At the stall angle the drag increases dramatically, and continues to rise throughout the range of angles of attack examined.

At lower velocities, Reynolds number plays an important role in establishing the lift characteristics of the baseline hydrofoil. At Reynolds numbers greater than $Re_c \approx 3.6 \times 10^5$, there is no significant effect on the C_L or C_D for the baseline hydrofoil; however below this value, both an increase in maximum lift and its corresponding angle of attack along with stall angle could be seen as a function of Reynolds number.

The effect of Reynolds number on the quarter chord moment coefficient, shown in Figure 17c, reveals that as the angle of attack is increased, $C_{M1/4}$ decreases nearly monotonically. This shows that, although the aerodynamic center does not remain constant throughout the range of angles tested, nor is the aerodynamic center lie on the quarter chord location. This is true for all calculated moment coefficients throughout this work. However, the small values of $C_{M1/4}$ even at high angle imply that the aerodynamic center is near the quarter chord location at any given angle of attack. At the stall angle $C_{M1/4}$ decreases dramatically. Little variation is seen in $C_{M1/4}$ at Reynolds numbers greater than $Re_c \approx 3.6 \times 10^5$.

The lift-to-drag ratio of the baseline hydrofoil is presented in Figure 17d, and shows a nearly linear increase in *L/D* at low angles of attack with gradually decreasing *L/D* at higher angles. In the post-stall regime *L/D* is nearly constant for all freestream velocities tested. Table 7 shows the lift and drag aerodynamic characteristics of the full-span baseline hydrofoil.

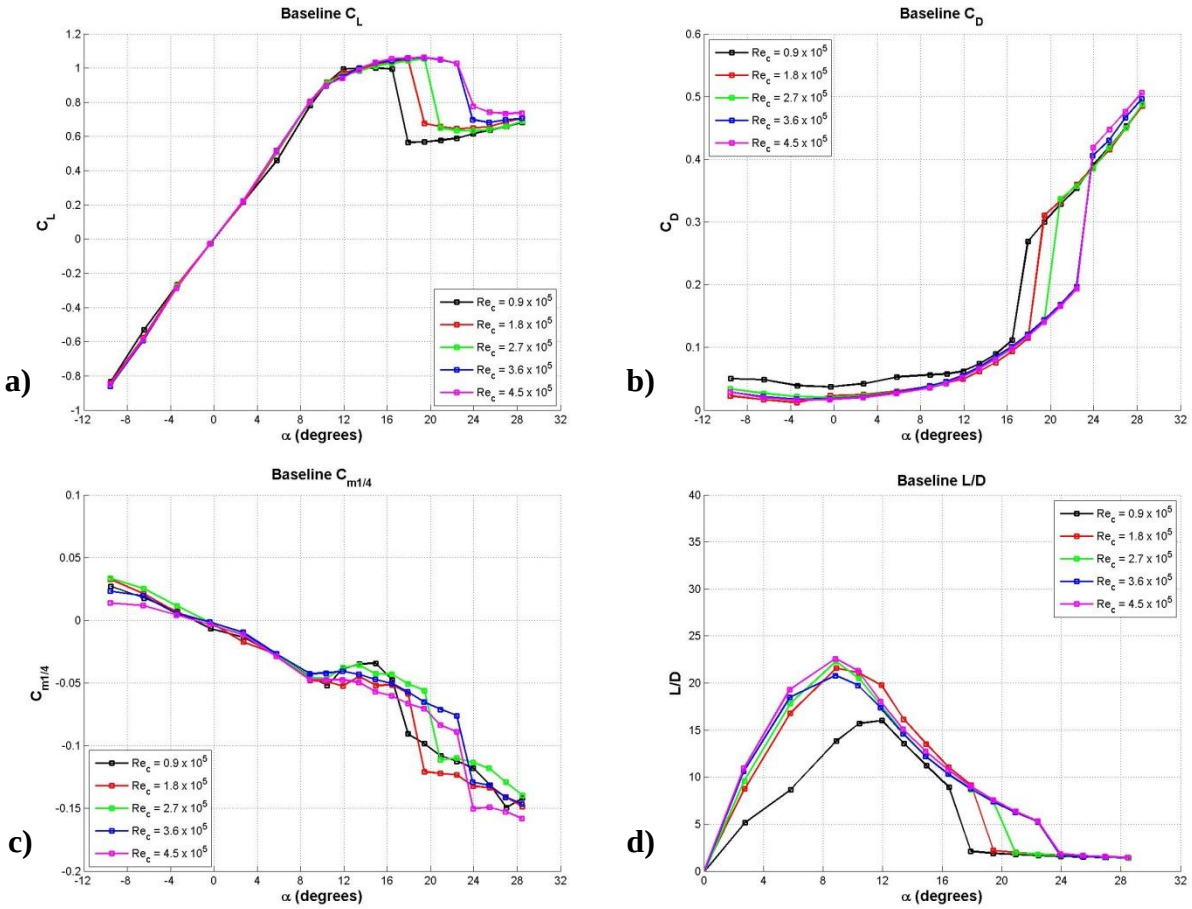

Figure 17: Full-span baseline hydrofoil load characteristics at multiple Reynolds numbers. a) lift coefficient, b) drag coefficient, c) quarter chord moment coefficient, d) L/D ratio.

Table 7: Aerodynamic characteristics of full-span baseline foil. Refer to Table 5 for corresponding uncertainties.

	$Re_c = 9.0 \times 10^4$	$Re_c = 1.8 \times 10^5$	$Re_c = 2.7 \times 10^5$	$Re_c = 3.6 \times 10^5$	$Re_c = 4.5 \times 10^5$
$\frac{dC_L}{d\alpha}$ [1/deg]	0.079	0.079	0.081	0.083	0.084
C_{Lmax}	1.00	1.05	1.06	1.06	1.06
α @ C_{Lmax} [deg]	15.0	18.0	19.5	19.4	19.4
C_{Dmin}	0.04	0.01	0.02	0.02	0.02
L/D_{max}	16.01	21.58	22.30	20.79	22.59
α @ L/D_{max} [deg]	12.0	8.9	8.9	8.8	8.8
α_{stall} [deg]	16.5	18.9	19.5	22.4	22.4

Baseline Comparison to Archival Data

The measured lift and drag coefficients on the full-span baseline hydrofoil at the highest Reynolds numbers of 3.6 and 4.5 × 10^5 were compared those calculated in the past by Abbott and von Doenhoff[28] in Figure 18. This was done to determine whether the measured forces presented here were capable of replicating past results. Ref. 28 shows a greater maximum lift coefficient and lift curve slope along with a lower minimum drag coefficient. These discrepancies can be accounted for by the increased Reynolds number and experimental setup used in Ref. 28. Whereas all Reynolds numbers examined in this work were of the same order of magnitude, Abbott and von Doenhoff conducted their tests at a Reynolds number nearly 7 times greater than that of the highest non-cavitating case presented in this report. Nevertheless, the overall trends in the lift and drag coefficients are nearly the same in both this investigation as well as the past study conducted by Abbott and von Doenhoff.

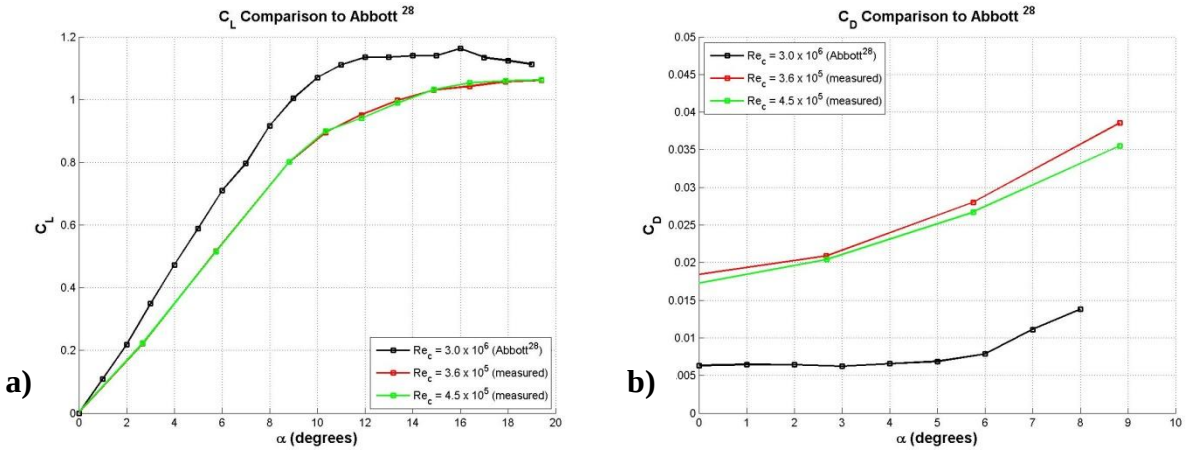

Figure 18: Comparison of measured full-span data at the highest Reynolds numbers tested to Abbott and Von Doenhoff[28] data for identical cross-sectional profile.

Modified Hydrofoil

The effect of protuberances on full-span hydrofoils is shown in Figures 19 - 23. Figure 19 shows the effect of Reynolds number on the modified hydrofoil. Reynolds number plays only a minor role in establishing the lift and drag characteristics of modified hydrofoils. Maximum C_L increases with Reynolds number, ranging from $0.9 \leq C_L \leq 1.01$, corresponding to Reynolds numbers of $Re_c = 9.0 \times 10^4$ and 4.5×10^5 respectively. In the linear regime, the lift curve slopes, $\frac{dC_L}{d\alpha}$, of the baseline and modified hydrofoils are similar, with values ranging from $0.078 \leq \frac{dC_L}{d\alpha} \leq 0.089$. There is little effect on the drag characteristics of modified hydrofoils over the entire range of Reynolds numbers tested. The quarter chord moment coefficient of the modified foil is shown in Figure 19c. An overall trend of decreasing $C_{M1/4}$ is shown for all angles of attack tested. The lowest moment coefficients seen corresponded to Reynolds numbers of up to $Re_c = 1.8 \times 10^5$, while $C_{M1/4}$ at Reynolds numbers equal to or greater than 2.7×10^5 showed little difference. The lift-to-drag ratio of the modified foil, shown in Figure 19d, reveals that *L/D* changes little at Reynolds numbers equal to or greater than $Re_c = 2.7 \times 10^5$ while low Reynolds number effects cause *L/D* to vary at lower Reynolds numbers.

The lift coefficient is shown in Figure 20. Similar to the baseline hydrofoil, there is a linear increase in C_L with angle of attack until $\alpha \approx 6°$. As α is increased past the linear regime, the lift becomes nearly constant, increasing at a much lower rate, and remaining nearly constant up to the highest angles of attack examined. This leveling off of C_L is an indication of separation. At angles of attack past the linear regime, the trend in the lift coefficient of modified hydrofoils deviates significantly from the baseline hydrofoil. In the pre-stall regime of the baseline hydrofoil, C_L is always less for any given Reynolds number. However, in the post-stall regime of

the baseline, C_L of the modified hydrofoil remains nearly constant; generating 31% – 49% more lift than the baseline hydrofoil.

The drag coefficient of the modified hydrofoil, shown in Figure 21, is nearly equivalent to the baseline hydrofoil at both very low angles of attack, $0° \leq \alpha \leq 6°$ and in the post-stall regime of the baseline hydrofoil. However, in the pre-stall regime of the baseline hydrofoil, C_D on modified hydrofoils is greater than the baseline by as much as ≈ 150%. Although the drag on modified hydrofoils can be significantly higher than that of the baseline in the pre-stall regime, there is no drag penalty in the post-stall regime. This indicates that in the post-stall regime of the baseline hydrofoil, as much as 50% more lift can be generated than the baseline hydrofoil with little or no drag penalty. The same trend was observed in past work by Johari et al. and Custodio[7,24].

The quarter chord moment coefficient of the full-span modified hydrofoil is compared to the baseline in Figure 22. With the exception of the two highest freestream velocities tested, $C_{M1/4}$ is generally very similar to or less than the baseline case for all positive angles of attack. At mid-range angles, $C_{M1/4}$ of the modified case can be significantly different than the baseline case. However, at post-stall angles, $C_{M1/4}$ of the modified case can be slightly greater than the baseline the highest freestream velocities.

Figure 23 shows the lift-to-drag ratio of the full-span cases examined. With the exception of Reynolds numbers below 1.8×10^5 over a limited range of angles, in which low Reynolds number plays a significant role in establishing the performance characteristics of the foils, *L/D* of the modified foil is generally less then or nearly equal to the baseline case. This implies that although the lift coefficient of the modified case can be significantly greater than the baseline at post-stall angles, the high drag values seen in all cases in turn render any increase in *L/D* nearly

negligible. Table 8 shows several important aerodynamic characteristics of the full-span modified hydrofoil at all Reynolds numbers tested.

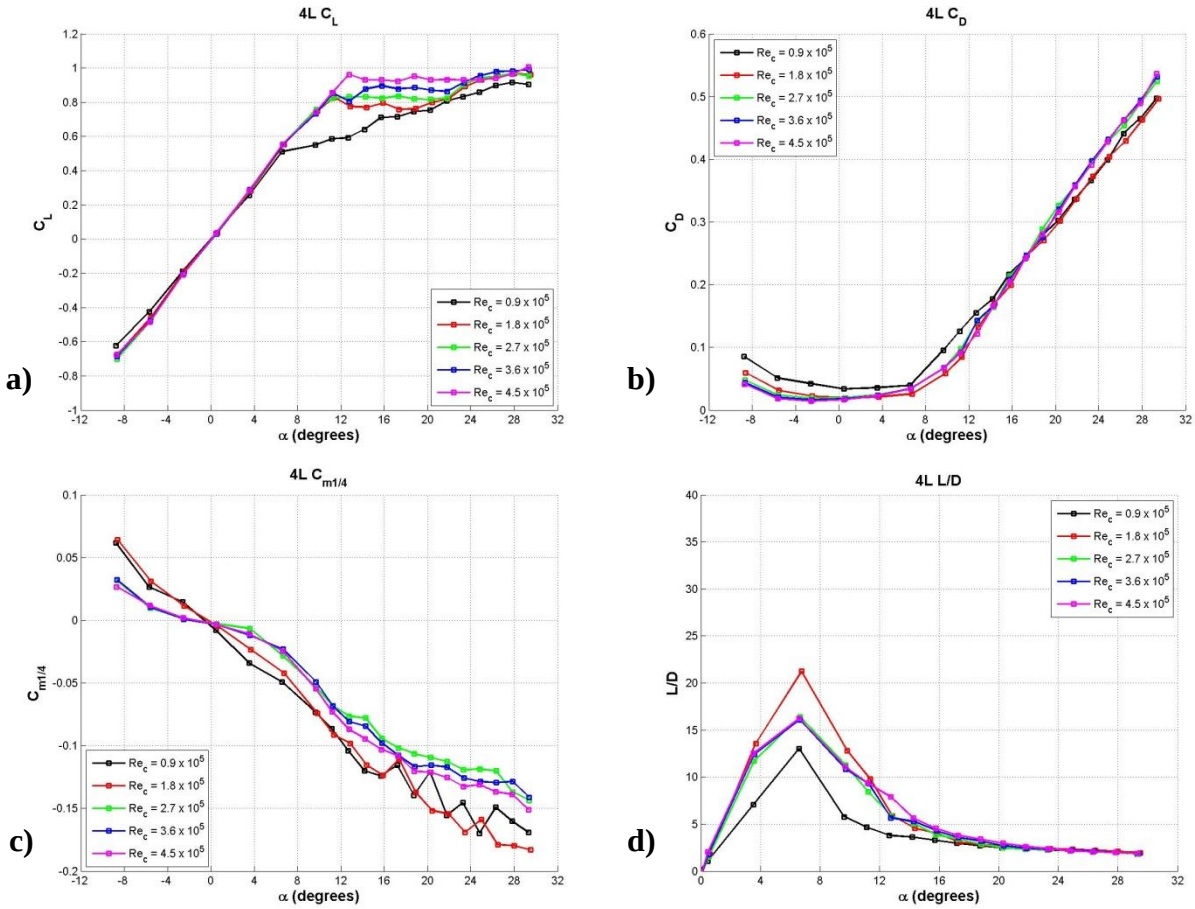

Figure 19: Infinite-span 4L hydrofoil load characteristics at multiple Reynolds numbers. a) lift coefficient, b) drag coefficient, c) quarter chord moment coefficient, d) L/D ratio.

Table 8: Aerodynamic characteristics of full-span 4L foil. Refer to Table 5 for corresponding uncertainties.

	$Re_c = 9.0 \times 10^4$	$Re_c = 1.8 \times 10^5$	$Re_c = 2.7 \times 10^5$	$Re_c = 3.6 \times 10^5$	$Re_c = 4.5 \times 10^5$
$\frac{dC_L}{d\alpha}$	0.072	0.077	0.080	0.081	0.080
C_{Lmax}	0.92	0.97	0.97	0.99	1.01
α @ C_{Lmax}	27.8°	28.0°	27.9°	29.4°	29.4°
C_{Dmin}	0.03	0.02	0.02	0.02	0.01
L/D_{max}	13.02	21.25	16.41	16.10	16.25
α @ L/D_{max}	6.6°	6.8°	6.7°	6.7°	6.6°
α_{stall}	N/A	N/A	N/A	N/A	N/A

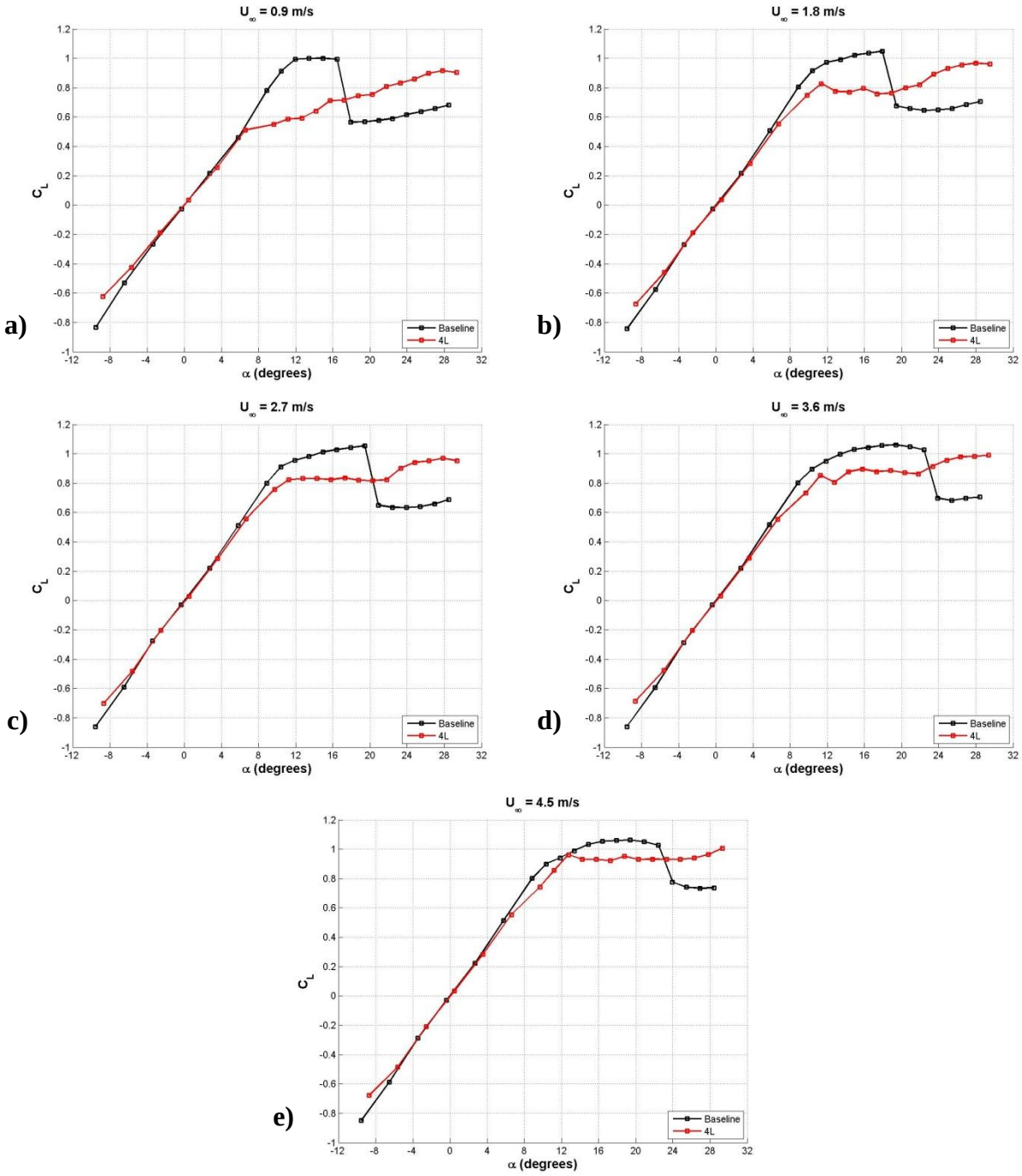

Figure 20: Infinite-span planform lift coefficient. a) $Re_c = 9.0 \times 10^4$, b) $Re_c = 1.8 \times 10^5$, c) $Re_c = 2.7 \times 10^5$, d) $Re_c = 3.6 \times 10^5$, e) $Re_c = 4.5 \times 10^5$.

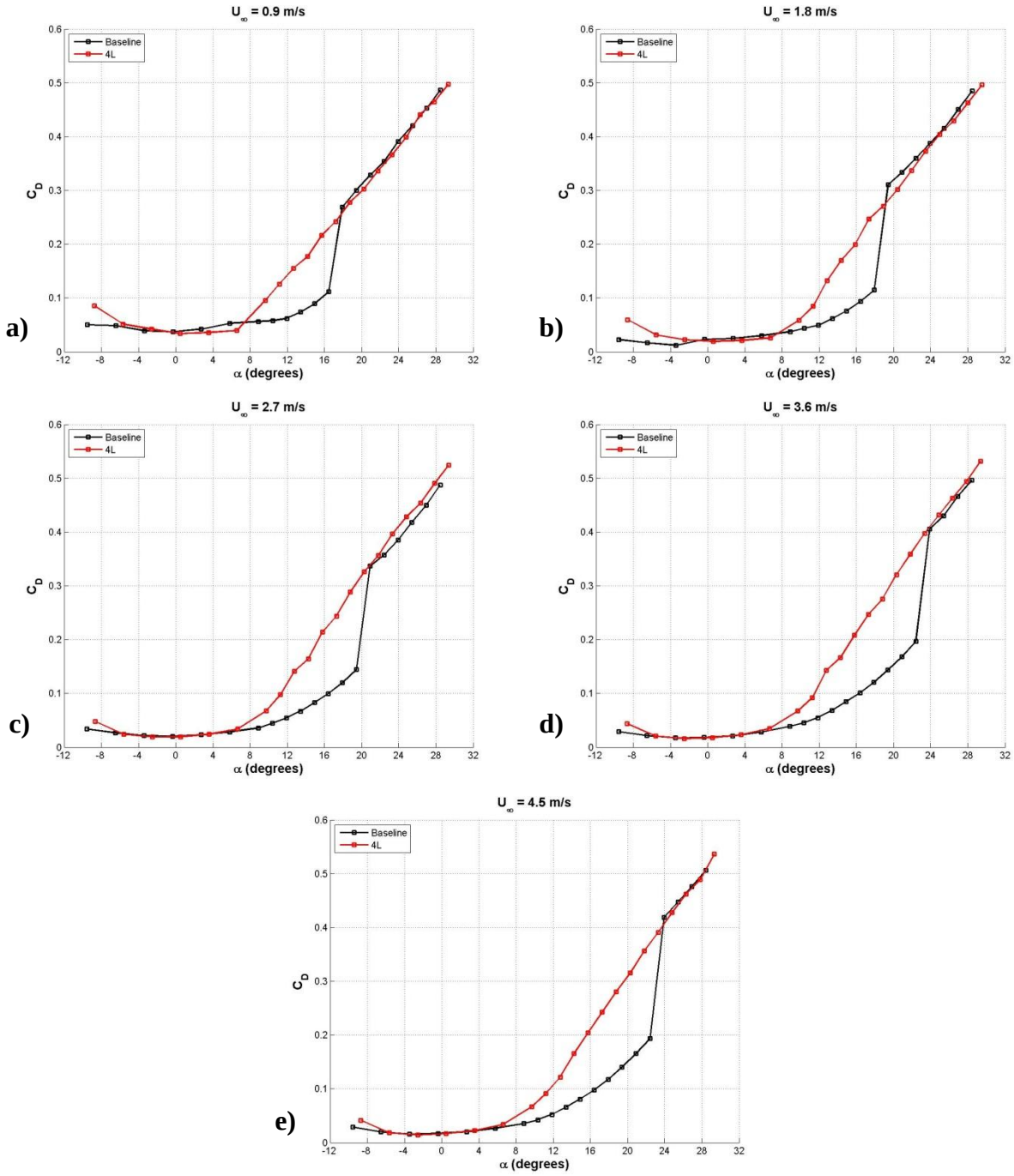

Figure 21: Infinite-span planform drag coefficient. a) $Re_c = 9.0 \times 10^4$, b) $Re_c = 1.8 \times 10^5$, c) $Re_c = 2.7 \times 10^5$, d) $Re_c = 3.6 \times 10^5$, e) $Re_c = 4.5 \times 10^5$.

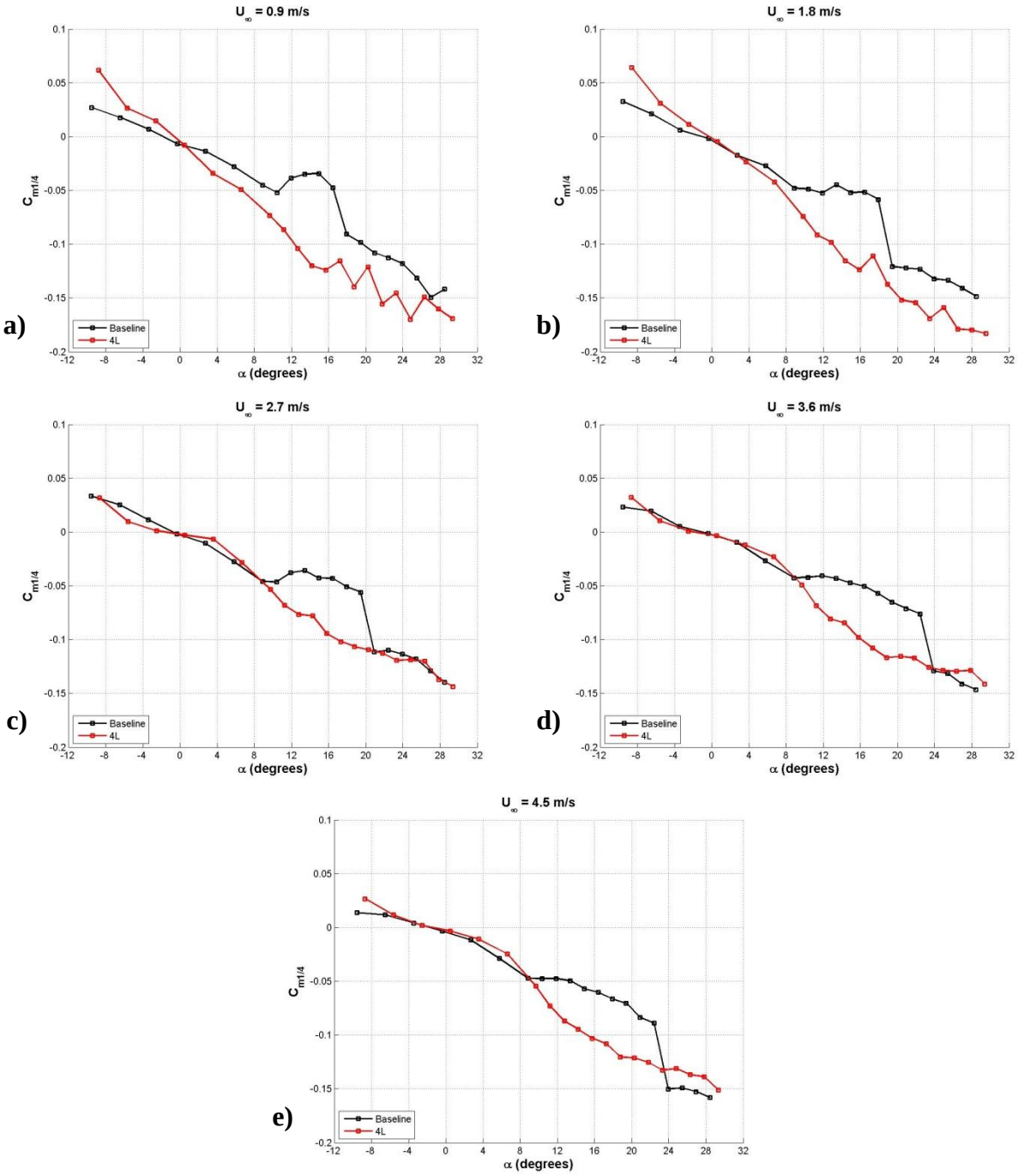

Figure 22: Infinite-span planform quarter chord moment coefficient. a) $Re_c = 9.0 \times 10^4$, b) $Re_c = 1.8 \times 10^5$, c) $Re_c = 2.7 \times 10^5$, d) $Re_c = 3.6 \times 10^5$, e) $Re_c = 4.5 \times 10^5$.

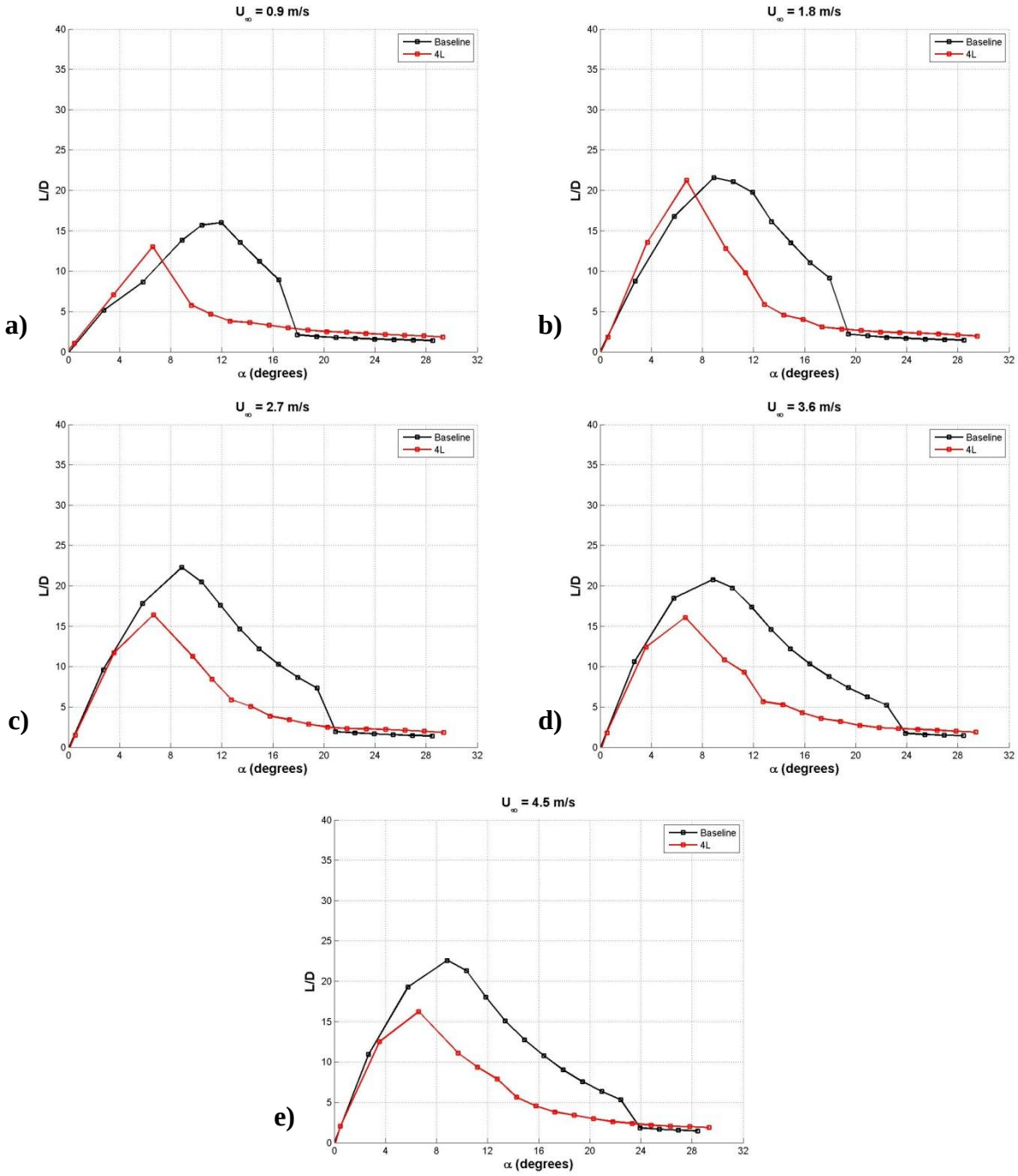

Figure 23: Infinite-span planform L/D ratio. a) $Re_c = 9.0 \times 10^4$, b) $Re_c = 1.8 \times 10^5$, c) $Re_c = 2.7 \times 10^5$, d) $Re_c = 3.6 \times 10^5$, e) $Re_c = 4.5 \times 10^5$.

Finite-span Rectangular Hydrofoils

An examination of the effect of leading edge protuberances on the lift, drag, and pitching moment characteristics was carried out on finite-span rectangular planform wings. Seven hydrofoils were examined: a baseline hydrofoil along with 4S, 4M, 4L, 8S, 8M, and 8L hydrofoils with a constant semi-span aspect ratio of $AR = 2.15$.

Baseline Hydrofoil

Reynolds number has a large effect on the lift and drag characteristics of the finite-span baseline hydrofoil at low speed. The stall angle and lift coefficient at post-stall angles are increased significantly as a function of Reynolds number. As Reynolds number is increased, the effect of stall is softened, becoming less abrupt. The effect of Reynolds number on the baseline hydrofoil diminishes with increasing Reynolds number and nearly disappears at values higher than $Re_c \approx 2.7 \times 10^5$. The maximum C_L is relatively unaffected by Reynolds number

The lift coefficient of the baseline hydrofoil, shown in Figure 24a, reveals comparable trends to the full-span baseline case, showing a linear increase in C_L with α that can be seen over the range of $0 \leq \alpha \leq 15°$. Past 15°, C_L levels off until the stall angle is reached, at which point lift decreases dramatically and is never recovered. In general, high Reynolds number affects the sharp loss in lift by 'softening' the stall characteristics. At the highest Reynolds number tested, $Re_c = 4.5 \times 10^5$, there is a gentle decrease in C_L at the stall angle.

The drag characteristics of the finite-span baseline hydrofoil, seen in Figure 24b, also show trends similar to the full-span baseline model. There is a quadratic increase in C_D with angle of attack at low α, ranging from $0 \leq \alpha \leq 15°$ with the minimum value at 0˚. As Reynolds number is increased to 3.6×10^5, the minimum drag coefficient decreases, however at higher Reynolds number, there is little change in the minimum drag coefficient. At the stall angle of

attack however, C_D increases dramatically and continues to increase over the range of angles examined.

The quarter chord moment coefficient of the baseline foil, shown in Figure 24c, reveals that there is an increase in $C_{M1/4}$ over a wide range of angles. With the onset of separation and stall effects, $C_{M1/4}$ gradually decreases over the remaining angles tested. At Reynolds numbers greater than 3.6×10^5 there is little change in $C_{M1/4}$ over the entire range of angles tested.

The lift-to-drag ratio of baseline, shown in Figure 24d, reveals that the maximum *L/D* increases with Reynolds number. Over a range of angles $14° \leq \alpha \leq 20°$, *L/D* for all Reynolds numbers tested is nearly the same while at Reynolds numbers greater than 3.6×10^5 there is little difference in *L/D* at any angle of attack. Table 9 shows several important aerodynamic characteristics of the finite-span baseline hydrofoil.

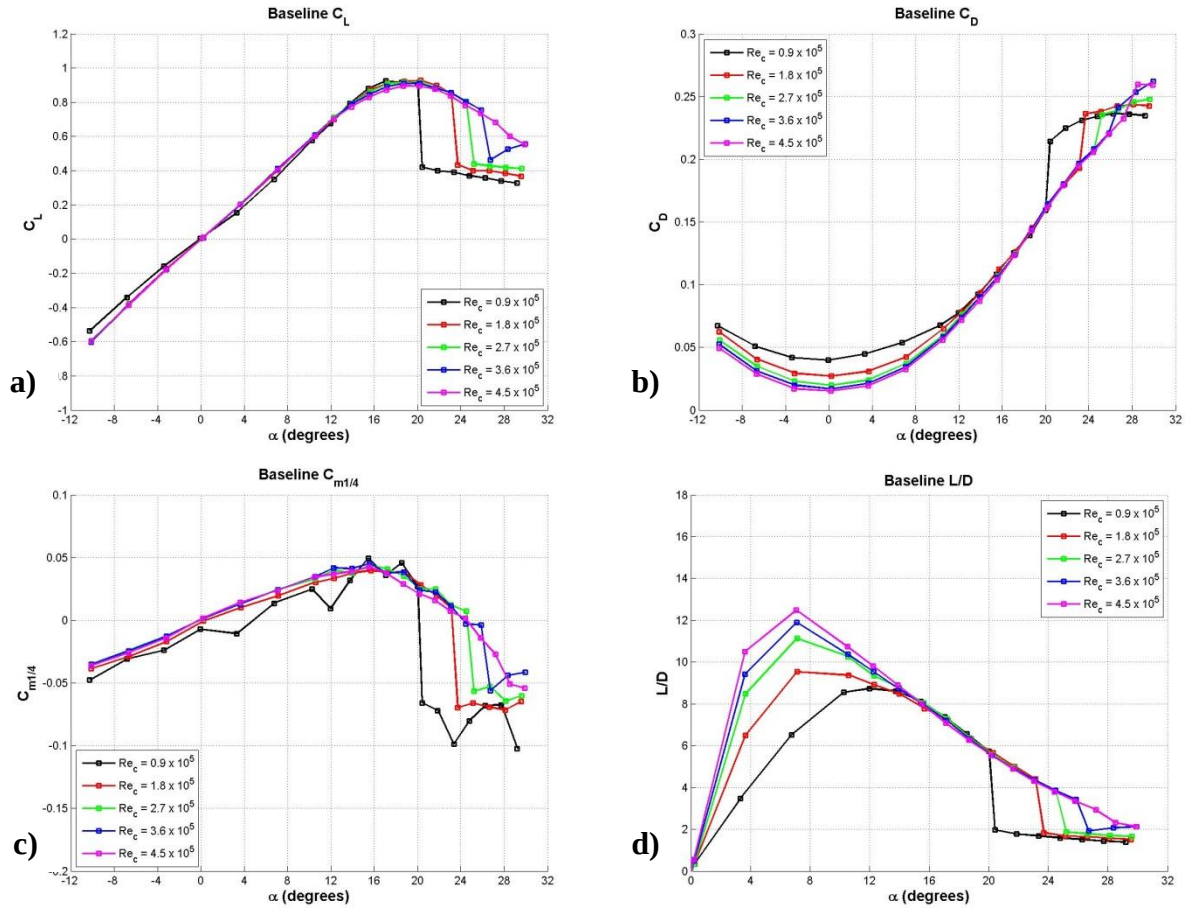

Figure 24: Effect of Reynolds number on the finite-span rectangular planform baseline hydrofoil load characteristics. a) lift coefficient, b) drag coefficient, c) quarter chord moment coefficient, d) *L/D* ratio.

Table 9: Aerodynamic characteristics of finite-span rectangular planform baseline foil. Refer to Table 5 for corresponding uncertainties.

	$Re_c = 9.0 \times 10^4$	$Re_c = 1.8 \times 10^5$	$Re_c = 2.7 \times 10^5$	$Re_c = 3.6 \times 10^5$	$Re_c = 4.5 \times 10^5$
$\frac{dC_L}{d\alpha}$ [1/deg]	0.047	0.055	0.056	0.055	0.056
C_{Lmax}	0.93	0.93	0.92	0.91	0.90
α @ C_{Lmax} [deg]	17.1	20.3	20.3	20.2	18.7
C_{Dmin}	0.04	0.03	0.02	0.02	0.02
L/D_{max}	8.73	9.53	11.13	11.91	12.48
α @ L/D_{max} [deg]	12.0	7.1	7.1	7.1	7.1
α_{stall} [deg]	20.0	23.1	24.5	25.9	N/A

Modified Hydrofoil

Effect of Reynolds Number

The effect of Reynolds number on the load characteristics of finite-span rectangular modified hydrofoils is shown in Figures 25 - 28. Up to $Re_c \approx 3.6 \times 10^5$, and with the exception of the pre-stall regime, all hydrofoils examined show a minor dependence on Reynolds number. As Reynolds number increases, the value of maximum lift increases along with the stall angle. For any given foil this trend remains the same. However, at a Reynolds number of $Re_c \approx 3.6 \times 10^5$ and higher, there is relatively little change in the lift characteristics of the hydrofoils. This implies that as the Reynolds number is increased past this point, there will be no change in the lift characteristics of modified hydrofoils. Reynolds number affects the minimum drag coefficient, reducing it significantly with increasing Reynolds number. Reynolds number clearly changes the stall effects seen in C_D, and at higher Reynolds numbers there is relatively no effect on the drag characteristics of modified hydrofoils due to Reynolds number at post-stall angles of attack. A similar trend can be seen in the quarter chord moment coefficient and lift-to-drag ratios for all foils tested; Reynolds number has little effect on $C_{M1/4}$ and L/D except at very low Reynolds number, in which low Reynolds number effects dominate. Also, low Reynolds number effects tend to dominate most significantly on foils with smaller amplitude protuberances. Table 10 - Table 15 show several important aerodynamic characteristics of the modified finite-span hydrofoils.

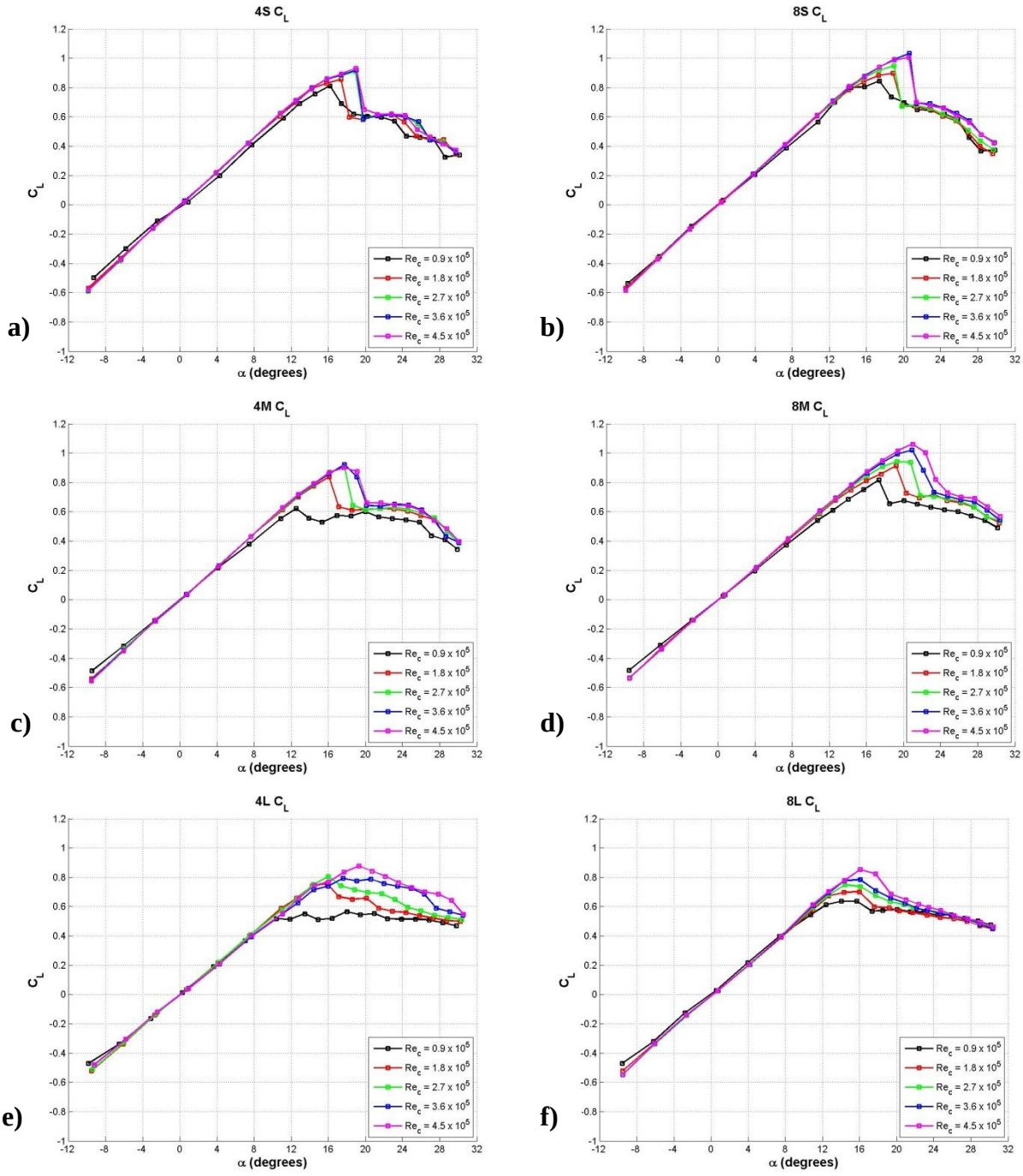

Figure 25: Effect of Reynolds number on the lift coefficient of finite-span rectangular planform modified hydrofoils. a) 4S, b) 8S, c) 4M, d) 8M, e) 4L, f) 8L.

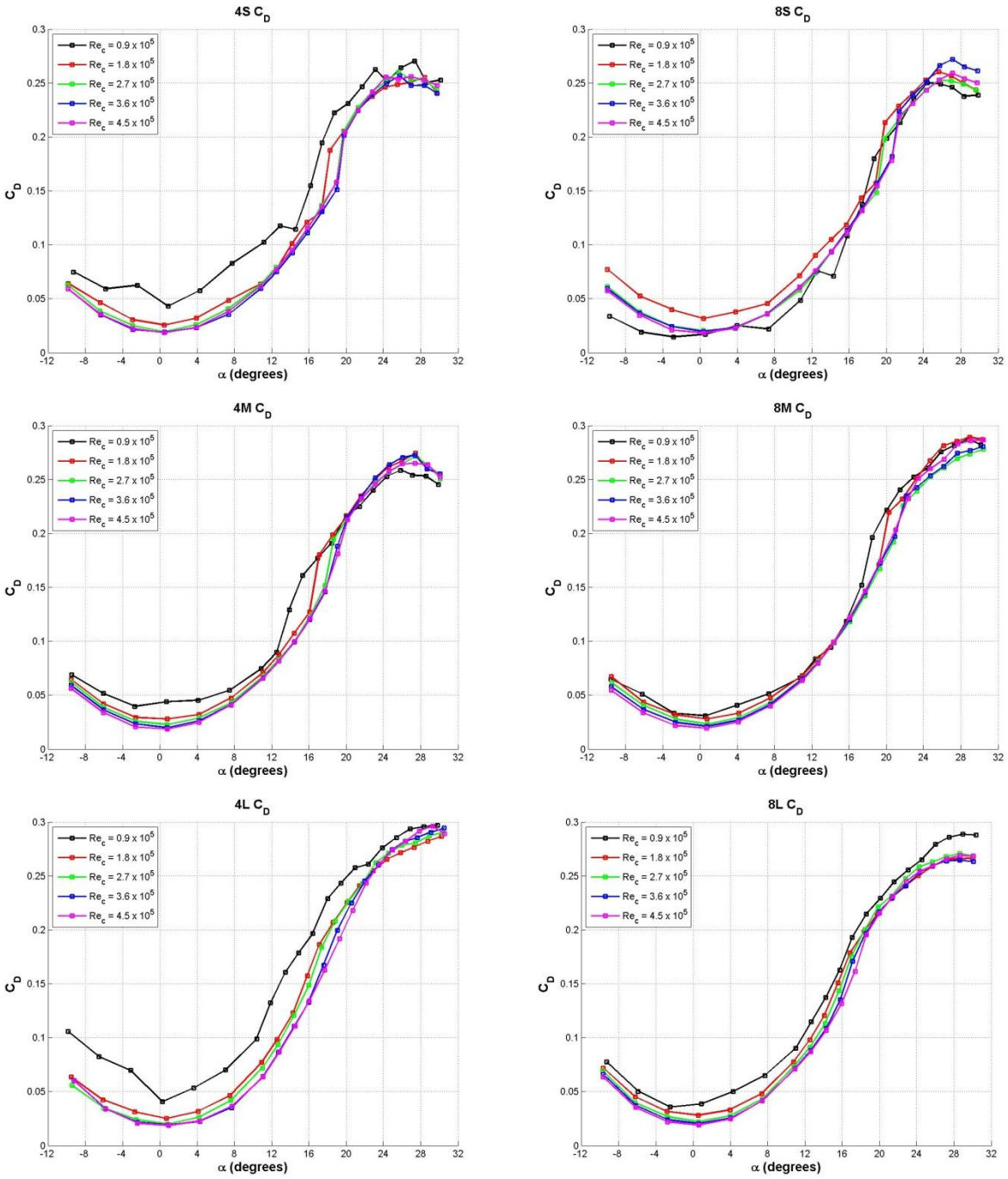

Figure 26: Effect of Reynolds number on the drag coefficient of finite-span rectangular planform modified hydrofoils. a) 4S, b) 8S, c) 4M, d) 8M, e) 4L, f) 8L.

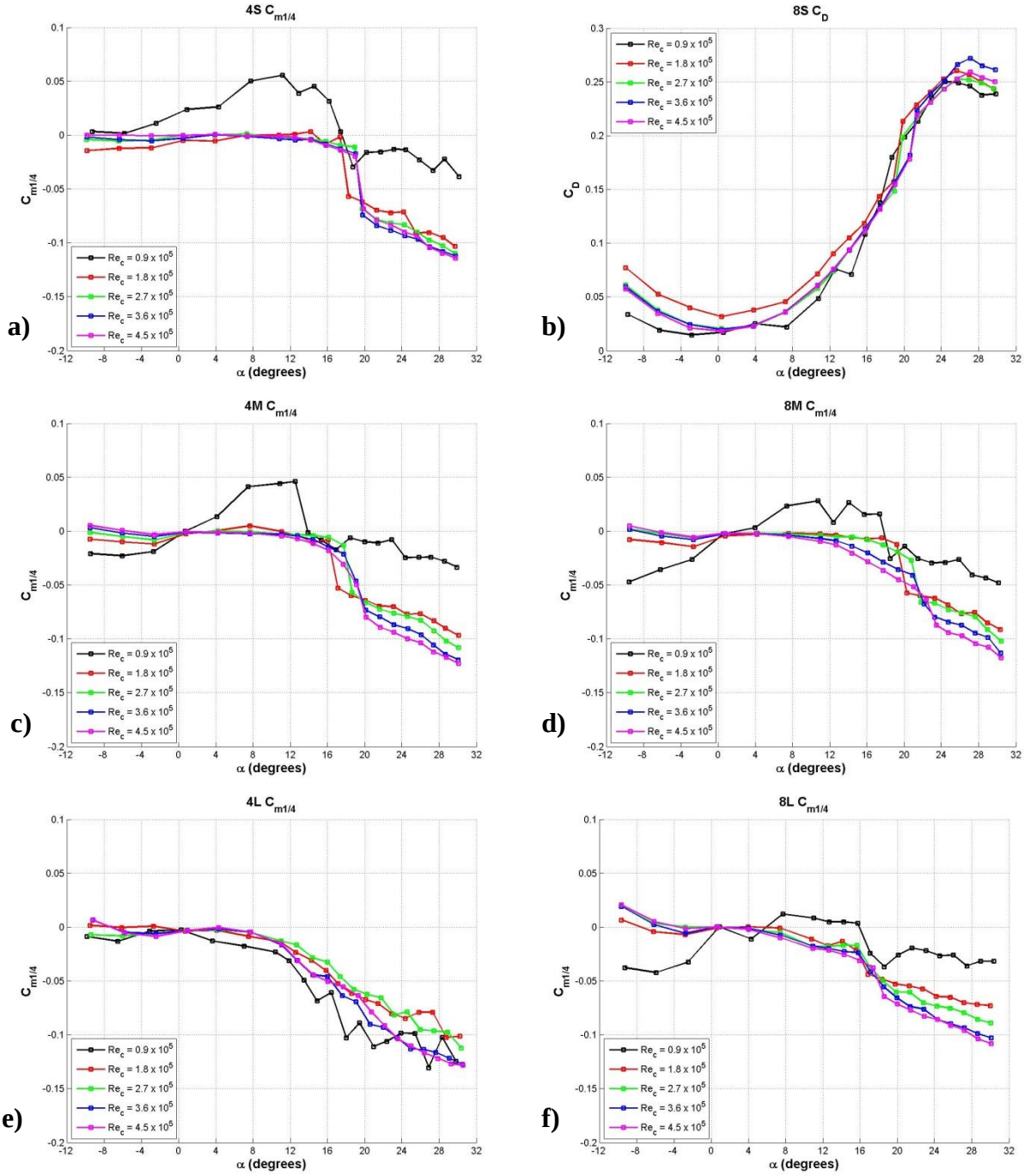

Figure 27: Effect of Reynolds number on the quarter chord moment coefficient of finite-span rectangular planform modified hydrofoils. a) 4S, b) 8S, c) 4M, d) 8M, e) 4L, f) 8L.

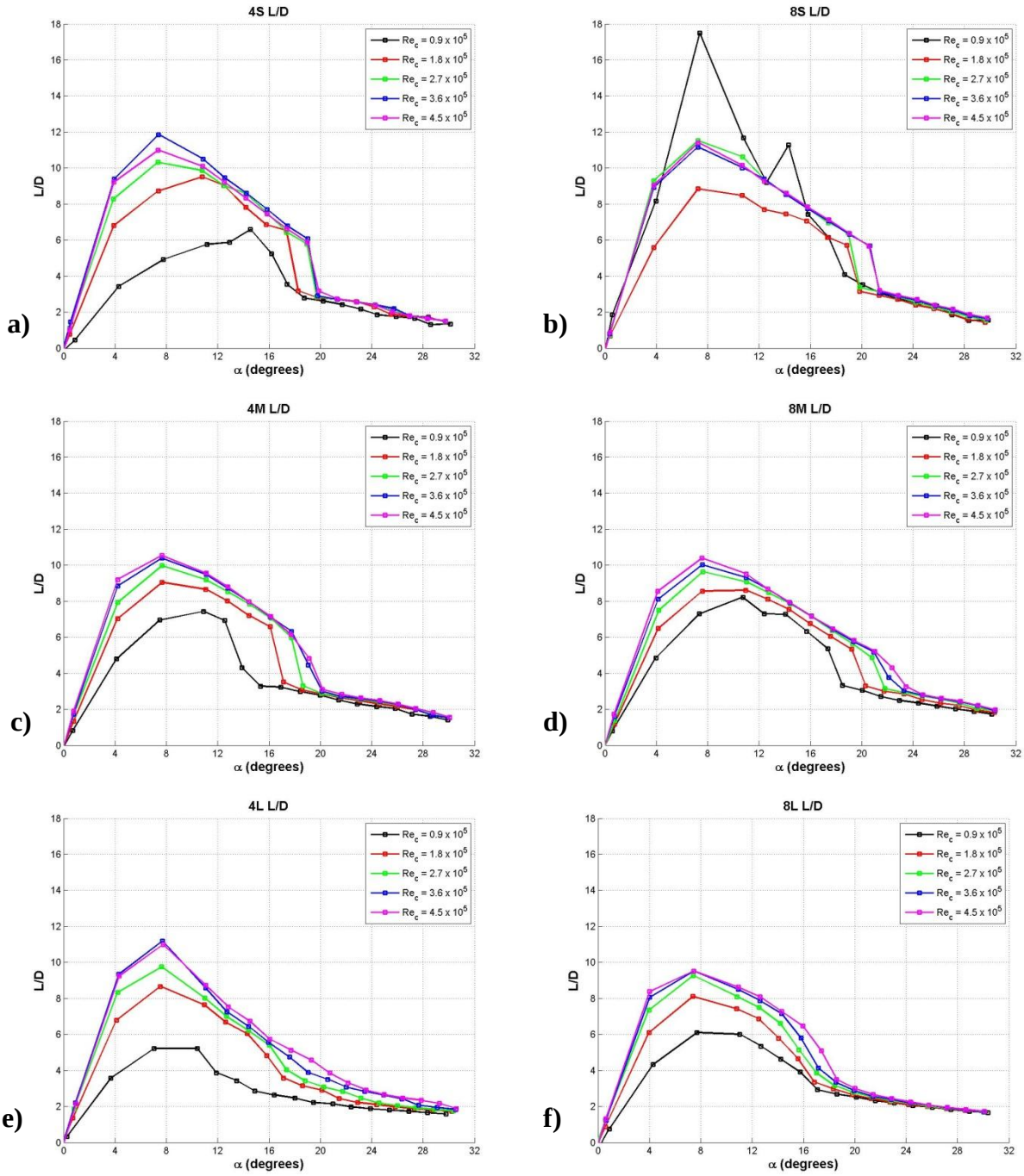

Figure 28: Effect of Reynolds number on the lift-to-drag ratio of finite-span rectangular planform modified hydrofoils. a) 4S, b) 8S, c) 4M, d) 8M, e) 4L, f) 8L.

Table 10: Aerodynamic characteristics of finite-span rectangular planform 4S foil. Refer to Table 5 for corresponding uncertainties.

	$Re_c = 9.0 \times 10^4$	$Re_c = 1.8 \times 10^5$	$Re_c = 2.7 \times 10^5$	$Re_c = 3.6 \times 10^5$	$Re_c = 4.5 \times 10^5$
$\frac{dC_L}{d\alpha}$ [1/deg]	0.046	0.056	0.055	0.055	0.055
C_{Lmax}	0.81	0.86	0.91	0.92	0.93
α @ C_{Lmax} [deg]	16.2	17.3	18.9	19.0	19.0
C_{Dmin}	0.04	0.03	0.02	0.02	0.02
L/D_{max}	6.60	9.52	10.32	11.85	11.00
α @ L/D_{max} [deg]	14.6	10.8	7.3	7.4	7.4
α_{stall} [deg]	16.2	17.3	18.9	19.0	19.0

Table 11: Aerodynamic characteristics of finite-span rectangular planform 4M foil. Refer to Table 5 for corresponding uncertainties.

	$Re_c = 9.0 \times 10^4$	$Re_c = 1.8 \times 10^5$	$Re_c = 2.7 \times 10^5$	$Re_c = 3.6 \times 10^5$	$Re_c = 4.5 \times 10^5$
$\frac{dC_L}{d\alpha}$[1/deg]	0.053	0.054	0.055	0.055	0.054
C_{Lmax}	0.62	0.84	0.91	0.92	0.90
α @ C_{Lmax} [deg]	12.5	16.1	17.7	17.7	17.7
C_{Dmin}	0.04	0.03	0.02	0.02	0.02
L/D_{max}	7.44	9.05	9.98	10.4	10.6
α @ L/D_{max} [deg]	10.9	7.66	7.7	7.7	7.7
α_{stall} [deg]	20.0	16.1	17.7	17.7	17.7

Table 12: Aerodynamic characteristics of finite-span rectangular planform 4L foil. Refer to Table 5 for corresponding uncertainties.

	$Re_c = 9.0 \times 10^4$	$Re_c = 1.8 \times 10^5$	$Re_c = 2.7 \times 10^5$	$Re_c = 3.6 \times 10^5$	$Re_c = 4.5 \times 10^5$
$\frac{dC_L}{d\alpha}$[1/deg]	0.052	0.052	0.052	0.049	0.049
C_{Lmax}	0.57	0.76	0.80	0.79	0.88
α @ C_{Lmax} [deg]	18.0	15.8	16.0	17.6	19.3
C_{Dmin}	0.04	0.03	0.02	0.02	0.02
L/D_{max}	5.23	8.67	9.76	11.20	11.00
α @ L/D_{max} [deg]	10.40	7.53	7.6	7.7	7.8
α_{stall} [deg]	N/A	N/A	N/A	N/A	N/A

Table 13: Aerodynamic characteristics of finite-span rectangular planform 8S foil. Refer to Table 5 for corresponding uncertainties.

	$Re_c = 9.0 \times 10^4$	$Re_c = 1.8 \times 10^5$	$Re_c = 2.7 \times 10^5$	$Re_c = 3.6 \times 10^5$	$Re_c = 4.5 \times 10^5$
$\frac{dC_L}{d\alpha}$[1/deg]	0.052	0.056	0.055	0.055	0.054
C_{Lmax}	0.85	0.90	0.95	1.03	1.01
α @ C_{Lmax} [deg]	17.4	18.9	19.0	20.6	20.6
C_{Dmin}	0.02	0.03	0.02	0.02	0.02
L/D_{max}	17.51	8.85	11.53	11.17	11.41
α @ L/D_{max} [deg]	7.4	7.2	7.3	7.2	7.3
α_{stall} [deg]	17.4	18.9	19.0	20.6	20.6

Table 14: Aerodynamic characteristics of finite-span rectangular planform 8M foil. Refer to Table 5 for corresponding uncertainties.

	$Re_c = 9.0 \times 10^4$	$Re_c = 1.8 \times 10^5$	$Re_c = 2.7 \times 10^5$	$Re_c = 3.6 \times 10^5$	$Re_c = 4.5 \times 10^5$
$\frac{dC_L}{d\alpha}$[1/deg]	0.050	0.052	0.052	0.053	0.053
C_{Lmax}	0.82	0.91	0.95	1.02	1.06
α @ C_{Lmax} [deg]	17.4	19.2	19.3	20.9	21.0
C_{Dmin}	0.03	0.03	0.02	0.02	0.02
L/D_{max}	8.22	8.61	9.65	10.02	10.39
α @ L/D_{max} [deg]	10.7	11.0	7.63	7.6	7.6
α_{stall} [deg]	17.4	19.2	20.8	20.9	22.1

Table 15: Aerodynamic characteristics of finite-span rectangular planform 8L foil. Refer to Table 5 for corresponding uncertainties.

	$Re_c = 9.0 \times 10^4$	$Re_c = 1.8 \times 10^5$	$Re_c = 2.7 \times 10^5$	$Re_c = 3.6 \times 10^5$	$Re_c = 4.5 \times 10^5$
$\frac{dC_L}{d\alpha}$[1/deg]	0.051	0.051	0.051	0.051	0.051
C_{Lmax}	0.64	0.70	0.75	0.79	0.85
α @ C_{Lmax} [deg]	14.2	15.6	14.2	15.8	15.95
C_{Dmin}	0.04	0.03	0.02	0.02	0.02
L/D_{max}	6.10	8.11	9.27	9.52	9.52
α @ L/D_{max} [deg]	7.7	7.4	7.4	7.4	7.4
α_{stall} [deg]	N/A	N/A	N/A	N/A	17.4

Effect of Protuberance Amplitude

The effect of amplitude on the load characteristics of modified hydrofoils can be seen in Figures 29 - 36.

Long Wavelength $\lambda = 0.50c$

Figure 29 shows the effect of protuberance amplitude on the lift coefficient of modified hydrofoils with leading edge protuberances of wavelength $\lambda = 0.50c$. In the linear regime, all hydrofoils examined shared very similar lift curve slopes, with a slight dependence on Reynolds number, that ranged from $0.056 \leq \frac{dC_L}{d\alpha} \leq 0.068$ up to $\alpha = 9°$. Past 9˚ however, results varied with Reynolds number. At lower freestream velocities within the range of $0.9 \leq U_\infty \leq 2.7$ m/s the trends in lift coefficient are generally the same. At angles of attack past the linear regime, all foils showed indications of separation, with the lift coefficient becoming nearly constant with angle of attack. In the pre-stall regime, the maximum lift coefficient was either very similar to or lower than the baseline on all hydrofoils with a wavelength of $0.50c$. As the amplitude of the protuberances was decreased, the maximum lift coefficient is increased while the general trends seen in the lift coefficient resembled the baseline lift coefficient to a greater extent as the baseline geometry was approached. Also, in the pre-stall regime, the 4S and 4M hydrofoils showed signs of stall while the 4L showed no signs of rapid or sudden stall throughout the range of angles of attack tested. All modified hydrofoils produced more lift in the early post-stall regime of the baseline hydrofoil, producing as much as ≈ 50% more lift than the baseline hydrofoil. However, at the highest angles of attack examined, the 4S and 4M performed equivalently to the baseline whereas the 4L hydrofoil continued to generate nearly ≈ 40% more lift than the baseline hydrofoil for the lowest freestream velocities tested.

At freestream velocities of U_∞ = 3.6 and 4.5 m/s, the lift characteristics of the 4S and 4M hydrofoils nearly identical (to within experimental uncertainty), with lift coefficients that were nearly equal to the baseline until the stall angle, at which point the 4S and 4M hydrofoils had lower lift. However, the performance of the 4L hydrofoil was very similar to the performance of the baseline at the highest freestream velocities tested, with no dramatic stall and lift coefficient values that were essentially the same.

The drag performance of hydrofoils with a protuberance wavelength of $\lambda = 0.50c$, shown in Figure 30, showed little dependence on Reynolds number. C_D for all hydrofoils was similar at a range of angles of attack $0 \leq \alpha \leq 9°$, with the rate of increase of drag past $\alpha = 9°$ becoming higher as protuberance amplitude was increased. In the pre-stall regime, all modified hydrofoils produced higher drag than the baseline hydrofoil. As the protuberance amplitude was increased, the drag in the pre-stall regime increased as well. In the post-stall regime of the baseline hydrofoil, the drag of all modified hydrofoils was either equal to (to within experimental uncertainty) or greater than the baseline hydrofoil.

The quarter chord moment coefficient is shown in Figure 31. For all positive angles of attack tested, $C_{M1/4}$ is significantly lower on modified foils than the baseline case. With the exception of the lowest freestream velocity tested, in which low Reynolds number effects dominate, $C_{M1/4}$ at mid-range angles decrease with amplitude and remain similar for all other angles tested. Whereas there are clear signs of stall on foils with protuberance amplitudes of $A = 0.025c$ and $0.05c$, with dramatic drops in moment at high angle, the 4L foil, which has the largest protuberances, $A = 0.12c$, showed little sign of a dramatic stall.

The lift-to-drag ratio, shown in Figure 32, reveals that foils with protuberances perform either poorer than or nearly equal to the baseline case. In general, at pre-stall angles of attack,

foils with smaller protuberances outperform the hydrofoil with the largest protuberance amplitude. All foils perform similarly at post-stall angles of attack.

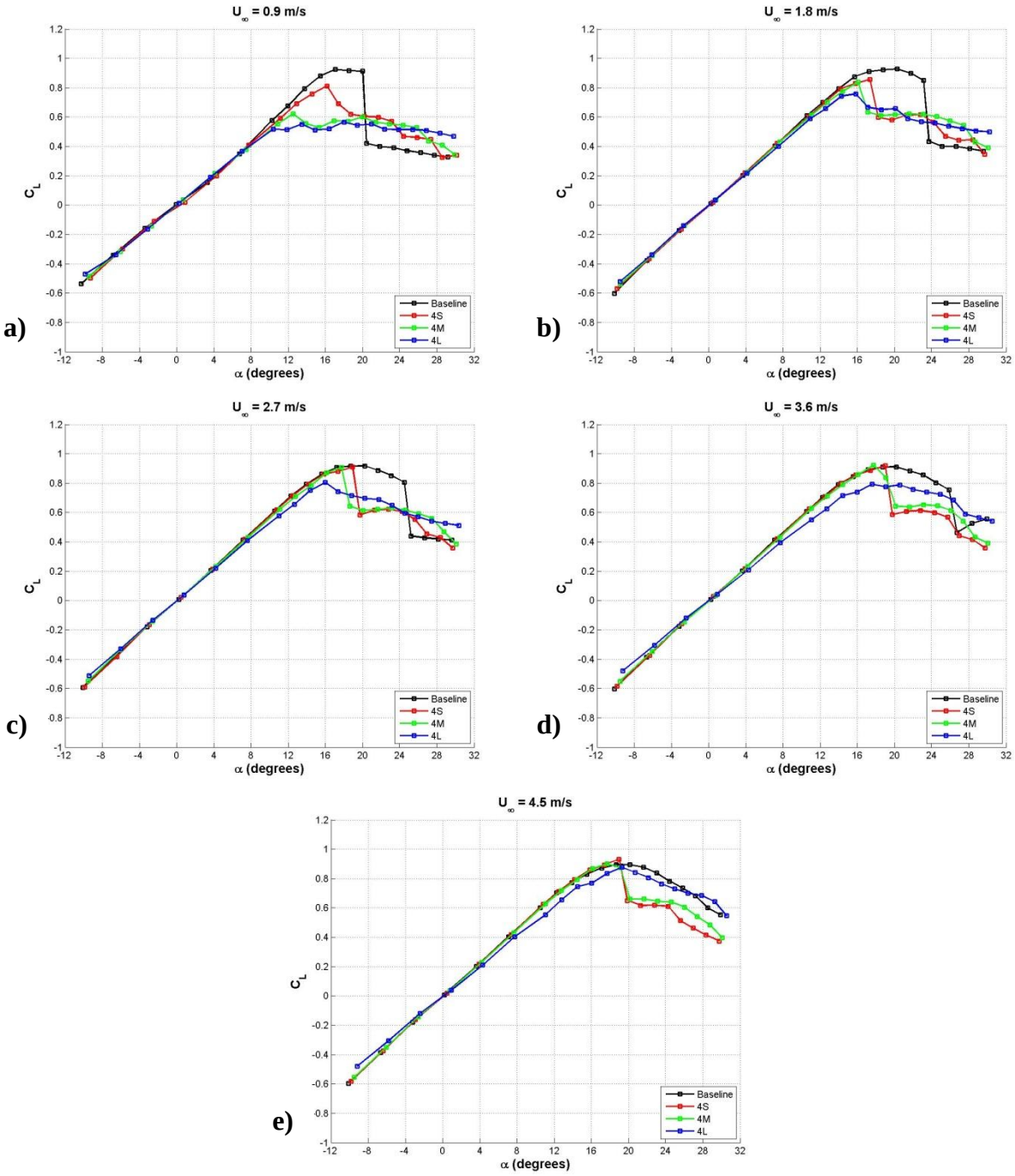

Figure 29: Effect of protuberance amplitude on the lift coefficient of finite-span rectangular planform hydrofoils, $\lambda = 0.50c$. a) $Re_c = 9.0 \times 10^4$, b) $Re_c = 1.8 \times 10^5$, c) $Re_c = 2.7 \times 10^5$, d) $Re_c = 3.6 \times 10^5$, e) $Re_c = 4.5 \times 10^5$.

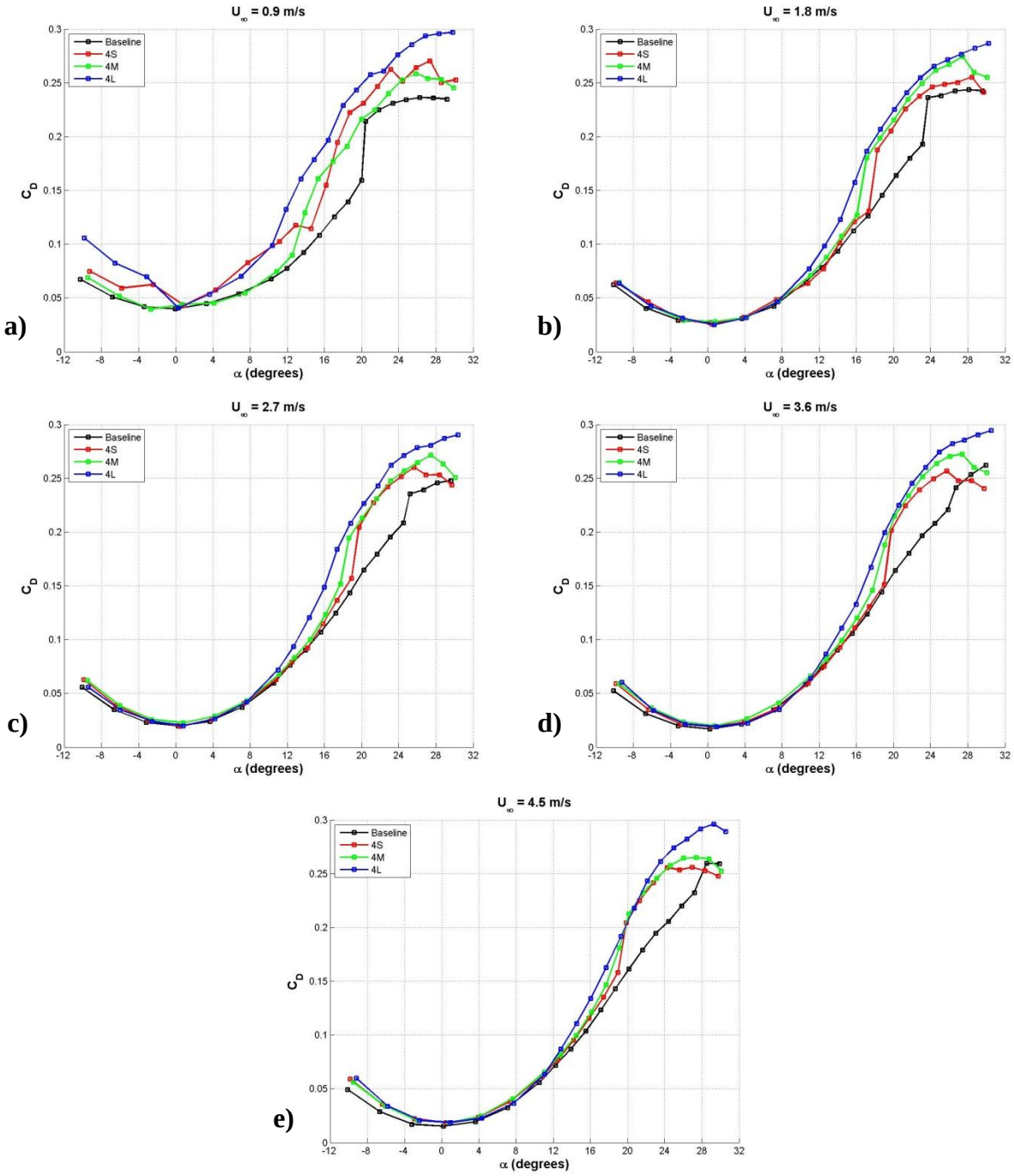

Figure 30: Effect of protuberance amplitude on the drag coefficient of finite-span rectangular planform hydrofoils, $\lambda = 0.50c$. a) $Re_c = 9.0 \times 10^4$, b) $Re_c = 1.8 \times 10^5$, c) $Re_c = 2.7 \times 10^5$, d) $Re_c = 3.6 \times 10^5$, e) $Re_c = 4.5 \times 10^5$.

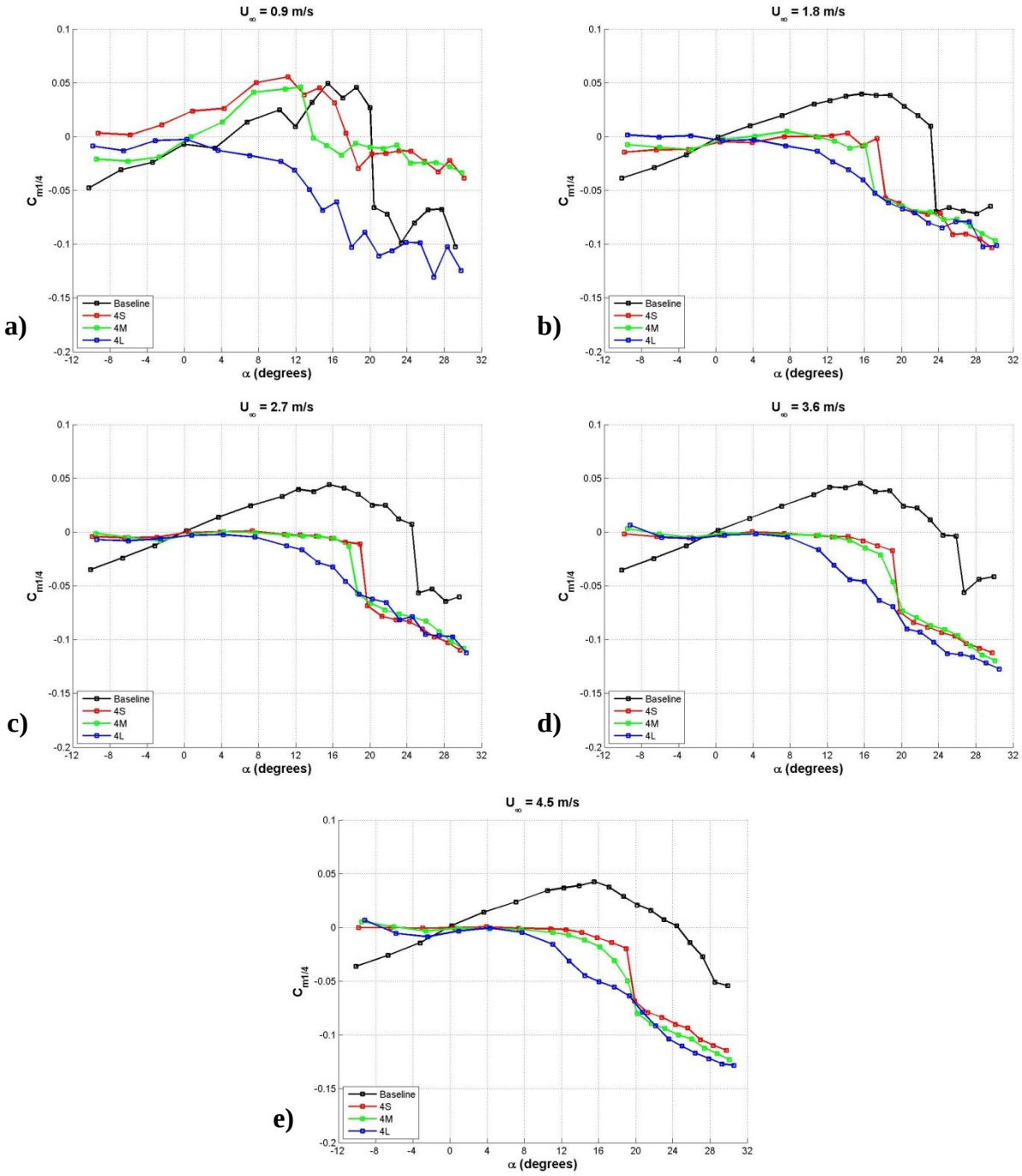

Figure 31: Effect of protuberance amplitude on the quarter chord moment coefficient of finite-span rectangular planform hydrofoils, $\lambda = 0.50c$. a) $Re_c = 9.0 \times 10^4$, b) $Re_c = 1.8 \times 10^5$, c) $Re_c = 2.7 \times 10^5$, d) $Re_c = 3.6 \times 10^5$, e) $Re_c = 4.5 \times 10^5$.

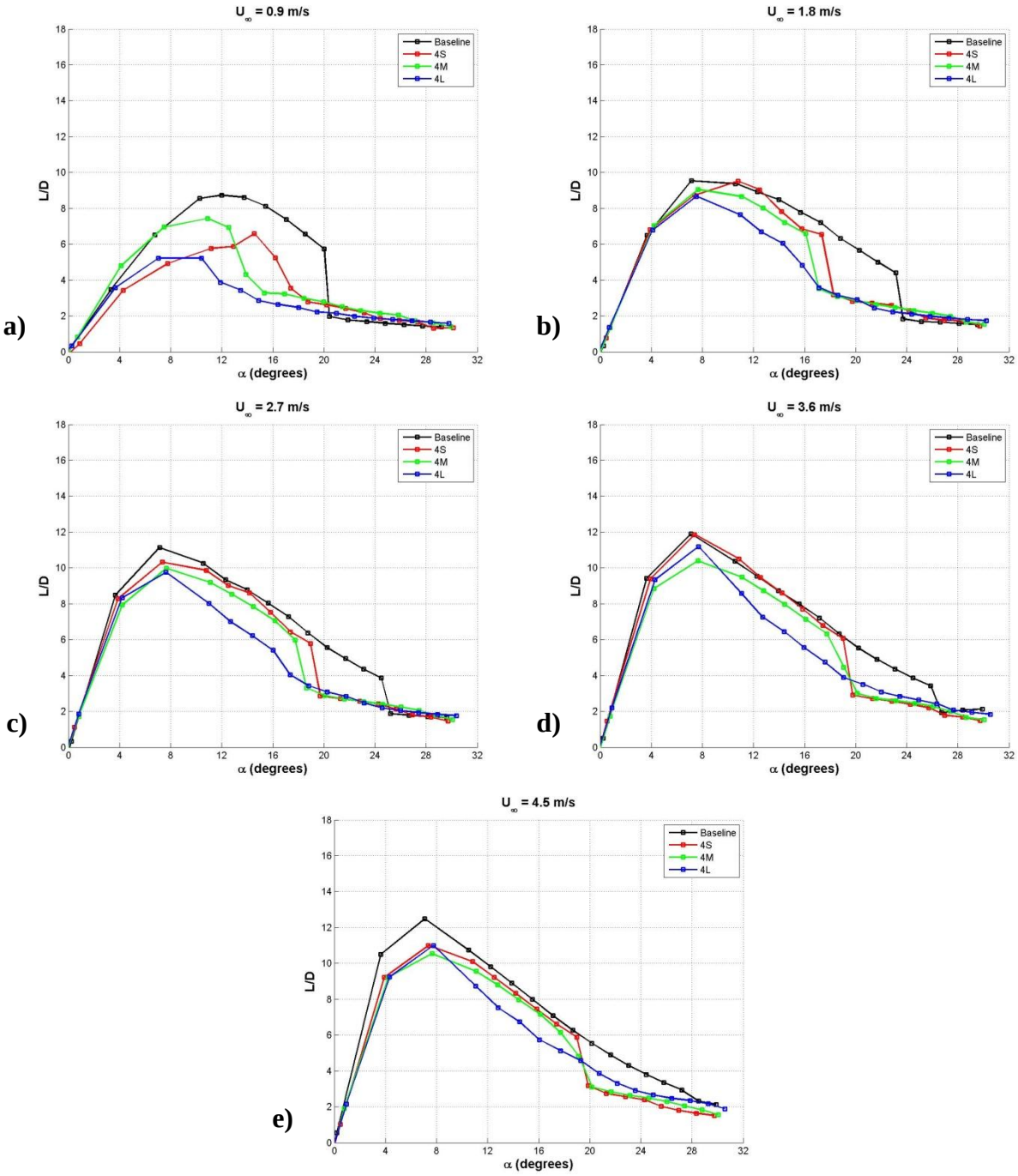

Figure 32: Effect of protuberance amplitude on the lift-to-drag ratio of finite-span rectangular planform hydrofoils, $\lambda = 0.50c$. a) $Re_c = 9.0 \times 10^4$, b) $Re_c = 1.8 \times 10^5$, c) $Re_c = 2.7 \times 10^5$, d) $Re_c = 3.6 \times 10^5$, e) $Re_c = 4.5 \times 10^5$.

Shorter Wavelength λ = 0.25c

The effect of protuberance amplitude on modified hydrofoils of wavelength $\lambda = 0.25c$ can be seen in Figure 33. At lower freestream velocities, within the range of $0.9 \leq U_\infty \leq 2.7$ m/s, the trends in lift coefficient are very similar to those seen in Figure 29 on hydrofoils of wavelength $\lambda = 0.50c$, with maximum lift coefficients either nearly equal to or lower than the baseline lift coefficient. All hydrofoils produced more lift in the early post-stall regime of the baseline hydrofoil generating as much as 65% more lift than the baseline hydrofoil. However, contrary to hydrofoils with longer protuberance wavelengths, the lift coefficient of the 8S hydrofoil is typically higher in the post-stall regime.

At freestream velocities of $3.6 \leq U_\infty \leq 4.5$ m/s, the 8S and 8M hydrofoils had higher maximum lift than the baseline hydrofoil, with the 8S foil generating nearly 13% more lift at a freestream velocity of 3.6 m/s and the 8M foil generating 18% more lift at 4.5 m/s. The baseline hydrofoil generally had a higher lift coefficient in the post-stall regime than the 8M and 8L hydrofoils, while the 8S hydrofoil typically produced nearly equal or higher lift than the baseline hydrofoil.

The drag characteristics are shown in Figure 34. Similar to modified cases with a protuberance wavelength of $\lambda = 0.50c$, the drag coefficient is either nearly equal to or greater than the baseline case at both intermediate and high angles of attack.

The quarter chord moment coefficient and lift-to-drag ratio of foils with a protuberance wavelength of $\lambda = 0.25c$, shown in Figures 35 and 36 show similar performance characteristics to those described in the previous section for modified foils with a protuberance wavelength of $\lambda = 0.50c$.

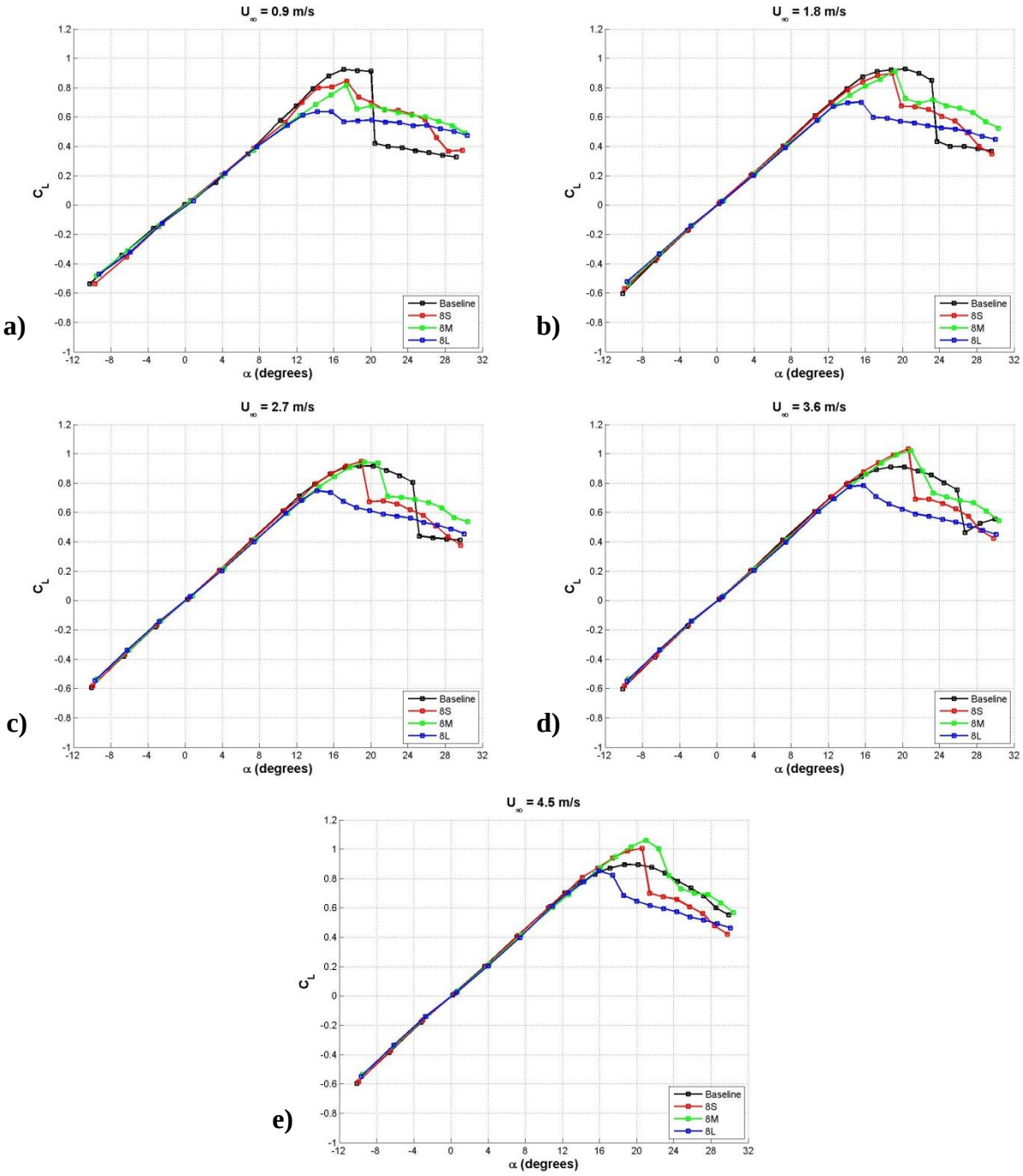

Figure 33: Effect of protuberance amplitude on the lift coefficient of finite-span rectangular planform hydrofoils, $\lambda = 0.25c$. a) $Re_c = 9.0 \times 10^4$, b) $Re_c = 1.8 \times 10^5$, c) $Re_c = 2.7 \times 10^5$, d) $Re_c = 3.6 \times 10^5$, e) $Re_c = 4.5 \times 10^5$.

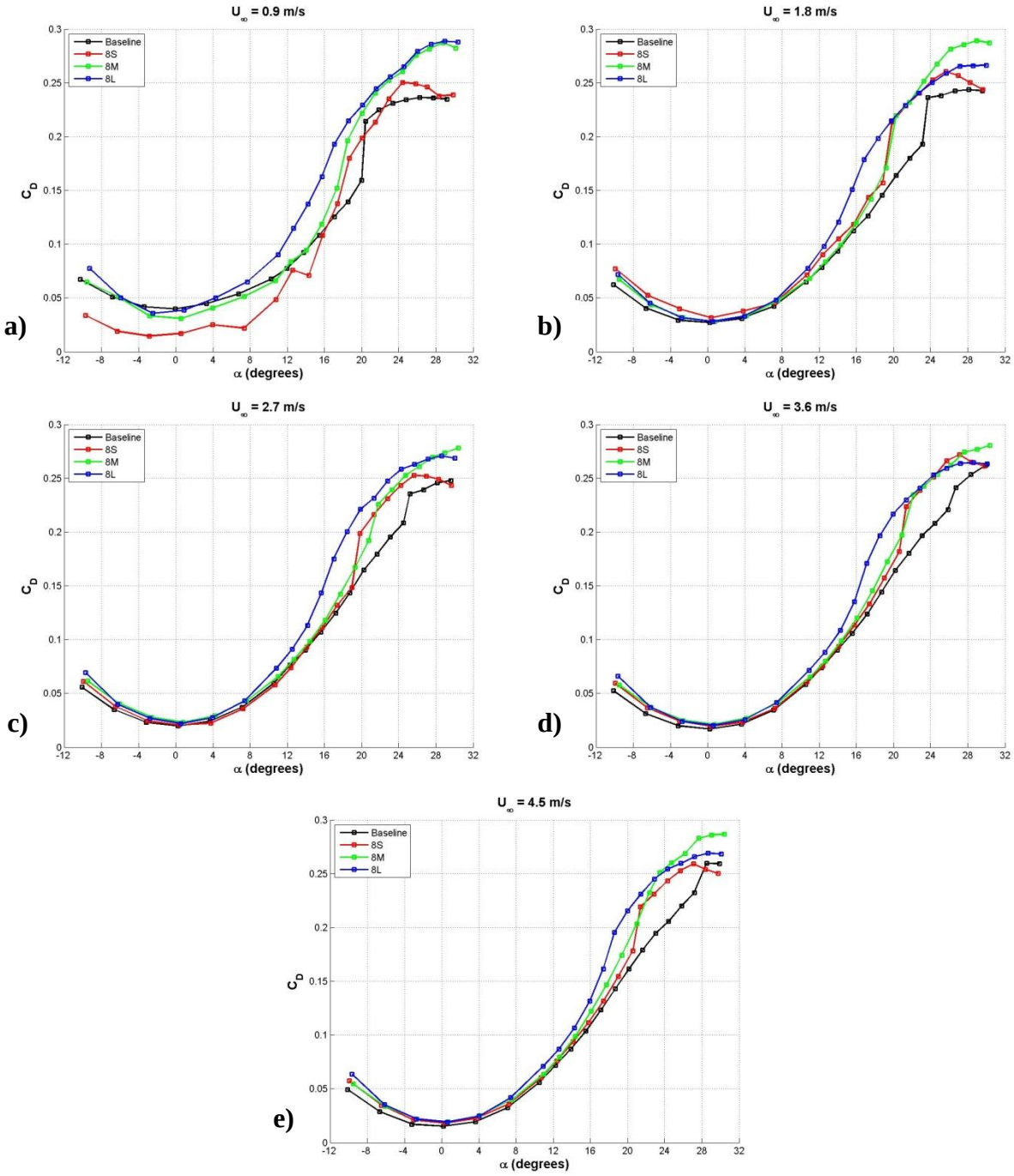

Figure 34: Effect of protuberance amplitude on the drag coefficient of finite-span rectangular planform hydrofoils, $\lambda = 0.25c$. a) $Re_c = 9.0 \times 10^4$, b) $Re_c = 1.8 \times 10^5$, c) $Re_c = 2.7 \times 10^5$, d) $Re_c = 3.6 \times 10^5$, e) $Re_c = 4.5 \times 10^5$.

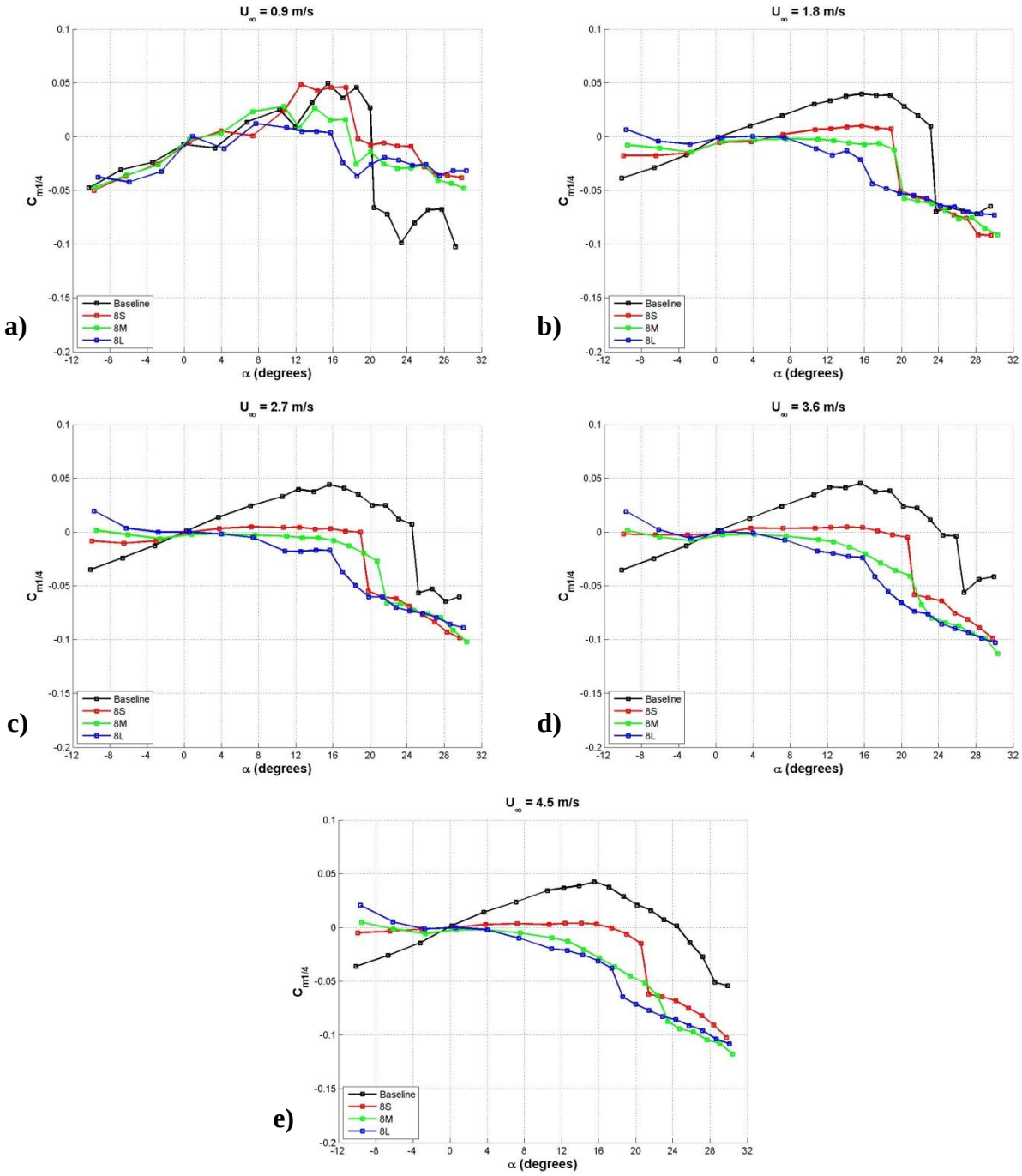

Figure 35: Effect of protuberance amplitude on the quarter chord moment coefficient of finite-span rectangular planform hydrofoils, $\lambda = 0.25c$. a) $Re_c = 9.0 \times 10^4$, b) $Re_c = 1.8 \times 10^5$, c) $Re_c = 2.7 \times 10^5$, d) $Re_c = 3.6 \times 10^5$, e) $Re_c = 4.5 \times 10^5$.

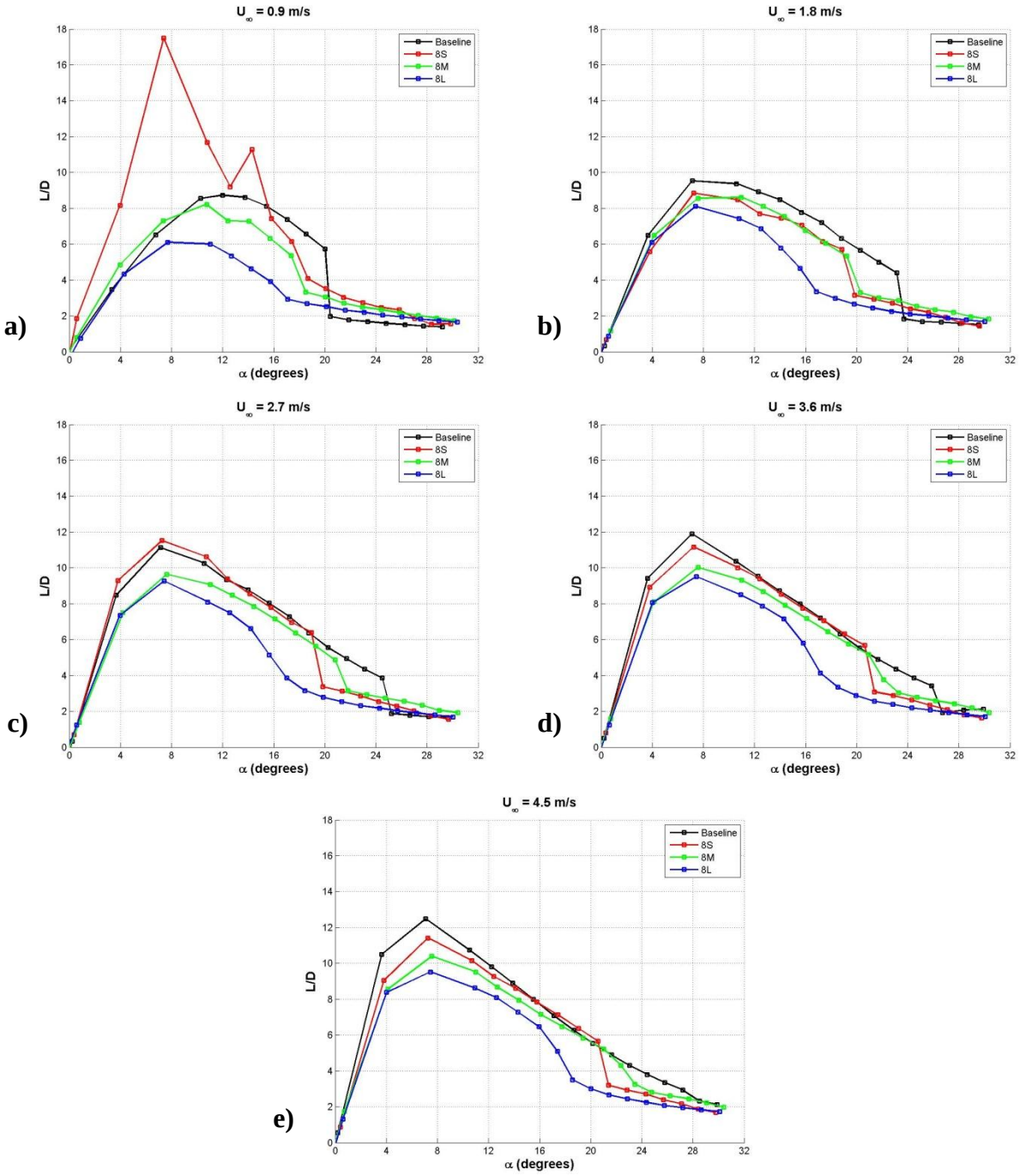

Figure 36: Effect of protuberance amplitude on the lift-to-drag ratio of finite-span rectangular planform hydrofoils, $\lambda = 0.25c$. a) $Re_c = 9.0 \times 10^4$, b) $Re_c = 1.8 \times 10^5$, c) $Re_c = 2.7 \times 10^5$, d) $Re_c = 3.6 \times 10^5$, e) $Re_c = 4.5 \times 10^5$.

Effect of Protuberance Wavelength

The following is an examination of the previously reported data presented in a way that examines the effect of wavelength on finite-span rectangular planform hydrofoils rather than the amplitude. Subsequently, an assessment of the lift curve slopes, as well as a comparison to the baseline hydrofoil has already been described in the previous section. An examination of performance differences between modified hydrofoils due to protuberance wavelength will follow.

Small Amplitude A = 0.025c

The effect of wavelength on the lift characteristics of modified hydrofoils with protuberance amplitude of $A = 0.025c$ can be seen in Figure 37. For all Reynolds numbers examined, C_L of the shorter wavelength 8S hydrofoil was either greater than or within experimental uncertainty to the longer wavelength 4S hydrofoil. At freestream velocities of $0.9 \leq U_\infty \leq 2.7$ m/s the lift characteristics of modified hydrofoils with protuberance amplitudes of $0.025c$ are very similar throughout the range of angles of attack examined. However, as freestream velocity is increased, the lift performance of the 8S hydrofoil at angles of attack from $15° \leq \alpha \leq 22°$ is slightly enhanced, with an increase in maximum C_L of 13% and 12% over both the baseline and 4S hydrofoils at freestream velocities of 3.6 and 4.5 m/s, respectively. While the trends seen in the lift coefficient of both the 4S and 8S hydrofoils differ significantly from the baseline hydrofoil, the lift coefficient of the modified hydrofoils is similar throughout the range of angles of attack tested examined.

The effect of wavelength on the drag characteristics of modified hydrofoils with protuberance amplitude of $0.025c$ can be seen in Figure 38. The drag characteristics of the modified hydrofoils at the lowest protuberance amplitude tested are very similar over the range of angles and Reynolds numbers tested.

With the exception of the lowest freestream velocity tested, in which low Reyolds number effects dominate, along with uncertainty associated with the measurement technique, wavelength affects the quarter chord moment coefficient in such a way that with decreasing wavelength, $C_{M1/4}$ is increased. At post-stall angles of attack, the foil with smaller protuberance wavelength has a slightly increased moment coefficient. The effect of protuberance wavelength on the quarter chord moment coefficient is shown in Figure 39.

At freestream velocities greater than U_∞ = 0.9 m/s, the lift-to-drag ratio is largely unaffected by protuberance wavelength. Both modified foils perform similarly or slightly poorer than the baseline foil. The foil with a smaller protuberance wavelength consistently has a slightly higher stall angle than that of the foil with a larger protuberance wavelength. The effects of protuberance wavelength on the lift-to drag ratios of modified foils are shown in Figure 40.

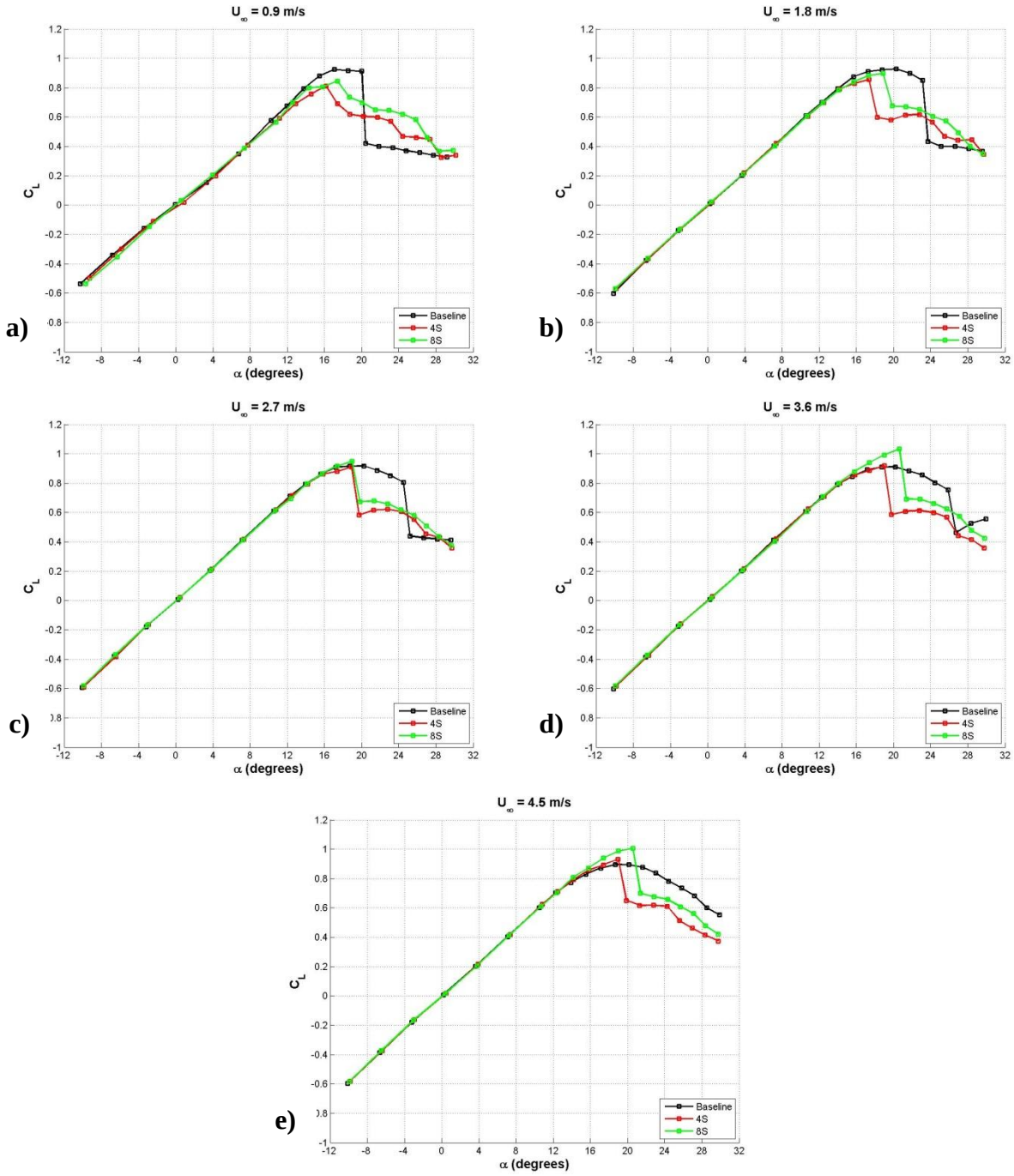

Figure 37: Effect of protuberance wavelength on the lift coefficient of finite-span rectangular planform hydrofoils, $A = 0.025c$. a) $Re_c = 9.0 \times 10^4$, b) $Re_c = 1.8 \times 10^5$, c) $Re_c = 2.7 \times 10^5$, d) $Re_c = 3.6 \times 10^5$, e) $Re_c = 4.5 \times 10^5$.

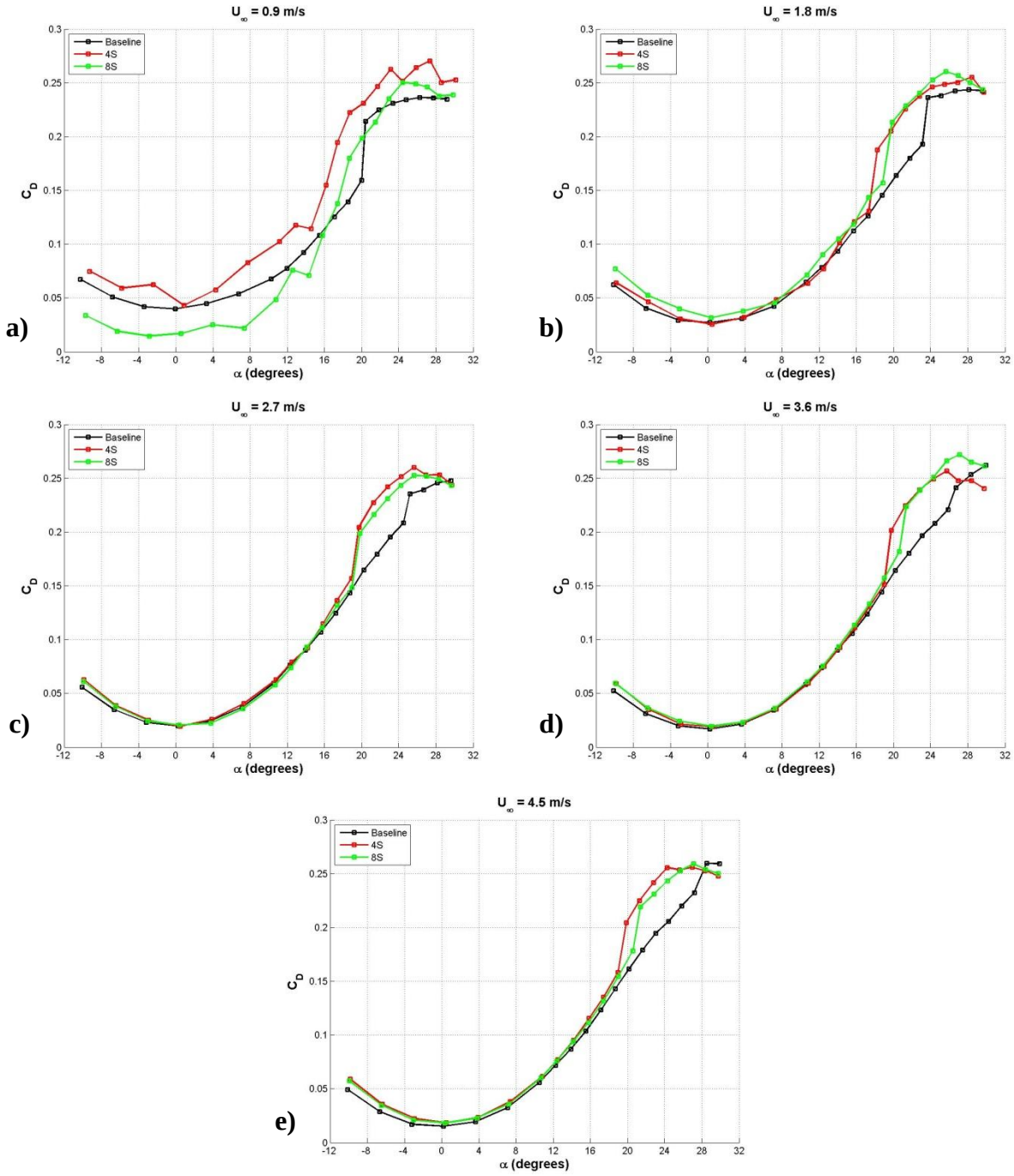

Figure 38: Effect of protuberance wavelength on the drag coefficient of finite-span rectangular planform hydrofoils, $A = 0.025c$. a) $Re_c = 9.0 \times 10^4$, b) $Re_c = 1.8 \times 10^5$, c) $Re_c = 2.7 \times 10^5$, d) $Re_c = 3.6 \times 10^5$, e) $Re_c = 4.5 \times 10^5$.

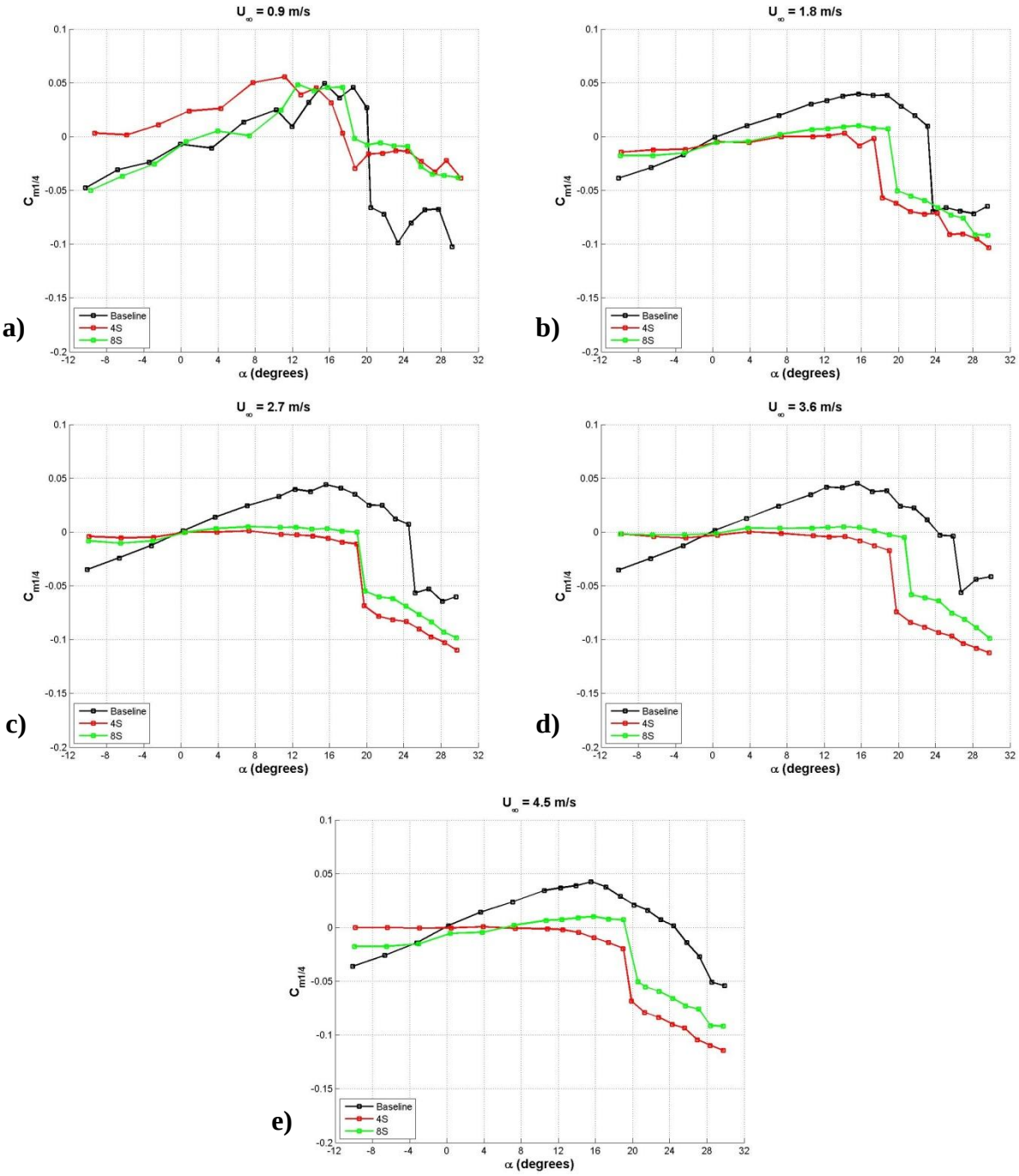

Figure 39: Effect of protuberance wavelength on the quarter chord moment coefficient of finite-span rectangular planform hydrofoils, $A = 0.025c$. a) $Re_c = 9.0 \times 10^4$, b) $Re_c = 1.8 \times 10^5$, c) $Re_c = 2.7 \times 10^5$, d) $Re_c = 3.6 \times 10^5$, e) $Re_c = 4.5 \times 10^5$.

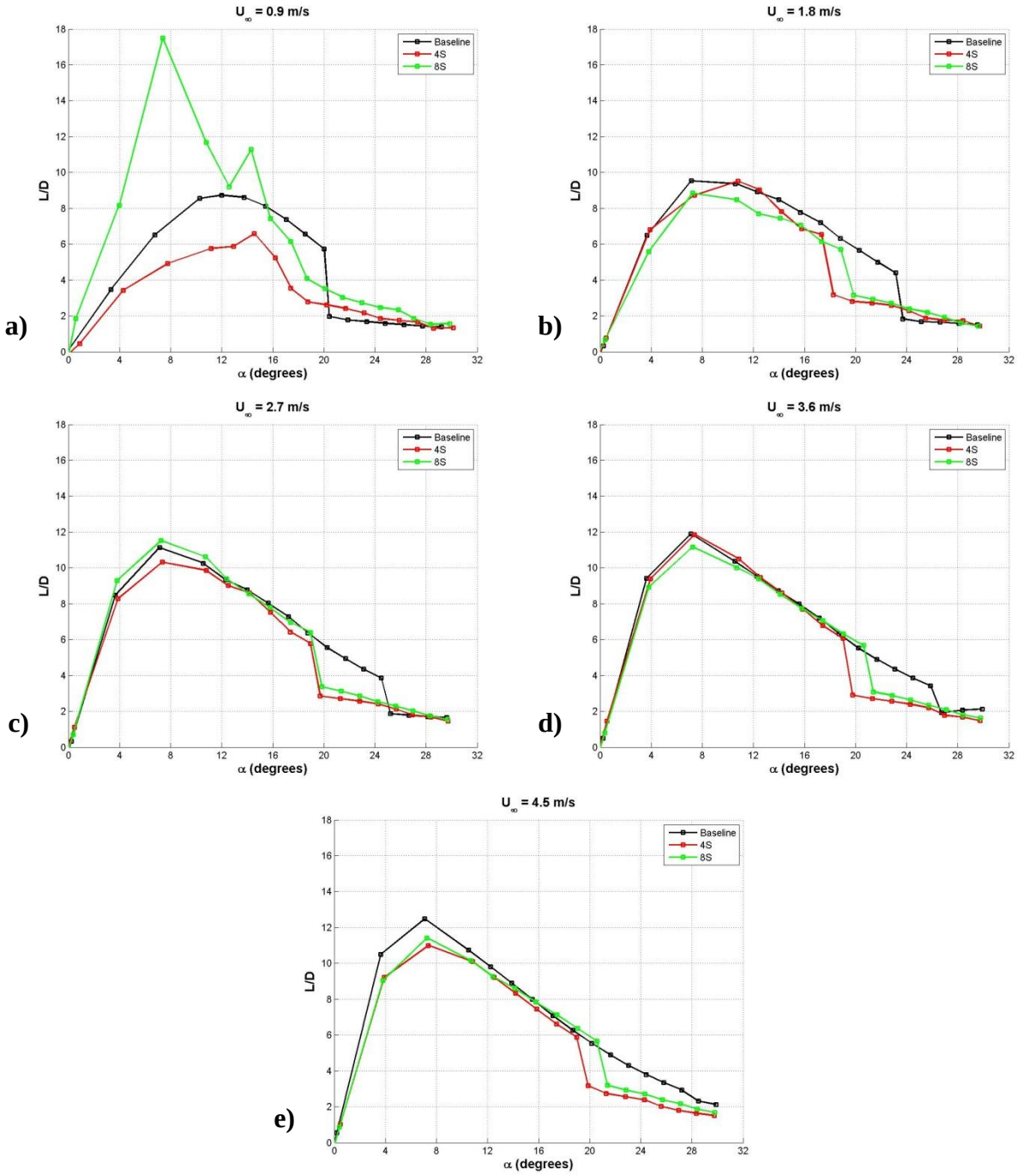

Figure 40: Effect of protuberance wavelength on the lift-to-drag ratio of finite-span rectangular planform hydrofoils, $A = 0.025c$. a) $Re_c = 9.0 \times 10^4$, b) $Re_c = 1.8 \times 10^5$, c) $Re_c = 2.7 \times 10^5$, d) $Re_c = 3.6 \times 10^5$, e) $Re_c = 4.5 \times 10^5$.

Medium Amplitude A = 0.050c

The effect of wavelength on the lift characteristics of modified hydrofoils with the medium protuberance amplitude of $A = 0.05c$ can be seen in Figure 41. For all Reynolds numbers tested, the shorter 8M hydrofoil consistently generated a similar or greater lift coefficient than the 4M hydrofoil over the range of angles examined, with a maximum difference between modified hydrofoils of nearly 60% at Reynolds numbers of $U_\infty = 3.6$ and 4.5 m/s. Both modified hydrofoils showed signs of stall, with the 8M hydrofoil consistently stalling at a higher angle of attack than the 4M hydrofoil. At freestream velocities of 3.6 and 4.5 m/s the 8M produced a lift coefficient that was nearly equal to or higher than the baseline hydrofoil throughout the range of angles attack examined. Over a range of angle of attack $15° \leq \alpha \leq 22°$ the 8M produced as much as 18% more lift than the baseline hydrofoil at an angle of attack of 21°.

The effect of wavelength on the drag characteristics of modified hydrofoils with protuberance amplitudes of $0.50c$ is shown in Figure 42. At freestream velocities of $0.9 \leq U_\infty \leq 2.7$ m/s, C_D of the 4M hydrofoil was as much as 36% greater than the 8M hydrofoil over a range of angles of attack of $15° \leq \alpha \leq 21°$. However, at freestream velocities of 2.7 and 3.6 m/s, C_D of the 4M and 8M hydrofoils similar to within experimental uncertainty. The likely cause of this phenomenon was the existence of stall at lower Reynolds numbers.

With the exception of post-stall angles of attack, in which both modified foils show similar $C_{M1/4}$, the general trends of both $C_{M1/4}$ and L/D on foils with a protuberance amplitude of $A = 0.05c$ show performance characteristics that are very similar to those seen in the previous section on foils with a protuberance amplitude of $A = 0.025c$. The quarter chord moment coefficient and lift-to-drag ratio of the modified foils with a protuberance amplitude of $A = 0.05c$ are presented in Figures 43 and 44.

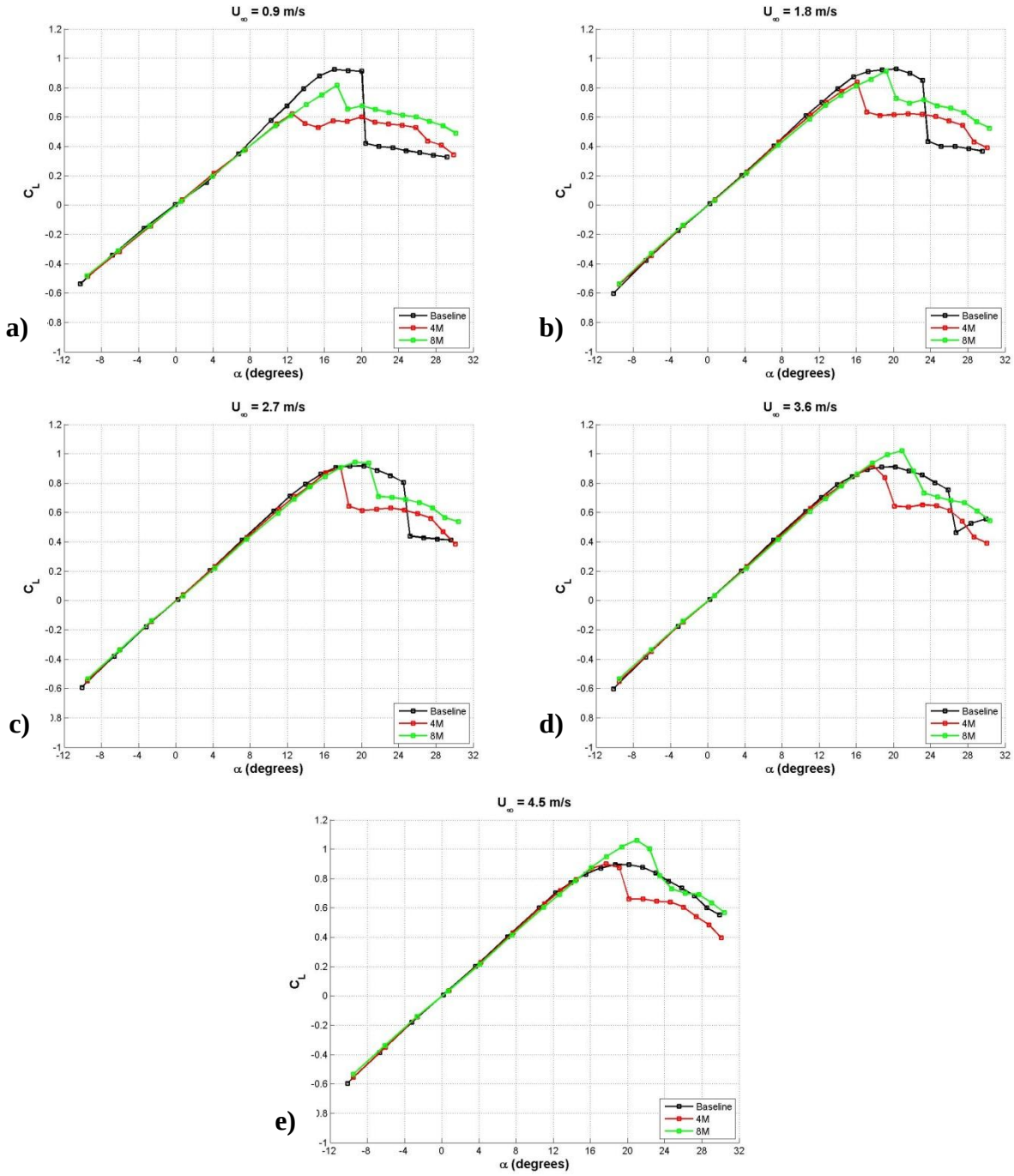

Figure 41: Effect of protuberance wavelength on the lift coefficient of finite-span rectangular planform hydrofoils, $A = 0.050c$. a) $Re_c = 9.0 \times 10^4$, b) $Re_c = 1.8 \times 10^5$, c) $Re_c = 2.7 \times 10^5$, d) $Re_c = 3.6 \times 10^5$, e) $Re_c = 4.5 \times 10^5$.

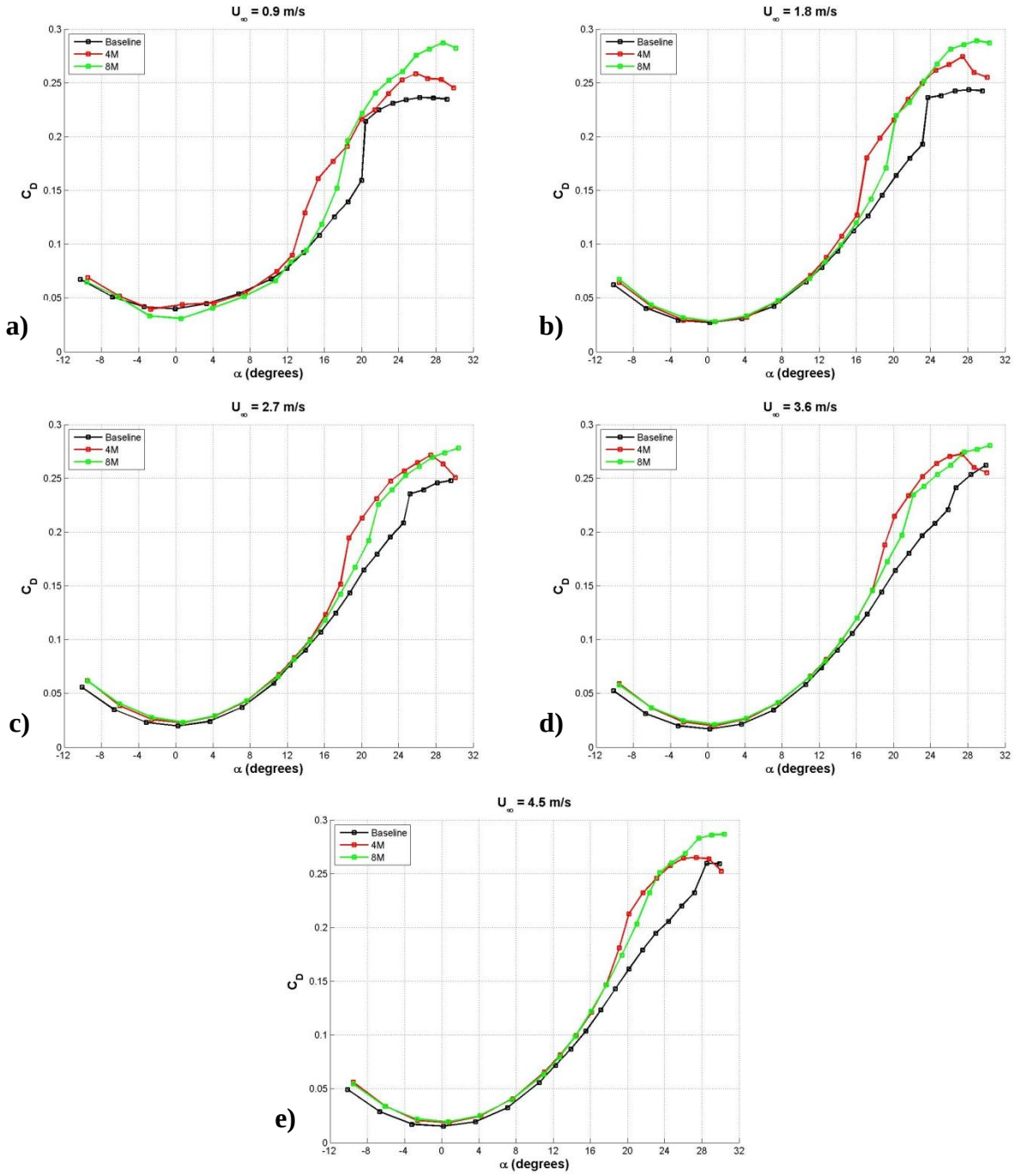

Figure 42: Effect of protuberance wavelength on the drag coefficient of finite-span rectangular planform hydrofoils, $A = 0.050c$. a) $Re_c = 9.0 \times 10^4$, b) $Re_c = 1.8 \times 10^5$, c) $Re_c = 2.7 \times 10^5$, d) $Re_c = 3.6 \times 10^5$, e) $Re_c = 4.5 \times 10^5$.

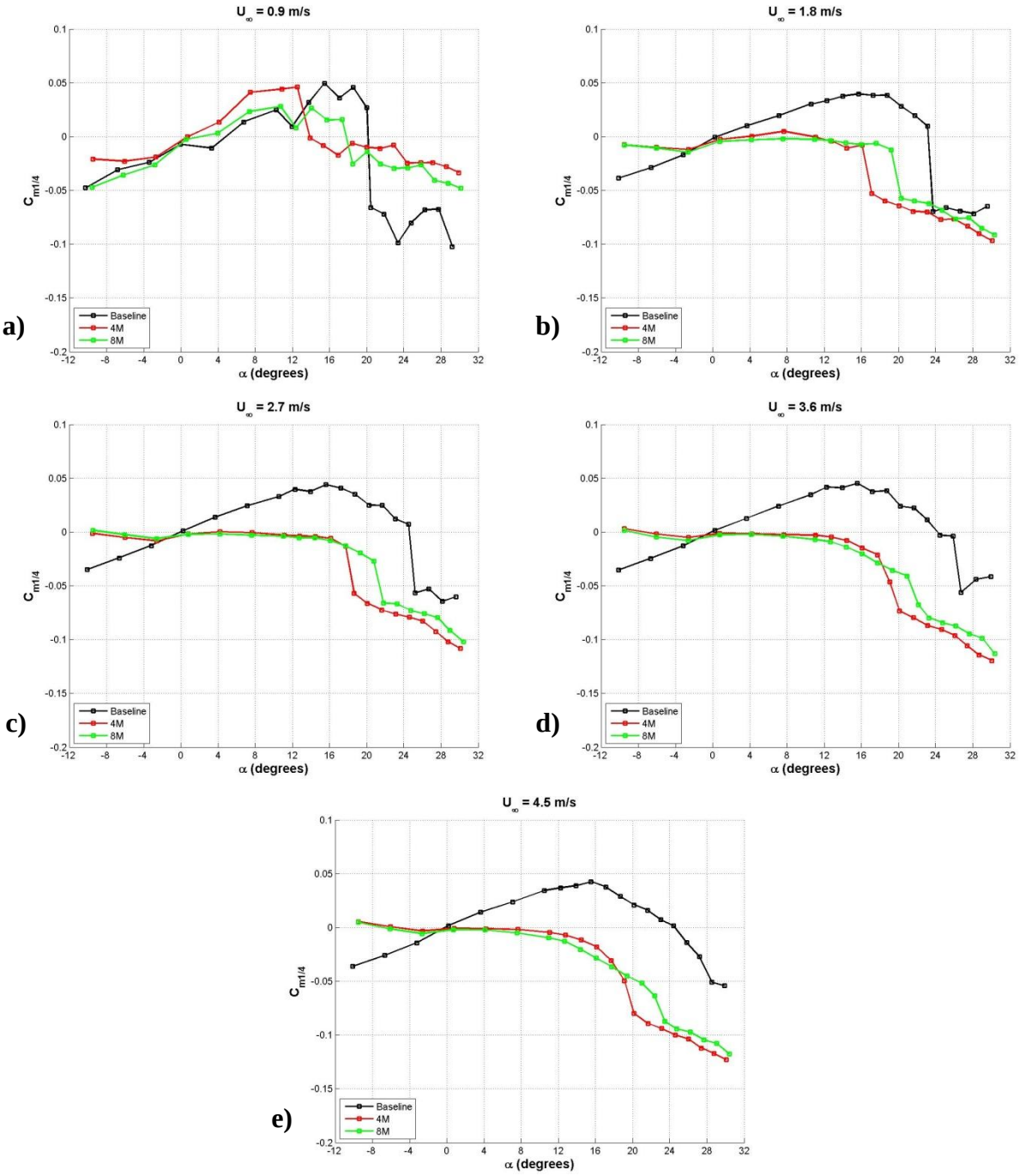

Figure 43: Effect of protuberance wavelength on the quarter chord moment coefficient of finite-span rectangular planform hydrofoils, $A = 0.050c$. a) $Re_c = 9.0 \times 10^4$, b) $Re_c = 1.8 \times 10^5$, c) $Re_c = 2.7 \times 10^5$, d) $Re_c = 3.6 \times 10^5$, e) $Re_c = 4.5 \times 10^5$.

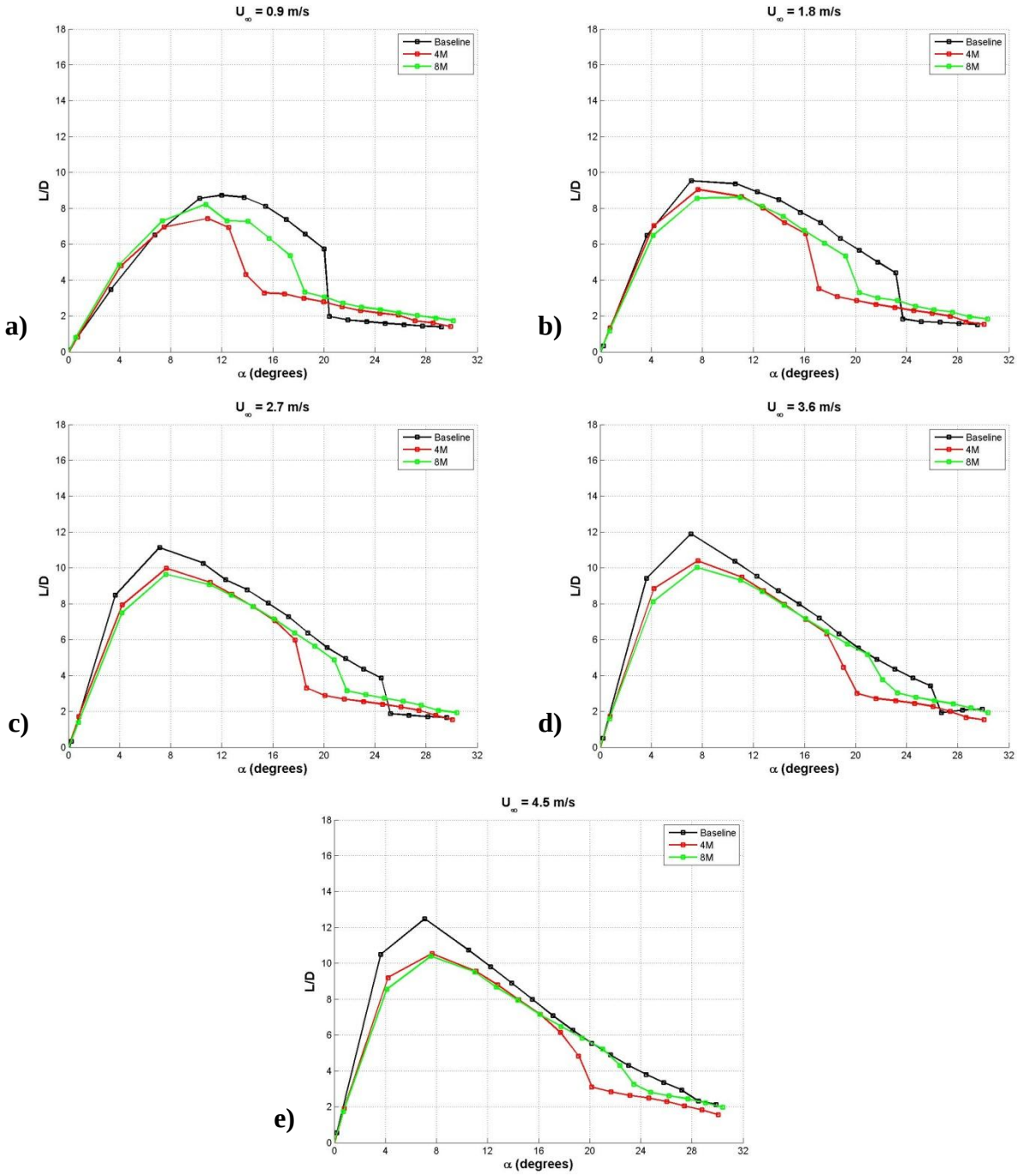

Figure 44: Effect of protuberance wavelength on the lift-to-drag ratio of finite-span rectangular planform hydrofoils, $A = 0.050c$. a) $Re_c = 9.0 \times 10^4$, b) $Re_c = 1.8 \times 10^5$, c) $Re_c = 2.7 \times 10^5$, d) $Re_c = 3.6 \times 10^5$, e) $Re_c = 4.5 \times 10^5$.

Large Amplitude A = 0.120c

The effect of wavelength on the lift characteristics of modified hydrofoils with the large protuberance amplitude of $A = 0.12c$ is shown in Figure 45. The lift coefficient trends on hydrofoils with large amplitude leading edge protuberances differ considerably from those seen on hydrofoils with smaller amplitudes. Whereas the lift coefficient on hydrofoils with a shorter protuberance wavelength typically produced a higher C_L than hydrofoils with a longer protuberance wavelength at the smaller amplitudes, this trend is reversed on hydrofoils with protuberance amplitudes equal to $0.12c$. At the lowest freestream velocity examined, $U_\infty = 0.90$ m/s, the C_L of the 4L and 8L hydrofoils are very similar. As the freestream velocity is increased, the difference in C_L between the 4L and 8L hydrofoils becomes significantly more pronounced. The 4L foil produces more lift than the 8L hydrofoils at all freestream speeds greater than 0.90 m/s, generating as much as 32% more lift than the 8L hydrofoil at $U_\infty = 4.5$ m/s. As freestream velocity is increased, the trends seen in the lift coefficient of both modified cases become increasingly similar to the baseline hydrofoil, with C_L of the 4L hydrofoil always being less than the baseline hydrofoil at 4.5 m/s.

The effect of wavelength on the drag characteristics of modified hydrofoils with protuberance amplitude $0.12c$ is shown in Figure 46. Protuberance wavelength plays only a minor role in establishing the drag characteristics of modified hydrofoils at the largest amplitude. For all freestream velocities examined, C_D was very similar for both protuberance wavelengths examined. However, at freestream velocities ranging from $1.8 \leq U_\infty \leq 4.5$ m/s, C_D of the 4L was generally higher at angles of attack ranging from $21° \leq \alpha \leq 30°$ with a maximum difference between the hydrofoils of 15%.

With the exception of very low freestream velocity, both $C_{M1/4}$ and L/D on foils with a protuberance amplitude of $A = 0.12c$ are very similar with only minor differences throughout the

range of angles of attack tested. The quarter chord moment coefficient and lift-to-drag ratio of the modified foils with a protuberance amplitude of $A = 0.12c$ are shown in Figures 47 and 48.

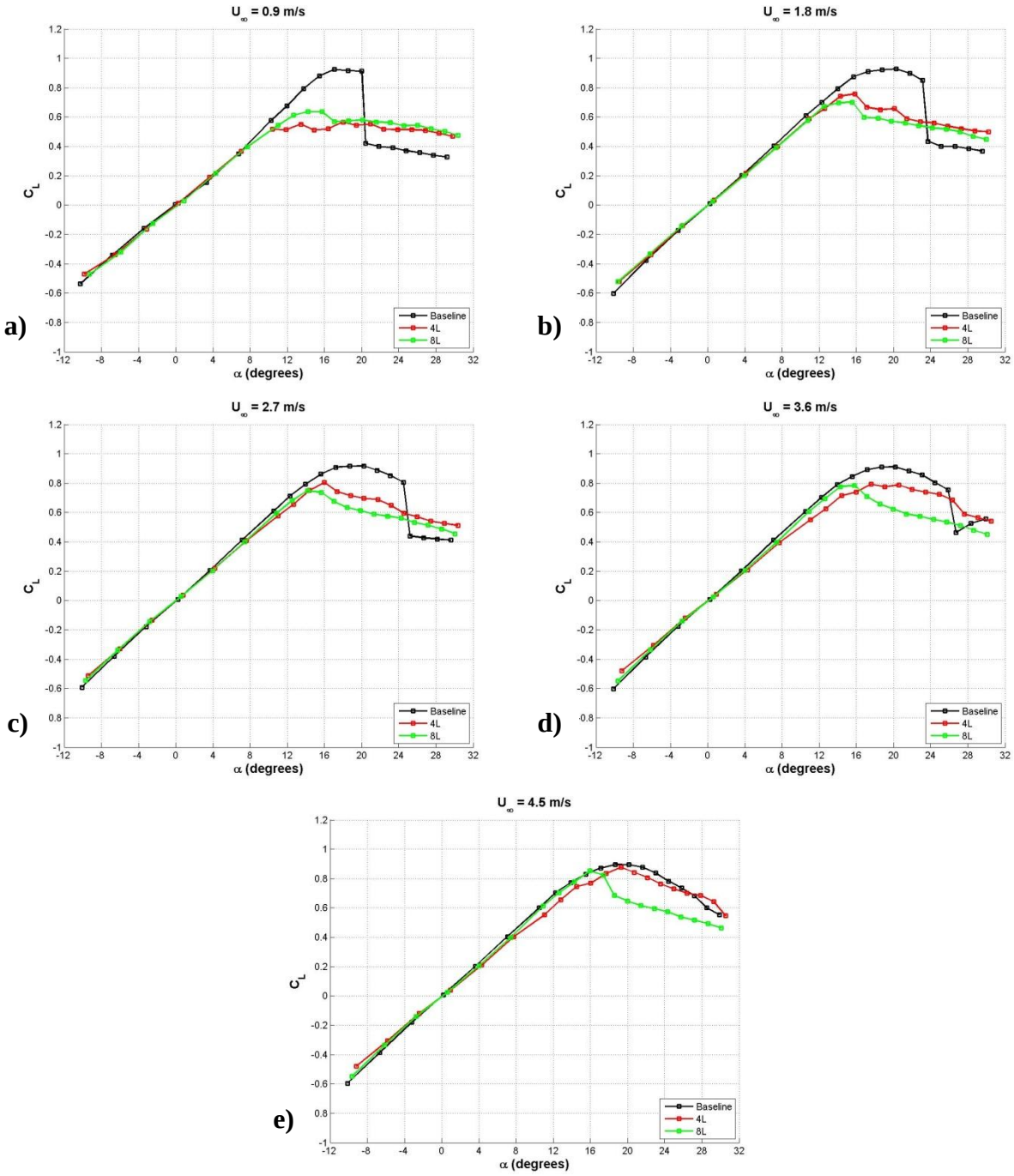

Figure 45: Effect of protuberance wavelength on the lift coefficient of finite-span rectangular planform hydrofoils, $A = 0.120c$. a) $Re_c = 9.0 \times 10^4$, b) $Re_c = 1.8 \times 10^5$, c) $Re_c = 2.7 \times 10^5$, d) $Re_c = 3.6 \times 10^5$, e) $Re_c = 4.5 \times 10^5$.

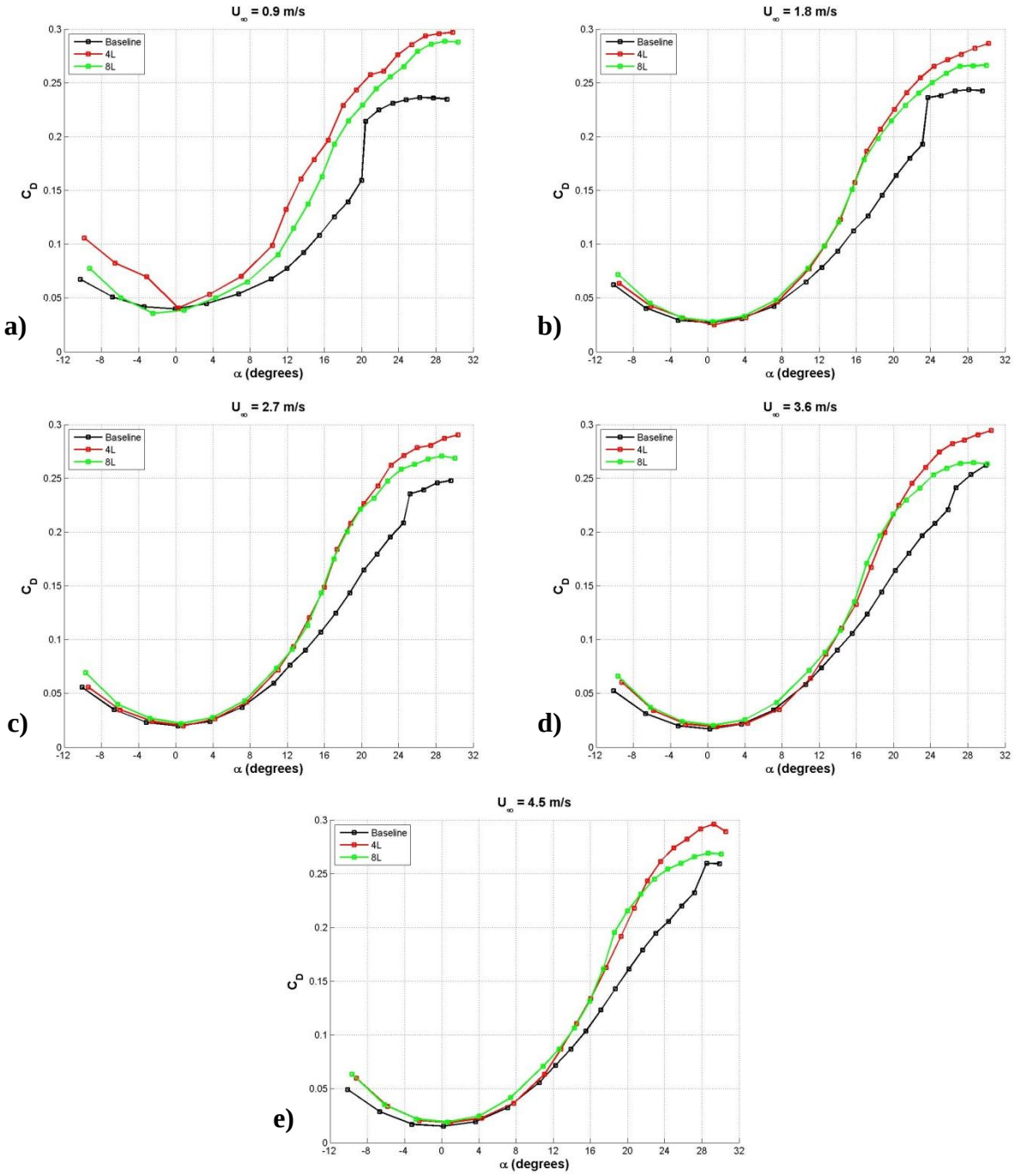

Figure 46: Effect of protuberance wavelength on the drag coefficient of finite-span rectangular planform hydrofoils, $A = 0.120c$. a) $Re_c = 9.0 \times 10^4$, b) $Re_c = 1.8 \times 10^5$, c) $Re_c = 2.7 \times 10^5$, d) $Re_c = 3.6 \times 10^5$, e) $Re_c = 4.5 \times 10^5$.

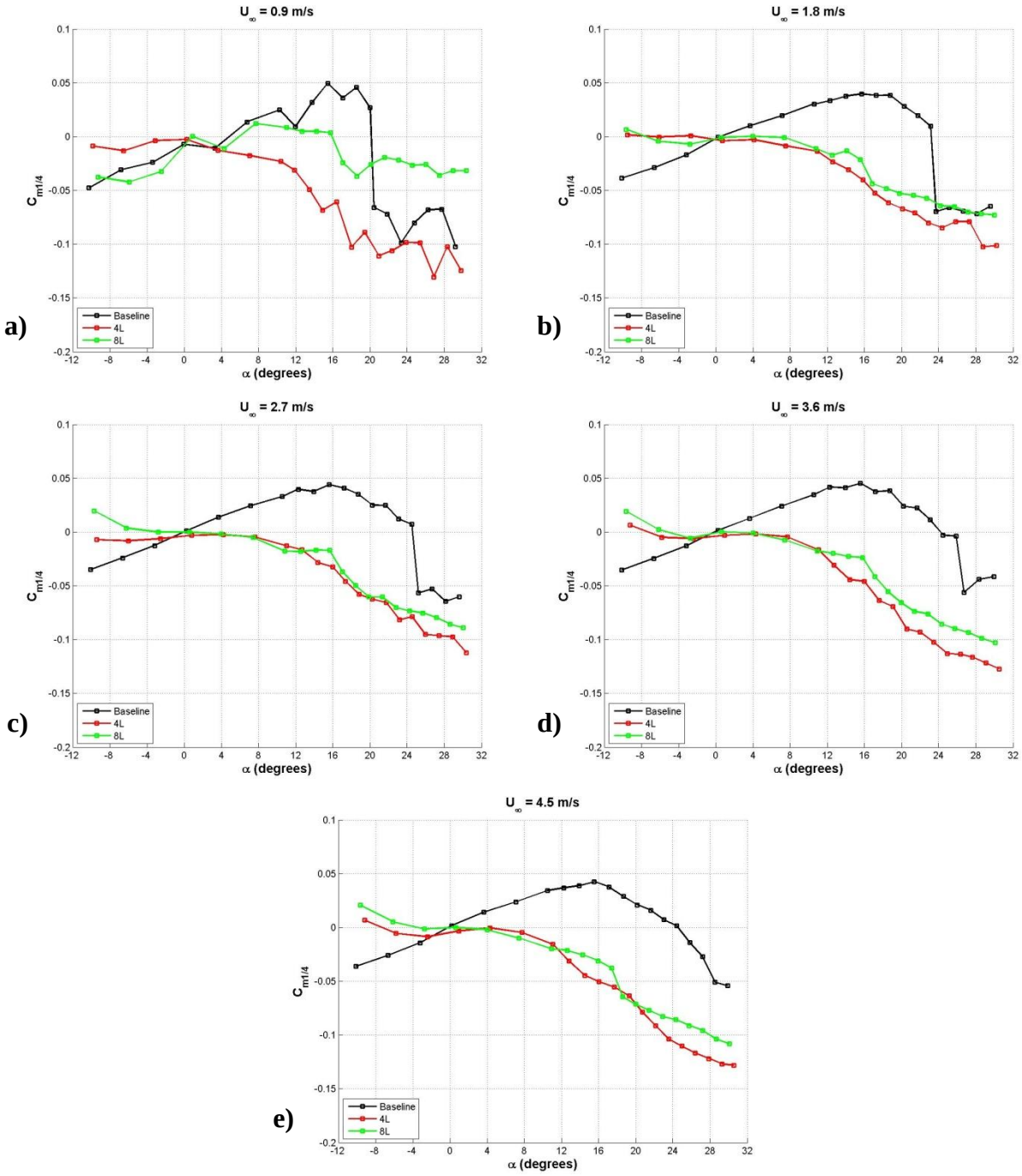

Figure 47: Effect of protuberance wavelength on the quarter chord moment coefficient of finite-span rectangular planform hydrofoils, $A = 0.120c$. a) $Re_c = 9.0 \times 10^4$, b) $Re_c = 1.8 \times 10^5$, c) $Re_c = 2.7 \times 10^5$, d) $Re_c = 3.6 \times 10^5$, e) $Re_c = 4.5 \times 10^5$.

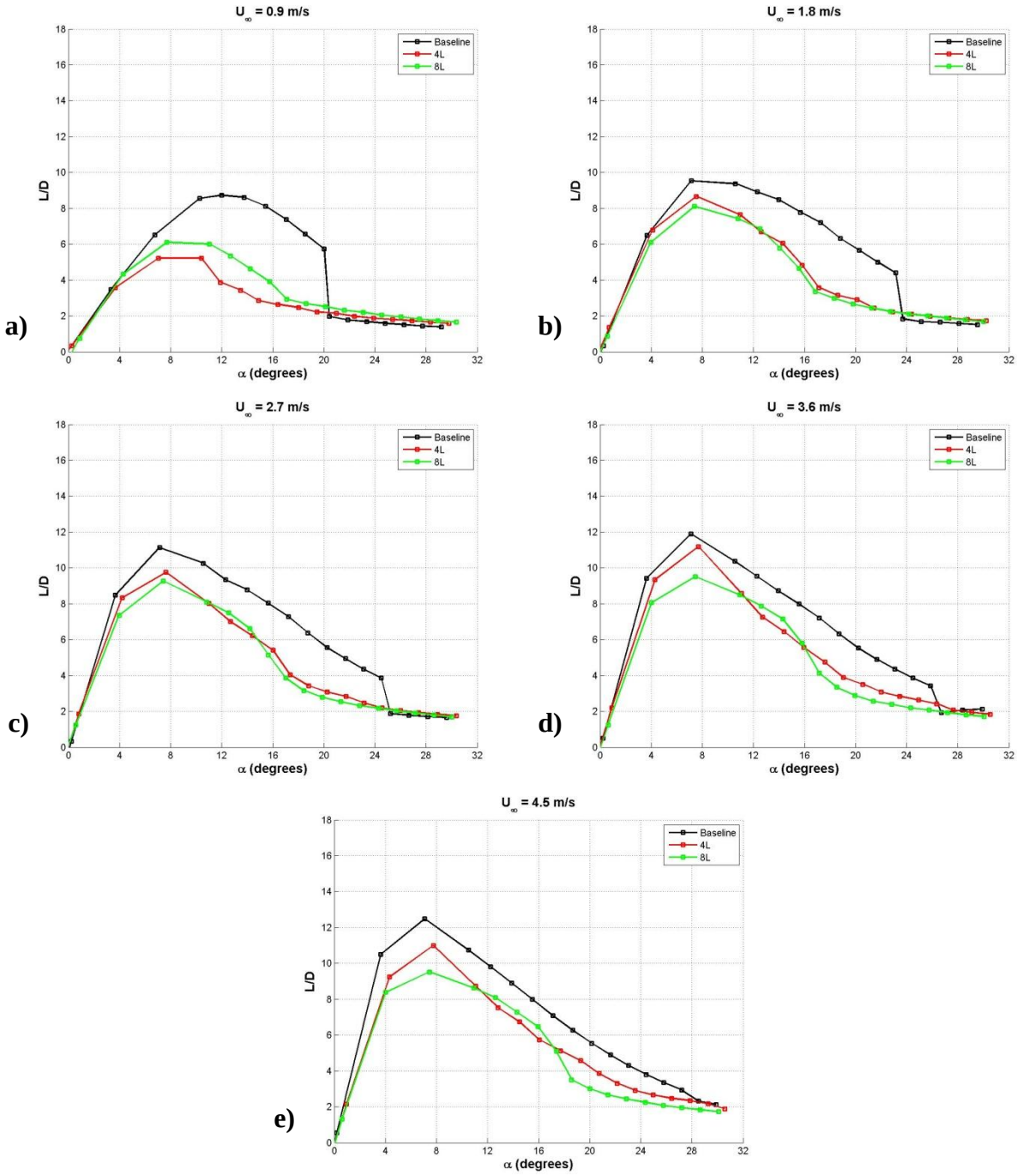

Figure 48: Effect of protuberance wavelength on the lift-to-drag ratio of finite-span rectangular planform hydrofoils, $A = 0.120c$. a) $Re_c = 9.0 \times 10^4$, b) $Re_c = 1.8 \times 10^5$, c) $Re_c = 2.7 \times 10^5$, d) $Re_c = 3.6 \times 10^5$, e) $Re_c = 4.5 \times 10^5$.

Swept Planform Hydrofoils

Baseline Model

The lift coefficient of the swept baseline hydrofoil, shown in Figure 49, reveals that there are two distinct Reynolds number regimes at which C_L behaves differently. These regimes correspond to freestream velocity ranges of $0.9 \leq U_\infty \leq 1.8$ m/s and $2.7 \leq U_\infty \leq 4.5$ m/s. At freestream velocities ranging from $0.9 \leq U_\infty \leq 1.8$ m/s, C_L increases linearly with angle of attack over a range of angles $0° \leq \alpha \leq 6°$. Past $\alpha = 6°$, flow separation is indicated by a leveling off of C_L. At high angle of attack C_L decreases at low rate, without any sign of abrupt stall.

For freestream velocities greater than $U_\infty = 1.8$ m/s, the linear regime of the lift coefficient is extended to significantly higher angle than for lower velocities with the linear regime of C_L lying in the range of angles of attack $0° \leq \alpha \leq 20°$. Past the linear regime, C_L once again shows indications of separation, though only over a very limited range of angles $21° \leq \alpha \leq 26°$. Stall is also apparent at the higher Reynolds number, with a dramatic decrease in C_L at freestream velocities higher than $U_\infty = 1.8$ m/s. The stall angle increases with Reynolds number as well. With the exception of stall angle, C_L is similar to within experimental uncertainty throughout all freestream velocities above 1.8 m/s.

The drag coefficient characteristics, shown in Figure 49, also reveal dependency on Reynolds number with two distinct regimes once again being present. While values for C_D are similar in either regime separately, the two regimes differ significantly, with as much as 32% higher C_D in the pre-stall regime. However, at very high and very low angles of attack, C_D lacks a significant dependence on Reynolds number.

With the exception of slightly increasing stall angle, at Reynolds numbers greater than $Re_c = 1.8 \times 10^5$, $C_{M1/4}$ and L/D are largely unaffected by Reynolds number. However, at low Reynolds numbers, a larger variance in the trends can be seen. This is likely due to low Reynolds

number effects in which flow is transitioning from laminar to turbulent, generating differences between higher and lower Reynolds number regimes. The effect of Reynolds number on $C_{M1/4}$ and *L/D*, is shown in Figure 49c and d. Table 16 shows the corresponding aerodynamic characteristics of the swept baseline hydrofoil.

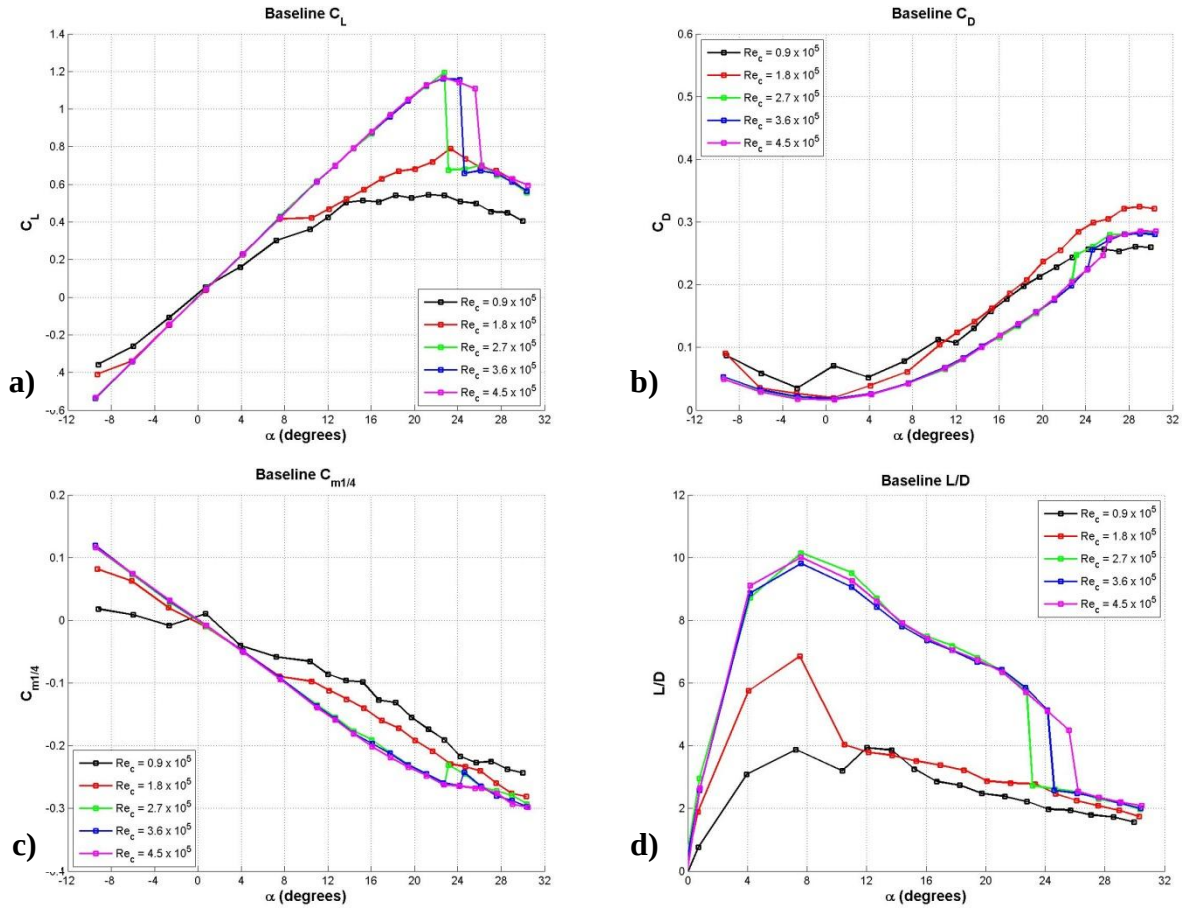

Figure 49: Effect of Reynolds number on the swept planform baseline hydrofoil load characteristics. a) lift coefficient, b) drag coefficient, c) quarter chord moment coefficient, d) L/D ratio.

Table 16: Aerodynamic characteristics of swept planform baseline foil. Refer to Table 5 for corresponding uncertainties.

	$Re_c = 9.0 \times 10^4$	$Re_c = 1.8 \times 10^5$	$Re_c = 2.7 \times 10^5$	$Re_c = 3.6 \times 10^5$	$Re_c = 4.5 \times 10^5$
$\frac{dC_L}{d\alpha}$ [1/deg]	0.041	0.055	0.055	0.055	0.055
C_{Lmax}	0.54	0.79	1.19	1.16	1.17
α @ C_{Lmax} [deg]	21.3	23.3	22.7	22.7	22.7
C_{Dmin}	0.04	0.02	0.02	0.02	0.02
L/D_{max}	3.93	6.84	10.15	9.81	10.01
α @ L/D_{max} [deg]	12.0	7.5	7.6	7.6	7.6
α_{stall} [deg]	N/A	23.3	22.7	24.2	25.6

Modified Model

The effect of Reynolds number on the modified swept hydrofoil can be seen in Figure 50. As with the baseline hydrofoil, there are two Reynolds number regimes in which the lift coefficient behaves differently, which correspond to freestream velocity ranges of $0.9 \leq U_\infty \leq 2.7$ m/s and $3.6 \leq U_\infty \leq 4.5$ m/s. Within each regime the lift coefficient is very similar for all freestream velocities tested. At angles of attack greater than $\alpha = 10°$, C_L at the higher Reynolds numbers is greater than the lower freestream velocities tested, with as much as 25% more lift generated at the highest freestream velocities tested. The drag coefficient of the modified hydrofoil was relatively unaffected by Reynolds number. The quarter chord moment coefficient of the modified swept foil is nearly unaffected by Reynolds number. However, similar transition effects to those seen in the lift coefficient can be seen in *L/D* due to transition effects being apparent in the lift coefficient while drag is left unaffected. The effect of Reynolds number on $C_{M1/4}$ and *L/D* is presented in Figure 50c and d.

The effect of leading edge protuberances on the load characteristics of the modified swept leading edge hydrofoil is shown in Figures 51 - 54. At freestream velocities of $0.9 \leq U_\infty \leq$ 1.8 m/s, the C_L of both the baseline and modified hydrofoils increases nearly linearly at lower angles of attack with the linear regime extending as the freestream velocity is increased. However, at low freestream velocities, the baseline C_L becomes level and reaches the stall angle prior to the modified hydrofoil. At higher angles of attack, C_L of the modified hydrofoil shows very little indication of stall, and generates as much as 150% more lift than the baseline hydrofoil. At freestream velocities greater than 1.8 m/s, both the baseline and modified hydrofoils show a linear increase in C_L with angle of attack at low angles. The baseline hydrofoil has a dramatic stall, as described in the previous section. At all freestream velocities examined above 1.8 m/s the modified hydrofoil shows a lower C_L than the baseline hydrofoil at pre-stall

angles of attack. However, in the post-stall regime, the swept hydrofoil generates much higher lift for all freestream velocities above 1.8 m/s, producing as much as 100% higher lift at a freestream velocity of U_∞ = 4.5 m/s. At freestream velocities of 3.6 and 4.5, m/s the maximum lift as well as angle of attack is increased, with 11% and 7% higher maximum lift generated on the modified hydrofoil than the baseline at 3.6 m/s and 4.5 m/s, respectively. Also, the lift curve slope is slightly different between the baseline and modified case, with values of $\frac{dC_{LBase}}{d\alpha}$ = .0544 and $\frac{dC_{LMod}}{d\alpha}$ = 0.048 and .049 corresponding to freestream velocities of U_∞ = 3.6 and 4.5 m/s, respectively. There are two distinct Reynolds number regimes apparent in the lift coefficient in which the lift coefficient at lower Reynolds number of $0.9 \times 10^4 \leq Re_c \leq 2.7 \times 10^5$ are very similar, while the lift coefficient at higher Reynolds numbers ranging from $3.6 \times 10^4 \leq Re_c \leq 4.5 \times 10^5$ are very similar. This implies that there is a transition region in which turbulent effects dominate at higher Reynolds numbers.

With the exception of very low angle of attack at the highest freestream velocities examined, the drag of the modified swept hydrofoil is significantly higher than the baseline for all angles of attack examined. Although the general trend of a quadratically increasing drag curve could be found at low angles in either the baseline or modified case, the value of C_D on the modified hydrofoil was either equal to, to within experimental uncertainty, or higher than the baseline for all freestream velocities examined, with as much as 100% higher drag at U_∞ = 3.6 m/s.

For all freestream velocities tested, $C_{M1/4}$ of the swept modified foil, shown in Figure 53, is always similar to the baseline with the differences being within the measurement uncertainty. The lift-to-drag ratio of the swept cases show that for all freestream velocities and angles of attack tested, *L/D* is either nearly equal to or less than the baseline case. The effect of

protuberances on the lift-to-drag ratio of the swept planform foil is shown in Figure 54. Table 17 shows the aerodynamic characteristics of the modified swept hydrofoil.

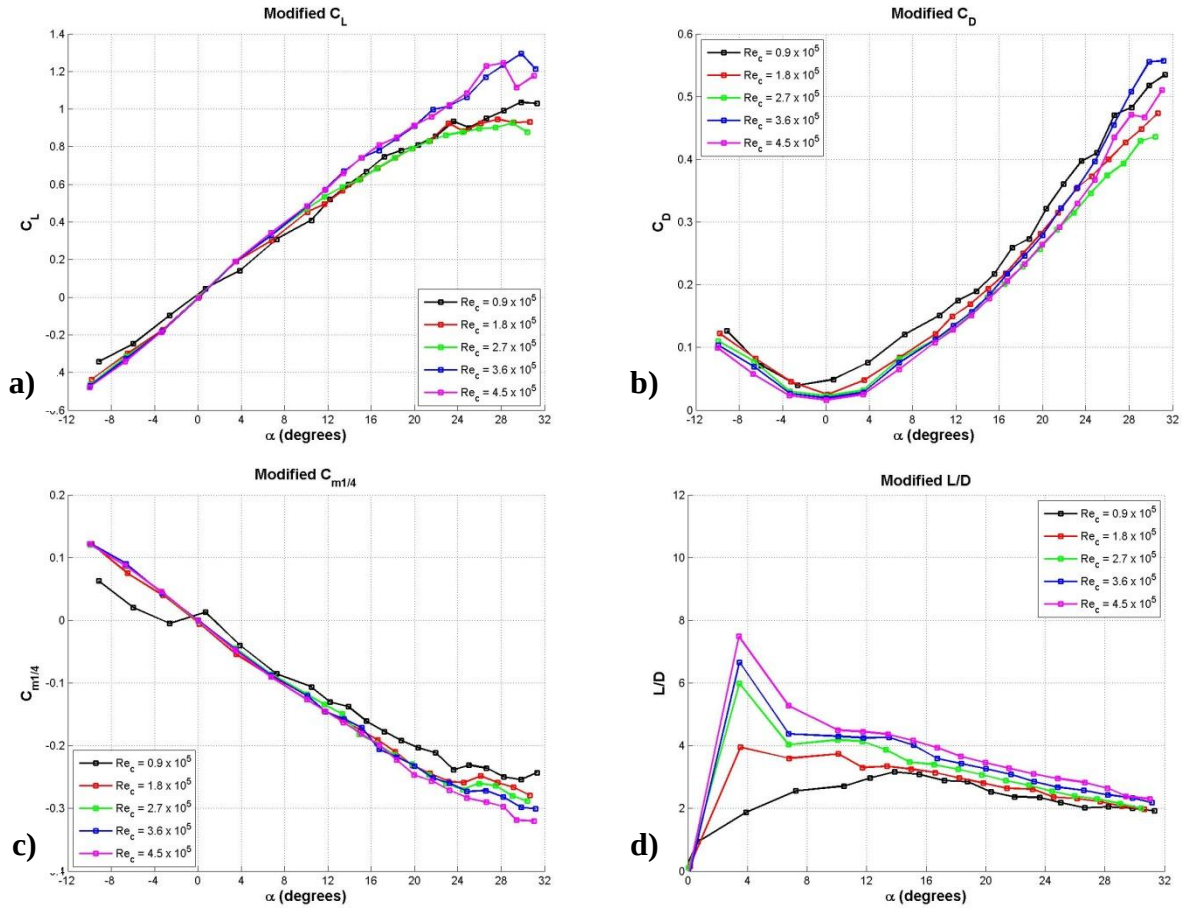

Figure 50: Effect of Reynolds number on the swept planform modified hydrofoil load characteristics. a) lift coefficient, b) drag coefficient, c) quarter chord moment coefficient, d) L/D ratio.

Table 17: Aerodynamic characteristics of swept planform modified foil. Refer to Table 5 for corresponding uncertainties.

	$Re_c = 9.0 \times 10^4$	$Re_c = 1.8 \times 10^5$	$Re_c = 2.7 \times 10^5$	$Re_c = 3.6 \times 10^5$	$Re_c = 4.5 \times 10^5$
$\frac{dC_L}{d\alpha}$ [1/deg]	0.037	0.053	0.055	0.055	0.055
C_{Lmax}	1.04	0.95	0.93	1.29	1.25
α @ C_{Lmax} [deg]	29.8	27.7	29.0	29.8	28.2
C_{Dmin}	0.04	0.03	0.02	0.02	0.02
L/D_{max}	3.16	3.95	5.98	6.66	7.49
α @ L/D_{max} [deg]	13.9	3.5	3.5	3.5	3.4
α_{stall} [deg]	N/A	N/A	N/A	N/A	N/A

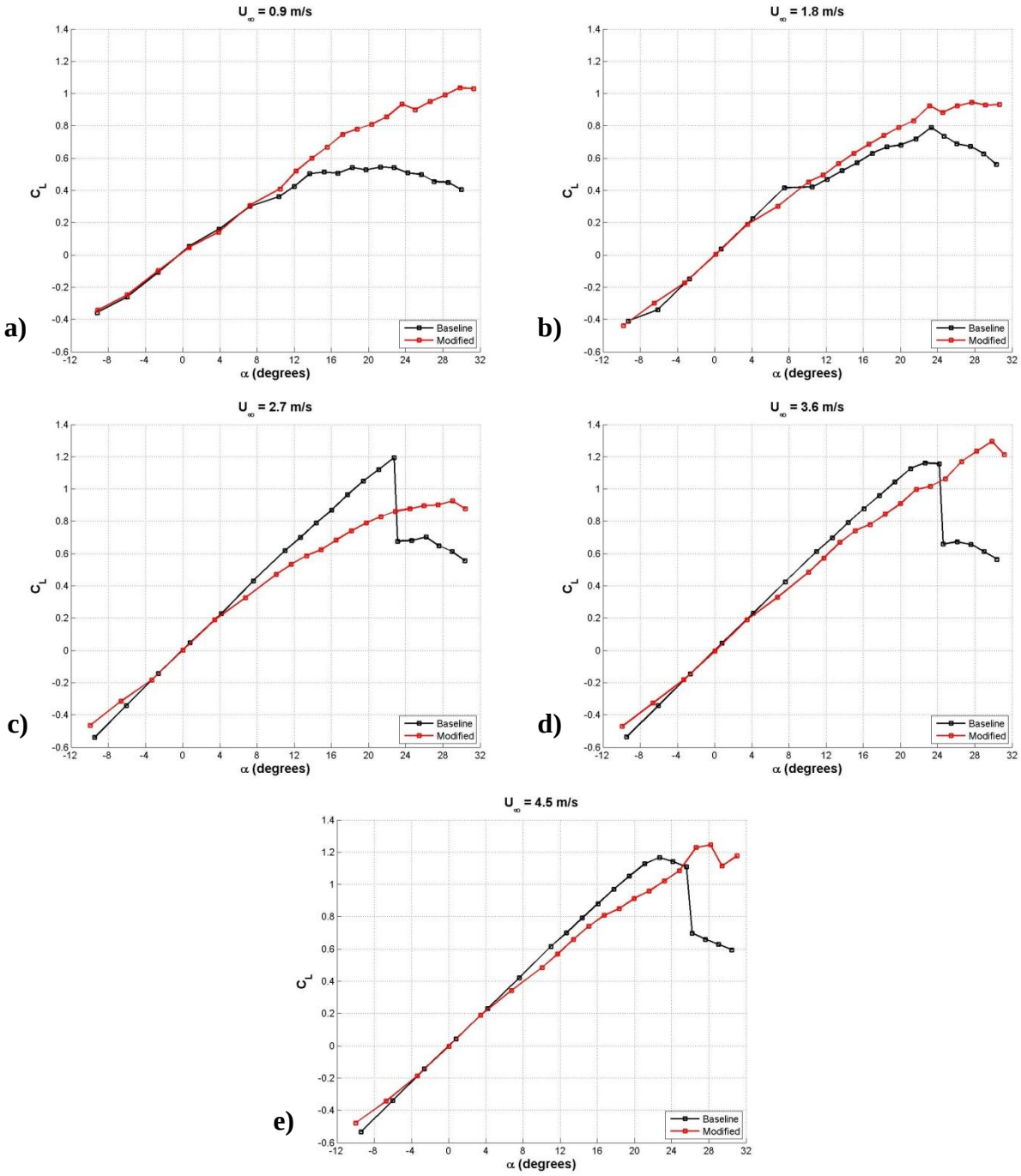

Figure 51: Swept planform lift coefficient. a) $Re_c = 9.0 \times 10^4$, b) $Re_c = 1.8 \times 10^5$, c) $Re_c = 2.7 \times 10^5$, d) $Re_c = 3.6 \times 10^5$, e) $Re_c = 4.5 \times 10^5$.

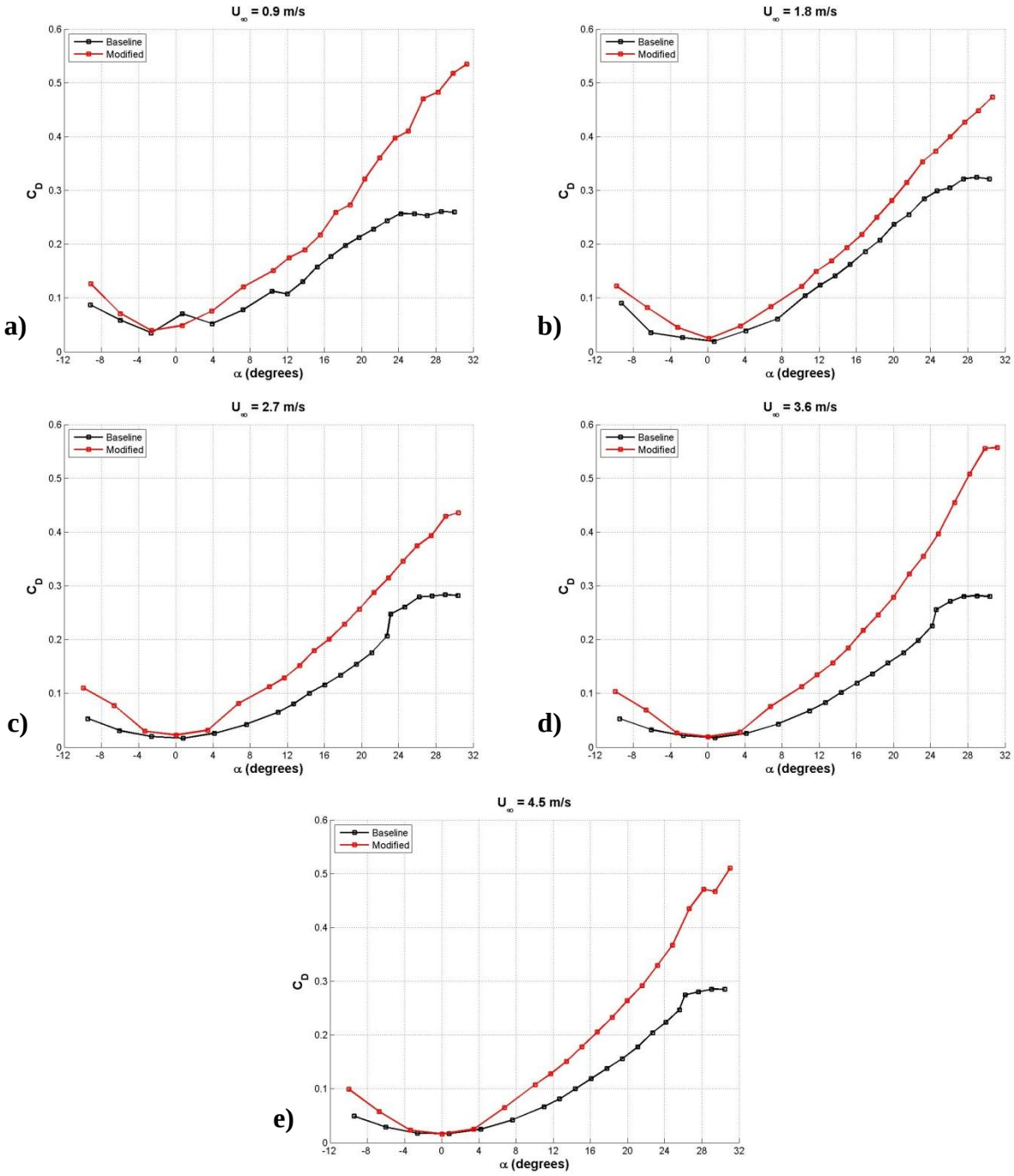

Figure 52: Swept planform drag coefficient. a) $Re_c = 9.0 \times 10^4$, b) $Re_c = 1.8 \times 10^5$, c) $Re_c = 2.7 \times 10^5$, d) $Re_c = 3.6 \times 10^5$, e) $Re_c = 4.5 \times 10^5$.

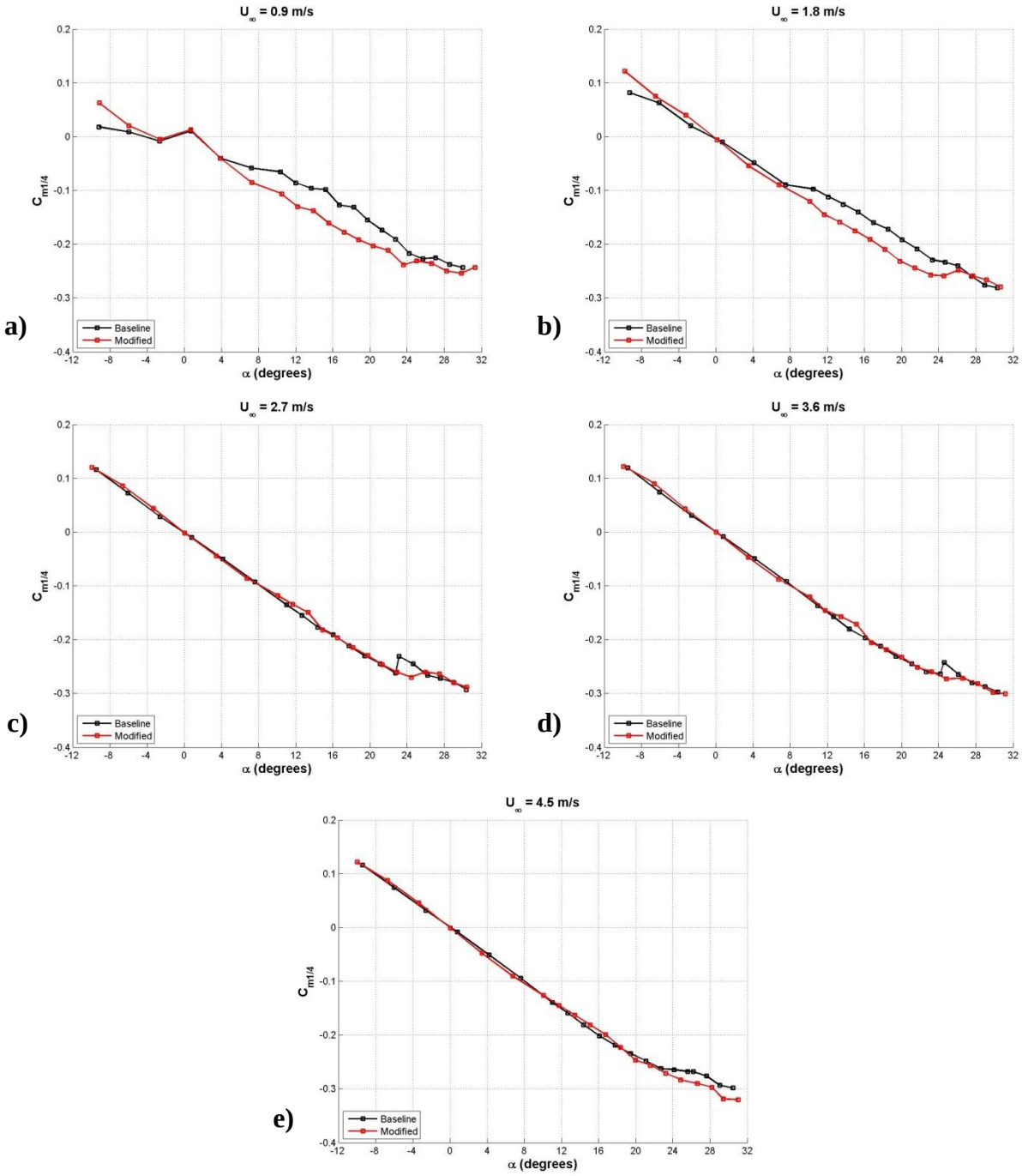

Figure 53: Swept planform quarter chord moment coefficient. a) $Re_c = 9.0 \times 10^4$, b) $Re_c = 1.8 \times 10^5$, c) $Re_c = 2.7 \times 10^5$, d) $Re_c = 3.6 \times 10^5$, e) $Re_c = 4.5 \times 10^5$.

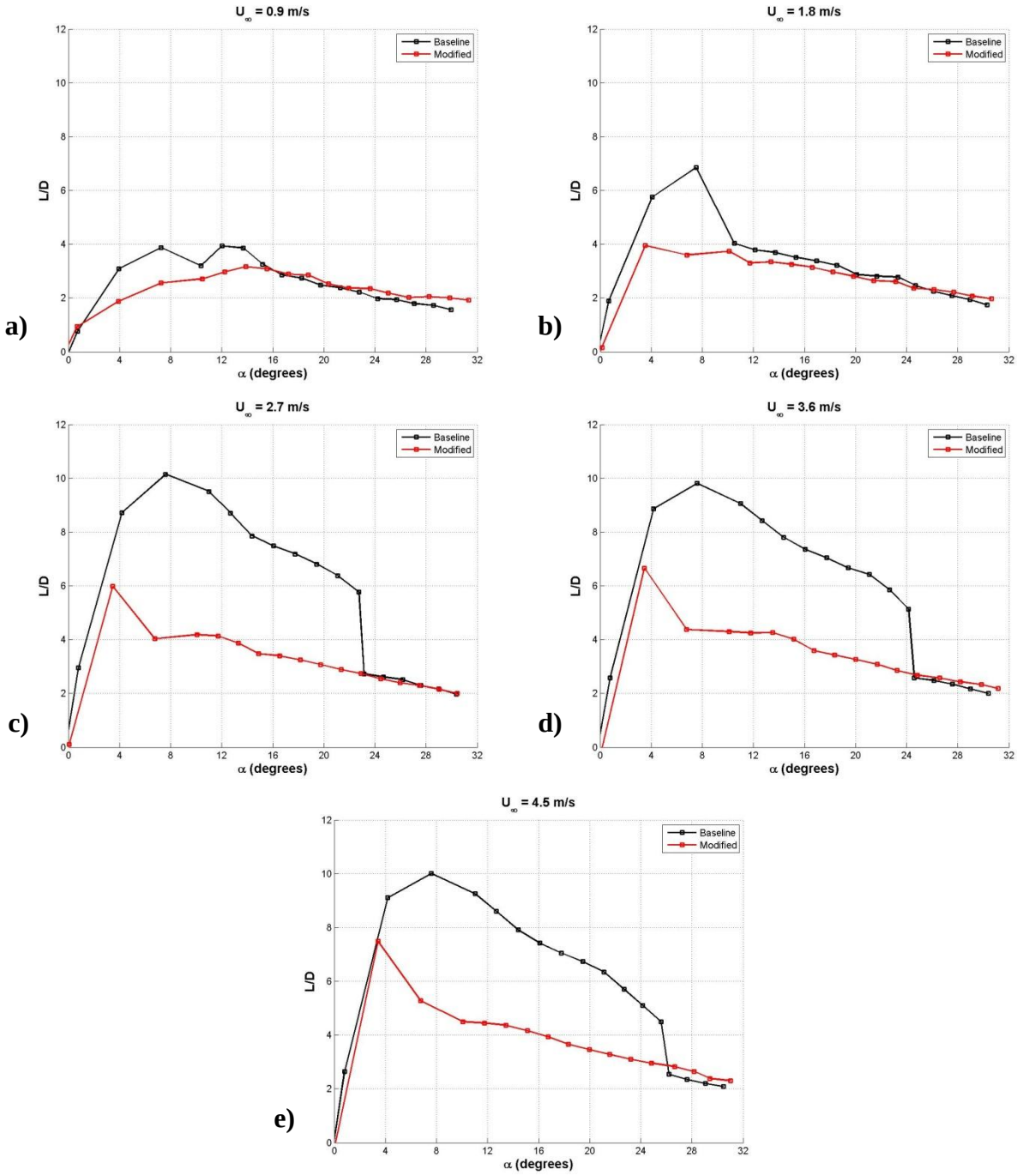

Figure 54: Swept planform L/D ratio. a) $Re_c = 9.0 \times 10^4$, b) $Re_c = 1.8 \times 10^5$, c) $Re_c = 2.7 \times 10^5$, d) $Re_c = 3.6 \times 10^5$, e) $Re_c = 4.5 \times 10^5$.

Flipper Planform Hydrofoils

Baseline Hydrofoil Model

The lift coefficient of the baseline flipper model is presented in Figure 55a. For all freestream velocities examined, there is a linear increase in C_L at low angles of attack. With the exception of U_∞ = 0.9 and 1.8 m/s, C_L increases linearly with angle of attack until the stall angle is either reached or very nearly reached. At freestream velocities of $2.7 \leq U_\infty \leq 4.5$ m/s, Reynolds number plays a minor role in establishing the lift characteristics of the baseline hydrofoil, with C_L being nearly constant over a limited range of angles $12° \leq \alpha \leq 15°$ indicating flow separation. At angles of attack past α = 15°, C_L decreases dramatically, indicating that stall has occurred. At a freestream velocity of U_∞ = 1.8 m/s, there is little sign of gradual separation over the entire range of angles of attack examined, with C_L increasing rapidly until the stall angle and then stalling abruptly. Tests conducted at a freestream velocity of U_∞ = 0.9 m/s show little sign of stall throughout the entire range of angles tested.

The drag coefficient of the baseline flipper model is shown in Figure 55b. At low angle of attack C_D increases in a quadratic manner. A dramatic increase in C_D occurs at the stall angle, while C_D increases at a lower rate at post-stall angles of attack. Figure 55b shows that as the Reynolds number is increased, C_D decreases significantly at low freestream velocities, while a limit is reached at high freestream velocities, with C_D being nearly independent of Reynolds number at freestream velocities higher than 2.7 m/s.

Whereas $C_{M1/4}$ is largely unaffected by Reynolds number, *L/D* is highly affected. *L/D* increases significantly at pre-stall angles of attack with every Reynolds number tested. However, at post-stall angles of attack *L/D* changes little at Reynolds numbers of 3.6×10^5 and greater. The effect of Reynolds number on $C_{M1/4}$ and *L/D* are presented in Figure 55c and d respectively. The aerodynamic characteristics of the baseline flipper model are presented in Table 18.

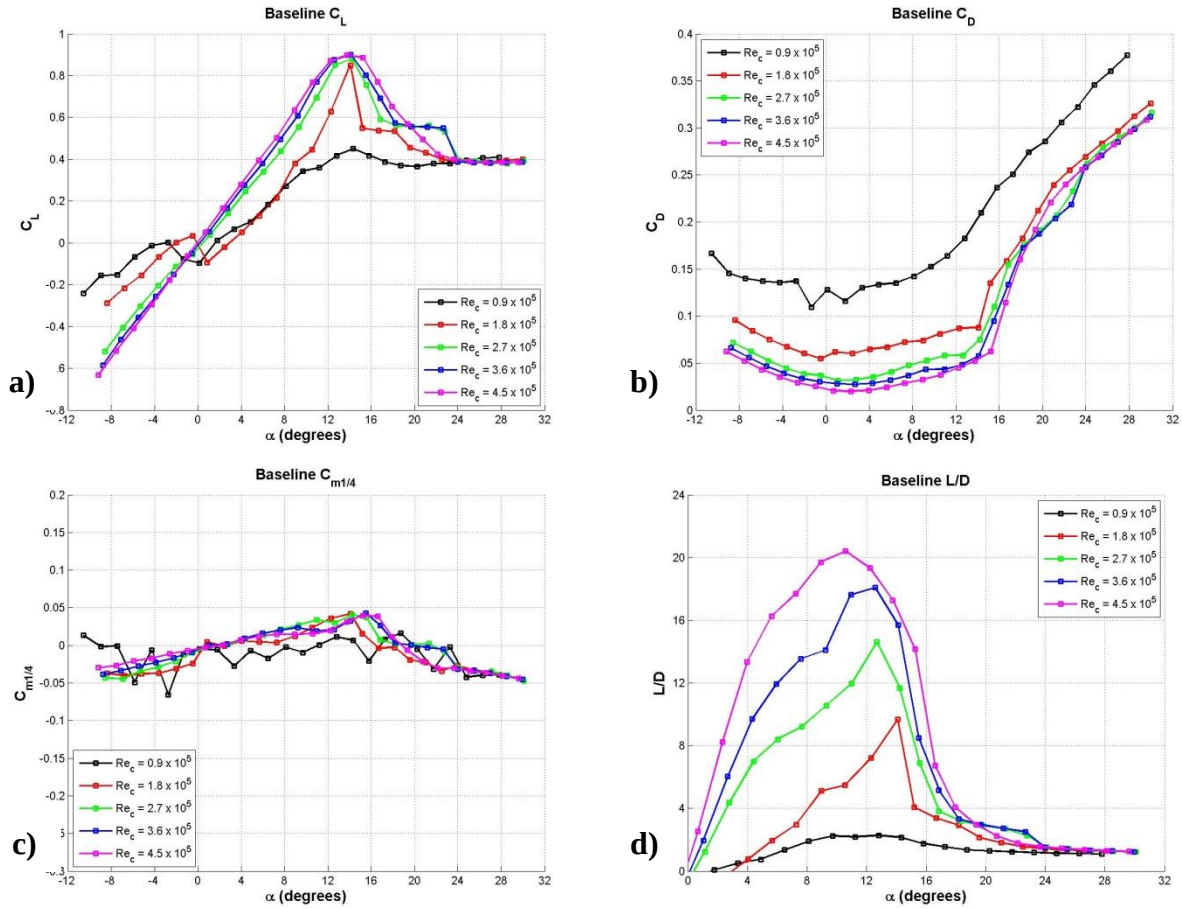

Figure 55: Effect of Reynolds number on the flipper model baseline hydrofoil load characteristics. a) lift coefficient, b) drag coefficient, c) quarter chord moment coefficient, d) L/D ratio.

Table 18: Aerodynamic characteristics of note on baseline flipper model. Refer to Table 5 for corresponding uncertainties.

	$Re_c = 9.0 \times 10^4$	$Re_c = 1.8 \times 10^5$	$Re_c = 2.7 \times 10^5$	$Re_c = 3.6 \times 10^5$	$Re_c = 4.5 \times 10^5$
$\frac{dC_L}{d\alpha}$ [1/deg]	0.044	0.049	0.059	0.063	0.070
C_{Lmax}	0.45	0.85	0.88	0.90	0.90
α @ C_{Lmax} [deg]	14.4	14.1	14.2	14.1	13.8
C_{Dmin}	0.11	0.06	0.03	0.03	0.02
L/D_{max}	2.29	9.69	14.60	18.08	20.41
α @ L/D_{max} [deg]	12.8	14.1	12.7	12.6	10.6
α_{stall} [deg]	N/A	14.1	14.2	14.1	15.3

Modified Model

The effect of Reynolds number on the lift coefficient of the modified hydrofoils can be seen in Figure 56a. The lift coefficient of the modified hydrofoil shows a dependence on Reynolds number for freestream velocities of 0.9 and 1.8 m/s. However, the lift coefficient corresponding to freestream velocities greater than U_∞ = 1.8 m/s is nearly independent of Reynolds number. The effect of Reynolds number on the drag coefficient of the modified flipper model is shown in Figure 56b. With the exception of angles of attack ranging from $0° \leq \alpha \leq 15°$ at a freestream velocity of U_∞ = 0.9 m/s, C_D is nearly unaffected by Reynolds number. With the exception of the lowest freestream velocity tested, U_∞ = 0.9 m/s, the effect of Reynolds number on $C_{M1/4}$ and *L/D*, shown in Figure 56c and d respectively, are very similar to that seen on the baseline case. Several notable aerodynamic characteristics are presented in Table 19.

The effect of leading edge protuberances on the lift coefficient of flipper models resembling the morphology of the humpback whale flipper are shown in Figure 57. At the lowest freestream velocity examined, U_∞ = 0.9 m/s, the lift coefficient of the modified hydrofoil is nearly equal to, to within experimental uncertainty, or higher than the baseline hydrofoil for all angles of attack. At freestream velocities less than 1.8 m/s, low Reynolds number effects are prominent, whereas at velocities greater than 1.8 m/s both the modified and baseline flipper models show similar lift characteristics at low angle. The lift coefficient of the modified hydrofoils increase at the same rate as the baseline hydrofoil until just prior to the baseline stall angle, at which point C_L of the modified flipper model is slightly lower than that of the baseline. The stall angle is increased by 1° - 3° depending on the freestream velocity with a maximum increase of nearly 50% in C_L at $\alpha \approx 18°$ over the baseline hydrofoil at a freestream velocity of U_∞ = 3.6 m/s. At U_∞ = 4.5 m/s the modified hydrofoil shows an increase in maximum lift of ≈ 53%

over the baseline. At the highest angles of attack examined, the modified flipper model and the baseline perform similarly, to within the range of experimental uncertainties.

The effect of leading edge protuberances on the drag coefficient of flipper models resembling the morphology of the humpback whale flipper can be seen in Figure 58. At a freestream velocity of U_∞ = 0.9 m/s, C_D of the modified hydrofoil is lower than the modified flipper model, producing nearly 100% less drag than the baseline hydrofoil, an artifact of low-Reynolds number. At freestream velocities ranging from $1.8 \leq U_\infty \leq 2.7$ m/s, C_D of the modified flipper model is shown to be very close to or slightly less than the baseline hydrofoil over a limited range of angles of attack. At freestream velocities ranging from $0.9 \leq U_\infty \leq 2.7$ m/s, the modified hydrofoil produces less drag in the pre-stall regime of the baseline hydrofoil at angles of attack ranging from $1° \leq \alpha \leq 12°$ while at angles of attack greater than α = 12° the drag coefficient of the baseline and modified flipper models are very similar. For freestream velocities ranging from 3.6 and 4.5 m/s, the modified hydrofoil shows slightly higher drag that the baseline hydrofoil in the pre-stall regime over a range of angles of attack $10° \leq \alpha \leq 15°$, and nearly equivalent C_D for all other angles of attack examined. At a freestream velocity of U_∞ = 4.5 m/s Figure 58e shows a 4% drag reduction over a small range of angles $15° \leq \alpha \leq 22°$.

At a freestream veloicity of U_∞ = 0.9 m/s, $C_{M1/4}$ of the modified foil is significantly different from the baseline case. This is likely due to the limitations of the measurement technique as well as low Reynolds number effects. With the exception of the lowest freestream velocity tested, $C_{M1/4}$ of the baseline and modified cases are very similar. $C_{M1/4}$ for all cases examined is shown in Figure 59.

The effect of leading edge protuberances on the flipper model is shown in Figure 60. At a freestrream velocity of U_∞ = 0.9 m/s, *L/D* is either greater than or equal (to within experimental

uncertainty) to the baseline case. However, at freestream velocities ranging from $1.8 \leq U_\infty \leq 3.6$ m/s, the modified case has increased *L/D* at low angle of attack as well as over a limited range of angles in the post-stall regime of the baseline foil. For a freestream velocity of $U_\infty = 4.5$ m/s an increased lift-to-drag ratio is only seen over a range of angles of $16° \leq \alpha \leq 22°$. Throughout the remaining angles of attack, *L/D* performs similarly to or poorer than the baseline case.

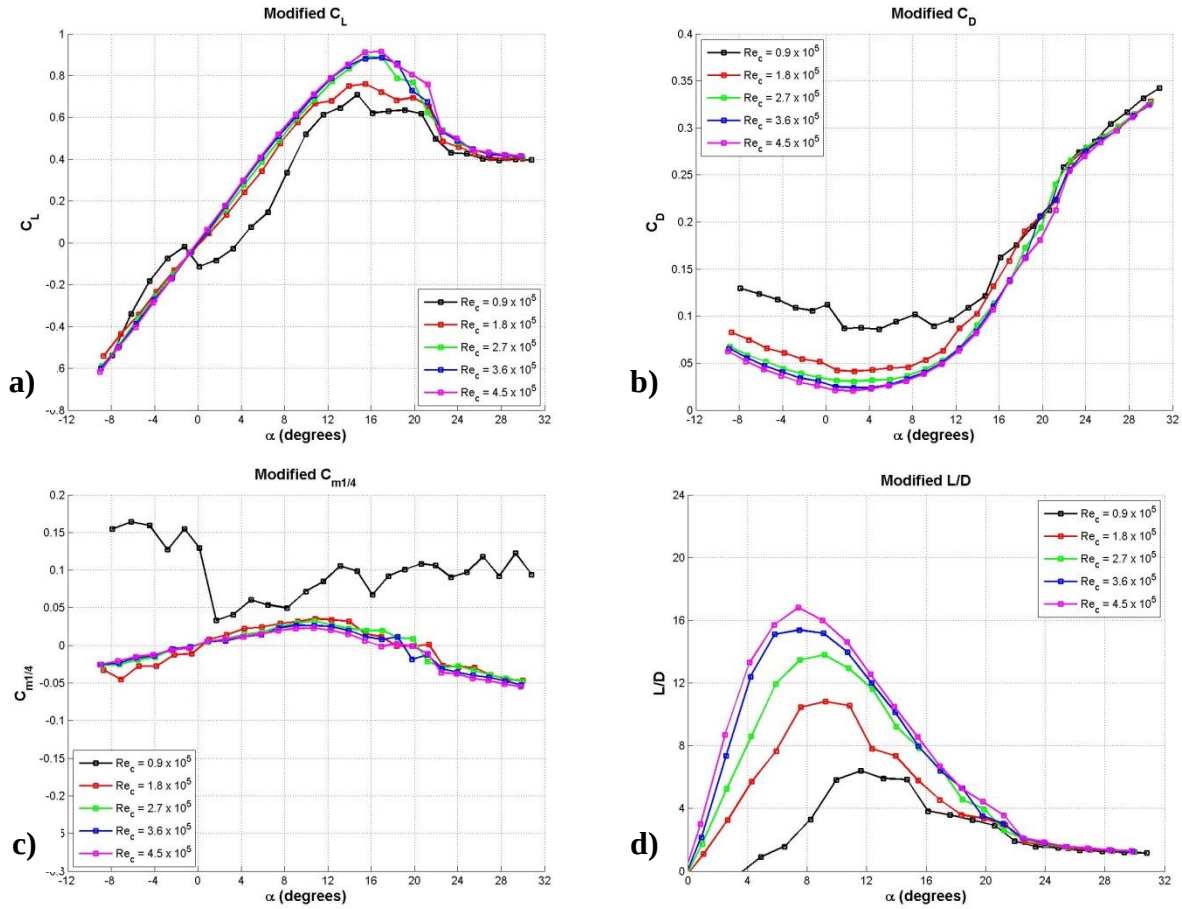

Figure 56: Effect of Reynolds number on the flipper model modified hydrofoil load characteristics. a) lift coefficient, b) drag coefficient, c) quarter chord moment coefficient, d) L/D ratio.

Table 19: Aerodynamic characteristics of note on modified flipper model. Refer to Table 5 for corresponding uncertainties.

	$Re_c = 9.0 \times 10^4$	$Re_c = 1.8 \times 10^5$	$Re_c = 2.7 \times 10^5$	$Re_c = 3.6 \times 10^5$	$Re_c = 4.5 \times 10^5$
$\frac{dC_L}{d\alpha}$[1/deg]	0.051	0.064	0.066	0.067	0.070
C_{Lmax}	0.71	0.76	0.89	0.89	0.91
α @ C_{Lmax} [deg]	14.7	15.5	15.5	17.0	16.9
C_{Dmin}	0.09	0.04	0.03	0.02	0.02
L/D_{max}	6.39	10.82	13.8	15.39	16.8
α @ L/D_{max} [deg]	11.6	9.2	9.2	7.5	7.4
α_{stall} [deg]	14.7	15.5	17.0	18.4	21.2

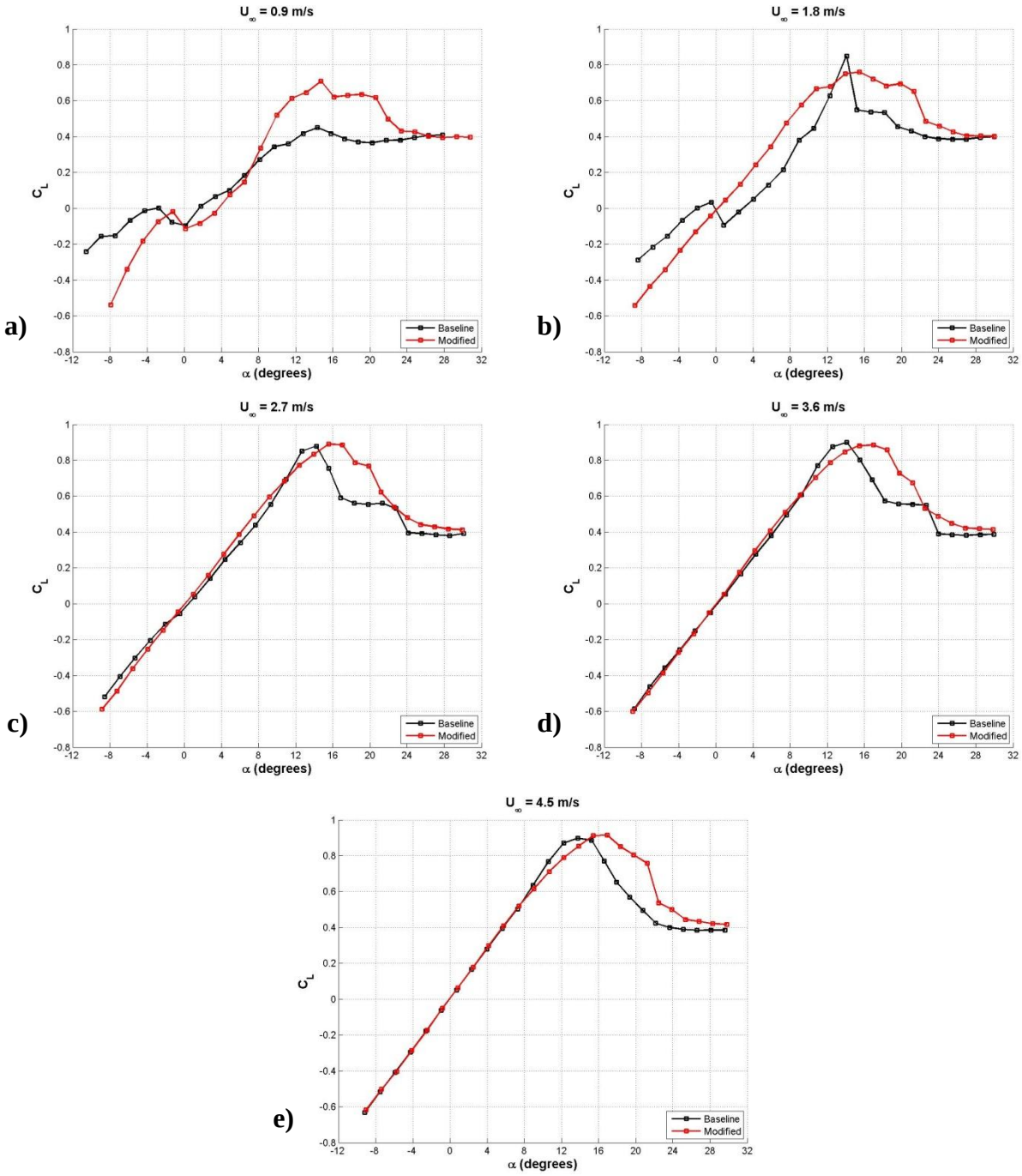

Figure 57: Flipper model lift coefficient. a) $Re_c = 9.0 \times 10^4$, b) $Re_c = 1.8 \times 10^5$, c) $Re_c = 2.7 \times 10^5$, d) $Re_c = 3.6 \times 10^5$, e) $Re_c = 4.5 \times 10^5$.

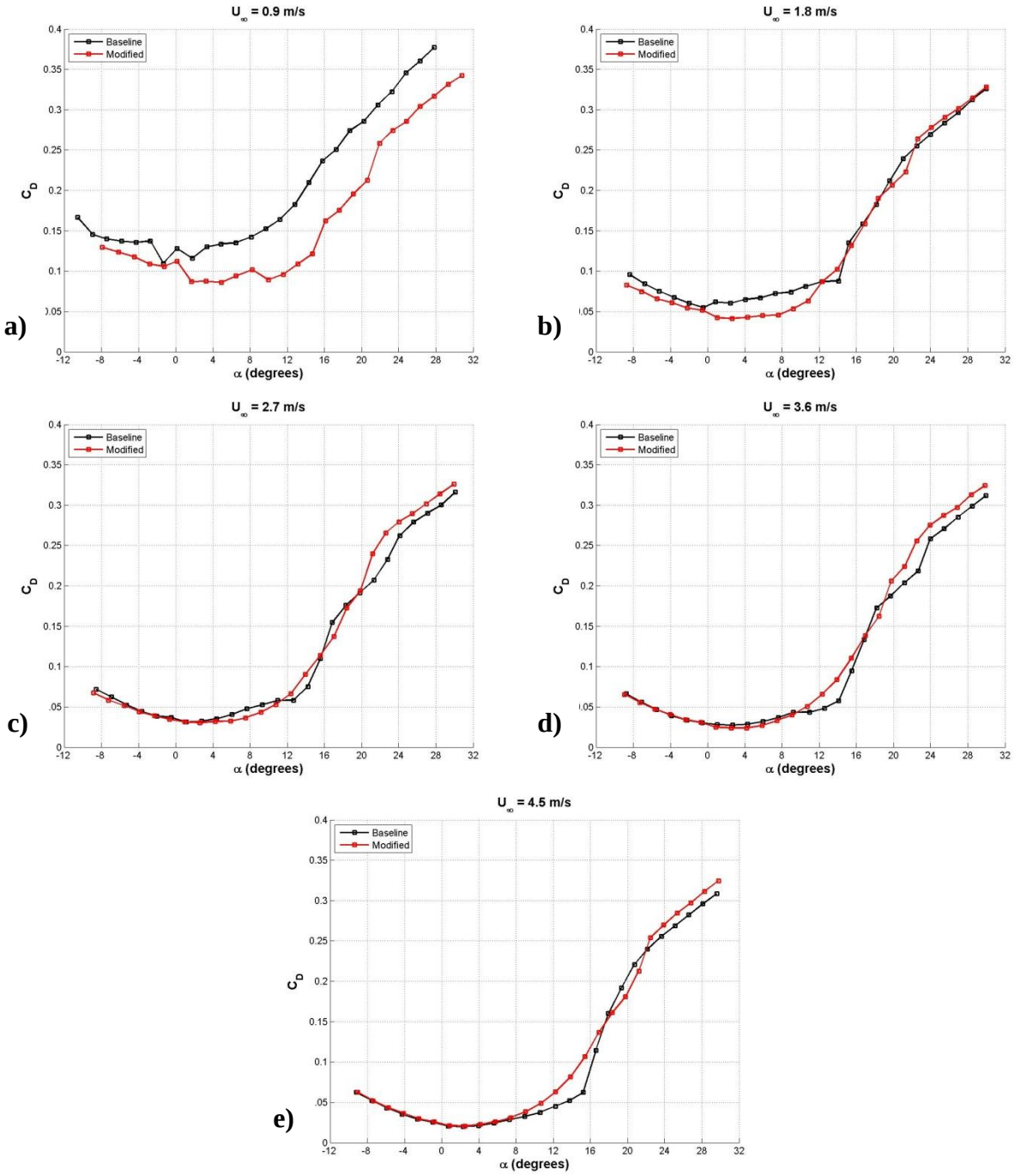

Figure 58: Flipper model drag coefficient. a) $Re_c = 9.0 \times 10^4$, b) $Re_c = 1.8 \times 10^5$, c) $Re_c = 2.7 \times 10^5$, d) $Re_c = 3.6 \times 10^5$, e) $Re_c = 4.5 \times 10^5$.

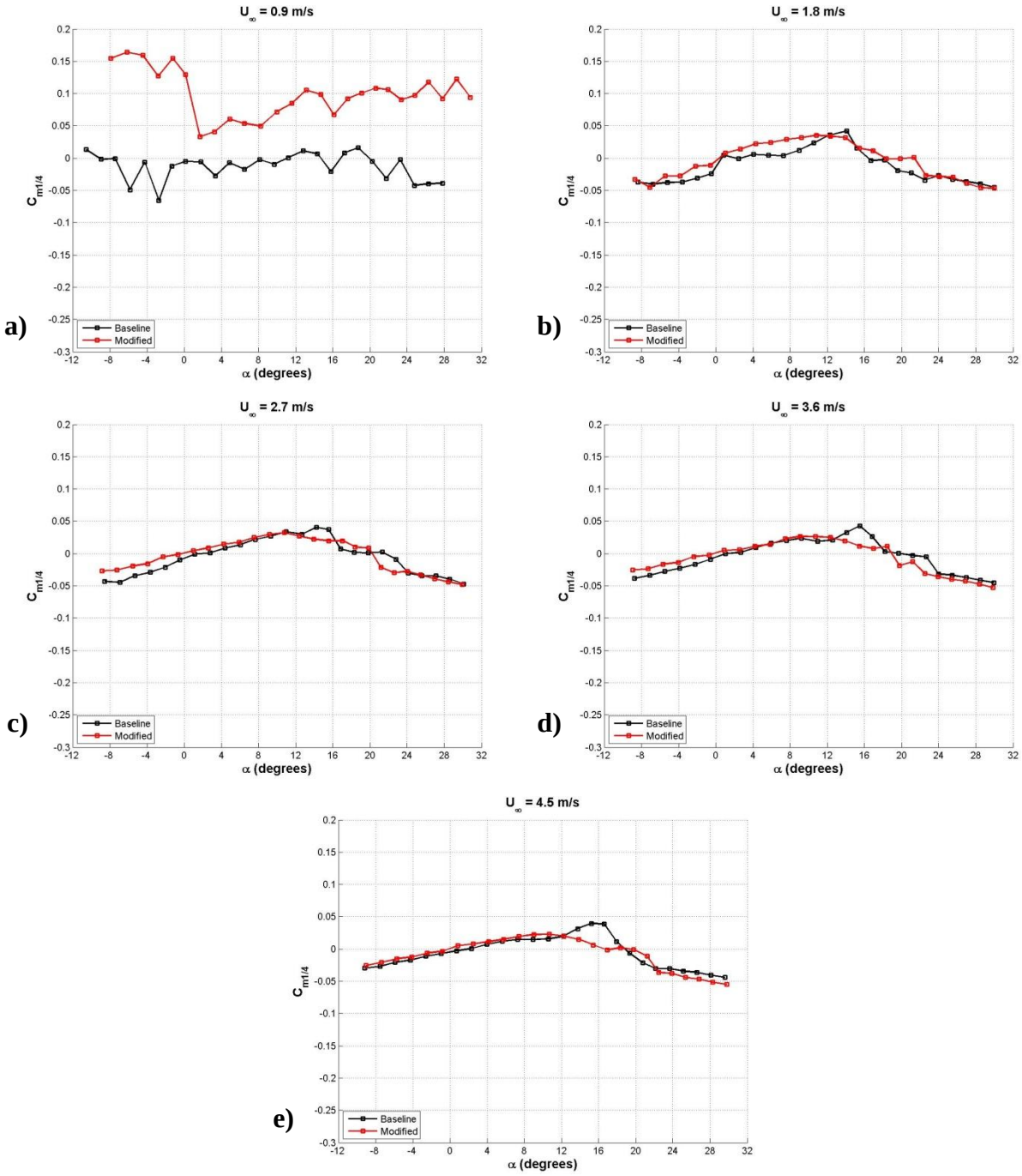

Figure 59: Flipper model quarter chord moment coefficient. a) $Re_c = 9.0 \times 10^4$, b) $Re_c = 1.8 \times 10^5$, c) $Re_c = 2.7 \times 10^5$, d) $Re_c = 3.6 \times 10^5$, e) $Re_c = 4.5 \times 10^5$.

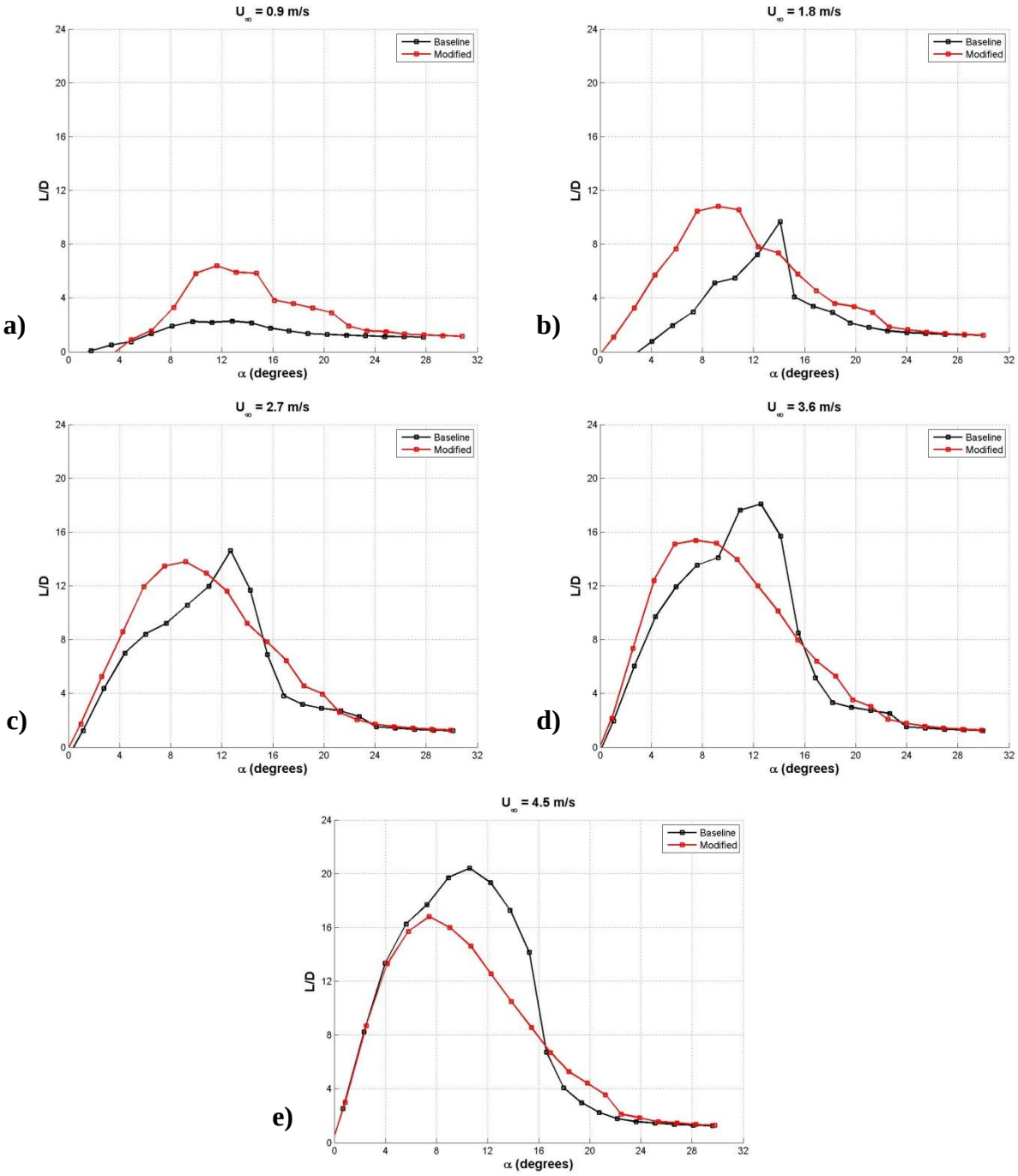

Figure 60: Flipper model lift-to-drag ratio. a) $Re_c = 9.0 \times 10^4$, b) $Re_c = 1.8 \times 10^5$, c) $Re_c = 2.7 \times 10^5$, d) $Re_c = 3.6 \times 10^5$, e) $Re_c = 4.5 \times 10^5$.

Full-Span Flow Field Measurements

To determine the effect of the streamwise vorticity on the performance differences seen in load measurements, 2D Particle Image Velocimetry (PIV) measurements were taken on a 4L hydrofoil. To examine the flow field surrounding the protuberances on the modified hydrofoils, low speed (U_∞ = 0.15 m/s) flow field measurements were conducted, higher speed measurements at U_∞ = 1.8 m/s and 4.5 m/s were also carried out for comparison to the low speed case.

Low Speed Measurements

The effect of angle of attack on the streamwise vorticity of modified hydrofoils at several chordwise spatial locations, *x/c*, are shown in Figures 61 - 65. The planes pictured are perpendicular to the freestream flow and are located on the suction surface of the hydrofoil looking upstream. Therefore, the direction of positive vorticity is perpendicular outward from the image plane, while negative vorticity is perpendicular inward. The diagram of the sinusoidal leading edge to the left of the images is to be used as a reference for determining the position of the vortices relative to the protuberances and is not drawn to mimic the proper direction of the leading edge. Streamwise vorticity stemming from protuberance shoulders can be seen in counter-rotating pairs. Vorticity on the uppermost and lowermost inflection points in Figures 61 - 65 is not seen in the vorticity contours due to experimental limitations on the edges of the area of interest.

Generally, vorticity in the core of the vortices tends to increase with angle of attack due to spanwise pressure gradients generated by the difference in leading edge radius from peak to valley. At spatial locations ranging from 0*c* to 0.12*c* the shape and size of the spanwise distribution of vortices tends to remain symmetric as the angle of attack is increased. However, at spatial locations greater than 0.12*c*, this symmetry breaks down. As the strength of neighboring vortices increases, interactions generate asymmetry within the vorticity distribution.

Streamwise vorticity on modified hydrofoils is affected by the chordwise spatial location. As the vortices move downstream, the proximity of both the hydrofoil surface as well as the neighboring vortices induce spanwise velocities. The spanwise velocity induced on the vortices causes neighboring vortices to interact, once again generating asymmetry throughout the vortex distribution. The height of the vortices changes with angle of attack as well, with vortices showing signs of lifting off of the surface at high angle. At spatial locations greater than 0.12*c* the neighboring vortices change in size and shape. Vortex interactions lead to the stretching and dissipation of vortices.

The direction of vorticity is identical to that of a delta wing. On a delta wing, positive vorticity develops on the starboard wingtip while negative vorticity develops on the port wingtip. The vortices on a delta wing are capable of increasing stall angle of attack and softening stall, both of which are similar characteristics to those seen on hydrofoils with protuberances. Therefore, the protuberances can be considered analogous to a series of spanwise delta wings along the leading edge of the hydrofoil.

High-Speed Measurements

The effect of angle of attack on streamwise vorticity at freestream velocities of U_∞ = 1.8 and 4.5 m/s and a chordwise location of x/c = 0.36*c* can be seen in Figure 65b and c. As expected, the values of vorticity in the core of vortices differ significantly from the lower freestream velocities tested; however, the overall trend of asymmetric vortices developing as a function of attack angle does not. Vorticity once again increases along with angle of attack. As was seen in low speed tests, the vortex distribution becomes highly asymmetric at high angle of attack. This is primarily due to interactions between neighboring vortices. In all cases tested, depending on the spanwise location and angle of attack, vortex interactions may lead to neighboring vortices moving toward one another, creating a convergence pattern, or away from

one another, creating a divergence pattern. A merging of neighboring vortices leads vortex stretching as well as lifting from the foil surface.

The pattern of vortices seen in the high-speed data differs, slightly, from the low-speed cases. At first glance, it seems as though the pattern changes with speed. On the contrary, the pattern remains the same; however the area of investigation on the foil surface is slightly different between the high and low speed cases. The pattern of vortex interaction is bi-periodic, and therefore since the area of investigation considers only two periods, there is visually a difference in the pattern. It was determined that the pattern of vortex interaction is independent of freestream velocity.

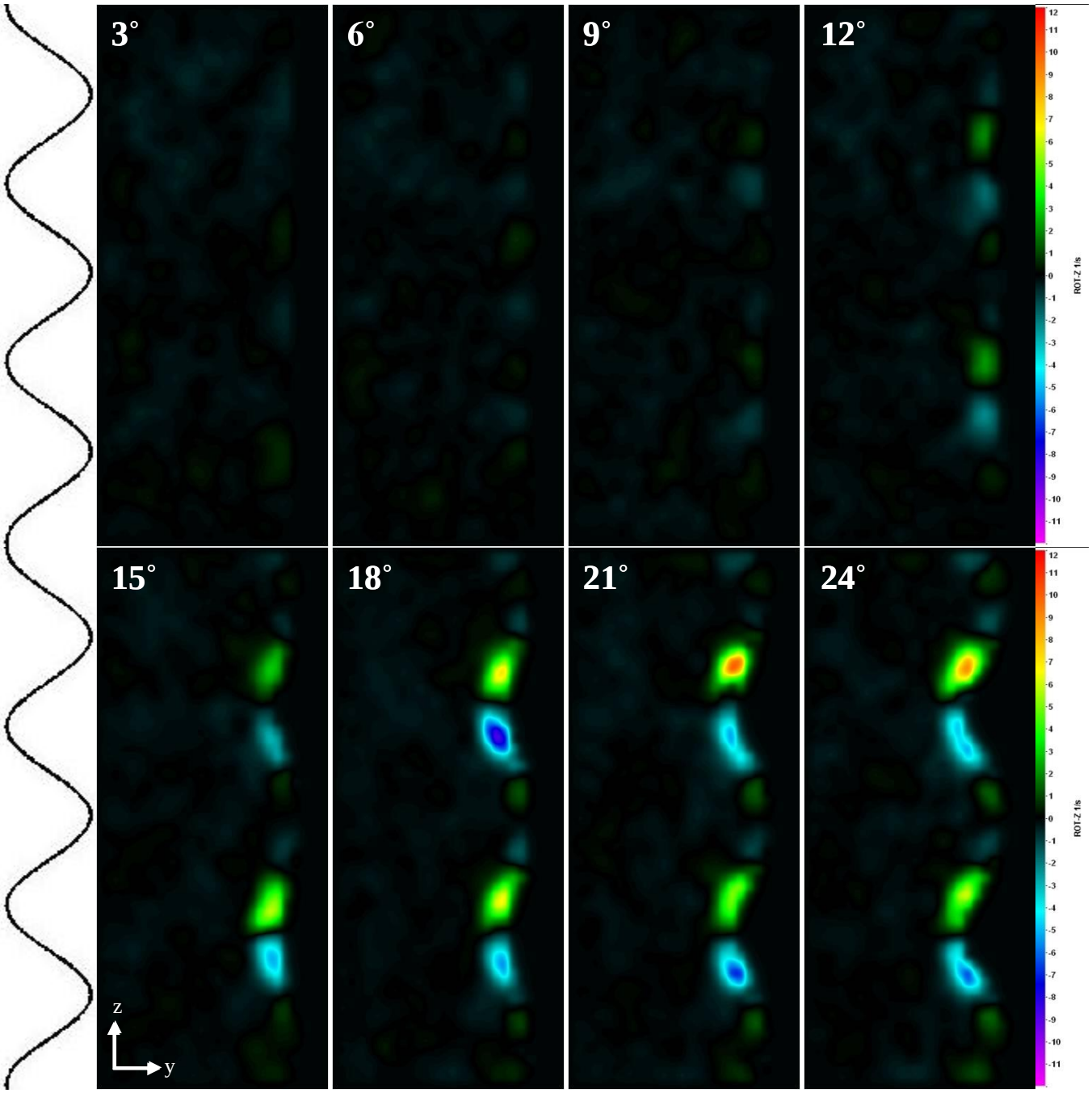

Figure 61: Streamwise vorticity, ω, contours on 4L hydrofoil as a function of angle of attack at a chordwise spatial location of 0*c*.

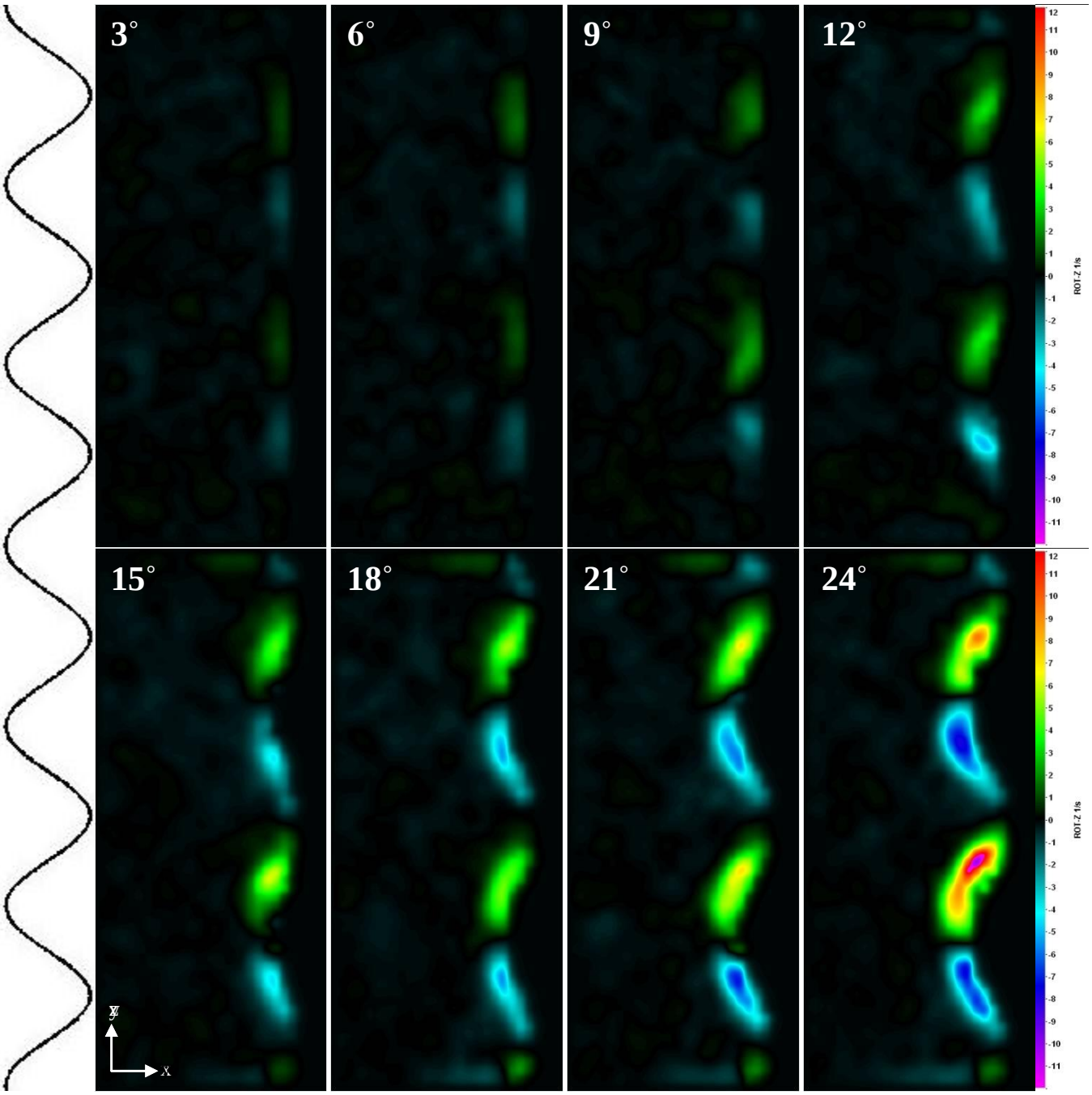

Figure 62: Streamwise vorticity, ω, contours on 4L hydrofoil as a function of angle of attack at a chordwise spatial location of 0.12*c*.

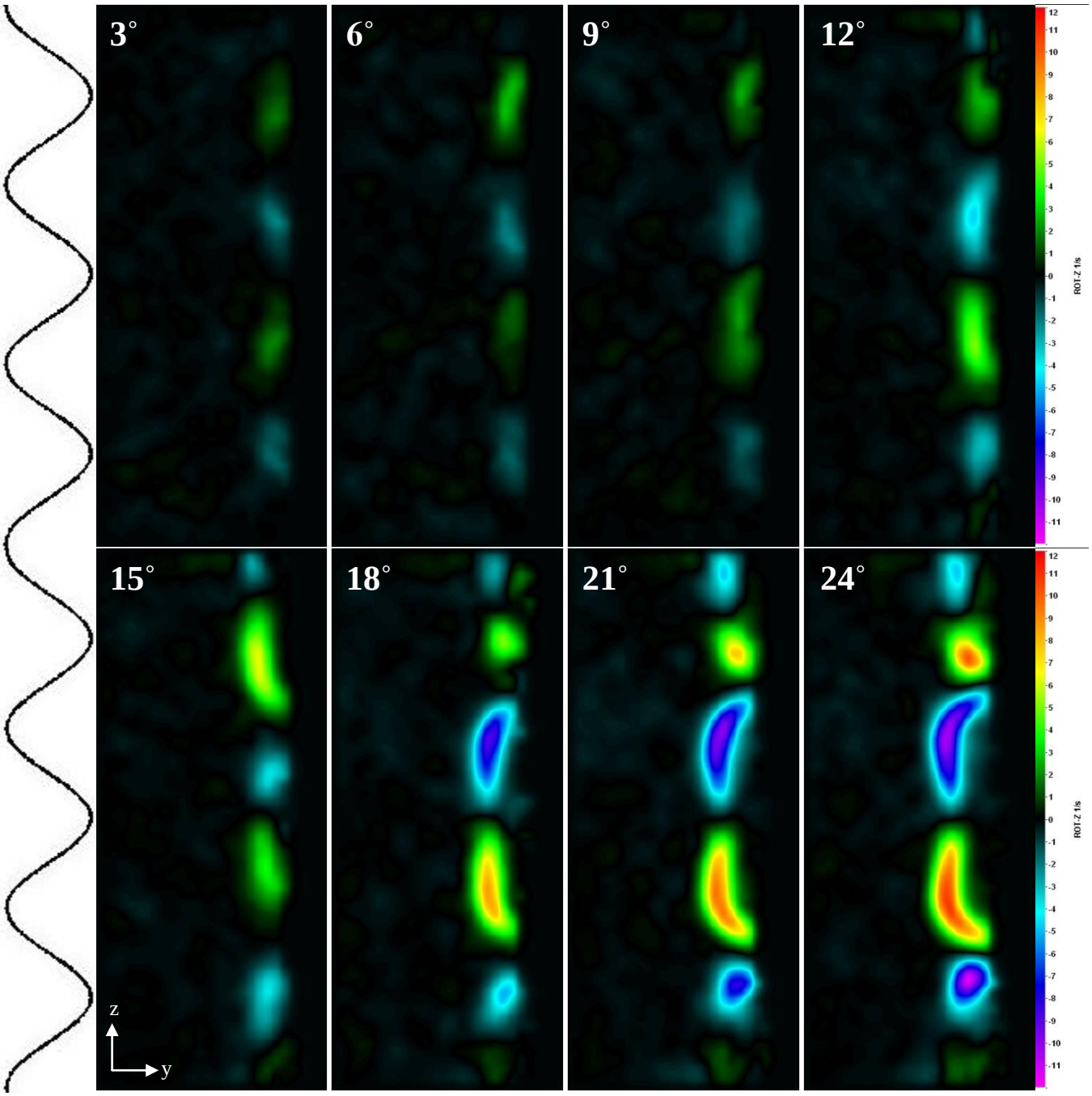

Figure 63: Streamwise vorticity, *ω*, contours on 4L hydrofoil as a function of angle of attack at a chordwise spatial location of 0.25*c*.

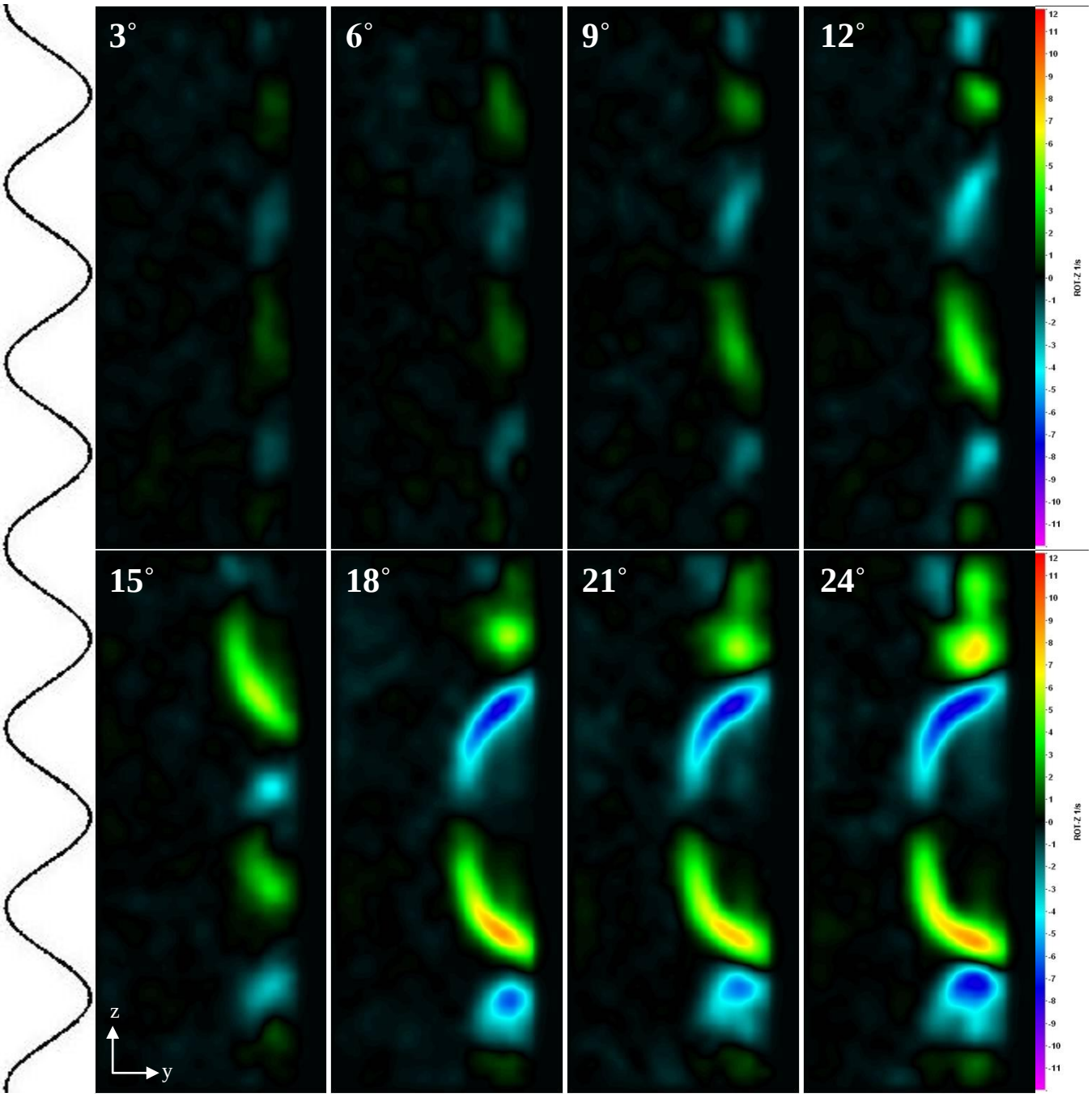

Figure 64: Streamwise vorticity, ω, contours on 4L hydrofoil as a function of angle of attack at a chordwise spatial location of 0.36*c*.

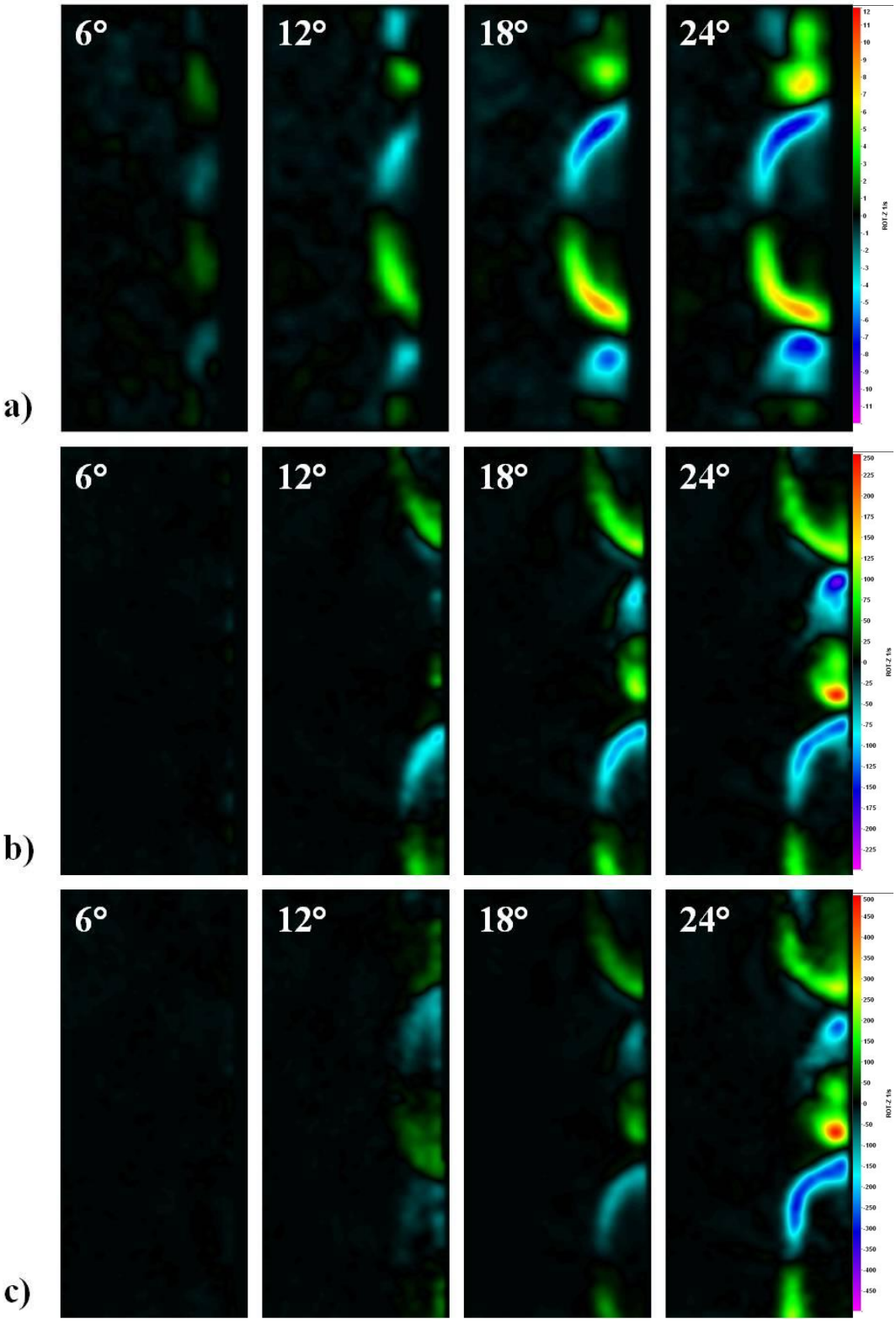

Figure 65: Streamwise vorticity, ω, contours on 4L hydrofoil as a function of angle of attack at a chordwise spatial location of 0.36*c*. a) U_∞ = 0.15 m/s, b) U_∞ = 1.80 m/s, c) U_∞ = 4.50 m/s.

Vortex Circulation

The circulation, Γ, of the vortices shown in Figures 61 - 65 were calculated as a function of angle of attack and chordwise spatial location. For ease of understanding the vortices examined in PIV experiments will have the following nomenclature: Vortices 1, 2, 3, and 4 each describe a single vortex according the top to bottom pattern seen in Figure 66. Figures 67 - 70 show the effect of angle of attack on the circulation of the vortices seen on the surface of the 4L full-span hydrofoil at spatial locations of $0c \leq x/c \leq 0.36c$, with $0c$ referring to the protuberance inflection points and $0.36c$ referring to the chordwise location aft of which the baseline and modified foils are identical, and refer only to tests carried out at a freestream velocity of U_∞ = 0.15 m/s. Figures 71 and 72, on the other hand, are direct comparisons to Figure 70 in that all parameters are identical with the exception of freestream velocity, which varied from U_∞ = 1.8 and 4.5 m/s so that the effect of Reynolds number on circulation could be determined.

Figure 67 shows that, similar to a delta wing, Γ increases monotonically for all vortices examined at a chordwise spatial location of $x = 0c$. A monotonic increase in Γ with angle of attack can be seen for all vortices. This implies that there is little vortex interaction at this spatial location. At a spatial location of $x = 0.12c$, shown in Figure 68, the monotonic increase in Γ with angle of attack is still evident, however the maximum values for Γ have increased significantly. This is most likely due to the large leading edge radius in the valleys of modified foils. Because the valley of the modified hydrofoils is the spanwise location at which the leading edge radius in greatest, it is this chordwise location that will have the largest pressure gradient, which in turn will produce the strongest vorticity. Figure 69 shows Γ as a function of angle of attack at the hydrofoil quarter chord spatial location, $x = 0.25c$. At the hydrofoil quarter chord, signs of vortex interactions begin to appear. At low angle of attack, Γ retains similar values for all of the vortices examined, however as the angle of attack is increased signs of asymmetry appear; vortices 2 and

3 have similar values for circulation, while the values of vortices 1 and 4 differ significantly by comparison. Also, at intermediate angles a transition region can be seen in which the circulation of certain vortices changes dramatically over a small range of angles. The reason for the dramatic change in circulation lies in the development of an asymmetric vorticity distribution along the leading edge. At low angle, vorticity is for the most part symmetric and stable, whereas at high angle vorticity is highly asymmetric and stable, however at intermediate angles of attack instabilities appear as the vortices begin to change size and shape. At high angle of attack, vortex interaction may inhibit the development of high circulation at certain spanwise locations, while at others it may enhance it. The same trends can be seen at a chordwise location of $x = 0.36c$, shown in Figure 70.

Figures 71 and 72 show that Reynolds number has little effect on the overall trend of circulation with angle of attack. Symmetry appears at low angle of attack, while at intermediate angles asymmetry and instabilities appear, leading to differences in circulation value. A stable separation of circulation values emerges at high angle which remains stable throughout the remaining angles of attack. Also, Reynolds number does not affect the values of normalized circulation, with the averaged circulation values of vortices 1 - 4 all being on the same order, see Figure 77, enhancing the conclusion that Reynolds number plays only a small role in establishing the vortex patterns seen on modified foils.

Figures 73 -76 show the effect of chordwise location on the vortices stemming from protuberance shoulders. Figure 73 shows that Γ are similar to within experimental uncertainty for all vortices examined at $\alpha = 6°$ over the range of spatial locations tested. This is due to the lack of vortex interactions at low angles of attack. At low angle of attack streamwise vorticity and circulation remain weak reducing the likelihood of vortex interactions. It will be shown later in

an analysis of spanwise vortex movement that vortex interaction is highly dependent on Γ; at low angles of attack circulation tends to remain low limiting vortex movement. As the angle of attack is increased to α = 12°, shown in Figure 74, signs of vortex interaction begin to appear. This is especially evident at spatial locations greater than x =0.12c with the circulation trends of vortices 1 – 4 differing significantly from vortices 2 – 3. This trend is also evident at angles of attack of 18° and 24°, shown in Figures 75 and 76, with a maximum Γ being reached at a spatial location of x = 0.12c. Circulation has a tendency to be reduced as the spatial location is increased. This is due to vortex interaction. Vortex interactions will be described in more detail later. As the counter-rotating vortices interact, vorticity is reduced and stall characteristics become apparent.

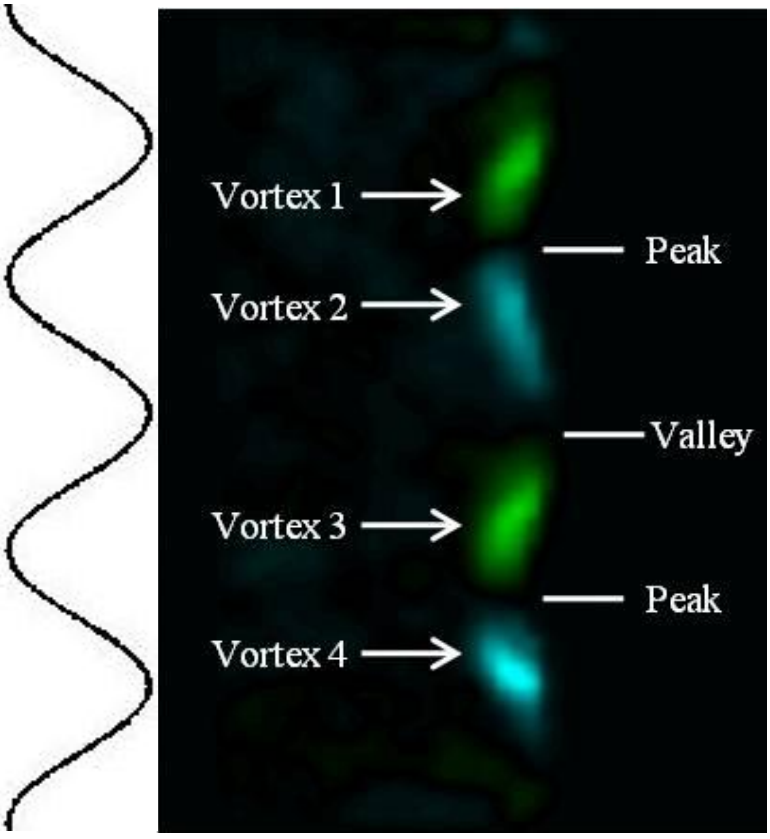

Figure 66: Vortex analysis nomenclature.

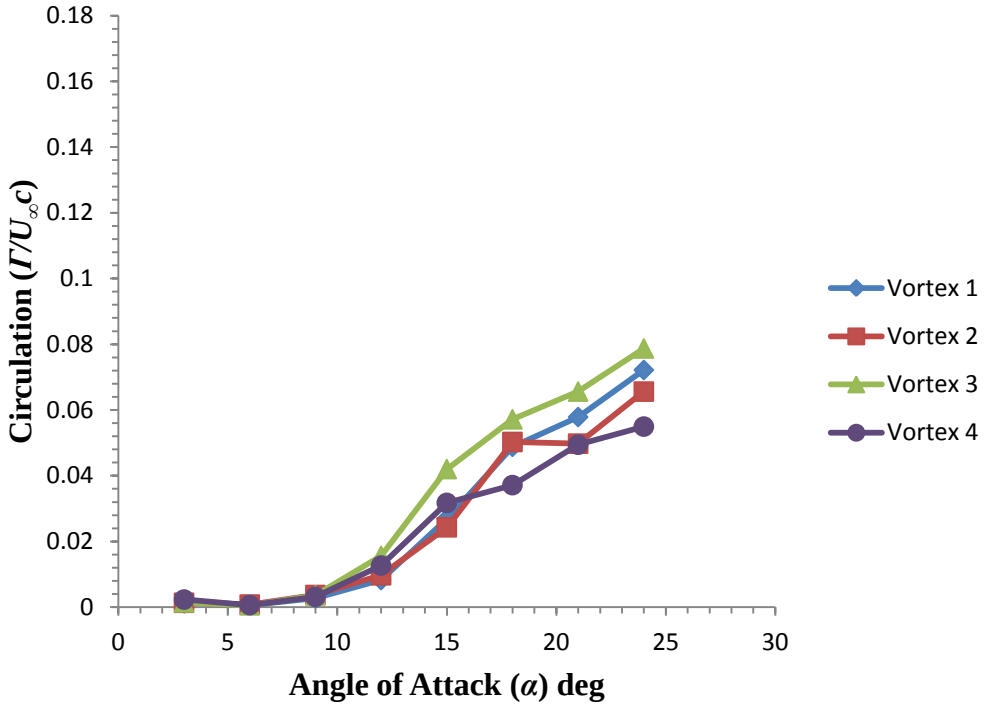

Figure 67: Γ as a function of α at a chordwise spatial location of x/c = 0c. U_∞ = 0.15 m/s.

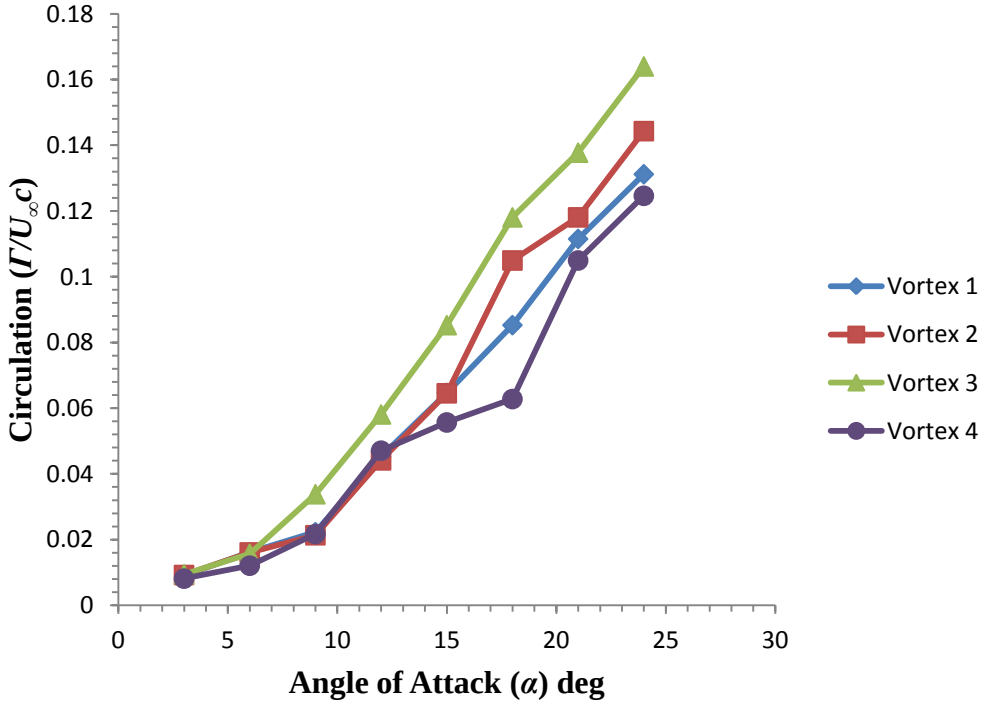

Figure 68: Γ as a function of α at a chordwise spatial location of x/c = 0.12c. U_∞ = 0.15 m/s.

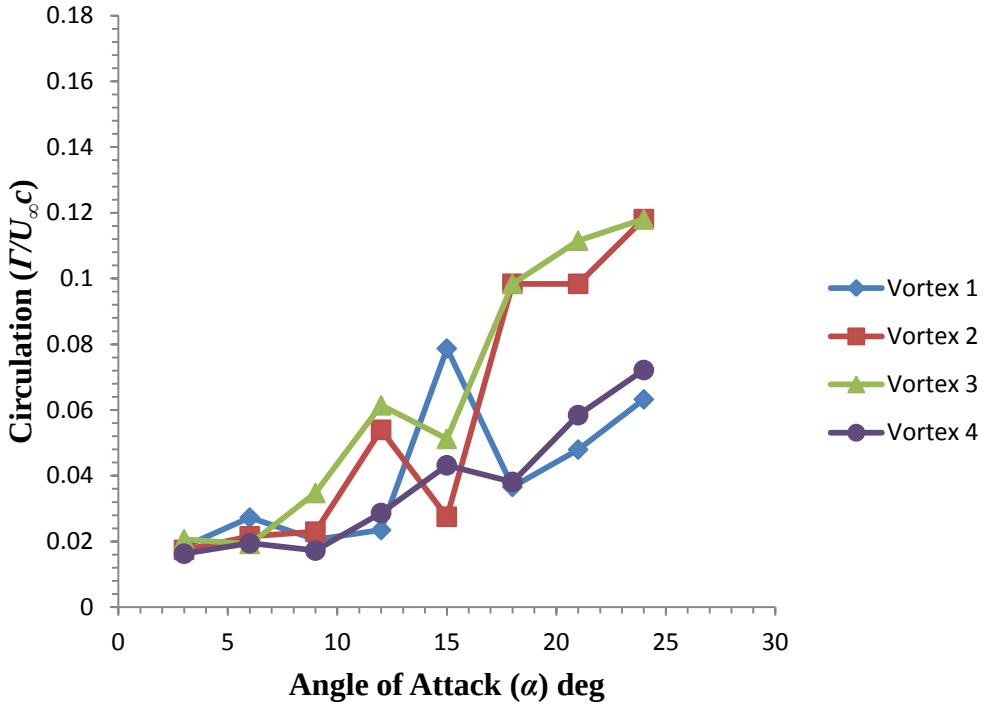

Figure 69: Γ as a function of α at a chordwise spatial location of x/c = 0.25c. U_∞ = 0.15 m/s.

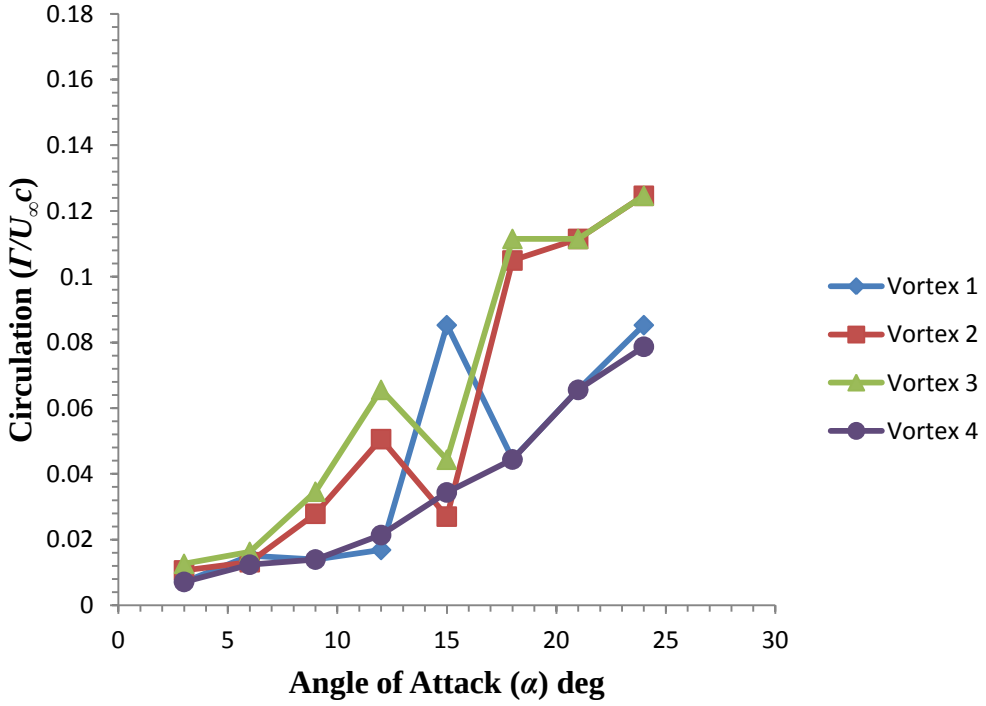

Figure 70: Γ as a function of α at a chordwise spatial location of x/c = 0.36c. U_∞ = 0.15 m/s.

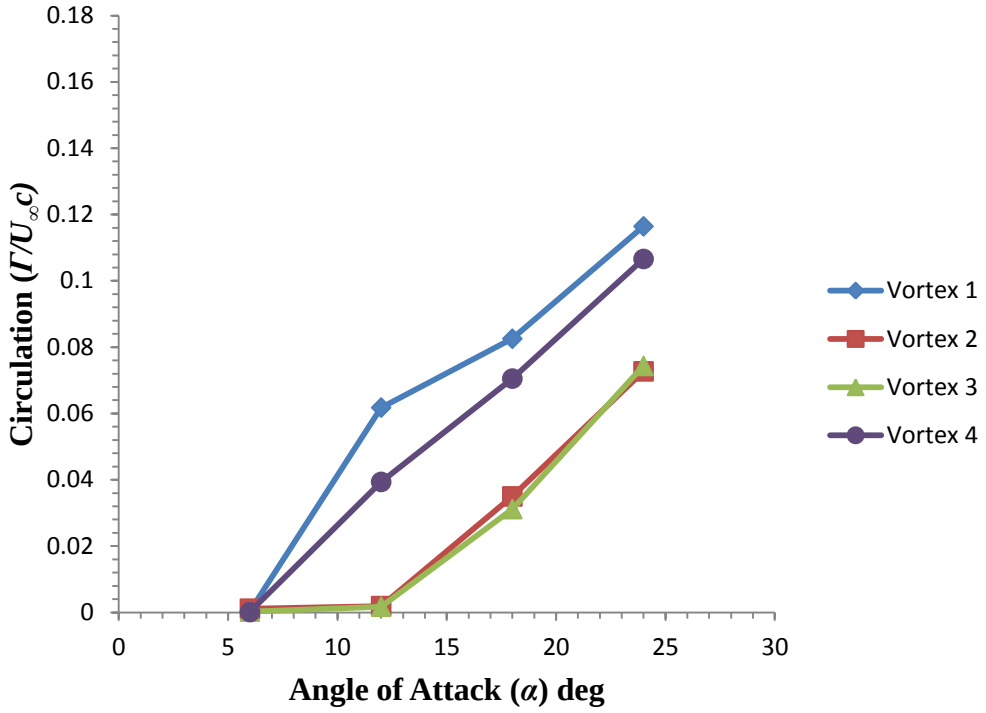

Figure 71: Γ as a function of α at a chordwise spatial location of x/c = 0.36c. U_∞ = 1.8 m/s.

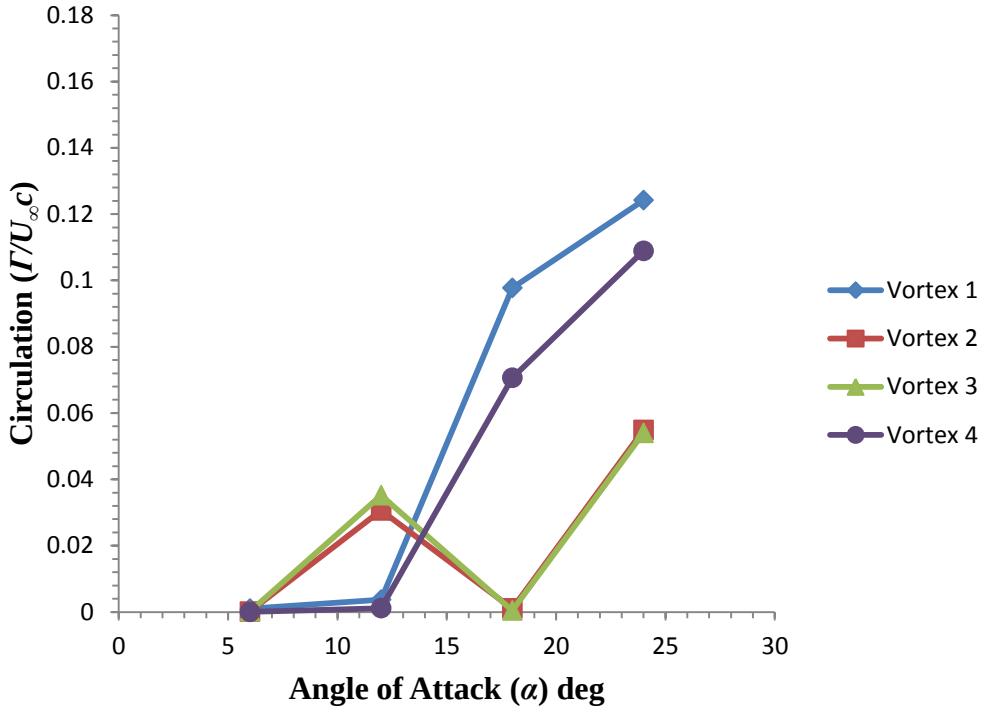

Figure 72: Γ as a function of α at a chordwise spatial location of x/c = 0.36c. U_∞ = 4.5 m/s.

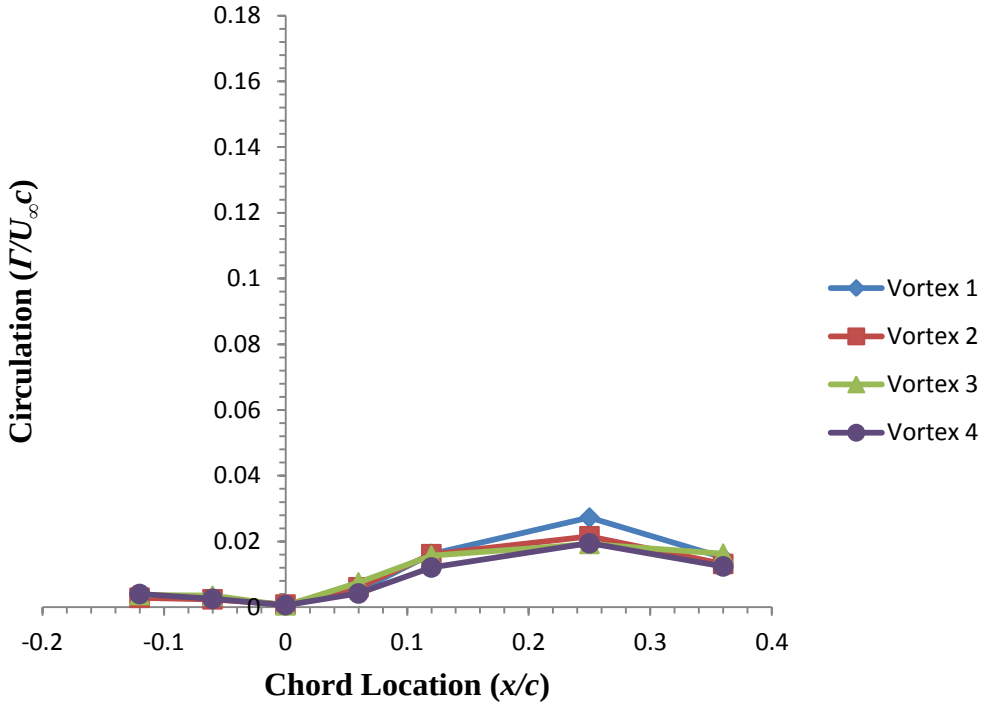

Figure 73: Γ as a function of chordwise spatial location for α = 6°. U_∞ = 0.15 m/s.

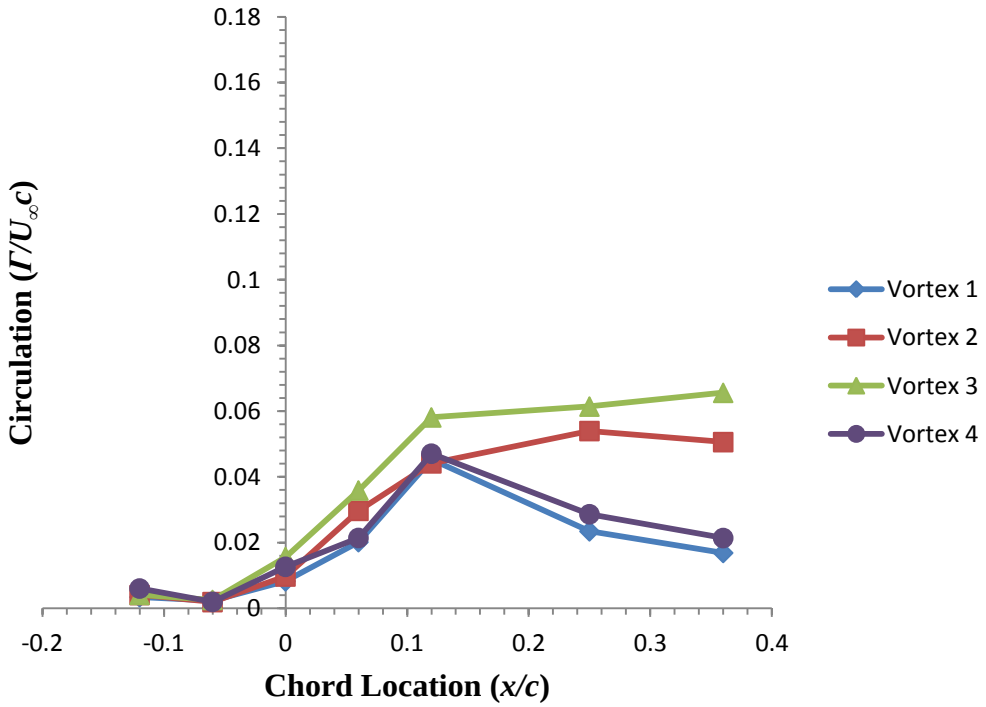

Figure 74: Γ as a function of chordwise spatial location for α = 12°. U_∞ = 0.15 m/s.

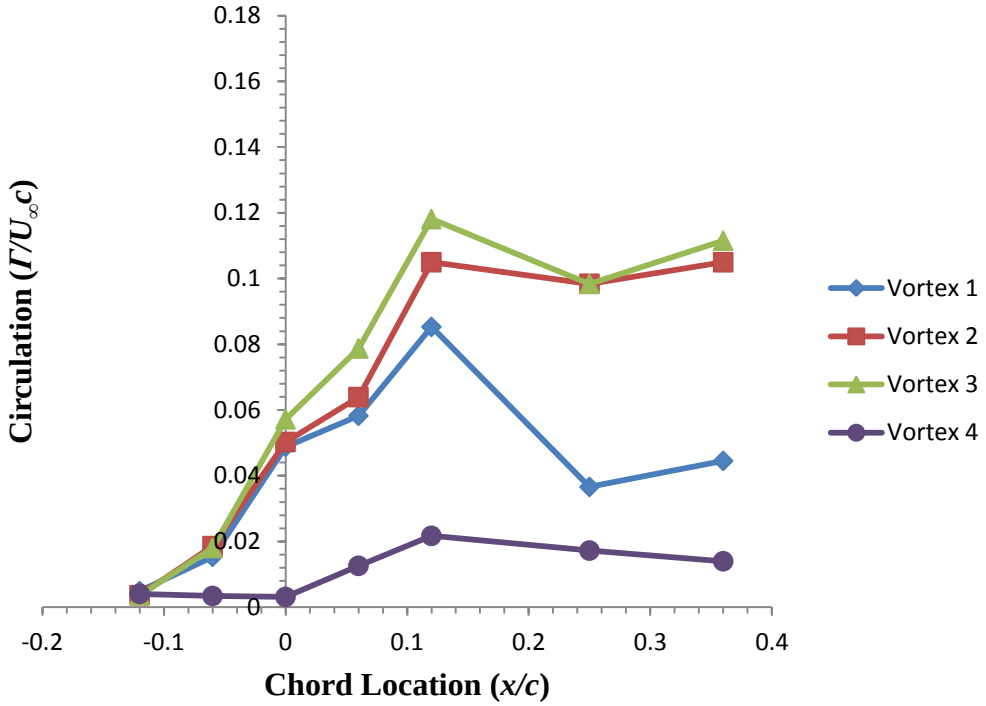

Figure 75: Γ as a function of chordwise spatial location for α = 18°. U_∞ = 0.15 m/s.

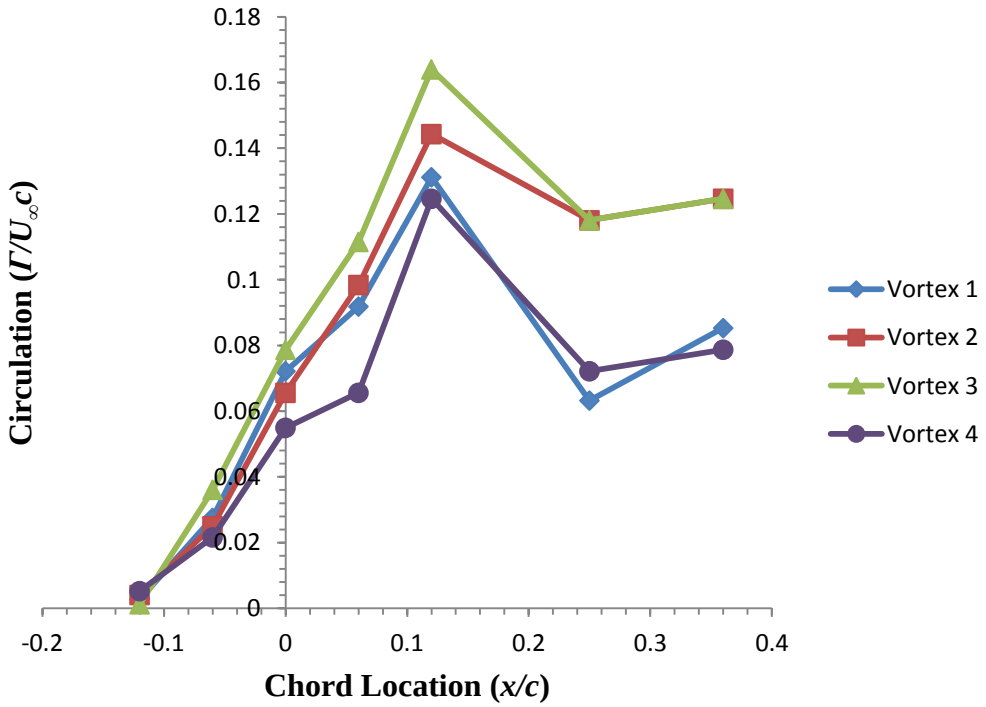

Figure 76: Γ as a function of chordwise spatial location for α = 24°. U_∞ = 0.15 m/s.

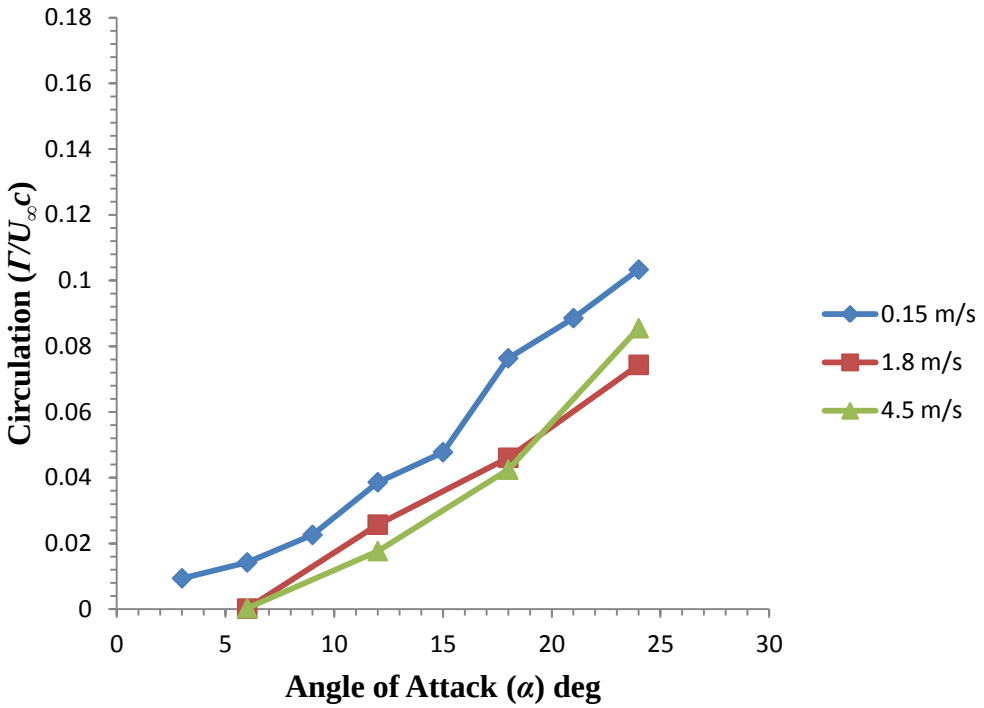

Figure 77: Averaged Γ of vortices 1-4 shown at multiple freestream velocities as a function of α at a chordwise spatial location of x/c = 0.36c.

Finite-Span Flow Field Measurements

The presence of a tip vortex of finite-span wings typically corresponds to both a loss of lift and an increase in drag. Therefore, an investigation into whether leading edge protuberances are capable of mitigating the detrimental effects of a tip vortex was carried out. A high-speed stereo-PIV flow field analysis of the tip vortex on modified foils at several angles and spatial locations is shown in Figures 78 - 81. Figures 78a and 79a show the development of the tip vortex on the baseline hydrofoil at two spatial locations, x = 1.5c and 3c respectively, at a freestream velocity of U_∞ = 1.8 m/s. Figure 78 shows that near the trailing edge, as the angle of attack is increased, both the shape and size of the tip vortex changes. As the angle of attack is increased to 12°, there is a corresponding increase in vortex size and strength. As the angle of attack is increased further to 18°, higher lift leads to growth of the vortex core. At an angle of 24° the tip vortex of the baseline hydrofoil has nearly dissipated completely due to stall effects. The loss in lift that corresponds to stall leads to this loss in vorticity. A similar trend can be seen on the baseline at a spatial location of x/c = 3c. Very similar characteristics exist on the baseline hydrofoil at a freestream velocity of U_∞ = 4.5 m/s, shown in Figures 80 and 81, with the exception of α = 24°. The tip vortex continues to exist at high angle due to high Reynolds number effects which reduce dissipation. PIV results correspond well to load tests which show that the lift and drag responses to high angle are not dramatic and remain ‘soft’ due to high Reynolds numbers.

The effect of leading edge protuberances on the tip vortex of the 4L foil is shown in Figures 78b - 81b. At a spatial location of x/c = 1.5c and a freestream velocity of U_∞ = 1.8 m/s the 4L hydrofoil shows very similar characteristics to the baseline at low angle of attack. However, at and angle of 24° the 4L hydrofoil shows less dissipation effects. At 24°, the foils

have surpassed the stall angle of the baseline, and the tip vortex of the baseline has nearly dissipated. Increased lift on modified hydrofoils seen at high angles of attack is primarily the result of tip vortex generation. This is responsible for potential lift enhancement on the suction surface of the hydrofoils.

Modified hydrofoils show a similar trend to the baseline at both spatial locations tested. However, whereas the baseline hydrofoil showed signs of complete tip vortex dissipation at post-stall angles of attack for a freestream velocity of 1.8 m/s, the modified foils do not. This correlates well with load data; in the post-stall regime of the baseline hydrofoil, the modified foils tested tend to generate more lift than the baseline model. The increased lift coefficient corresponds directly to an increase in tip vorticity. The similarity of the lift coefficients cause the tip vortex to be affected little by the presence of protuberances at a freestream velocity of 4.5 m/s.

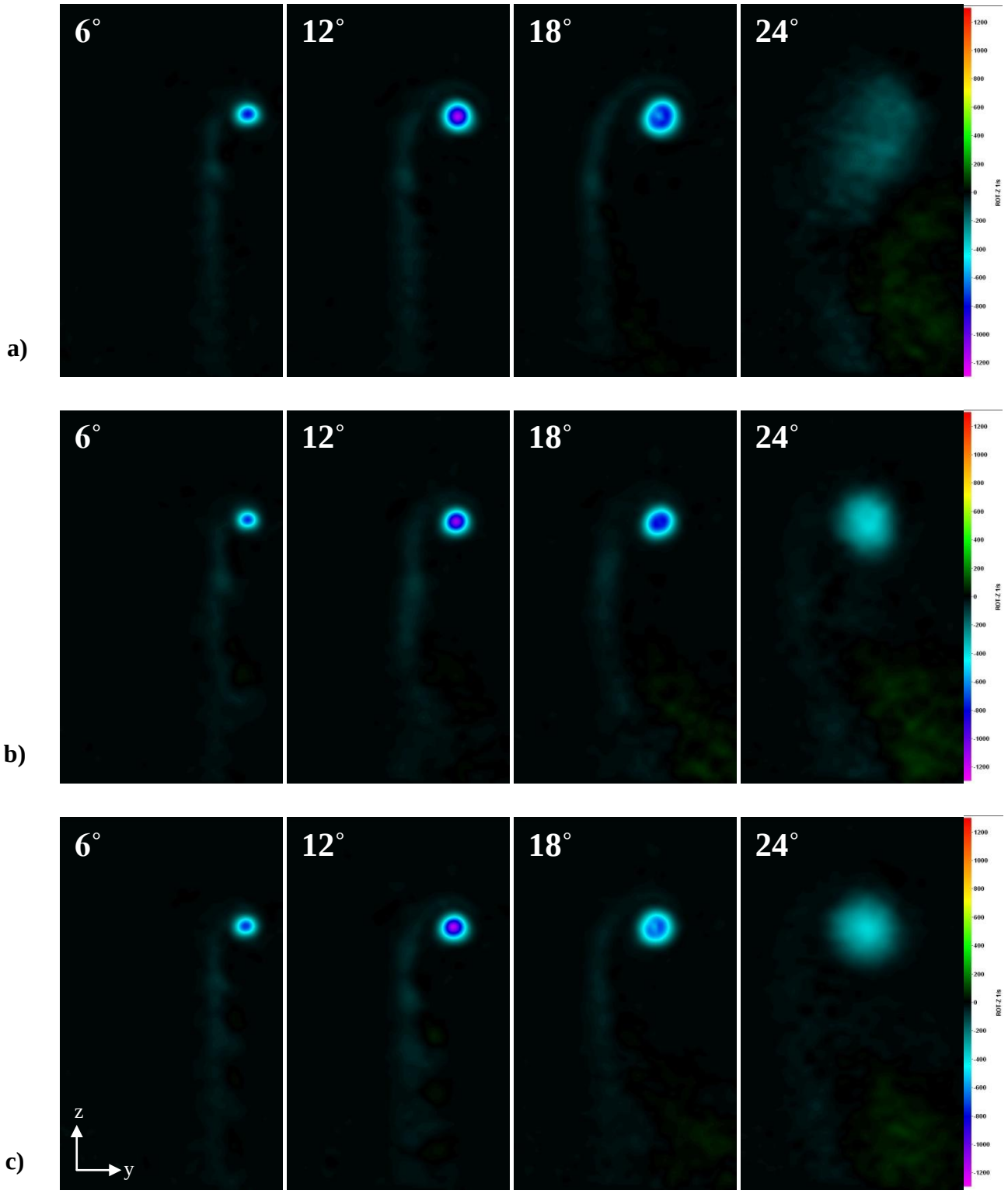

Figure 78: Streamwise vorticity contours of the tip vortex on finite-span rectangular hydrofoils 1.50*c* downstream of baseline hydrofoil leading edge. $U_\infty = 1.8$ m/s. a) Baseline b) 4L c) 8M.

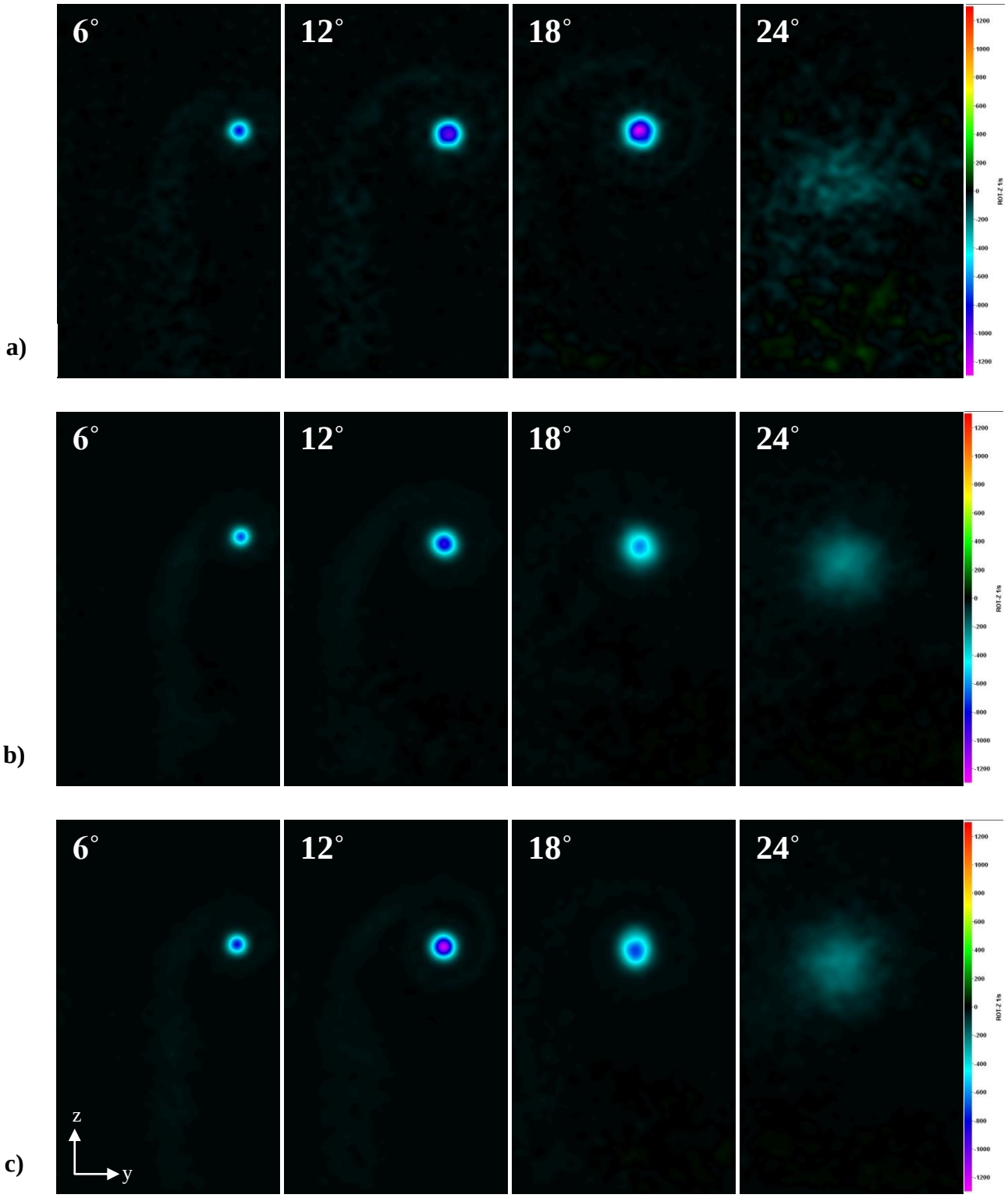

Figure 79: Streamwise vorticity contours of the tip vortex on finite-span rectangular hydrofoils 3.00*c* downstream of baseline hydrofoil leading edge. $U_\infty = 1.8$ m/s. a) Baseline b) 4L c) 8M.

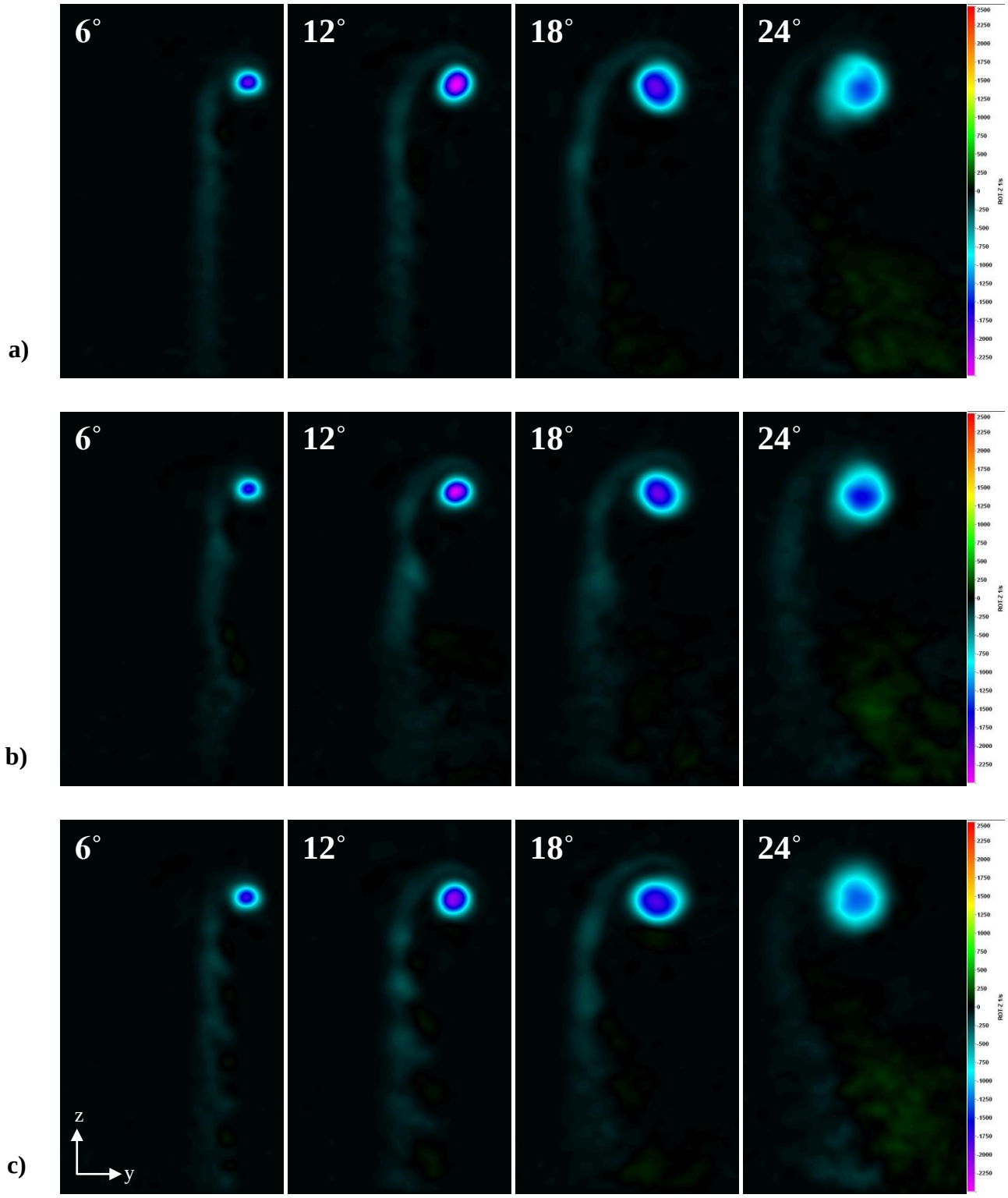

Figure 80: Streamwise vorticity contours of the tip vortex on finite-span rectangular hydrofoils 1.50*c* downstream of baseline hydrofoil leading edge. $U_\infty = 4.5$ m/s. a) Baseline b) 4L c) 8M.

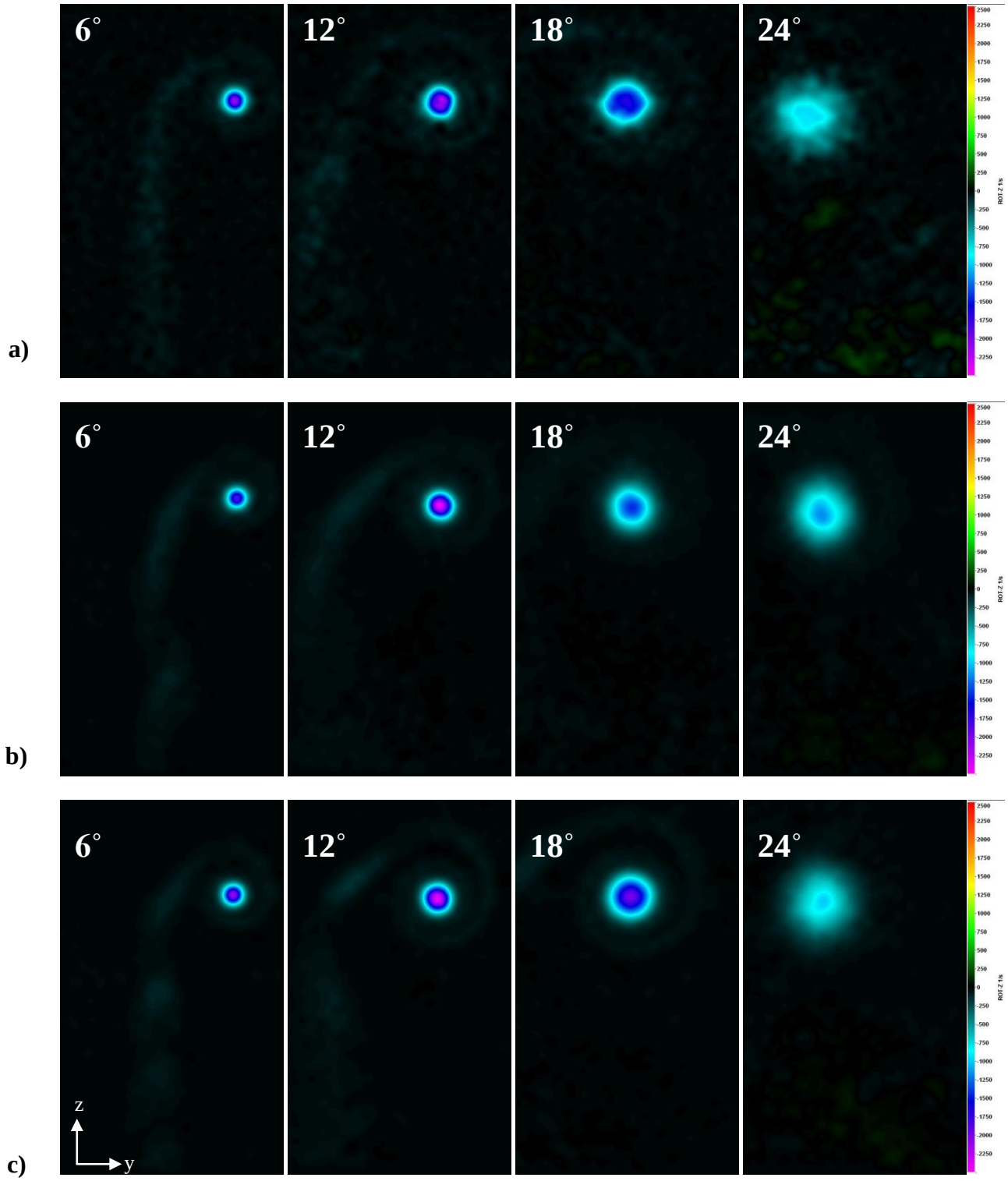

Figure 81: Streamwise vorticity contours of the tip vortex on finite-span rectangular hydrofoils 3.00*c* downstream of baseline hydrofoil leading edge. $U_\infty = 4.5$ m/s. a) Baseline b) 4L c) 8M.

Dye Visualization

The following chapter is presented here in truncated form, as a full-description of these results have been given in Custodio, 2007[24]. The following results are worth mentioning as they correspond directly to the low speed full-span PIV testing that was discussed in the last section. It describes the qualitative flow field on a protuberance modified hydrofoil at identical angle of attack, $0° \leq \alpha \leq 24°$, and freestream velocities, U_∞ = 0.15 m/s, as Figures 61 -64.

The baseline foil behaves typically for the type of airfoil profile tested. At low angles of attack, shown in Figures 82 - 87, little spanwise flow can be seen with the exception of the foil ends. Coherent lines of dye indicate flow attachment, and as the angle of attack is increased separation effects are seen in the dissipation and breakup of dye near the trailing edge of the foil. The extent of separation increases with increasing angle of attack. At angles of attack greater than α = 15°, shown in Figures 88 - 90, stall effects are clearly distinguishable with the breakup of dye initiating at the leading edge of the foil. At angles of attack greater than α = 18° the foils remain stalled and flow attachment is never regained.

Figures 82 and 83 show that at low angle of attack the flow patterns on the modified foil are symmetric, with vorticity and spanwise flow developing even at low angle of attack. As the angle of attack is increased to α = 9°, vortex interactions begin to take place with converging and diverging patterns similar to that seen in PIV testing being clearly distinguishable. An increase in angle of attack past α = 9° leads to an increase in vorticity, which in turn produces interactions that take place near the leading edge of the modified foil. At angles of attack ranging from $12° \leq \alpha \leq 18°$, which correspond to Figures 86 - 88, vorticity continues to increase producing increasingly intense vortex interactions. At these moderately high angles of attack a bi-periodic flow pattern has emerged with vortex interactions producing either converging or diverging

patterns of vortex merging. The physical mechanisms for these interactions are described later in this report in a physical model of vortex interaction. Although, the interaction patterns vary with span, separation effects are produced behind the valleys nonetheless. As the angle of attack is increased past the stall angle of the baseline, shown in Figures 88 - 90, the pattern remains the same with vorticity increasing with angle and the chordwise interaction point becoming increasingly closer to the foil leading edge.

Although both hydrofoils tested show signs of flow attachment at low angle of attack, they show distinctly different patterns at higher angles. Spanwise flow and vorticity not seen in the baseline case develops on the shoulders of the protuberances on the modified foils. At post-stall angles of attack, attachment is lost on both foils, with a limited attachment seen on the peaks of the protuberances on the modified foil. However, vorticity strength increases with increasing angle on the modified foil throughout the range of angles examined, leading to both an increase in lift as well as an increase in drag.

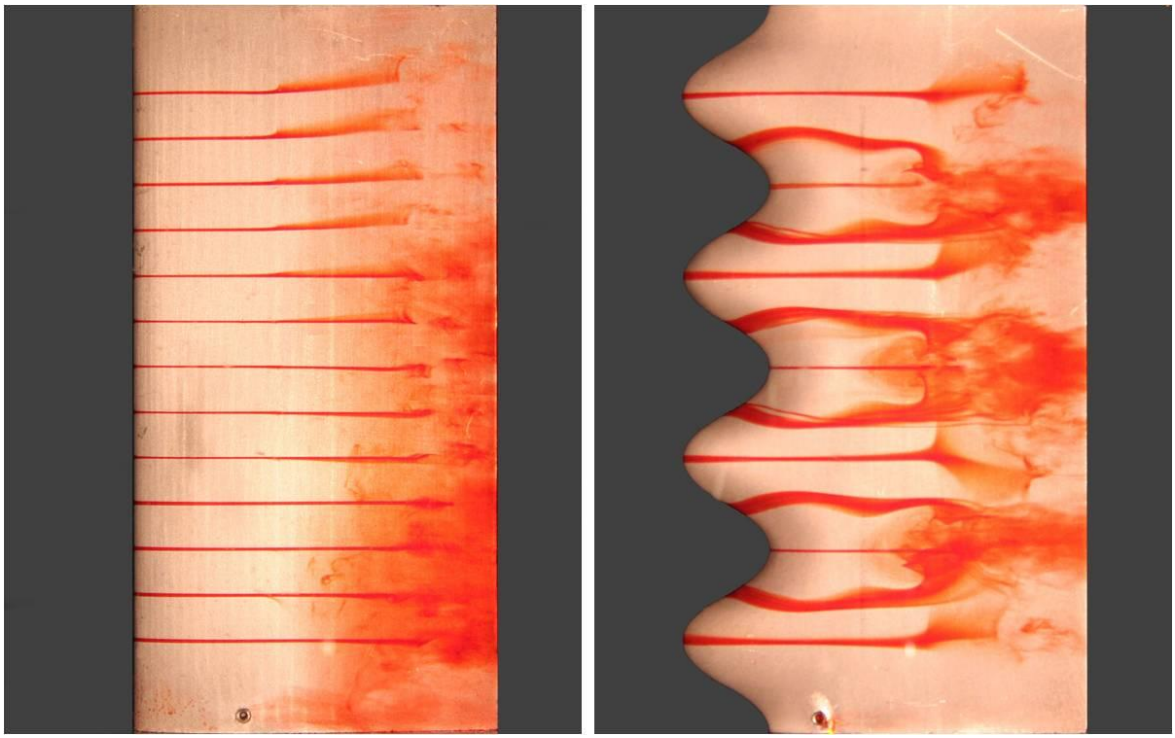

Figure 82: Dye flow visualization α = 0°.

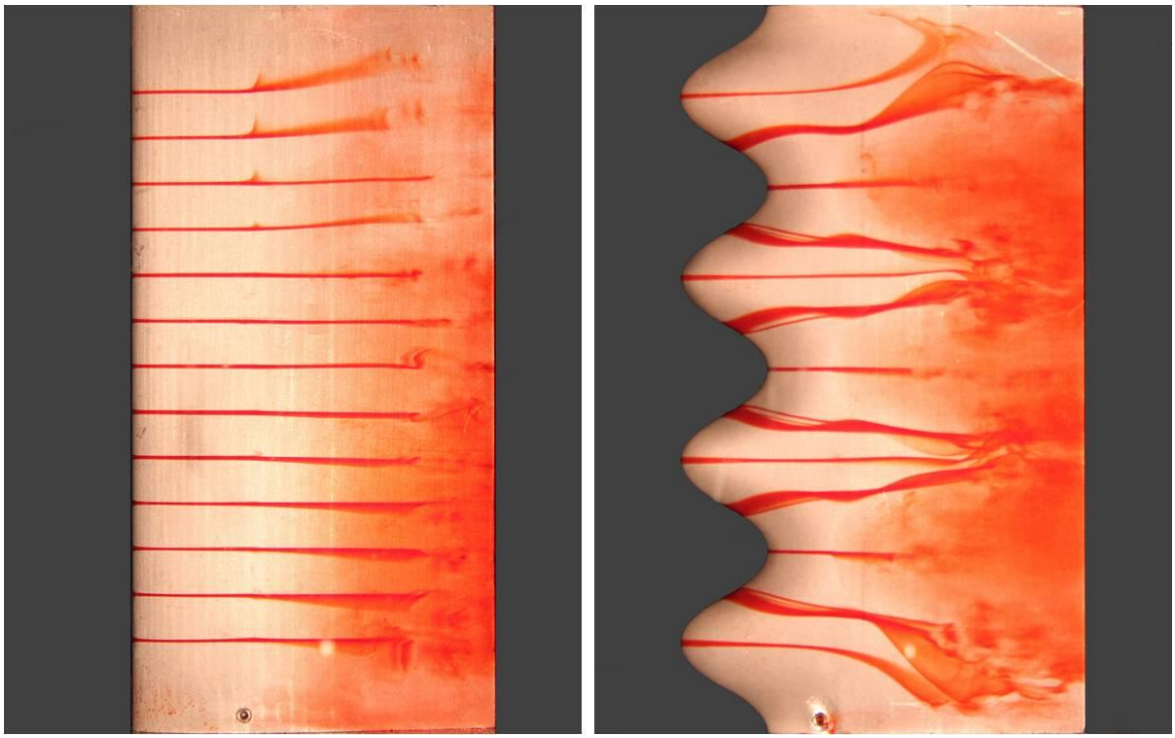

Figure 83: Dye flow visualization α = 3°.

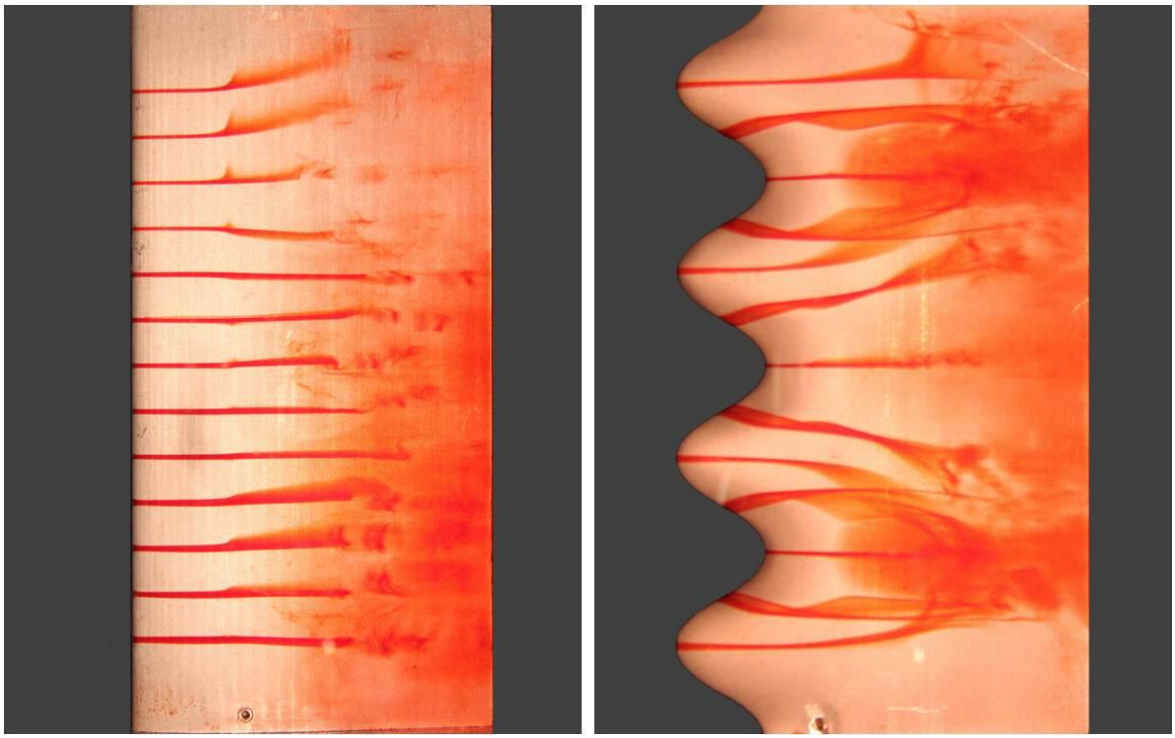

Figure 84: Dye flow visualization α = 6°.

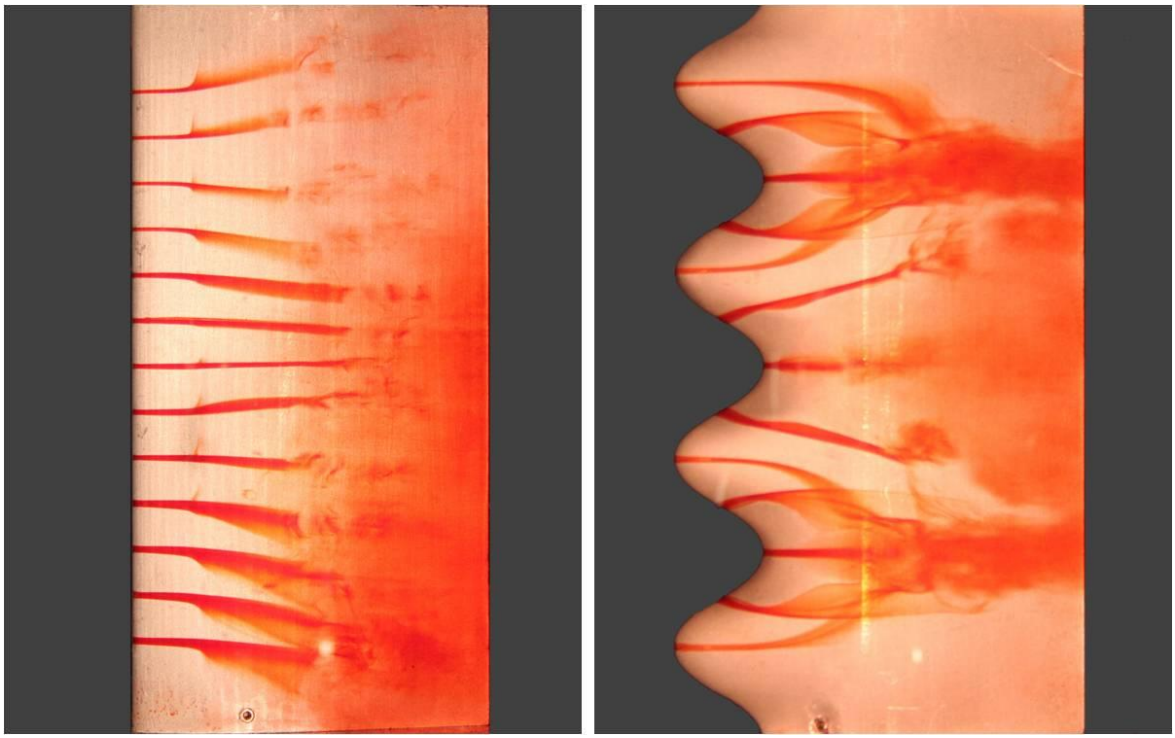

Figure 85: Dye flow visualization α = 9°.

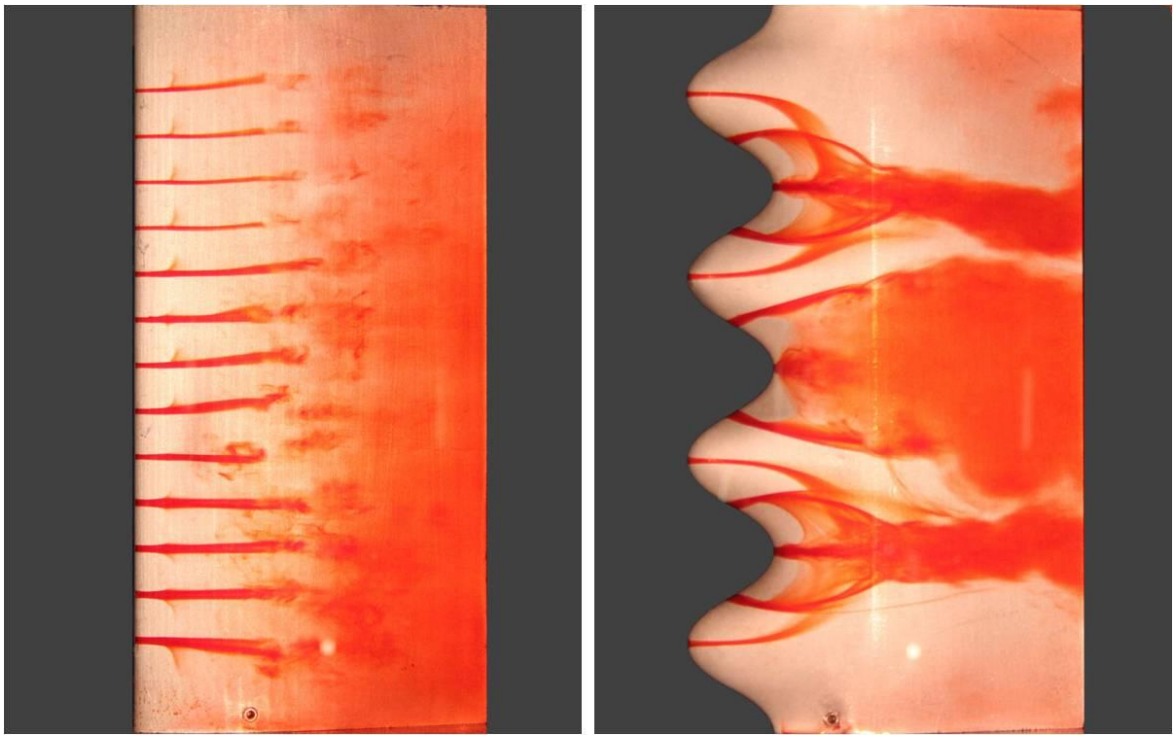

Figure 86: Dye flow visualization α = 12°.

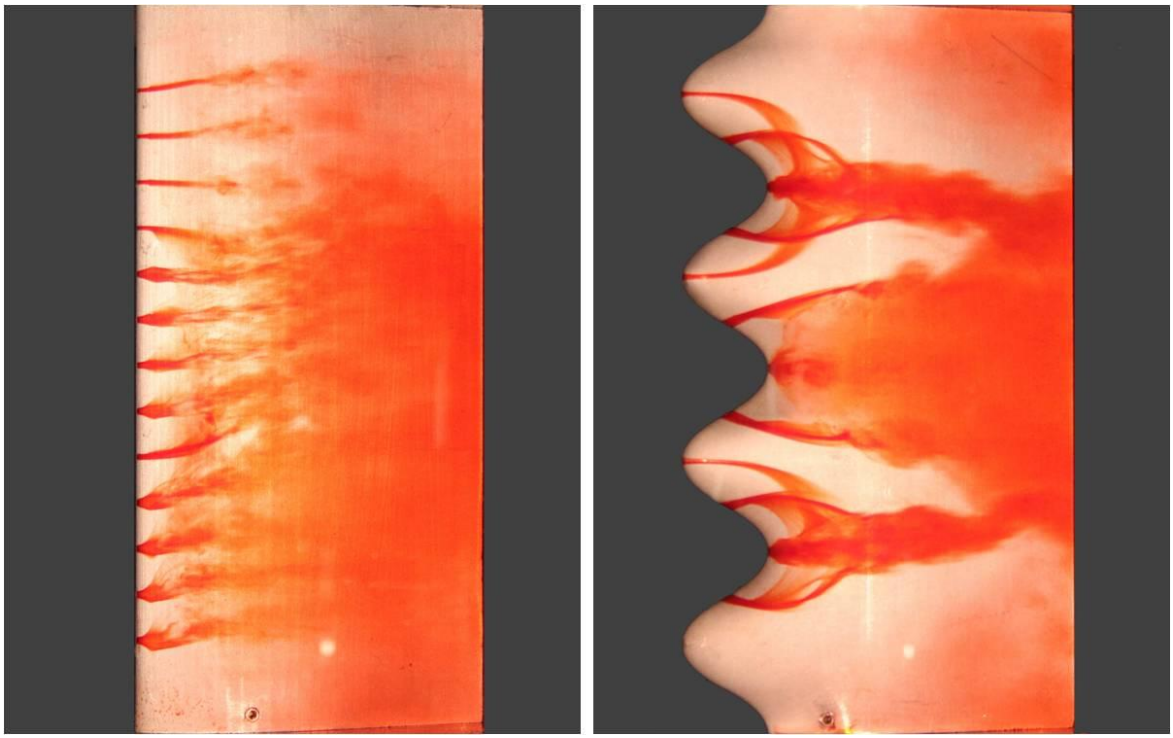

Figure 87: Dye flow visualization α = 15°.

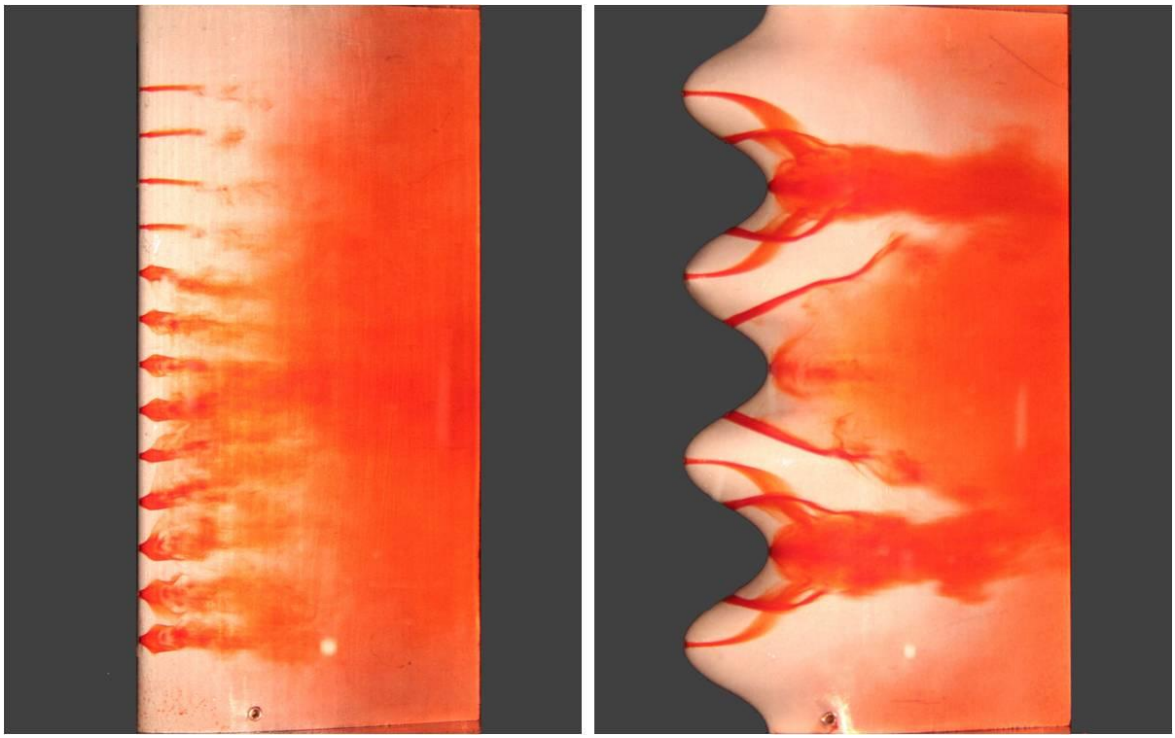

Figure 88: Dye flow visualization α = 18°.

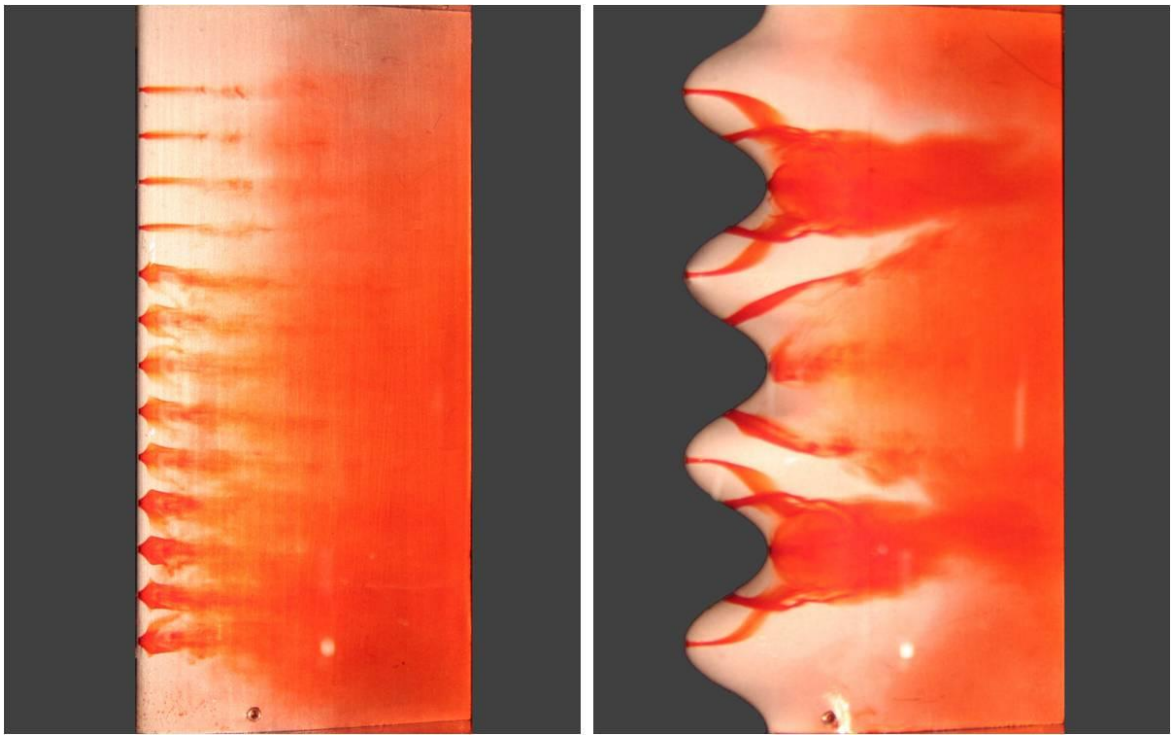

Figure 89: Dye flow visualization α = 21°.

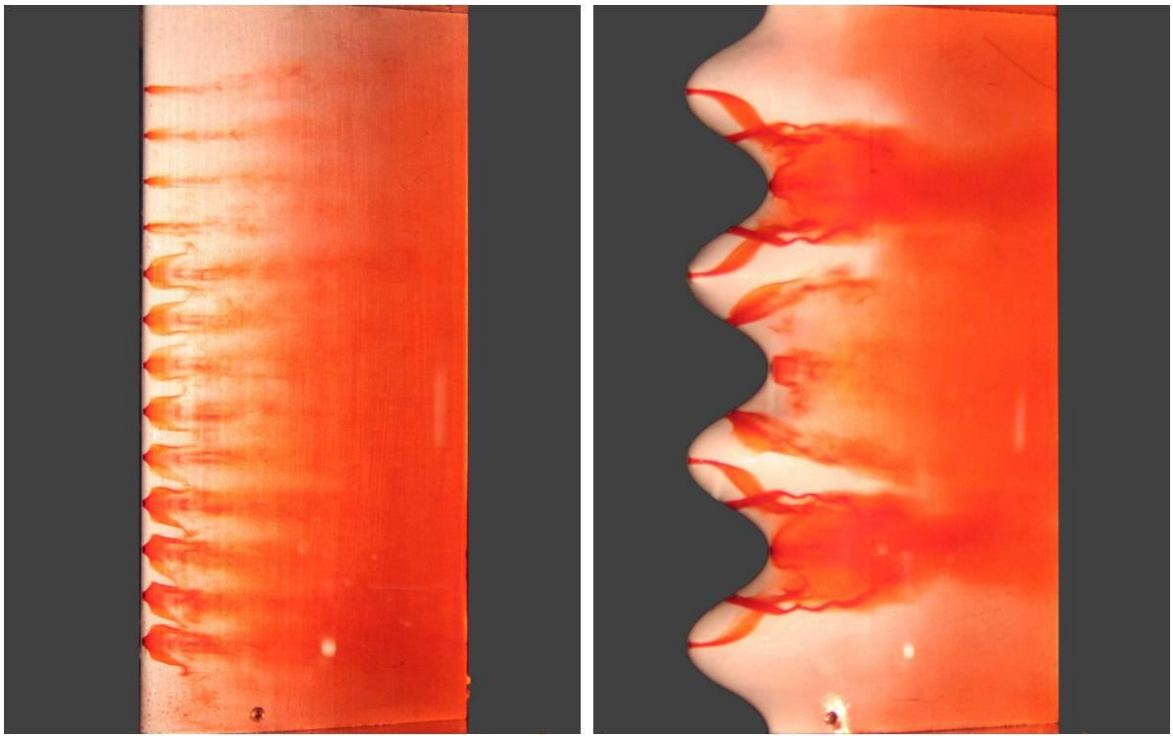

Figure 90: Dye flow visualization α = 24°.

Cavitation

Finite-Span Rectangular Hydrofoils

Photographs were taken of finite-span rectangular and swept hydrofoils at a freestream velocity of U_∞ = 7.2 m/s to determine the effect of protuberances on hydrofoil cavitation. The images are shown in Figures 91 - 93. Cavitation can be distinguished by the white color of the vapor that is produced when cavitation occurs. Vaporous cavitation indicates that locally, the pressure has become at least equal to or less than the vapor pressure of water, which leads to a change in phase.

Tip Vortex Cavitation

Figure 91 shows the effect of protuberances with a wavelength of $\lambda = 0.50c$ on the cavitation characteristics of modified hydrofoils. Cavitation effects on the baseline foil are shown in Figure 91a. Cavitation is produced by low pressure in the core of the tip vortex and is apparent at the lowest angle of attack tested, $\alpha = 12°$. As the angle of attack is increased, the amount of cavitation produced by the tip vortex grows until $\alpha = 21°$, after which point the amount of cavitation in the tip vortex decreases as a result of stall and the loss of lift at high angle. Figures 89b and 90b show that modified hydrofoils with a protuberance amplitude of $A = 0.025c$ have tip vortex cavitation characteristics similar to the baseline hydrofoil, with an increase in the vortex cavity size until $\alpha = 18°$. At angles of attack greater than $\alpha = 18°$ the size of the cavity generated by the tip vortex decreases gradually. Figure 91c shows that the 4M foil produces a vortex cavity that diminishes at an earlier angle than the baseline while the 8M foil, shown in Figure 92c, reveals a trend similar to that of the baseline. Figures 89d and Figures 90d show that foils with the largest amplitude protuberances tested, the 4L and 8L, cause the tip vortex cavity to diminish at an earlier angle than the baseline. At high freestream velocities, Reynolds number effects lead to sustained flow attachment on the baseline hydrofoil producing a

higher lift coefficient than modified foils with large protuberances. This creates a stronger tip vortex on the baseline foil, in turn generating a larger tip vortex cavity.

Leading Edge Cavitation

The rapid acceleration of flow near the leading edge of the foils leads to cavitation along the leading edge of the foils as well. Similar to the cavitation that occurs in the tip vortex, leading edge cavitation is also modified by the presence of leading edge protuberances. Figure 91a shows that sheet cavitation develops on the leading edge of the baseline hydrofoil as the angle of attack is increased. Incipient cavitation occurs on the baseline hydrofoil at an angle of 15°. At α = 18°, sheet cavitation has developed along the leading edge of the baseline foil. As the angle of attack is increased to 21° sheet cavitation increases in the spanwise direction and remains essentially the unchanged at an angle of 24°.

For all modified hydrofoils, incipient sheet cavitation on modified hydrofoils initiates in the valleys of the protuberances. This is due to the large leading edge radius in the valleys of modified foils which is responsible for accelerating the freestream flow to the greatest extent, leading to the lowest local pressures. Modified hydrofoils with a protuberance amplitude of $A = 0.12c$ show incipient cavitation at angles as low as α = 12° whereas all other modified foils show the incipient condition at an angle of α = 15°. Foils with a protuberance amplitude of $A = 0.025c$, shown in Figures 91b and 92b, show growth of the cavitation sheet that is similar to the baseline hydrofoil, with increasing sheet size corresponding to an increase in angle of attack and nearly the full extent of the span cavitating at high angle. However, contrary to the baseline hydrofoil, sheet cavitation along the leading edge is limited to a small fraction of the chord and behind the protuberance peaks.

At high angle of attack, turbulence produced by vortex interactions leads to increased pressures and transient cavitation cells behind the valleys. Therefore, cavitation along the leading

edge of modified hydrofoils is somewhat unsteady. This is true for all modified hydrofoils at high angle of attack. At high angle of attack, modified foils with large protuberance amplitudes show cavitation immediately behind the valley with cavitation along the entire leading edge no longer being apparent. At high angle of attack, vortex interactions lead to transient cavitation effects, causing cavitation cells to become unsteady at high angle, especially on foils with large protuberance amplitudes. Hydrofoils with middle and large amplitude protuberances have similar cavitation characteristics.

Wavelength plays little role in establishing the cavitation patterns seen on modified foils. In general, wavelength seems to delay the development of full leading edge sheet cavitation. Also, foils with a short wavelength develop transient cavitation cells at higher angles than foils with a longer wavelength.

Swept Hydrofoils

Figure 93 shows the effect of protuberances on the cavitation characteristics of finite-span swept hydrofoils. The tip vortex of the baseline foil cavitates at the lowest angles tested. However, at angles of attack past $\alpha \geq 18°$, tip vortex cavitation disappears all together. This is likely caused by stall effects occurring at the tip of the foil that result in increased pressures. Little to no cavitation is apparent on the leading edge of the baseline hydrofoil until an angle of $\alpha = 21°$ is reached. At angles of attack $\alpha \geq 21°$, leading edge sheet cavitation occurs over nearly 1/3 – 1/2 of the span. The lack of cavitation near the root of the hydrofoils as well as the tip are the result of low-speed and/or spanwise flow at these locations

Figure 93b shows the cavitation characteristics of the modified swept foil. Contrary to the baseline foil, tip vortex cavitation is apparent at all angles of attack tested, with similar characteristics throughout the entire range of angles tested. Incipient sheet cavitation can be seen in the valleys of the modified hydrofoil at angles as low as 12°. As the angle of attack is

increased, the extent of cavitation along the span increases slightly. Vortex interactions account for lack of cavitation in the central valley of the modified swept foil at $\alpha \geq 18°$.

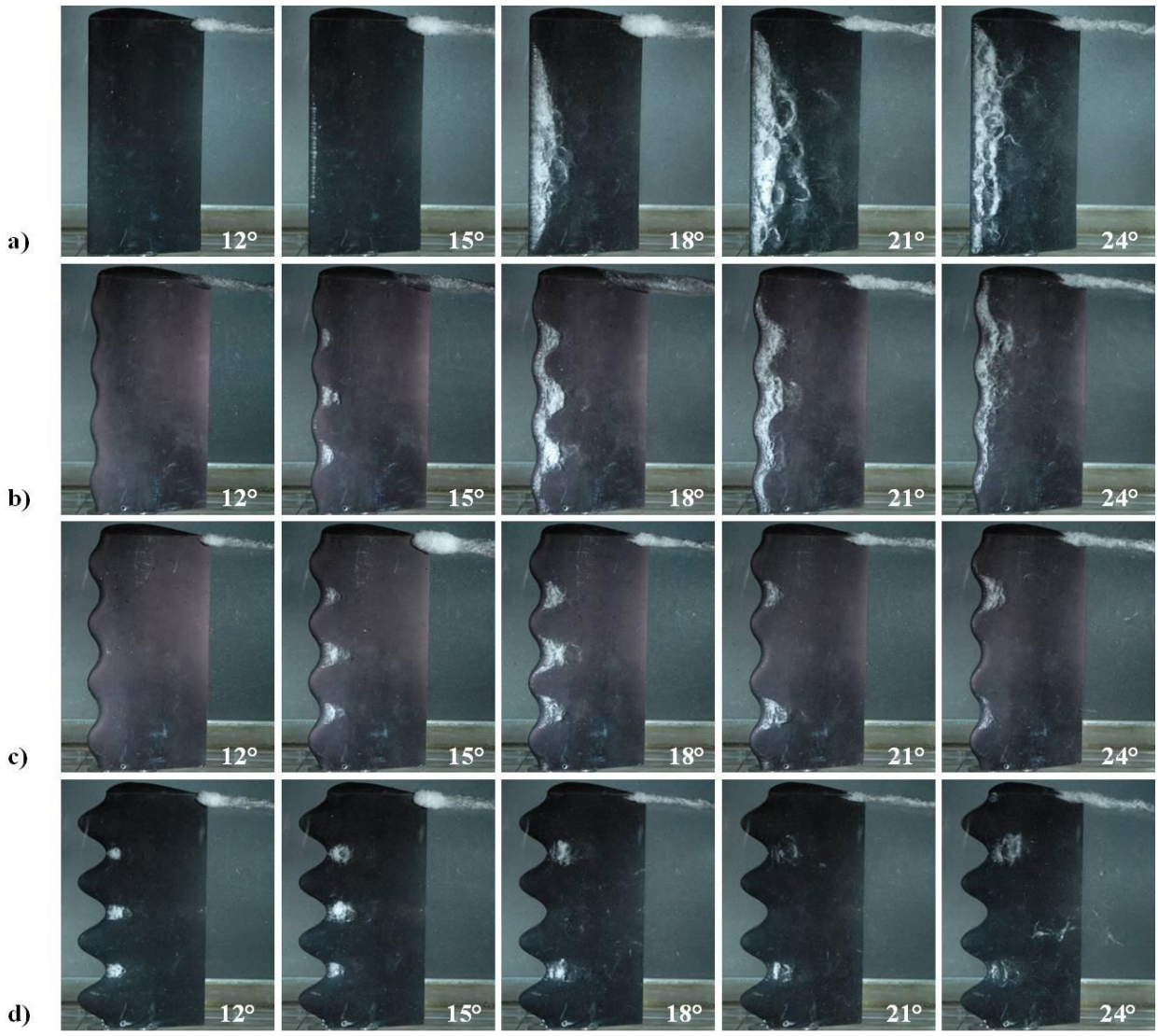

Figure 91: Vaporous cavitation on the leading edge and tip vortex of finite-span rectangular hydrofoils; a) baseline, b) 4S, c) 4M, and d) 4L.

Figure 92: Vaporous cavitation on the leading edge and tip vortex of finite-span rectangular hydrofoils; a) baseline, b) 8S, c) 8M, and d) 8L.

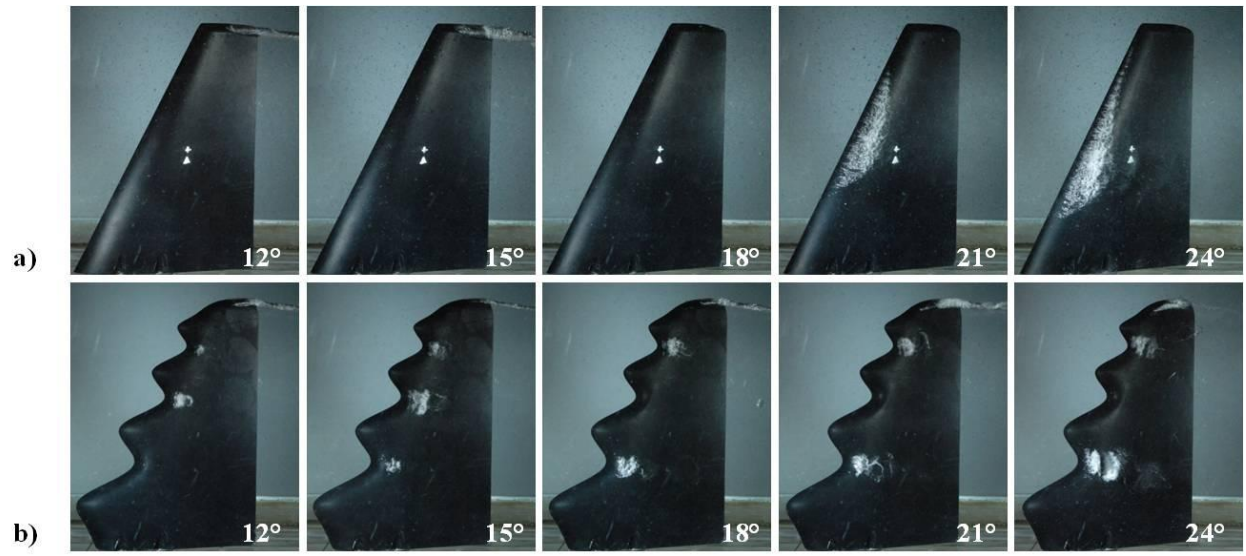

Figure 93: Vaporous cavitation on the leading edge and tip vortex of finite-span swept hydrofoils; a) baseline, b) modified.

Finite-Span Rectangular Hydrofoil Loading with Cavitation

Load measurements were taken on the finite-span rectangular and swept planform hydrofoils to determine the effect of cavitation on the load characteristics of modified finite-span hydrofoils. The following tests were performed at a freestream velocity of U_∞ = 7.2 m/s, which corresponds to the freestream velocity at which incipient leading edge sheet cavitation occurs on the baseline hydrofoil at an angle α = 15°. At angles of attack $\alpha \geq 15°$ all foils tested showed leading edge sheet cavitation as well as cavitation in the tip vortex. At angles of attack $\alpha \leq 15°$ all foils showed indications of tip vortex cavitation only, with leading edge cavitation apparent on select modified foils as described previously. All tests were conducted using the same procedure as described previously in low-speed load measurement tests.

The lift coefficient of the baseline foil, shown in Figure 94a, increases linearly at low angle of attack and continues to produce increasing lift with angle until $\alpha \approx 22°$, after which point a gradual stall and loss of lift occurs. Cavitation plays little role in the lift characteristics of the baseline foil. The likely cause of this is that the extent of cavitation is limited to a section of the foil that is only very near the leading edge, thereby reducing the potential detrimental effects

of cavitation. The drag coefficient of the baseline foil, shown in Figure 94a, increases quadratically with angle of attack throughout the entire range of angles tested, with stall effects being mitigated by high Reynolds number effects that lead to increased flow attachment. Table 20 shows important aerodynamic characteristics of the finite-span rectangular hydrofoils under cavitating conditions.

Table 20: Aerodynamic characteristics of finite-span rectangular planform hydrofoils under cavitation conditions.

$Re_c = 7.2 \times 10^5$	$\frac{dC_L}{d\alpha}$ [1/deg]	C_{Lmax}	α @ C_{Lmax} [deg]	C_{Dmin}	L/D_{max}	α @ L/D_{max} [deg]	α_{stall} [deg]
Baseline	0.055	1.12	22.3	0.02	11.43	7.2	23.7
4S	0.055	1.06	20.8	0.02	11.4	7.4	20.8
4M	0.054	1.05	19.5	0.02	10.83	7.6	21.0
4L	0.048	0.91	17.8	0.02	8.61	7.6	19.2
8S	0.054	1.07	20.7	0.02	11.27	7.3	22.2
8M	0.052	1.02	20.9	0.02	10.50	7.6	20.9
8L	0.051	0.77	15.8	0.02	9.7	7.5	18.7

Effect of Amplitude

Figures 94 and 95 show the effect of protuberance amplitude on the load characteristics of modified hydrofoils under cavitating conditions. The lift coefficient of modified foils with a protuberance amplitude of $\lambda = 0.50c$, shown in Figure 94a, reveals that the all foils perform similarly at angles of attack ranging from $0° \leq \alpha \leq 16°$. However, over a small range of angles of attack of $16° \leq \alpha \leq 20°$, the lift coefficient of the 4S and 4M foils are slightly greater than that of the baseline. With this exception, the baseline lift coefficient outperforms all modified cases. The same trend is also true for modified hydrofoils with a wavelength of $\lambda = 0.25c$, shown in Figure 95a. Foils with protuberances amplitudes of $A = 0.025c$ and $0.050c$ perform similarly to each other, while foils with a protuberance amplitude of $A = 0.12c$ have the poorest lift coefficient performance of all foils tested.

The drag coefficients of modified foils are shown in Figures 94b and 95b. They are very similar to the baseline hydrofoil. This trend is much different than that shown in cases in which no cavitation effects were present. Whereas the drag on modified foils is significantly higher than that of the baseline at lower freestream velocity where no cavitation was apparent, the drag of modified foils is very similar to the baseline when significant cavitation is present.

Effect of Wavelength

The load characteristics of foils with protuberances amplitudes of $A = 0.025c$ - $0.12c$ are shown in Figures 96 -98 respectively. The series of plots reveals that, with the exception of modified foils with protuberance amplitudes of $A = 0.12c$, wavelength does not play a major role in establishing the load characteristics on cavitating hydrofoils throughout the range of angles tested.

The lift coefficient of modified foils with a protuberance amplitude of $A = 0.12c$ is shown in Figure 98a. All foils shown perform similarly until $\alpha \approx 15°$, at which point C_L of the modified

foils shows similar trends throughout. The lift coefficient of the modified foils decreases gradually at angles of attack greater than $\alpha \approx 15°$, with a nearly 7% difference in lift coefficient values of the 4L and 8L foils over a large range of angles.

The drag coefficient of the modified foils with a protuberance amplitude of $A = 0.12c$, shown in Figure 98b, reveals that there is relatively no difference in C_D between modified cases at low angle of attack. However, at angles of attack greater than 20°, drag characteristics become increasingly different, with C_D of the 8L foil becoming nearly constant and the 4L foil producing drag at a reduced rate.

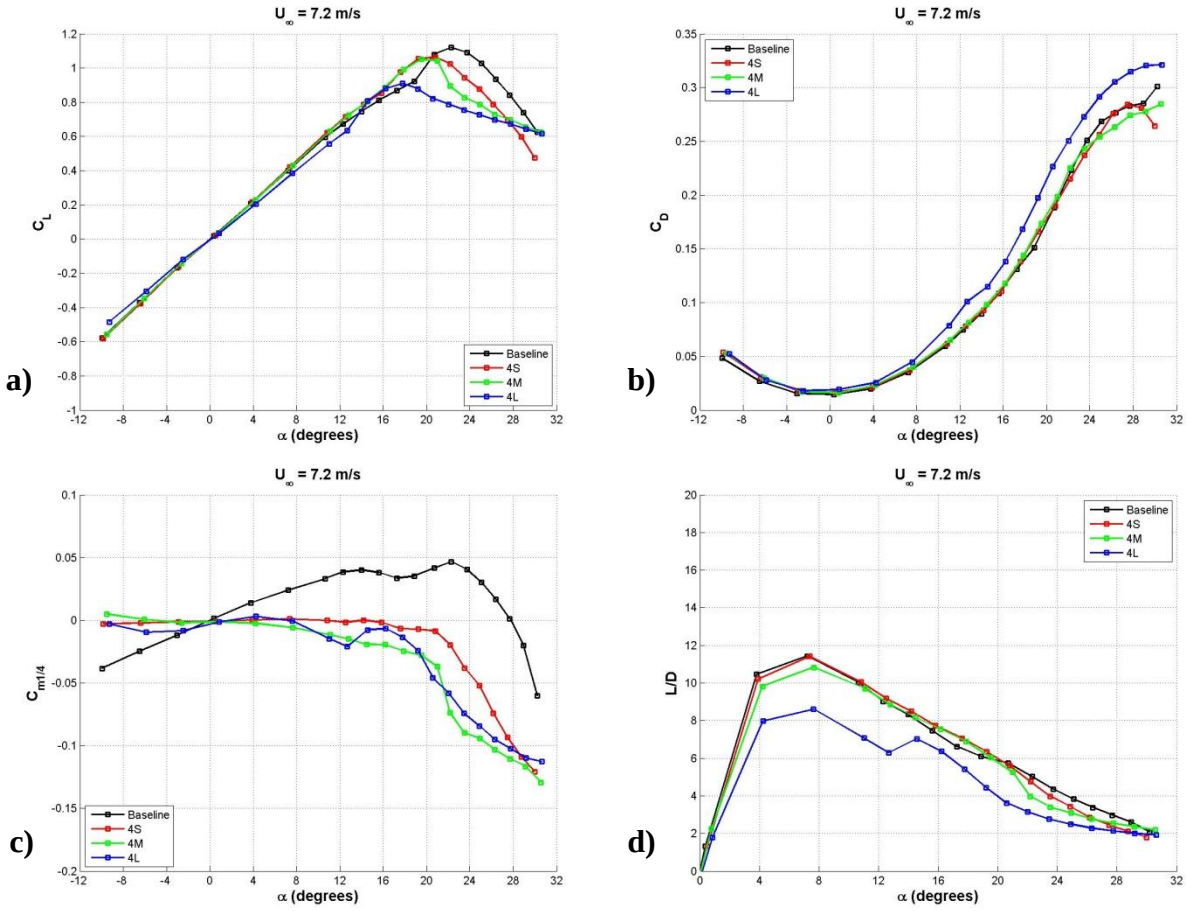

Figure 94: Effect of protuberance amplitude on the load characteristics of cavitating hydrofoils with a protuberance wavelength of $\lambda = 0.50c$; a) lift coefficient, b) drag coefficient, c) quarter chord moment coefficient, d) lift-to-drag ratio.

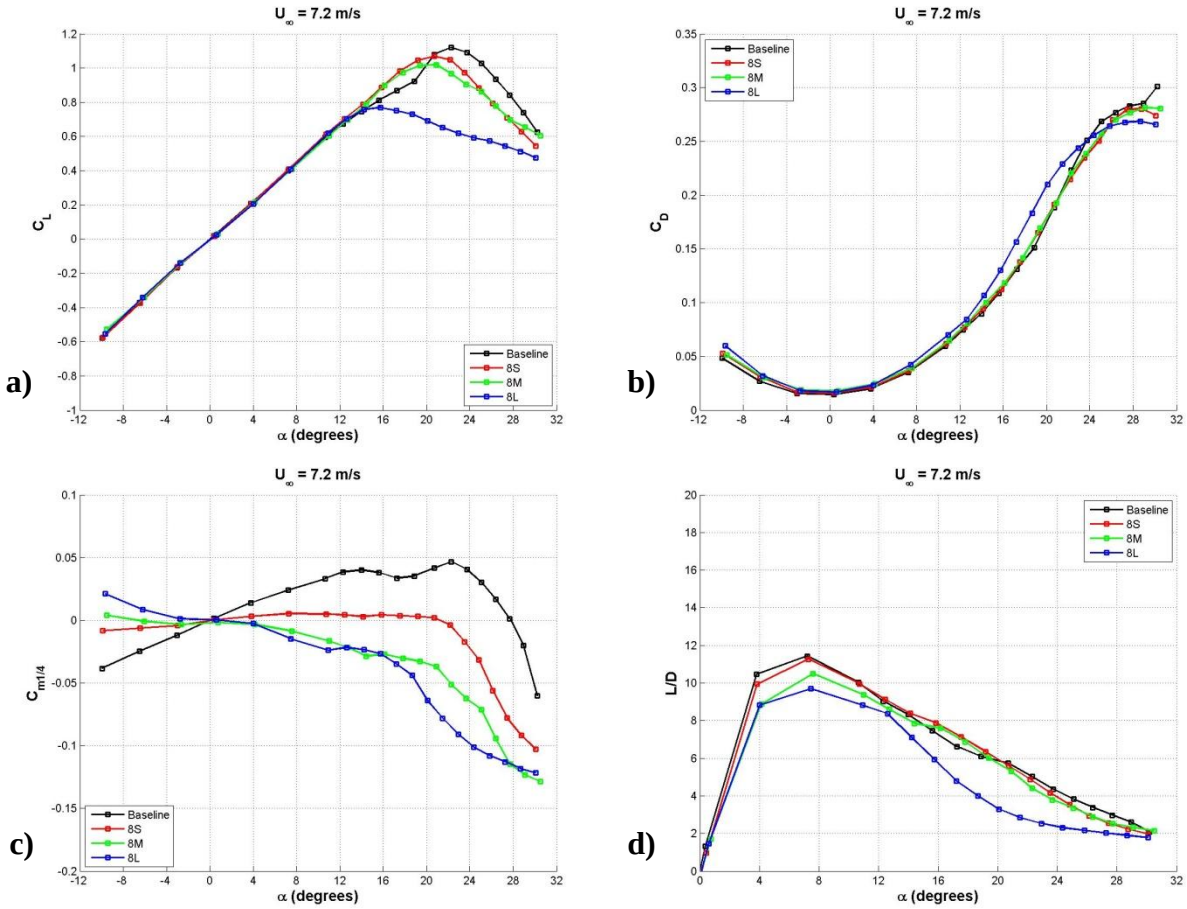

Figure 95: Effect of protuberance amplitude on the load characteristics of cavitating hydrofoils with a protuberance wavelength of λ = 0.25*c*; a) lift coefficient, b) drag coefficient, c) quarter chord moment coefficient, d) lift-to-drag ratio.

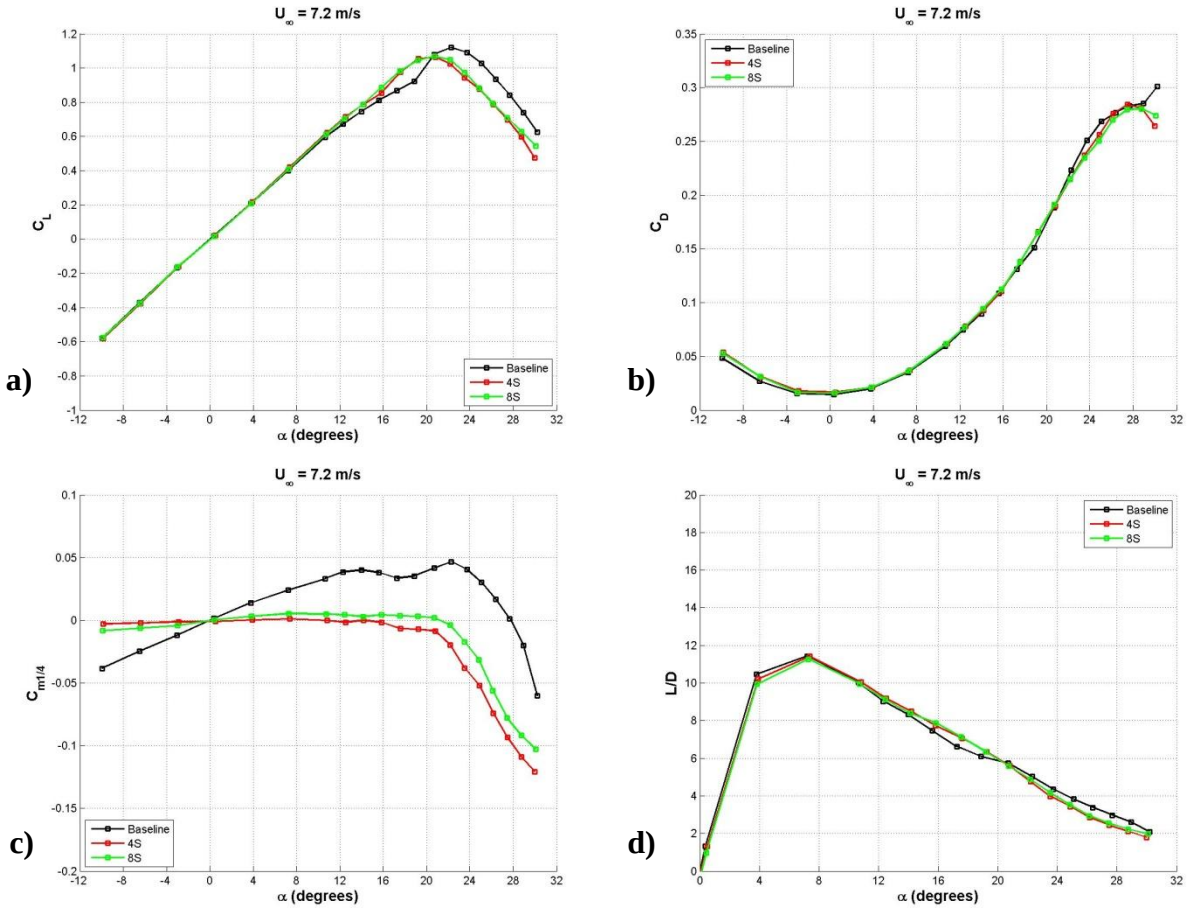

Figure 96: Effect of protuberance wavelength on the load characteristics of cavitating hydrofoils with a protuberance amplitude of $A = 0.025c$; a) lift coefficient, b) drag coefficient, c) quarter chord moment coefficient, d) lift-to-drag ratio.

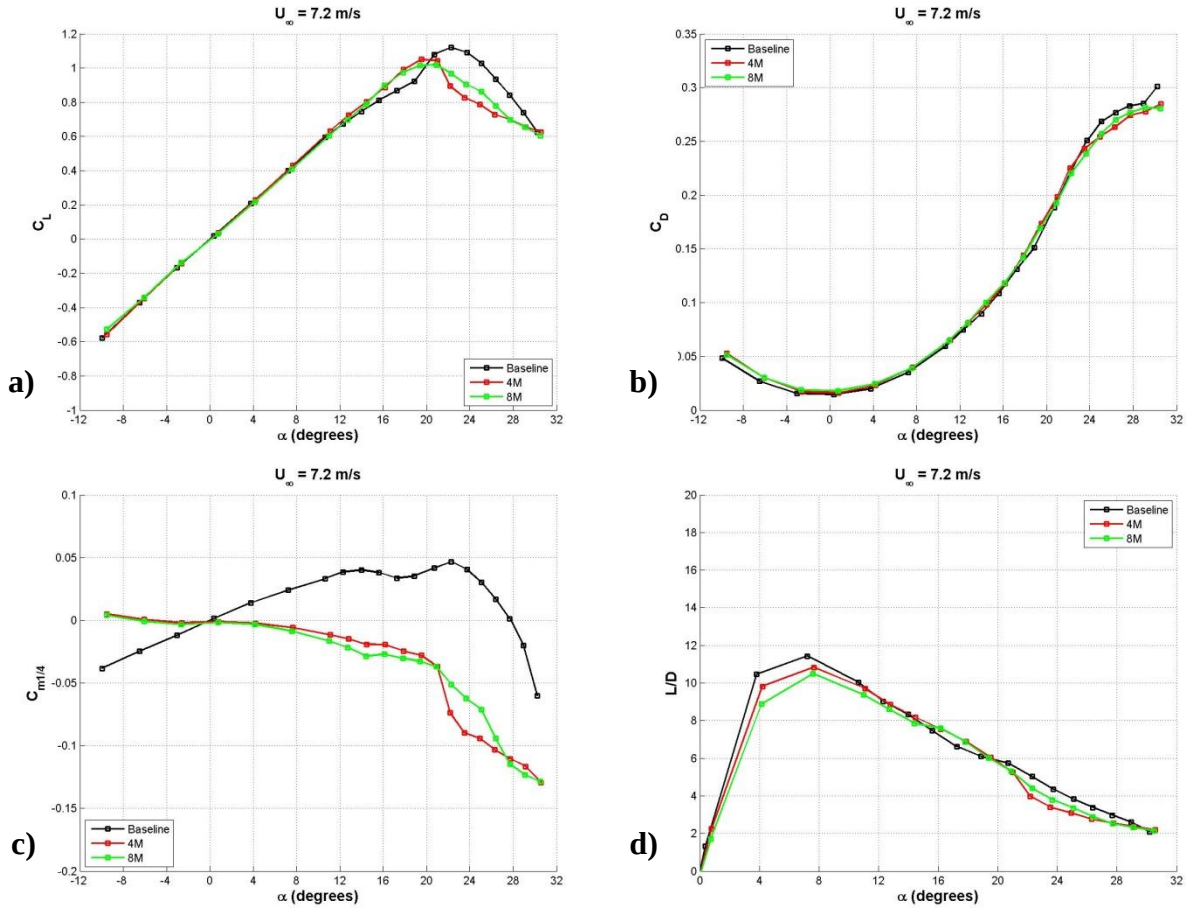

Figure 97: Effect of protuberance wavelength on the load characteristics of cavitating hydrofoils with a protuberance amplitude of $A = 0.050c$; a) lift coefficient, b) drag coefficient, c) quarter chord moment coefficient, d) lift-to-drag ratio.

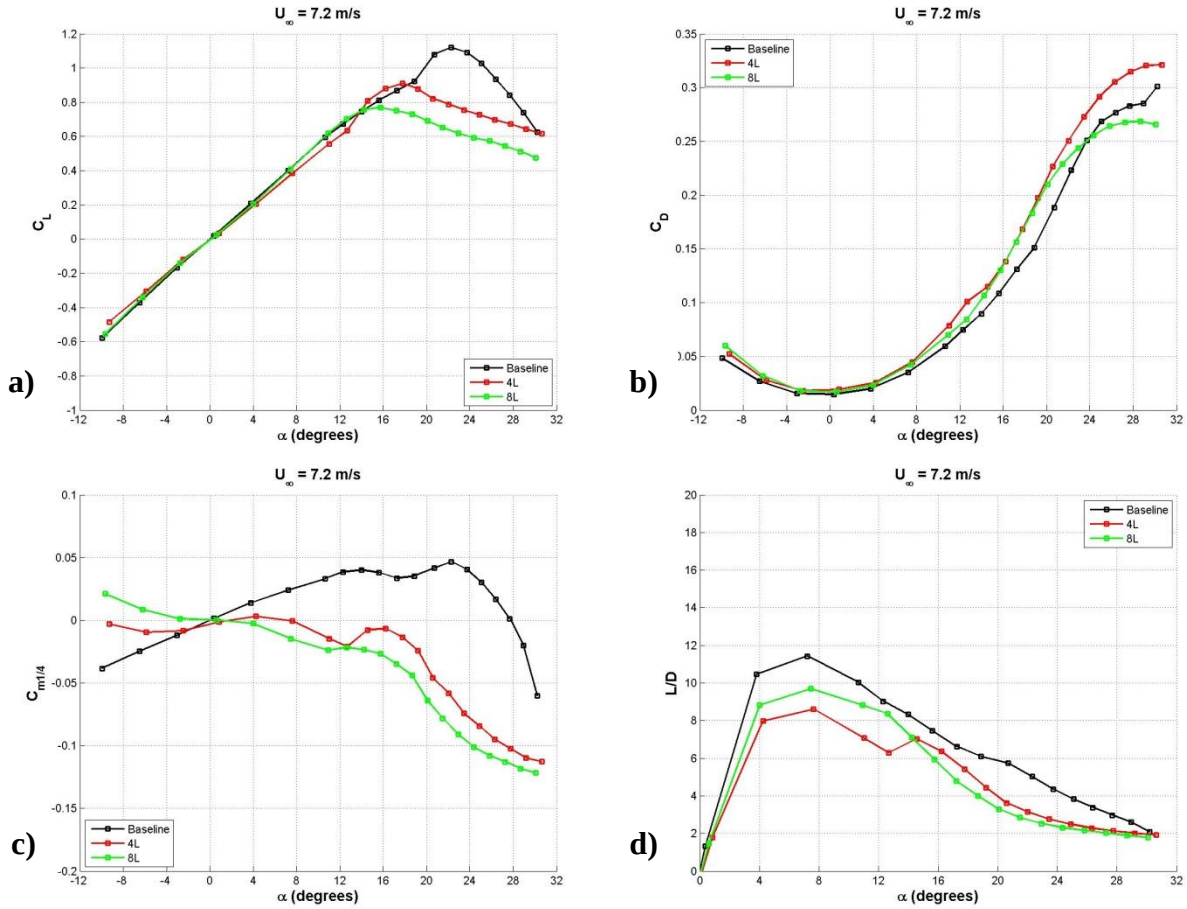

Figure 98: Effect of protuberance wavelength on the load characteristics of cavitating hydrofoils with a protuberance amplitude of $A = 0.12c$; a) lift coefficient, b) drag coefficient, c) quarter chord moment coefficient, d) lift-to-drag ratio.

Swept Hydrofoil Loads with Cavitation

The load characteristics of the modified swept foil are compared to the baseline hydrofoil in Figure 99. Figure 99a shows that for all angles of attack tested, the lift coefficient of the baseline foil is either greater than or nearly equal to that of the modified case. There is a gradual of 'soft' stall in both cases with no signs of a dramatic loss of lift at high angle of attack. The baseline lift is significantly greater than the modified case over a wide range of angles of attack of $15° \leq \alpha \leq 29°$ producing as much as 20% more lift than the modified foil.

The drag coefficient of the swept hydrofoils is shown in Figure 99b. The drag coefficient is nearly for both foils tested at all angles of attack prior to $\alpha \approx 15°$. Over a range of angles $15° \leq \alpha \leq 29°$, C_D of the modified case is slightly greater than that of the baseline with an increase in drag of ≈12%, after which point the drag of the modified and baseline foils become nearly equal, to within experimental uncertainty. Table 21 shows important aerodynamic characteristics of the swept hydrofoils under cavitating conditions.

Table 21: Aerodynamic characteristics of swept planform hydrofoils under cavitation conditions.

$Re_c = 7.2 \times 10^5$	$\frac{dC_L}{d\alpha}$ [1/deg]	C_{Lmax}	α @ C_{Lmax} [deg]	C_{Dmin}	L/D_{max}	α @ L/D_{max} [deg]	α_{stall} [deg]
Baseline	0.056	1.15	24.1	0.01	10.09	7.6	28.4
Modified	0.055	0.91	24.6	0.01	9.28	7.0	N/A

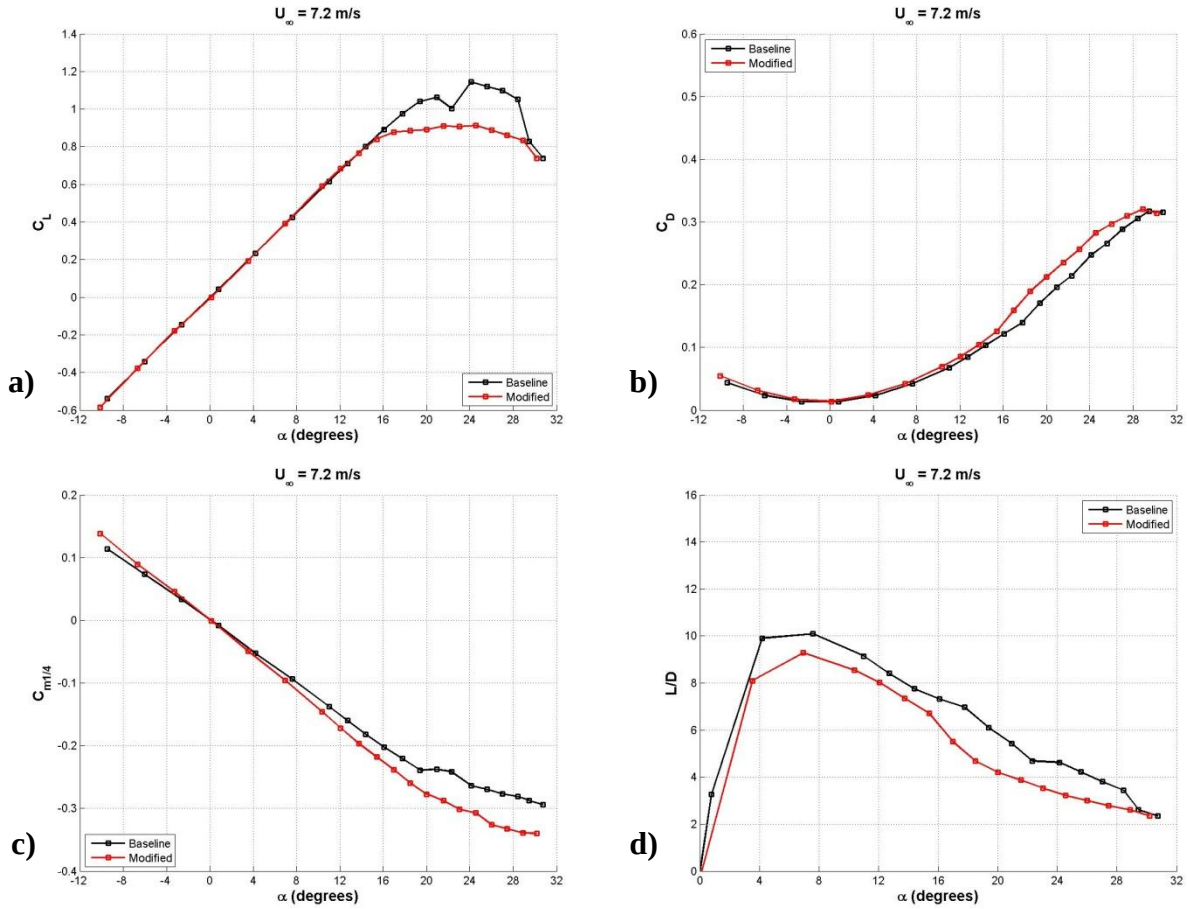

Figure 99: Effect of protuberances on the load characteristics of cavitating swept hydrofoils; a) lift coefficient, b) drag coefficient, c) quarter chord moment coefficient, d) lift-to-drag ratio.

Cavitation Number

The cavitation numbers of finite-span rectangular and swept modified foils were compared to their baseline counterparts over a range of angles of attack $3° \leq \alpha \leq 24°$. The cavitation number was calculated at the incipient leading edge cavitation condition, i.e. when sheet cavitation was first apparent on the leading edge of the hydrofoils. Cavitation number was calculated in the following manner:

$$k = \frac{p - p_v}{\frac{1}{2}\rho U_\infty^2}$$

where p is the freestream static pressure, p_v is the vapor pressure of water, ρ is the density of water, and U_∞ is the freestream velocity. Cavitation number is essentially the ratio of local static pressure to the dynamic pressure and is a way of quantifying the cavitation characteristics of the hydrofoils. Consequently, higher values for cavitation number imply that, for a given local static pressure and angle of attack, incipient cavitation will occur at a lower freestream velocity. This set of tests essentially shows the range of speeds that a foil will operate without cavitation occurring.

Finite-Span Rectangular Hydrofoils

The cavitation number as a function of angle of attack on finite-span rectangular hydrofoils is shown in Figure 100. The baseline cavitation number was less than the modified foils for all angles of attack tested. Modified foils with protuberance amplitudes of $A = 0.025c$ and $0.050c$ perform similar to the baseline with incipient cavitation being nearly independent of protuberance wavelength. The cavitation numbers of foils with smaller amplitudes are always higher than that of the baseline with a maximum difference of ≈ 20% at high of angle of attack. Past an angle of attack of $\alpha = 6°$, the 4L foil produces a cavitation number consistently higher than the baseline and modified foils with an equivalent protuberance wavelength, generating ≈

25% greater cavitation number than the baseline foil. Figure 100 also shows that the incipient cavitation number of foils with the largest protuberance amplitudes, $A = 0.12c$, are highly dependent on wavelength. The 8L foil, which has a wavelength that is half that of the 4L, shows a maximum cavitation number that is nearly 72% and 125% greater than that of the 4L and baseline foils, respectively. In terms of freestream velocities at which the foils will cavitate; Figure 100 shows that if at an angle of $\alpha = 15°$ the baseline foil shows incipient leading edge cavitation at a freestream velocity of $U_\infty = 7.2$ m/s, as shown in Figures 91 and 92, the 4L and 8L foils will show signs of incipient cavitation at freestream velocities of $U_\infty = 5.49$ and 4.8 m/s respectively for the same angle of attack and a local static pressure.

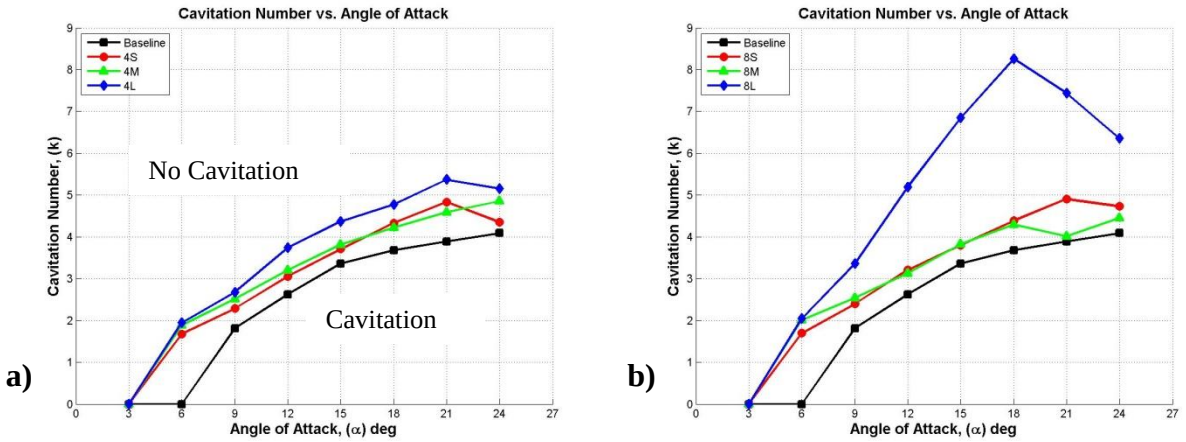

Figure 100: Incipient cavitation number of finite-span rectangular modified foils as a function of angle of attack; a) $\lambda = 0.50c$, and b) $\lambda = 0.25c$.

Finite-Span Swept Hydrofoils

The cavitation numbers of the swept planform hydrofoils are shown in Figure 101. For all angles of attack at which leading edge cavitation was present, the cavitation number of the modified swept foil ranged from ≈ 50% greater than the baseline foil. Consequently, this implies that for a given angle of attack and local static pressure, the modified case will cavitate at freestream velocities 19% lower than the baseline case. In general, the values for cavitation

numbers of the modified hydrofoils are a nearly constant percentage greater than the baseline case.

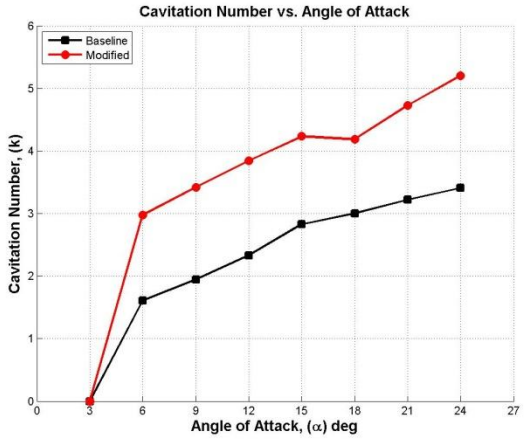

Figure 101: Incipient cavitation number as a function of angle of attack of the modified swept foil.

IV. Vortex Interaction Model

It was shown in Chapter III that vortex interactions occur between neighboring counter-rotating vortices stemming from protuberance shoulders. The following chapter will present a physical description of the mechanism of vortex interaction so that a prediction of the chordwise interaction point of two neighboring vortices can be made. To understand the mechanisms of spanwise vortex interaction on modified hydrofoils, an analysis analogous to the dynamics of vortex interactions on a flat surface was carried out.

Vortex motion and interaction above the surface can be described using the method of vortex images commonly used in potential flow theory. An infinite row of counter-rotating vortices of known vorticity was considered at a height, *h*, above a flat surface. Figure 102 shows an example of the vortex pairs along with their images,

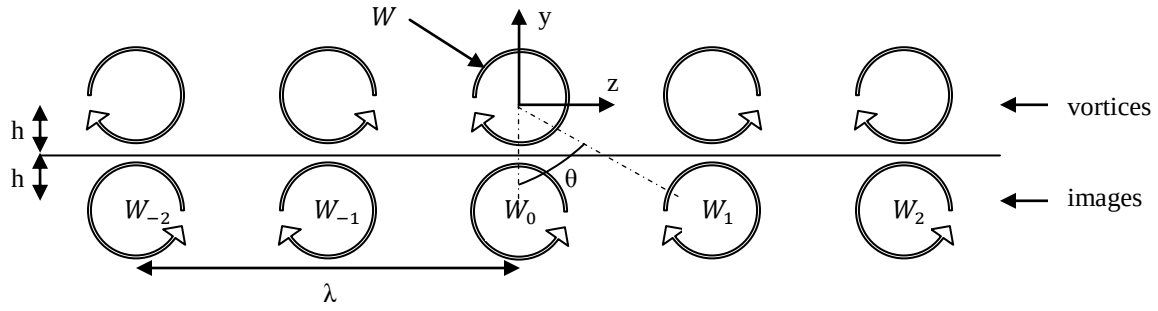

Figure 102: Counter-rotating vortices with image pairs.

where λ is one protuberance wavelength on a modified foil and *h* is the vertical distance of the vortex core from the flat surface. Considering only the central vortex, *W*, will have an induced velocity, $u_{induced}$ in the z-direction that is generated by interactions with vortex images. Neighboring vortices above the surface will have no influence on *W* due to symmetry. To determine the induced velocity on *W*, it is necessary to sum the influence of each vortex image on *W*. Induced velocity due to any single vortex image on *W* can be written in the following way,

$$u = \frac{\Gamma}{2\pi\delta_j}$$

where j= 1,2,3,4,5 ... n, Γ is the circulation of W and δ_j is the distance from the core of W to the core of a given vortex image inducing a velocity on W. The influence of any image on W can be calculated assuming that δ_j and Γ are known. Since the distance between neighboring counter-rotating vortices is known to be $\frac{\lambda}{2}$, set by the wavelength of the modified foil, δ_j can be written in the following way,

$$\delta_j = \sqrt{\left(z - z_j\right)^2 + \left(y - y_j\right)^2} = \sqrt{j\left(\frac{\lambda}{2}\right)^2 + (2h)^2}$$

Since only spanwise vortex interaction is being examined, the induced velocity of W in only the spanwise direction is of interest,

$$u_{induced} = \sum_{j=1}^{\infty} \frac{\Gamma}{2\pi\delta_j} \cos\theta_j \tag{1}$$

where,

$$\cos\theta = \frac{2h}{\delta_j}$$

Assuming that the spanwise velocity, $u_{induced}$, of any vortex is constant until vortex convergence occurs, the spanwise location of the vortex can be determined the following way,

$$\Delta z = u_{induced}\Delta t = u_{induced}\left(\frac{x}{U_\infty}\right) \tag{2}$$

where, x is the position of a vortex core along the chord of the modified foil and U_∞ is the freestream velocity. Also, based on physical evidence seen in experiments on modified foils, it is valid to assume that counter-rotating vortex pairs occur at half wavelengths between

protuberances, while the merging of vortex cores is seen at the midpoint between adjacent vortices. This allows for the following expression,

$$\frac{\lambda}{4} \approx u_{induced}\left(\frac{x}{U_\infty}\right) \tag{3}$$

For an infinite row of vortices, $u_{induced}$ can now be rewritten the following way,

$$u_{induced} = u_0 + 2\sum_{j=1}^{\infty} u_j = -\frac{\Gamma}{4\pi h} + 2\sum_{j=1}^{\infty}(-1)^{j-1}\frac{\Gamma}{2\pi}\frac{2h}{\left(j\left(\frac{\lambda}{2}\right)^2 + (2h)^2\right)} \tag{4}$$

which, after factorization and simplification yields,

$$u_{induced} = -\frac{\Gamma}{4\pi h}\left[1 - \sum_{j=1}^{\infty}(-1)^{j-1}\frac{32h^2}{(j\lambda^2 + (16h)^2)}\right]$$

Also, from Equation (3), the chord normalized vortex core position is known to be,

$$\frac{x}{c} = \frac{\lambda U_\infty}{4u_{induced}c} \tag{5}$$

Equation (5) can be rewritten as,

$$\frac{x^*}{c} = \left(\frac{\lambda}{4c}\right)\left(\frac{h}{c}\right)\left(\frac{\Gamma}{4\pi U_\infty c}\right)^{-1}\left[1 - \sum_{j=1}^{\infty}(-1)^{j-1}\frac{32h^2}{j\lambda^2 + 16h^2}\right]^{-1} \tag{6}$$

where $\frac{x^*}{c}$ can be defined the chord location at which two adjacent counter rotating vortices will meet at their spanwise midpoint. A closed solution can be substituted for the summation in Equation (6) in the form of the Lerch transcendent,

$$\Phi(z, s, a) = \sum_{k=0}^{\infty}\frac{z^k}{(a+k)^s}$$

Allowing the summation in $\frac{x^*}{c}$ to be rewritten as,

$$\sum_{i=1}^{n}(-1)^{j-1}\ \frac{32h^2}{j\lambda^2+16h^2}=\frac{32h^2\left(\Phi\left(-1,1,\frac{16h^2}{\lambda^2}+1\right)-1(-1)^n\Phi\left(-1,1,\frac{16h^2}{\lambda^2}+n+1\right)\right)}{\lambda^2}$$

Equation (6) allows for an understanding of the way that an infinite row of evenly spaced vortices interact with each other. With knowledge of the circulation and core height of a single vortex, it is possible to determine the chordwise location, $\frac{x^*}{c}$, at which the vortex of interest has moved a spanwise distance of $\frac{\lambda}{4}$. This, in essence, determines at which point in the chordwise location at which two adjacent vortices will interact.

To understand how Equation (6) behaves, $\frac{x^*}{c}$ was plotted as a function of normalized circulation, $\frac{\Gamma}{U_\infty c}$, at various values of $\frac{h}{c}$, shown in Figure 104, as well as a function of $\frac{h}{c}$ at various values of $\frac{\Gamma}{U_\infty c}$, shown in Figure 103. While $\frac{x^*}{c}$ retains a linear dependence on $\frac{h}{c}$, it can be seen in Figure 103 that $\frac{x^*}{c}$ is highly nonlinear as circulation approaches zero.

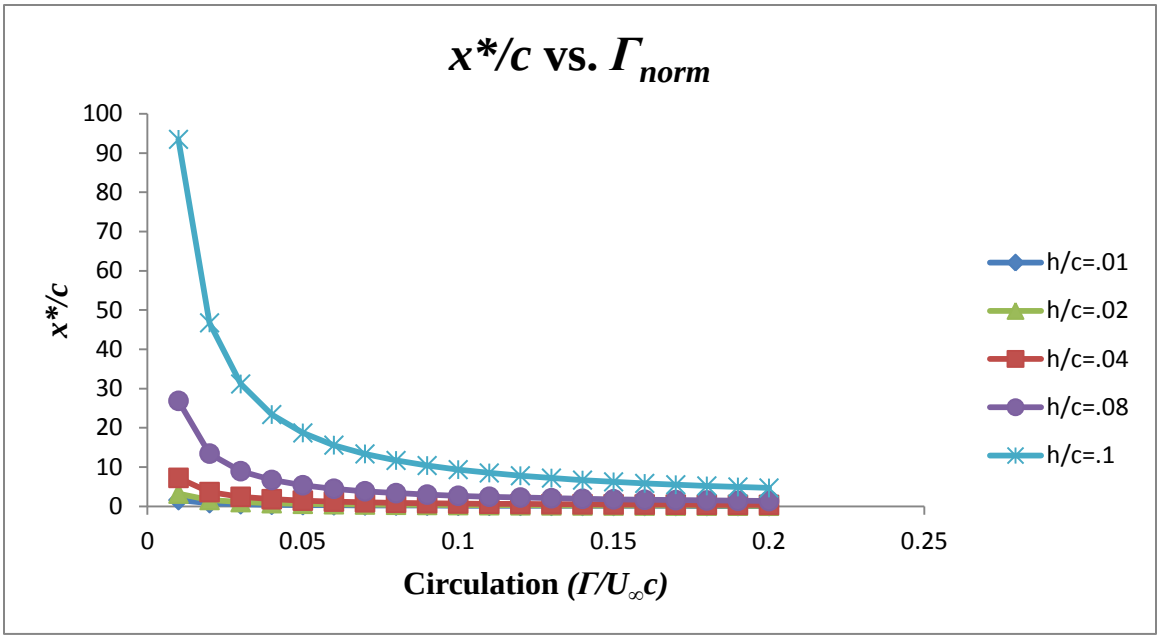

Figure 103: Effect of Γ on $\frac{x^*}{c}$

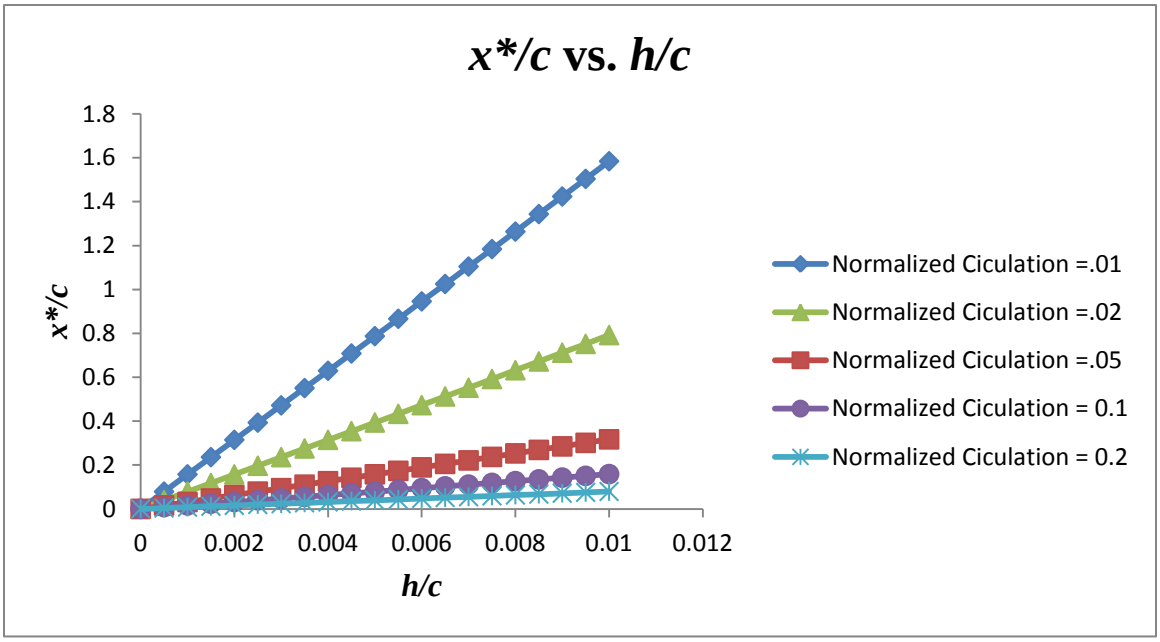

Figure 104: Effect of *h/c* on $\frac{x^*}{c}$

To determine whether the prior analysis is valid, a comparison was made between the dye visualization results and 2D Particle Image Velocimetry (PIV) on modified hydrofoils. Dye visualization allowed for the qualitative observation of vortex interaction, while PIV experiments allowed for a quantitative examination of the vortex characteristics.

Using the dye injection images, it was possible to determine an point of interaction, $\frac{x^*_{dye}}{c}$. By determining the point of interaction empirically, a comparison could be made to a calculated $\frac{x^*_{PIV}}{c}$ using Equation (6). If $\frac{x^*_{PIV}}{c}$ showed the same trends as $\frac{x^*_{dye}}{c}$, Equation (6) could be validated for hydrofoils with protuberances.

Equation (6) was applied to PIV time averaged vorticity data taken for a hydrofoil with protuberances. It was used as an attempt to predict the chordwise position, $\frac{x^*_{PIV}}{c}$, at which two adjacent vortices will interact. Although the surface geometry of the hydrofoils are not flat like the surface examined in the prior analysis, the characteristics of the near surface vortices on the shoulders of hydrofoil protuberances were similar to the row of vortices expressed earlier on the previously mentioned flat surface.

The hydrofoil section that was observed in PIV experiments allowed four vortices in the central portion of the hydrofoil to be examined. The necessary parameters used to determine $\frac{x^*}{c}$, Γ and h, were calculated by taking a geometric average over these four vortices. All other parameters were independent and held constant (i.e. $U_\infty = .15$ m/s, $c = .101$ m, $\lambda = .0508$ m) between experiments. Values for Γ and h were determined at eight angles of attack $3° \leq \alpha \leq 24°$ in increments of 3° for seven different chordwise spatial locations starting from the protuberance peaks and moving towards the trailing edge, $x = 0c, .06c, .12c, .18c, .24c, .37c, .48c$.

The procedure by which $\frac{x^*_{dye}}{c}$ was compared to $\frac{x^*_{PIV}}{c}$ is as follows:

1. Through an examination of the dye visualization photographs, the interaction point of two adjacent vortices, $\frac{x^*_{dye}}{c}$, was measured and recorded at all relevant angles of attack. Since it is valid to assume, due to symmetry, that without vortex interaction, dye streams emanating from the peaks of protuberances would continue in a straight line, the criteria used to determine $\frac{x^*_{dye}}{c}$ was the chordwise location at which the dye streams emanating from the protuberance peaks would deviate from a straight line and turn in the spanwise direction.
2. $\frac{x^*_{dye}}{c}$ was used to determine the chordwise location, for a given angle of attack, at which the parameters necessary for $\frac{x^*_{PIV}}{c}$ would be calculated.
3. Since only seven chordwise locations were examined in PIV experiments, a linear interpolation between examined chordwise locations was used to calculate the parameters needed for $\frac{x^*_{PIV}}{c}$ at chordwise locations for which PIV data was not directly available.
4. For each angle of attack, $\frac{x^*_{dye}}{c}$ was determined alongside a calculation of $\frac{x^*_{PIV}}{c}$ using Equation (6) along with the data determined in steps 1-3.

The results of this procedure can be seen in Figure 105. The plot shows $\frac{x^*_{PIV}}{c}$ vs. $\frac{x^*_{dye}}{c}$ at all relevant angles of attack. Also, a trendline has been added to show that $\frac{x^*_{PIV}}{c} \neq \frac{x^*_{dye}}{c}$. However, if a proportional constant equal to 1 divided by slope of the trendline is multiplied by $\frac{x^*_{PIV}}{c}$ (i.e. $\frac{x^*_{PIV}}{c} = \frac{x^*_{dye}}{c}$, where $B = \frac{1}{4.5701}$), Equation (6) may be used a valid description of the interaction of vortices on the 4L hydrofoil.

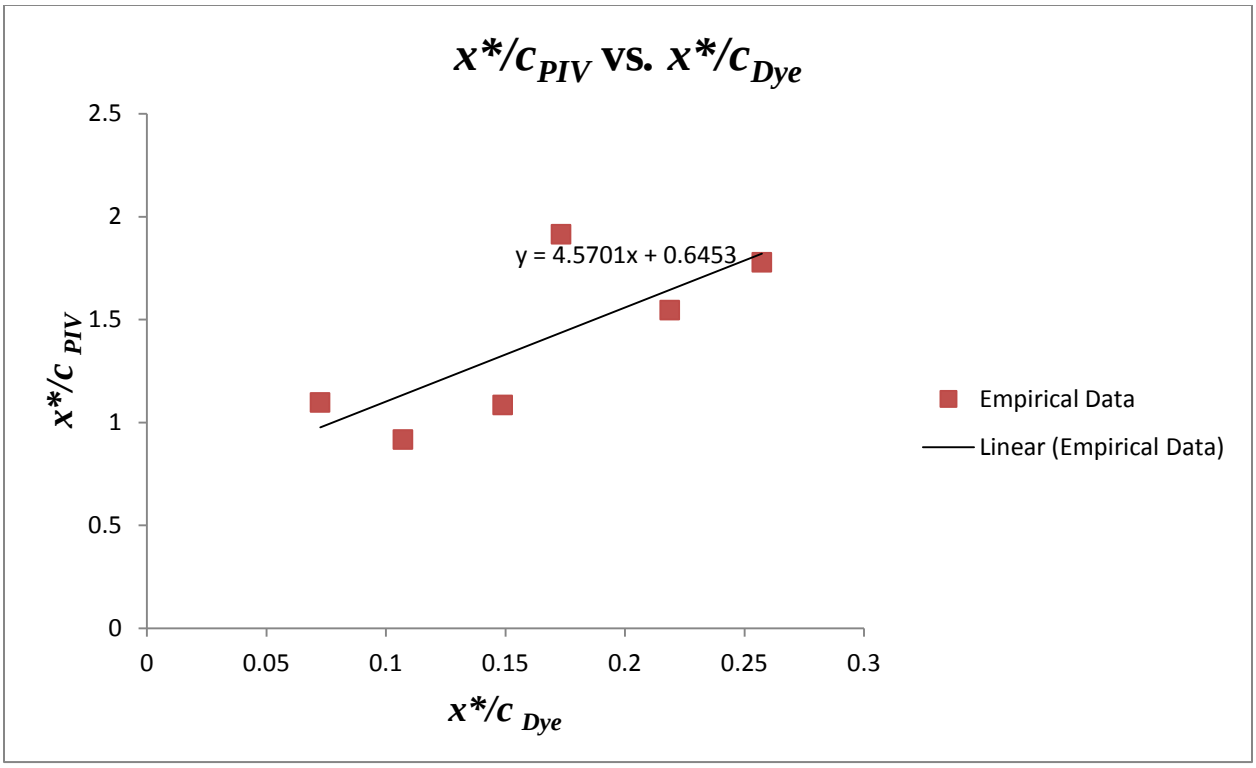

Figure 105: Comparison of the observed vortex interaction point seen in dye images to the calculated interaction point, $\frac{x^*_{PIV}}{c}$, using Equation (6).

While Figure 105 shows that there may be a proportional relationship between $\frac{x^*_{PIV}}{c}$ and $\frac{x^*_{dye}}{c}$, it is worthwhile to keep in mind the following; (1) that Equation (6) assumes that an infinite row of vortices is present. This was not true in dye experiments where a maximum of 8 vortices were present, and (2) different criteria were used to define vortex interaction for $\frac{x^*_{PIV}}{c}$ and $\frac{x^*_{dye}}{c}$. Where $\frac{x^*_{dye}}{c}$ was determined by assuming that the chordwise vortex interaction point between neighboring vortices was where dye streamlines began to veer from their straight path, $\frac{x^*_{PIV}}{c}$ was determined with the assumption that the interaction of two vortices occurred at the chordwise location that two neighboring vortex cores met.

V. Discussion

Although the inspiration of this project was drawn from the humpback whale flipper, the goal was not to determine the flow field dynamics on the flipper itself. It is clear that the flow field surrounding the flipper will be altered significantly by the presence of protuberances, and though the whale may have evolved to take advantage of the specific pattern of leading edge protuberances on its flipper, it is unlikely that this pattern is optimal for practical engineering purposes. The goal of this research was to determine the effects of protuberances on practical hydrofoil geometries using a systemic approach, examining the effect of easily understood parameters such as amplitude and wavelength rather than simply to determine the effect of protuberances on the humpback whale flipper. This type of approach promotes the optimization process in which certain applications may call for specific protuberance geometries. This section will discuss the potential implications of the work that was presented in this report.

Load measurements on modified foils show significant performance differences from their baseline counterparts. Protuberance amplitude and wavelength can play a large role in establishing the lift and drag characteristics of hydrofoils. Protuberances generate streamwise vorticity which in turn affects the foils in the following way; 1) increased lift over the baseline is produced at high angle of attack due to the low pressures generated in the core of the vortices, and 2) the streamwise vorticity is responsible for increased drag. At very low angle of attack, flow attachment governs the lift and drag characteristics of all foils tested, essentially causing the effect of protuberances to be minor. With the exception of a select few cases, at intermediate pre-stall angles the excess vorticity causes the lift and drag performance to suffer when compared to the baseline foil. However, at post-stall angles of attack, it is this vorticity that is responsible for increased lift. Also, at post-stall angels of attack, there is no drag penalty seen on the full-span

modified hydrofoil because it, along with the baseline, is acting as bluff body at very high angle, allowing additional drag due to the protuberances to be neglected.

Protuberance amplitude is the primary factor in establishing the strength of the vortices. The geometry of the modified foil leading edges produces a change in leading edge radius along the hydrofoil span. For example, the leading edge radius changes by 23% from peak to valley on the 4L and 8L hydrofoil. On the 8L hydrofoil, which has a wavelength of 0.25*c*, this change in leading edge radius is quite severe over such a small region of the hydrofoil span. The change in leading edge radius from peak to valley causes flow to accelerate at different rates along the span, and creates a pressure gradient that is responsible for generating streamwise vorticity. A larger pressure gradient is produced by larger protuberance amplitudes, in turn causing smaller amplitude protuberances to allow for baseline-like performance characteristics.

Wavelength seems to be responsible primarily for the chordwise location at which neighboring vortices will interact. It is likely that vortex interaction does not enhance the lift and drag performance characteristics of modified hydrofoils as it generates turbulence and separation effects. On the other hand, under high-speed conditions, it is responsible for eliminating the cavitation over select spanwise sections on modified hydrofoils by generating high pressure along the span.

The response of certain planform geometries to protuberances is quite complex. The response of rectangular foils to protuberances is different than the response of swept foils and flipper models. Protuberances have a dramatic effect on the spanwise flow on hydrofoils. Depending on the application, this may be beneficial. In the case of full-span models there is little spanwise flow to begin with; therefore, the addition of protuberances increases spanwise flow. This is only beneficial at high angle of attack, typically past the stall angle of the baseline

foil. Full-span models only produce enhanced loads at high angle of attack with significantly increased lift over the baseline with little to no drag penalty. Finite-span rectangular hydrofoils are capable of producing increased maximum lift of up to 13% and 18% in specific cases such as the 8S and 8M foils respectively, at the highest Reynolds number tested with very little drag increase at high angle. Interestingly, at the same Reynolds numbers, swept models produce a near linear increase in lift coefficient with angle throughout the entire range of angles of attack tested. However, any potential benefit seen in the lift performance is offset by the poor drag performance which lowers the lift-to-drag ratio such that it never outperforms the baseline at any angle. Although the values of lift coefficient were low relative to the other planform shapes tested, the flipper model also showed significant lift enhancement at high angles and at high Reynolds number, with a slight reduction in drag over a very small range of angle of attack. Although this created beneficial lift-to-drag ratio characteristics, the values were always significantly lower than the baseline counterpart at its maximum point.

It should also be noted that the maximum lift coefficient on the baseline models can vary significantly when different planform geometries are examined. For example, up to a 23% difference in maximum lift coefficient was seen when the baseline swept model and baseline swept model were compared. This should be taken into account when attempting to design practical hydrofoils for use in engineering applications. Although some of the most significant increases in performance were seen on the modified flipper model, the baseline lift performance is poor in comparison with other planform geometries.

With the response of planform geometry to leading edge protuberances kept in mind, the span efficiency factor, *e*, which is an indicator of how closely the lift distribution on a wing is to

being elliptical, was calculated for the finite-span rectangular baseline and 4L hydrofoils using the following methods[29]:

$$a = \frac{a_0}{1 + \frac{a_0}{e\pi AR}} \tag{1}$$

$$C_D = C_{D0} + \frac{C_L^2}{e\pi AR} \tag{2}$$

where a is the lift curve slope of the finite-span case of interest, a_0 is the lift curve slope of the corresponding infinite-span case, C_{D0} is the minimum drag coefficient, and AR is the wingspan aspect ratio. The above relations only hold true in the range of angles in which the lift coefficient increases linearly with angle of attack. To calculate the efficiency factor using method 2, a polynomial of order two was fit to Equation (2) for several cases in which C_D on C_L were known. The form of the curve fit was the following:

$$y = Ax^2 + B$$

where,

$$y = C_D,\ x = C_L^2,\ A = \frac{1}{e\pi AR},\ B = C_{D0}$$

The purpose of the curve fit was to determine whether measured data on both the baseline and modified foils showed that C_D held a parabolic dependency on C_L as a typical rectangular finite-span hydrofoil should. Ref. 29 shows that, using the above relations, the efficiency factor of a finite-span rectangular hydrofoil of equivalent aspect ratio to the baseline examined in this report should theoretically, under infinite Reynolds number conditions, be nearly 0.90. An efficiency factor of 0.90 indicates that the lift distribution on the finite-span rectangular hydrofoil tested should be nearly elliptical. However, Table 22 shows that regardless of the method used, the efficiency factor of neither the baseline nor modified foil is equal to the theoretical efficiency

factor, with the baseline hydrofoil lift distribution typically being closer to elliptical than the 4L hydrofoil at all Reynolds numbers examined.

The drag coefficient is shown in Figure 106 as a function of lift coefficient. The plots show that it is possible to closely predict the drag coefficient of the baseline foil at both high and low Reynolds numbers due to the parabolic dependency of C_D on C_L. However, a prediction of the drag coefficient on the modified foil is less easily made because protuberances introduce additional drag that causes the C_D to increase at a rate that does not share an identical dependency on C_L as a typical rectangular foil. It can also be inferred from the efficiency factor that leading edge protuberances affect the lift distribution on finite-span rectangular hydrofoils as well. Given the efficiency factors presented in Table 22, the effect of aspect ratio on the lift and drag coefficient can be determined using Equations 1 and 2.

Table 22: Span efficiency factor of the baseline and 4L finite-span rectangular hydrofoils.

	$Re_c = 1.8 \times 10^5$	$Re_c = 2.7 \times 10^5$	$Re_c = 3.6 \times 10^5$	$Re_c = 4.5 \times 10^5$
Baseline (relation 1)	0.75	0.76	0.70	0.72
Modified (4L) (relation 1)	0.70	0.64	0.53	0.53
Baseline (relation 2)	0.73	0.71	0.70	0.69
Modified (4L) (relation 2)	0.52	0.50	0.47	0.48

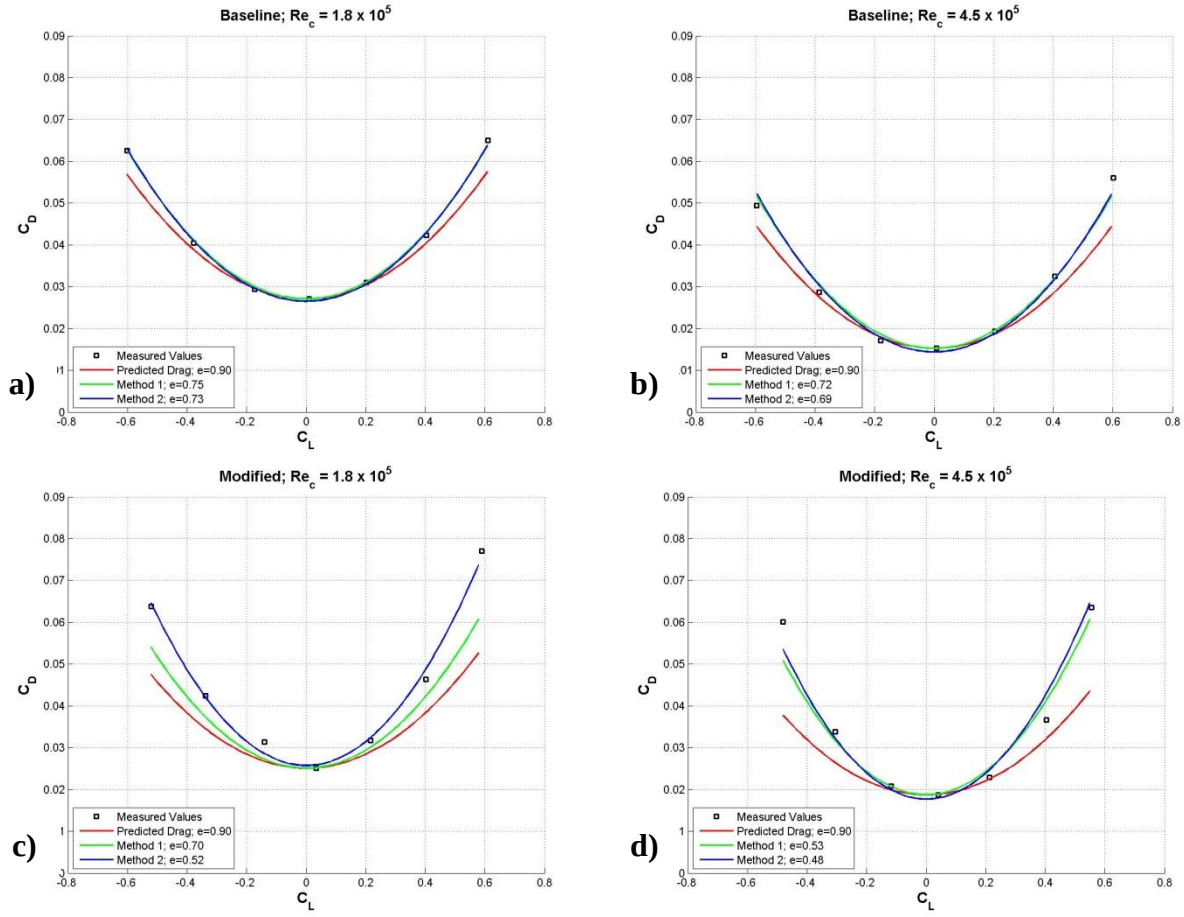

Figure 106: Drag coefficient predictions using calculated span efficiency factors. a) Baseline foil at low Re_c b) Baseline foil at high Re_c c) 4L foil at low Re_c d) 4L foil at high Re_c.

Another likely cause of performance modifications by foils with protuberances lies in their ability to alter spanwise flow. It was shown in flow visualization experiments that foils with protuberances direct flow towards or away from the valleys of the protuberances. Pressure

leakage at the wingtip is likely to diminish as the protuberances are essentially acting as fences, globally directing flow in the chordwise direction.

Reynolds number plays a small role in modifying the lift and drag of modified hydrofoils. Whereas the load characteristics show that the stall angle and angle of maximum lift change with Reynolds number up to $Re_c = 3.6 \times 10^5$, little to no change occurs at higher non-cavitating Reynolds numbers. This implies that predictions of the load characteristics can be made for high Reynolds number flows.

The general pattern of vortex interactions stemming from protuberance shoulders can be described using potential flow theory and the vortex dynamics of a series of vortices near a flat surface. Although the vortex interaction model presented in this report is an attempt to predict the chordwise location at which two neighboring vortices will interact, it is a static model and does not take into account that the system is dynamically changing. The vortex interaction model presented here predicts that instabilities arise even in a symmetric system of vortices. It also predicts that the pattern is bi-periodic with neighboring vortices either merging or diverging; patterns which were seen qualitatively in dye experiments. Also, the dependency of induced vortex velocities associated with the vortices on circulation and vortex height above the foil surface are seen in qualitative dye experiments. Because vortex circulation is dependent on the hydrofoil angle of attack, it was shown that interaction point of two neighboring vortices moves toward the leading edge with increasing angle, another feature of vortex interactions seen in qualitative experiments. Although the model does not perfectly predict the interaction point of two neighboring vortices, the mechanisms of several important characteristics of the streamwise vorticity seen on the protuberances could be explained.

It seems as though the use of leading edge protuberances must be specific to the application being considered. Specific protuberance geometries must be chosen carefully for specific applications. For example, potential applications on control surfaces may be plausible. In many naval applications high speed turning maneuvers are necessary, therefore with prior knowledge that a protuberance pattern resembling that of the 8M rectangular hydrofoil is capable of generating a higher maximum lift coefficient at high angle of attack than its baseline equivalent, it may be possible that similar leading edge geometries could be taken advantage of. However, it must be considered that most engineered systems do not cross the stall angle, with typical control surfaces remaining in the linear regime of lift coefficient. To use the load characteristics of protuberances to their full potential, it may be necessary to implement them into an active flow control mechanism which only uses protuberances at high angle of attack. This would avoid excessive drag produced at low angle of attack. For all tests presented in this dissertation, the maximum aerodynamic efficiency (L/D) of modified foils was never greater than the baseline. This implies that modified foils may not be useful on applications which require high glide ratios such as airplane wings and submarine bow planes.

On the other hand, if cavitation effects outweigh the load performance of a hydrofoil application, it is possible that the cavitation may be mitigated by the addition of protuberances. Once again, because incipient cavitation numbers can be significantly higher on modified foils, an active mechanism which takes advantage of protuberances at high angle is likely to be most beneficial.

This dissertation presents the first set of tests on the effect of parameters such as protuberance size and shape on hydrofoil performance. However, several protuberance geometries that were tested produced various and often non-intuitive results. Therefore, it is clear

that geometry optimization is necessary to apply this work to existing airfoil and hydrofoil technology.

VI. Conclusions

The work presented here represents the initial systematic study examining the effect of leading edge protuberances on hydrofoil performance. The geometries chosen for these studies are meant to be reasonable in a general sense, with the goal of practical applications for hydrofoils with protuberances in mind.

Load Measurements

The load characteristics of modified foils with protuberances were examined. Several protuberance geometries and planform shapes were examined at a variety of Reynolds numbers ranging from $9.0 \times 10^4 \leq Re_c \leq 4.5 \times 10^5$. The tests revealed a number of performance differences between modified foils and their baseline counterparts. Although the load measurements were performed at several Reynolds numbers, the following statements will be made for Reynolds numbers above $Re_c = 1.8 \times 10^5$ because due to experimental limitations, tests at lower Reynolds numbers produced results with the highest uncertainties. With this in mind the following can be said for the force and moment measurements:

1. Whereas the baseline hydrofoils performed typically for the type of airfoil profile tested, modified foils showed increases in angle of attack, stall characteristics that were softened or eliminated altogether, and in select cases increased maximum lift and reduced drag coefficient was seen.
2. Reynolds number has little effect on the lift and drag coefficients of all foils. Stall angle, angle of maximum lift, and maximum lift coefficient increase with Reynolds number up to $Re_c = 3.6 \times 10^5$. However, past a Reynolds number of $Re_c = 3.6 \times 10^5$ the lift characteristics change negligibly. The drag coefficient changes little over the entire range of angles tested for all hydrofoil planform shapes.

3. With the exception of the modified flipper model, which showed a lower drag coefficient than its baseline equivalent over a limited ranges of angles of attack of $17° < \alpha < 22°$, all foils showed comparable or greater values for drag coefficient than their baseline counterparts over all angles of attack and Reynolds numbers tested.
4. With the exception of the modified swept hydrofoil, which showed a reduced lift curve slope in the linear regime, all other foils showed lift curve slopes comparable to their baseline counterparts.
5. The 8S and 8M rectangular planform hydrofoils showed from 13% - 18% higher maximum lift coefficients than their baseline counterpart at several Reynolds numbers over a range of angles of $16° \leq \alpha \leq 22°$. All other modified foils showed a maximum lift coefficient comparable to their baseline equivalents, within experimental uncertainty.
6. The modified flipper model showed slightly greater lift-to-drag ratio at high Reynolds number than the baseline case over a limited range of angles of $16° \leq \alpha \leq 22°$. The values at these angles, however, are significantly lower than the maximum values of the baseline model. All other modified foils showed lift-to-drag ratios either lower than or comparable to the baseline case.
7. Of all planform cases tested, protuberances affect the swept foil most. Drag is much higher than the baseline case over the range of angles and Reynolds numbers tested. On the other hand, the lift coefficient remains nearly linear throughout the entire range of angles tested. It is likely that the introduction of protuberances affects the spanwise flow characteristics of the baseline foil.

Flow Visualization Measurements

Particle Image Velocimetry (PIV) experiments were carried out on full-span and finite-span hydrofoils. The objective of the tests was to examine the flow field at both low and high Reynolds number to determine the physical mechanisms responsible of any performance alterations seen in load testing. The following conclusions can be drawn from flow visualization measurements:

1. Streamwise vorticity produced by a spanwise pressure gradient that is generated by the change in leading edge radius from peak to valley is responsible for generating lift at high angle of attack.
2. Neighboring vortices produced by the leading edge of modified foils are counter-rotating and the circulation of these vortices increases with angle of attack.
3. The proximity of neighboring vortices to each other and to the hydrofoil surface causes them to interact.
4. Knowledge of vortex circulation and proximity to the hydrofoil surface, allows for a prediction to be made as to the chordwise position at which neighboring vortices interact.
5. Protuberances have little effect on the wingtip vortex at low angles of attack. However, depending on the Reynolds number, at high angle of attack, the additional lift generated by modified foils is responsible for keeping the wingtip vortex intact past the stall angle of the baseline hydrofoil.

Cavitation

A series of tests were conducted to determine the effect of protuberances on the cavitation on the performance of finite-span rectangular and swept modified foils. Load

measurements were performed along with corresponding photographs and incipient cavitation number calculations. From these experiments, the following can be concluded:

1. The lift coefficient of the modified finite-span rectangular foils is greater than the baseline foil over a limited range of angles of attack of $17° < \alpha < 22°$ under cavitating conditions. The swept planform hydrofoils do not outperform the baseline case over the entire range of angles tested.
2. With the exception of the rectangular planform hydrofoils with a protuberance amplitude of $A = 0.12c$, which showed a modified drag coefficient at high angle of attack, drag on the modified foils remained comparable to the baseline throughout all modified cases.
3. Images show that cavitation on modified foils is most severe directly behind the troughs of protuberances, whereas the baseline hydrofoil showed sheet cavitation over the entire foil span.
4. The incipient cavitation number of the baseline foil is always less than the modified cases, implying that for a given local static pressure, modified foils will always cavitate at lower velocities than their baseline counterparts.
5. At high angle of attack, the cavitation number of the 8L foil is much greater than all other foils tested. This is most likely due to the proximity of protuberances, which leads to the most significant peak-to-valley pressure gradient of all foils tested.

VII. Future Work

Several extensions of this work should be considered. This work has examined the effect of only a few possible protuberance geometries and planform shapes, occasionally showing varied results. Because of this, the results presented here are somewhat limited in their scope. Introducing various parameters to the study presented here could lead to a more complete understanding of the altered flow and performance characteristics that were seen throughout this work. Some geometrical features that should be studied are as follows: 1) the effect of a dynamically changing angle of attack, 2) the response of a flexible hydrofoil to leading edge protuberances, 3) the effect of non-sinusoidal and non-uniform protuberance geometries.

Due to the limited range of planform and protuberance geometries studied here, an optimization study showing how the protuberance geometry generally affects the performance of hydrofoils would be extremely useful as some of the results presented here lead to the conclusion that the implementation of leading edge protuberances are application specific. An optimization study on the effect of protuberance geometry would enhance the understanding of how certain protuberance geometries could be effectively applied to existing hardware.

The flipper morphology is very complex. The features that make the flipper unique, such as the planform shape and the distribution of protuberances should be examined further. This work showed that streamwise vorticity and vortex interactions arise prominently on spanwise uniform protuberances. However, the flipper geometry is not uniform and varies with span. This may imply that there is an optimal protuberance geometry that leads to diminished detrimental effects. Therefore, an investigation on the humpback whale morphology would be a very useful supplement to this research.

References

1. Fish, F. E. and Battle, J. M., "Hydrodynamic Design of the Humpback Whale Flipper," *Journal of Morphology*, Vol. 225, 1995, pp. 51-60.

2. Fish, F. E. and Lauder, G. V., "Passive and Active Flow Control by Swimming Fishes and Mammals," *Annual Review of Fluid Mechanics*, Vol. 38, Jan. 2006, pp. 193-224.

3. Bushnell, D. M. and Moore, K. J., "Drag Reduction in Nature," *Annual Review of Fluid Mechanics*, Vol. 23, January 1991, pp. 65-79.

4. Fish, F. E., "Performance Constraints on the Maneuverability of Flexible and Rigid Biological Systems," *Proceedings of the Eleventh International Symposium on Unmanned Untethered Submersible Technology (UUST)*, UUST99, Durham, New Hampshire, August 1999, pp. 394-406.

5. Miklosovic, D. S., Murray, M. M., Howle, L. E., and Fish, F. E., "Leading-edge Tubercles Delay Stall on Humpback Whale (*Megaptera novaeangliae*) Flippers," *Physics of Fluids*, Vol. 16, No. 5, May 2004, pp. L39-42.

6. Miklosovic, D. S., Murray, M. M., and Howle, L. E, "Experimental Evaluation of Sinusoidal Leading Edges," *Journal of Aircraft; Engineering Notes*, Vol. 44, No. 4, July-August 2007, pp. 1404-1407.

7. Johari, H., Henoch, C., Custodio, D., and Levshin, A., "Effects of Leading Edge Protuberances on Airfoil Performance," *AIAA Journal*, Vol. 45, No. 11, 2007, pp. 2634-2642.

8. Weber, P. W., Howle, L.E., Murray, M. M., "Lift, Drag, and Cavitation Onset on Rudders with Leading-Edge Tubercles," *Marine Technology*, Vol. 47, No. 1, January 2010, pp. 27-36.

9. Bearman, P. W. and Owen, J. C., "Reduction of Bluff-Body Drag and Suppression of Vortex Shedding by the Introduction of Wavy Separation Lines," *Journal of Fluids and Structures*, Vol. 12, 1998, pp. 123-130.

10. Bearman, P. W. and Tombazis, N., "The Effect of Three-Dimensional Imposed Disturbances on Bluff Body Near Wake Flows," *Journal of Wind Engineering and Industrial Aerodynamics*, Vol. 49, 1993, pp. 339-350.

11. Owen, J. C. and Bearman, P. W., "Passive Control of VIV with Drag Reduction," *Journal of Fluids and Structures*, Vol. 15, 2001, pp. 597-605.

12. Sunada, S., Sakaguchi, A., and Kawachi, K., "Airfoil Section Characteristics at a Low Reynolds Number," *Journal of Fluids Engineering*, Vol. 119, March 1997, pp. 129-135.

13. Tanner, M., "A Method of Reducing the Base Drag of Wings with Blunt Trailing Edges," *Aeronautical Quarterly*, Vol. 23, 1972, pp. 15-23.

14. Tombazis, N. and Bearman, P. W., "A study of Three-Dimensional Aspects of Vortex Shedding from a Bluff Body with a Mild Geometric Disturbances," *Journal of Fluid Mechanics,* Vol. 330, 1997, pp. 85-112.

15. Cebeci, T., Clark, R.W., Chang, K.C., Halsey, N.D. and Lee, K., "Airfoils with Separation and the Resulting Wakes," *Journal of Fluid Mechanics*, Vol. 163, 1986, pp.323-347.

16. Hoarau, Y., Braza, M. Ventikos, Y., Faghani, D., and Tzabiras, G., "Organized Modes and Three-dimensional Transition to Turbulence in the Incompressible flow around a NACA0012 Wing," *Journal of Fluid Mechanics,* Vol. 496, September 2003, pp. 63-72.

17. Gad-el-Hak, M. and Bushnell, D.M., "Separation Control: Review," *Journal of Fluids Engineering*, Vol. 113, 1991, pp. 5-30.

18. Watts, P. and Fish, F. E., "The Influence of Passive, Leading Edge Tubercles on Wing Performance," *Proceedings of Unmanned Untethered Submersible Technology (UUST),* UUST01, Autonomous Undersea Systems Institute, Durham, New Hampshire, August 2001.

19. Stein, B., Murray, M. M., "Stall Mechanism Analysis of Humpback Whale Flipper Models," *Proceedings of Unmanned Untethered Submersible Technology (UUST), UUST05*, Durham, New Hampshire, August 2005.

20. Murray, M. M., Miklosovic, D. S., Fish, F. E., and Howle, L., "Effects of Leading Edge Tubercles on a Representative Whale Flipper Model at Various Sweep Angles," *Proceedings of Unmanned Untethered Submersible Technology (UUST), UUST05, Durham*, New Hampshire, August 2005.

21. Pedro, H.T.C. and Kobayashi, M.H., "Numerical Study of Stall Delay on Humpback Whale Flippers," *46th AIAA Aerospace Sciences Meeting and Exhibit,* Reno, NV, January 2008, AIAA paper 2008-0584.

22. Hansen, K. L., Kelso, R. M., and Daily, B. B., " An Investigation of Three-Dimensional Effects on the Performance of Tubercles at Low Reynolds Numbers," *Proceedings of 17th Australasian Fluid Mechanics Conference*, Auckland, New Zealand, December 2010.

23. Naumann, A., Morsbach, M., and Kramer, C., "The Conditions of Separation and Vortex Formation Past Cylinders*," AGARD conference proceedings no. 4, Separated Flows*, 1966, pp. 539-574.

24. Custodio, D., "The Effect of Humpback Whale-Like Leading Edge Protuberances on Hydrofoil Performance," M.S. Thesis, Worcester Polytechnic Institute, Worcester, MA, 2007.

25. Pope, A. and Rae, W.H., *Low-Speed Wind Tunnel Testing*, 2nd ed., Wiley, NY, 1984, Chap. 6.

26. Wheeler, A. J. and Ganji, A. R., *Introduction to Engineering Experimentation*, Prentice-Hall, Inc., NJ, 1996, Chap. 7.

27. Coleman, H. and Steel, W., "Experimentation and Uncertainty Analysis for Engineers," Wiley-Interscience, 1989.

28. Abbott, I.H., and von Doenhoff, A.E., "Theory of Wing Sections," Dover, New York, 1959.

29. Anderson, J.D., "Fundamentals of Aerodynamics," McGraw-Hill, New York, 2001.

30. Lock, C., "Are Propellers Fin-nished," sciencenewsforkids.com/2012/04/like-mother-nature/, Science News, April 2012.

31. Oosthoeck, S., "Cool Jobs: Like Mother Nature," sciencenewsforkids.com/2004/09/are-propellers-fin-ished-2/, Science News, September, 2004.